Thermal Plumes from Staged Multiport Diffusers in Uniform Quiescent Environment

Thesis by
Kit Yin Ng

In Partial Fulfillment of the Requirements
for the Degree of
Doctor of Philosophy

California Institute of Technology
Pasadena, California

1990

(Submitted October 16th, 1989)

ACKNOWLEDGEMENTS

I wish to express my deepest gratitude to my advisor, Dr. Norman H. Brooks. He has always been patient, understanding, and encouraging. I admire his sharp physical insight, and am most grateful for his invaluable advice during the preparation of this thesis. I am very fortunate to have had him as my advisor. Special thanks go to Dr. Robert C. Y. Koh for his constant support in many ways. I am deeply impressed by his MAGIC, and honestly think that everyone should learn how to use it. His great help will always be remembered. I also want to thank Drs. E. J. List, Frederic Raichlen and Edward E. Zukoski for serving in my thesis committee.

This project was sponsored by the Southern California Edison Company. In particular, I would like to thank Robert Grove, John Palmer and Jennifer Yuge for their technical support.

The assistance of Joe Fontana, Hai Vu and Rich Eastvedt in the setting up of my experiments is greatly appreciated. It has been a very enjoyable experience working in the subbasement because of them. Joan Mathews and Frances Matzen have been very kind and helpful. I always enjoy the usual "8-minutes" chatting before the meetings with my advisor. Rayma Harrison and Gunilla Hastrup are the most wonderful librarians on campus. Together, they made Keck Lab a very warm place to be. Pat Rankin has been very helpful on many occasions. Nancy Tomer assisted in drafting most of the figures in the thesis.

Many people have contributed in keeping my life at Caltech free from boredom. I shall start with my former and present officemates. I enjoyed all the long hours of the Friday afternoon discussions with Dennis A. Lyn on topics of life, intervened with a little bit of fluid mechanics. Mike Scott has initiated my appreciation of American history. Mark Schlautman has been a loving and caring friend, though he might never have thought that my last stage of thesis preparation would accidentally become his

nightmare during the last month (if he still got some time to sleep). Without his help, it would have been quite impossible for me to have finished my thesis now. Theresa Wang, Liyuan Liang, J. J. Wu, Francis Ting, Russell Mau, Marco Rasi, Sandy Elliot and Stanley Grant have shared and brightened up many moments at Keck. I am also thankful to Dr. Jeff Zelt for helping me get started on the Tex macros. It has always been joyful being a friend of Billy and Justin. Elena has been very nice to me. Although the time we have known each other is short, it has been definitely memorable, and I shall never forget the note that she wrote me. Bubble and May May are my most adorable roommates at Del Mar. I enjoyed very much being a roommate of Adiel Guinzburg and of Andrea Donnellan.

My six dear friends; Kan, Chestnut, Fried Chicken, Credit, Macho Wai and Michael; although they are in Hong Kong, I always have them in my mind. The wonderful memories that we have had together always lightened up the depressing moments. The helpfulness and gentleness of Margaret Lee are greatly appreciated.

I treasure the very precious friendship of Andy Waite and Agnes Allard. During my first-year struggle at Caltech, Andy was always there to offer his support. His caring and loving stay with me forever. Although our friendship started only six months ago, Agnes already has helped me regain myself in my toughest days. Knowing her is the best thing that has happened to me at Caltech.

Andy Hong is a very special friend of mine. Together we have gone through many sunny days and stormy days. He has been both supportive and encouraging, especially at times of difficulties.

My best friend Ying-Keung Poon has a strong influence in my growing-up process. The list of things for which I want to thank him is endless; for one thing, he got me interested in coming to the States for graduate study. I cannot help but thank him for being my best friend.

Being the youngest, I have had the "disadvantage" of being spoiled by every member of my family. They always support wholeheartedly whatever I choose to do. Even though we are thousands of miles apart, their love is alway heartfelt. They are forever most important to me. Here, I dedicate my thesis to my family.

ABSTRACT

The behavior of thermal plumes discharged from staged diffusers has been investigated experimentally. A staged diffuser is a type of submerged multiport diffuser characterized by an offshore orientation of the individual nozzles. It is commonly employed for the discharge of heated water from coastal power plants into the ocean because of its effective mixing capability, which does not depend on the prevailing longshore-current directions.

Experiments have been performed to measure the temperature distribution of the plume in a quiescent receiving water. The three-dimensional thermal field is reconstructed from the results of two groups of measurements, the centerline experiments in which the temperature in the vertical plane along the diffuser axis is measured, and the scanning experiments in which the lateral temperature profiles are measured. The emphasis is on a homogeneous ambient receiving water, but a few illustrative experiments with ambient stratification have been carried out. The number of variables associated with the problem is very large, making it difficult to perform a generic study. Nevertheless, five of the variables (the number of ports, n, the initial jet diameter, D_0, the horizontal orientation of the jet, α, the total discharge flow rate, Q_{T0}, and the water depth, H) have been examined.

Experimental observations support the hypothesis of a near field dominated by

momentum jet mixing, and an intermediate field dominated initially by turbulent mixing and eventually by gravitational spreading. H, n and D_0 are the governing parameters in both the near field and the intermediate field. By coupling dimensional analysis with experimental results, several empirical relationships have been established to give a first-order approximation relating the mean characteristics of the plume to the governing parameters. It is found that the near-field dilution can be described adequately by the simple jet model with an adjustment factor based on n. The dilution in the intermediate field, however, is relatively insensitive to n. It is also concluded that the horizontal orientation of the jet, at $\pm 25°$ to the diffuser axis, helps to spread the plume over a wider extent, thereby reducing the maximum temperature rise. Results from stratified experiments indicate that for weak stratification, the dynamics of the plume is not significantly modified.

TABLE OF CONTENTS

Chapter Page

Chapter Page

Chapter Page

LIST OF TABLES

Table Page

LIST OF FIGURES

Figure Page

Figure Page

Figure Page

Figure Page

Figure Page

Figure Page

Figure Page

Figure | Page

Figure Page

Figure Page

LIST OF SYMBOLS

a_1 empirically determined coefficient (3.3.2)

A_0 area of individual jet at discharge ($\pi D_0^2/4$) (6.2.1)

$A_{0.1}$ surface area with $\Delta T/\Delta T_0 \geq 10\%$ (5.5)

$A_{0.2}$ surface area with $\Delta T/\Delta T_0 \geq 20\%$ (5.5)

b nominal half-width of jets and plumes (2.6.1)

b_0 discharge kinematic buoyancy flux per unit length of diffuser (used in Almquist and Stolzenbach's model) (2.4.3)

b_1 width of plume at end of the diffuser zone, taken as the total width of the surface temperature profiles with $\Delta T/\Delta T_0 \geq e^{-1}(T_{s1})$ (5.5) (6.2)

b_2 the total plume width at x_t (5.5)

b_{I0} characteristic width of the surface layer at the initial section of the intermediate field (3.3.3)

B width of equivalent slot orifice ($D_0^2\pi/4s$) (2.4.2)

B_{i0} initial buoyancy flux per individual jet (3.3.1) (5.1)

B_{I0} buoyancy flux at the initial section of the intermediate field (3.3.3)

B_{T0} total initial buoyancy flux per diffuser (3.3.1) (5.1)

$c_1 ... c_6$ empirically-determined coefficients (Chapter 6)

C_c coefficient of contraction (5.6)

C_D discharge coefficient (5.6)

C_p specific heat capacity (4.6)

d pipe diameter (5.6)

D_0 initial diameter of individual jet (at vena contracta) (2.4.2) (3.1) (5.1)

D_0' orifice diameter (5.1) (5.6)

D_T distance along the trajectory of the jet from the source to the water surface (6.2.2)

E_T head of water (depth above the center level of the orifice) (5.6)

f', F general functions (3.3.1) (3.3.2)

Fr_0 densimetric Froude number of individual jet ($u_0/\sqrt{g'_0 D_0}$) (3.3.2) (5.1)

g gravitational acceleration (981 cm/s^2) (3.3)

g' reduced gravity ($g\Delta\rho/\rho$) (3.3.1) (4.3) (5.1)

g'_0 initial reduced gravity of the discharge (4.3)

h depth of the mixed layer (4.6)

h characteristic thickness of the surface layer (4.3)

h_1 characteristic thickness of the surface layer at end of the diffuser zone, defined as the depth from surface to $\Delta T_c/\Delta T_0 = T_{b1} + e^{-1}(T_{s1} - T_{b1})$ (5.5) (6.2)

h_2 the charcteristic thickness of the surface layer at x_t (5.5)

h_{I0} characteristic thickness of the surface layer at the initial section of the intermediate field (3.3.3)

H water depth above discharge level (2.4.3) (3.1) (5.1)

H' depth of water from the sea bottom to jet level (3.1)

k temperature decay constant ($k = 1/x'_t$) (6.3.4)

K diffuser parameter used by Jirka (1982) and Almquist and Stolzenbach (1980). ($K = \sqrt{4HL/n\pi D_0^2}$ in Jirka's model and $= \sqrt{(4HL\cos\alpha\cos\beta)/n\pi D_0^2}$ in Almquist and Stolzenbach's model) (2.6.1) (6.2.1)

K_e entrance loss coefficient (5.6)

K_h surface heat exchange coefficient (4.6)

ℓ characteristic length scale (1.4)

ℓ'_B length scale for buoyancy in a stratified ambient (3.3.1)

ℓ_m momentum length scale for equivalent slot orifice used by Jirka (1982) and Almquist and Stolzenbach (1980) (2.4.3)

ℓ'_M length scale for momentum in a stratified ambient (3.3.1)

ℓ_M momentum length scale of individual jet (3.3.1) (5.1)

ℓ_Q length scale for the size of a three-dimensional jet (3.3.1) (5.1) (6.2.1)

L length of diffuser (L is 90 cm for 16-port diffuser, 18 cm for 4-port cases and again taken as 90 cm for the single-port case for normalizing purposes) (2.6.1) (5.1)

L_r geometric ratio (1.4)

L_s length scale for the temperature decline in the intermediate field defined as $L_s = \ell_M^{1/2}(\sqrt{n}\ell_Q)^{1/6}H^{1/3}$ (6.3.4)

m_0 discharge kinematic momentum flux per unit length of diffuser (2.4.3) (2.6.1)

$M(x)$ total integrated momentum flux at section x (2.6.1)

M_{i0} discharge kinematic momentum flux for individual jet (3.3.1) (5.1)

M_{I0} kinematic momentum flux at the initial section of the intermediate field (3.3.3)

M_{T0} total discharge kinematic momentum flux per diffuser (3.3.1) (5.1)

n number of ports in the diffuser (2.6.1) (3.1) (5.1)

q_0 discharge volumetric flux per unit length of diffuser (2.6.1)

Q flow rate discharging through a nozzle (in air) (5.6)

Q_e entrained volumetric flux used by Almquist and Stolzenbach (1980) (2.6.1)

Q_{i0} discharge volumetric flux for individual jet (3.3.1) (5.1)

Q_{I0} volumetric flux at the initial section of the intermediate field (3.3.3)

Q_{T0} total discharge volumetric flux per diffuser (3.1) (5.1)

Re Reynolds number ($u\ell/\nu$) (1.4) (3.3.1)

Re_0 discharge Reynolds number of individual jet ($u_0 D_0/\nu$) (1.4)

s spacing of jets (2.4.2) (3.1) (5.1)

S flux-averaged dilution (6.2.1)

S_2 intermediate-field dilution (6.3)

S_a asymptotic value for dilution in the near field used by Jirka (1982) and Almquist and Stolzenbach (1980) (6.2.5)

S_c minimum near-field surface dilution, defined as $(T_{peak})^{-1}$ (3.3) (6.2.1)

S_{bulk} volumetric bulk dilution (2.6.1) (3.3.2)

$(s/H)_{cr}$ critical spacing-to-depth ratio for jet merging (3.3.2) (6.6)

T temperature (3.3.1)

T_0 discharge temperature of effluent (3.3)

T_{kL} Surface $\Delta T_c/\Delta T_0$ (along diffuser axis) at kL downstream of end of diffuser, for $k = 1/2, 1, 2, 4$. The length L is taken as the diffuser length for the 16-port experiments (90.0 cm = 15 spacings) and for the 4-port experiments (18.0 cm = 3 spacings). For the single jet experiments the length L was arbitrarily taken as 90.0 cm for data presentation. (5.5)

T_{mH} Surface $\Delta T_c/\Delta T_0$ (along diffuser axis) at mH downstream of end of diffuser for $m = 4, 8, 16, 32, 64, 128$. (5.5)

T_a ambient temperature (3.3)

T_{b1} centerline bottom $\Delta T_c/\Delta T_0$ at end of the diffuser zone (5.5)

T_{b2} the bottom $\Delta T_c/\Delta T_0$ corresponding to T_{asym} (5.5)

T_{s1} centerline surface $\Delta T_c/\Delta T_0$ at end of the diffuser zone (6.3.2)

T_{asym} asymptotic value of $\Delta T_c/\Delta T_0$ beyond surface buoyant jet zone (5.5) (6.3)

T_{peak} peak surface $\Delta T_c/\Delta T_0$ (along diffuser axis) (5.5) (6.2)

ΔT temperature excess of the plume relative to ambient temperature $(T(x,y,z) - T_a(x,y,z))$ (2.6.1)

$\Delta T(h_1)$ temperature excess of discharge relative to ambient at the depth h_1 (6.2.3)

ΔT_0 initial temperature excess of discharge relative to ambient at discharge level $(T_0 - T_a)$ (2.6.1) (3.1) (5.1)

$\Delta T_c(x)$ temperature excess of discharge relative to ambient along the centerline (diffuser axis) (6.2.1)

ΔT_{s1} temperature excess of discharge relative to ambient at the end of the diffuser zone (5.5) (6.3.2)

ΔT_{asym} asymptotic temperature excess of discharge relative to ambient in the intermediate field (6.3.1)

ΔT_{bottom} temperature excess of discharge relative to ambient at the bottom of the water column (6.2.3)

ΔT_{peak} maximum temperature excess of discharge relative to ambient along the centerline (diffuser axis) (6.2.2)

$\Delta T_{surface}$ temperature excess of discharge relative to ambient at the water surface (6.2.3)

u characteristic discharge velocity (1.4)

u_0 discharge velocity of an individual jet (3.3)

v gravitational spreading velocity (4.3)

V_a cross-flow velocity (2.6.1)

V_t propagation velocity of the center of the radially spreading plume in the intermediate field (5.5)

$w_1 ... w_4$ geometric distances between jet boundaries (3.3.2)

x downstream distance in the direction of the diffuser axis (2.6.1)

x' downstream distance referenced from the end of the diffuser; for single-port cases, end of diffuser is taken as the port itself (6.3.4)

$x_{0.1}$ distance downstream from end of diffuser with $\Delta T_c/\Delta T_0 \geq 10\%$ (5.5)

$x_{0.2}$ distance downstream from end of diffuser with $\Delta T_c/\Delta T_0 \geq 20\%$ (5.5) (6.4)

x_t the "transition distance" from end of the near field to the corresponding longitudinal position of T_{asym} (5.5) (6.3)

x'_t distance from the end of the diffuser zone to the position

where $(\Delta T(x) - \Delta T_{asym})/(\Delta T_{s1} - \Delta T_{asym}) = e^{-1}$ (6.3.4)

x_T transition distance from three-dimensional flow field to two-dimensional flow field used by Almquist and Stolzenbach (1980) (2.6.1)

x_ν virtual source distance used in Jirka's staged diffuser model (1982) (2.6.1) (6.2.1)

y lateral distance perpendicular to the diffuser axis (2.6.1)

z vertical distance from jet level (3.3)

α horizontal orientation of the jet with respect to the diffuser axis (2.2) (3.1) (5.1)

α_p coefficient of thermal expansion (3.3)

β vertical angle of the jet up from horizontal (2.4.3) (3.1) (5.1)

β_k spreading angle of the half-width of a 3-D simple jet (3.3.2)

δ $-g/\rho_a(\partial\rho/\partial z)$ (3.3.1)

ϵ lateral growth rate of total plume width at surface (5.5) (6.2)

γ entrainment coefficient for a general buoyant jet (2.6.1) (6.2.1)

γ_c cross-flow entrainment coefficient (2.6.1)

γ_{rj} entrainment coefficient for round jet (2.4.1)

γ_{rp} entrainment coefficient for round plume (2.4.1)

γ_{sj} entrainment coefficient for slot jet (plane jet) (2.4.1)

γ_{sp} entrainment coefficient for slot plume (2.4.1)

κ spreading rate of the half-width of the concentration profiles of a three-dimensional simple jet (2.6.1)

λ spreading ratio of heat versus momentum (6.2.1)

ν kinematic viscosity (1.4) (3.3)

ϕ_i variables representing mean characteristics of the plume (3.3)

ρ fluid density (4.6)

ρ_0 density of the initial discharge effluent (3.3)

ρ_a density of the ambient water (3.3)

$\Delta\rho$ $\rho - \rho_a$ (3.3.1)

$\partial\rho/\partial z$ density gradient in the vertical direction (3.3)

$\partial\rho_a/\partial z$ density gradient of the ambient in the vertical direction (3.3)

$\xi_1 ... \xi_7$ empirically determined powers (Chapter 6)

1. Introduction

1.1 Historical Background

Waste-heat disposal has always been a concern in the electric power generation process. Because the overall efficiencies of nuclear and fossil-fueled power plants are between 30% to 40%, a vast quantity of unusable thermal energy is inevitably released to the environment. With the ever increasing global demand for electrical power and, at the same time, an increasing awareness of environmental impacts, the concern becomes more acute.

Cooling water recirculation systems such as closed-cycle cooling and once-through cooling have been developed to transfer the waste heat from condensers of power plants. In closed-cycle operations, the cooling water continuously recirculates in the system, and the disposal of the excess thermal energy relies on direct heat loss to the atmosphere from cooling ponds, or from wet or dry cooling towers. The once-through cooling alternative operates by withdrawing cool water from a large natural body of water and discharging heated water through an outfall back to the same water body. The excess heat (10°C to 20°C rise in temperature) in the effluent is reduced initially by turbulent mixing with the ambient water and eventually by heat transfer to the atmosphere. The once-through cooling method proves to be economically and

technically viable when nearby receiving water bodies are available and sufficiently large.

Early designs of thermal outfalls for cooling water disposal in once-through systems usually took the form of a surface discharge or a simple submerged discharge. The surface discharge employs an open channel which ends at a shoreline of a nearby beach, river or tidal estuary. The simple submerged discharge utilizes a single pipe that extends to the bottom of an adjacent lake or coastal ocean.

Because of the tremendous amount of waste heat to be rejected, thermal outfalls of inadequate design for mixing and dispersion can at times create stressful situations to sensitive aquatic environments. One problem often encountered with thermal outfalls in practice is localized areas of high temperature resulting from insufficient dilution of the effluent under low tide and/or slow current conditions. Another common problem is the attachment of a surface discharge thermal plume to the shoreline in the presence of a slight cross current, thus raising the temperature in the near-shore region. Such events may be undesirable because of their adverse impact on the ecological balance of the ambient environment, especially in smaller receiving water bodies which are less capable of assimilating the waste heat.

1.2 The Use of Multiport Diffusers for Thermal Outfalls

The history of thermal outfalls entered a new era in the early 1970's, when regulatory agencies imposed more stringent temperature standards on cooling water discharges. For example, the California water-quality control plan for thermal waste discharge in coastal waters (State Water Resources Control Board, 1975) specified that the maximum temperature of the discharge shall not exceed the natural temperature of the receiving water by more than 11.1°C (20°F). Furthermore, the resulting increase in the temperature of the receiving water should not exceed 2.2°C (4°F) at

(a) the shoreline, (b) the surface of any ocean substrate, or (c) the ocean surface beyond 305 m (1000 ft) from the discharge system. The surface-temperature limitation has to be complied with for at least 50% of the duration of any complete tidal cycle. Traditional open channel or submerged single-port outfalls do not meet the new standard for discharge mainly because the initial dilution is insufficient. Therefore, multiport diffusers were introduced for new projects.

A multiport diffuser is an outfall structure consisting of an array of nozzles through which the effluent is discharged to the receiving ambient as a row of individual buoyant jets. The nozzles are usually risers protruding from a supply pipe. At the end of the risers are orifices for the discharge of the effluent. Multiport diffusers have been utilized in sewage disposal for several decades. They have proved to be effective discharging devices because of the high initial dilution achieved.

On the basis of the arrangement of the individual nozzles, thermal diffusers can be classified into three general types: the unidirectional, staged, and alternating diffusers. The selection of a particular type of diffuser for a specific site depends on the temperature requirements and the characteristics of both the discharge and the receiving water, as well as on the physical configuration of the diffuser.

Predictive models of the induced flow field and temperature field of specific types of diffusers have been developed, but they are often overly simplified to be valid for general application. In addition, a unified analytical treatment for all diffuser types has not yet been derived because of the complexity of the problem. Since good theoretical support is not available, almost every existing submerged thermal multiport diffuser has been designed with the assistance of hydraulic model experiments to ensure compliance with the thermal standards.

With the increasing number of thermal discharges, it is crucial that their impact on the receiving environment can be predicted and minimized. In view of this, regu-

latory authorities have mandated that some power production companies implement a series of field-monitoring programs to study the influence of their thermal outfalls. The collected data can also be used to evaluate the performance of the related hydraulic model. Large amounts of field data have been gathered in recent years. These include continuous time-history data of current, temperature and water quality at fixed stations, infrared imagery, and towed thermistor chain data. Various types of information have been extracted in an ad-hoc manner; a systematic method of analysis, such as a definitive model-to-prototype comparison standard, on the collected data set is not available.

1.3 A Case Study

The San Onofre Nuclear Generating Station (SONGS) is located on the Pacific coast approximately 80 km (50 miles) south of Los Angeles. Its proximity to the ocean makes it an excellent site to employ a once-through cooling water recirculation system with submerged outfalls for waste-heat disposal. SONGS has three units: Unit 1 produces 436 Mw(e) power and Units 2 and 3 produce 1100 Mw(e) power each. The nominal operational temperature increase (across the condenser) of the cooling water is 12.2°C (22°F) for Unit 1 and 11.1°C (20°F) for Units 2 and 3. The flow rates are 20.2 m^3/s (713 cfs) for Unit 1 and 52.4 m^3/s (1850 cfs) each for Units 2 and 3. The outfall system consists of a single submerged outlet for Unit 1 and two staged diffusers, each 750 m (2462 ft) long with 63 ports, for Units 2 and 3. It is the first cooling water system that uses the staged diffuser concept. Both Unit 2 and Unit 3 diffusers are perpendicular to the shoreline, with the individual nozzles oriented in an offshore direction with horizontal angles ±25° from the diffuser axes. The Unit 2 diffuser is located immediately offshore of the diffuser for Unit 3, but the two are separated by a longshore distance of about 305 m (1000 ft). The depth of

water is approximately 10 m at the beginning of the Unit 3 diffuser and increases gradually in the offshore direction to about 15 m at the far end of the Unit 2 diffuser.

The design of the SONGS diffuser system was assisted by a hydraulic model study undertaken by the Keck Hydraulics Laboratory at the California Institute of Technology (Koh et al., 1974). The study was conducted to seek the optimal configuration that would satisfy the stringent California thermal requirements. The model was based on internal Froude similitude and had a distortion ratio of 4:1, i.e., the horizontal scale (800:1) was different from the vertical scale (200:1). The ambient temperature in all experiments was homogeneous, but a variety of longshore current conditions, both steady and reversing, were simulated. Surface temperature distributions were measured and the results were presented in isothermal maps of normalized temperature excess.

Physical oceanographic and water-quality data have been collected at predetermined stations in the vicinity of SONGS since the 1960's, spanning the preoperational and operational periods of the diffusers. The time series, for example, of current and temperature, have provided information on the short-term as well as on the long-term variations in the nearby coastal waters. Besides continuous measurements, thermistor chain data and infrared imagery have been collected for several scenarios, and the combination of the two has provided a reasonable approximation of a synoptic view of the thermal plume.

Comparison of prototype and model data (Ng and Koh, 1986) indicates that the hydraulic model has performed accurately. The diffusers at SONGS are found to be very effective in achieving rapid initial mixing so that the California thermal regulations are always satisfied. The high dilution efficiency supplied by the staged diffusers has resulted in an insignificant plume signal in the measured field data when compared to background variations.

1.4 Objectives and Scope of this Study

Through carefully designed experiments, the present study investigates the mean behavior of the induced thermal field of submerged staged diffusers over a range of conditions. The objectives are to:

(1) understand the three-dimensional flow field and the physics of the underlying mixing processes;

(2) establish the governing parameters in staged diffuser discharge, and

(3) evaluate existing predictive tools and give suggestions in future formulations.

The results can be applied, in practice, to:

(1) provide guidelines in the future designs of thermal diffusers;

(2) assist in the design of more effective field monitoring programs, and

(3) provide information on the three-dimensional flow pattern to assist regulators in formulating thermal standards.

In the experiments, temperature distributions were measured both at the surface and down through the water column in order to construct three-dimensional pictures of the thermal field. Because of the size limitation of the experimental setup, the effect of the Reynolds number can be significant in certain regions of the plume. (The Reynolds number of the thermal plume, Re, is defined as $u\ell/\nu$, where u and ℓ are the characteristic velocity and length scale, respectively, and ν is the kinematic viscosity of the plume fluid.) Laboratory values of Re are usually several orders of magnitude smaller than that in the field. For example, the discharge Reynolds number, Re_0, of SONGS diffusers (prototype) is approximately $2.2\text{x}10^6$ compared to $2.2\text{x}10^3$ of the model diffusers. (The ratio of the prototype Reynolds number to the

model Reynolds number is proportional to $(L_r)^{3/2}$, where L_r is the geometric ratio, provided that the kinematic viscosity of the fluid in the prototype and in the model is the same.) While the thermal plume in the field is fully turbulent, it is not generally true in the laboratory, especially at farther downstream locations where the plume velocity is largely reduced. The discharge Reynolds number of the present study ranges approximately from 10^3 to 10^4 (a few experiments with Re_0 less than 10^3 are reported but their results are not included in the detail analysis). For a thermal plume with a typical velocity of 5 cm/s (laboratory value) at some downstream location (beyond 2 to 3 diffuser lengths) and a layer thickness of about 1 cm, the Reynolds number is on the order of $5x10^2$, indicating a laminar flow field. The effect of the fluid viscosity, therefore, cannot be ignored in this flow regime. However, practical interests for plume characteristics usually focus on an area reasonably close (on the order of 2 to 3 diffuser lengths) to the structure, where the flow field is in general turbulent and momentum mixing is still active. Moreover, the laminar regime is usually not present in the field since the effect of the ambient current will dominate the flow field in the farther downstream region. Although temperature measurements were collected for a much larger extent (more than 7 diffuser lengths), the analysis of the results was emphasized on the turbulent region in the proximity of the diffuser.

The use of flow-visualization techniques enhanced the understanding of the plume behavior. Surface velocity was also surveyed in selected experiments to provide information on the induced flow field. Although the majority of the experiments were conducted for a uniform and quiescent ambient environment, a few exploratory tests were performed with stratified ambient conditions. However, the experiments were only partially successful because of the difficulties in creating a stratified receiving water body. As a result, the ambient stratifications obtained in those experiments were not sufficient to change the dynamics of the thermal plume as would be expected in a strongly stratified environment. The details and results of the stratified ambient

experiments are discussed in Appendix C.

1.5 Structure of the Thesis

A review of the previous research on the related areas of buoyant jets and diffuser discharges is presented in Chapter 2. A description of the physical processes taking place in the various regions of the induced flow field and the resulting temperature field of staged diffusers is given in Chapter 3. The experimental considerations, instrumentation, procedures and limitations are discussed in Chapter 4. A list of all the experiments and the experimental conditions are summarized in Chapter 5. Also presented in Chapter 5 are the complete results from one set of experiments in a homogeneous ambient fluid. In addition, the changes in the behavior of the thermal plumes under various diffuser and ambient configurations are examined. The interpretation and discussion of the experimental results are given in Chapter 6. Conclusions for the present study and recommendations for future work are presented in Chapter 7. A sample program for data acquisition is listed in Appendix A, whereas examples of the calibration curves for the thermistors and potentiometers are given in Appendix B. Results of the stratified ambient experiments are presented and discussed in Appendix C. Finally, the experimental variables and key results of the homogeneous ambient experiments are tabulated in Appendix D.

2. Literature Review

2.1 Introduction

Multiport diffusers have first been introduced for municipal waste-water disposal in the ocean and are still widely used because of their effective mixing characteristics. A number of studies, both experimental and analytical, have been carried out to investigate the various fluid mechanical properties of sewage diffusers, including the initial dilution, the buoyant jet merging process and its significance, the waste-field thickness, the maximum height of rise of the submerged field in a stratified ambient fluid, and the effects of a cross-flow.

Submerged multiport diffusers have been employed in the disposal of waste heat from power generation plants since the early 1970's. The induced flow configurations, however, are found to be drastically different from those of sewage discharges because of the different ambient and discharge characteristics (generally, much larger discharges of less buoyancy, shallower depths and shorter distances offshore). One of the important differences is the instability sometimes observed in the immediate vicinity of a thermal diffuser versus a stable mixed zone over a sewage diffuser. Such observations have been described by Jirka and Harleman (1973, 1979) and Andreopoulos et al. (1986).

Because of the different dilution objectives (approximately 10 and 100 for thermal and sewage discharges, respectively), submerged thermal outfalls can usually be located in shallower water bodies compared to sewage outfalls. Furthermore, the volumetric flow rate associated with thermal discharges is much larger than for sewage discharges. As a result, the discharge momentum flux is initially dominant in thermal outfalls, whereas buoyancy flux is more important for sewage outfalls. The coupling of a strong discharge momentum (a destabilizing factor) with a shallow water depth may result in instability in thermal discharges. Consequently, a different approach has to be employed in the analysis of the dynamics of thermal diffusers.

2.2 Different Types of Multiport Thermal Diffusers

On the basis of the orientation of individual nozzles that governs the overall diffuser dynamics, existing thermal diffusers can generally be grouped into three catagories: staged, unidirectional, and alternating diffusers. Figure 2.1 is a schematic diagram of the common diffuser types for thermal discharge.

The mixing characteristics and hence the performance of multiport diffusers depend on various factors and physical processes. With a unidirectional diffuser for which the nozzles point in a direction perpendicular to the feeder pipe, the mixing is efficient under stagnant ambient conditions and is further improved with co-flowing current (i.e., current in the same direction as the jets from the nozzles). The performance, on the other hand, will decrease with flow parallel to the diffuser (i.e., ambient current perpendicular to the discharge angle) because of the reduction in the effective area for entrainment. Therefore, the unidirectional diffuser is best employed in sites where there is a predominant current direction as in a large river. The Fitzpatrick station, the Zion station and the Quad Cities station are examples of power plants that employ unidirectional diffusers for waste-heat disposal.

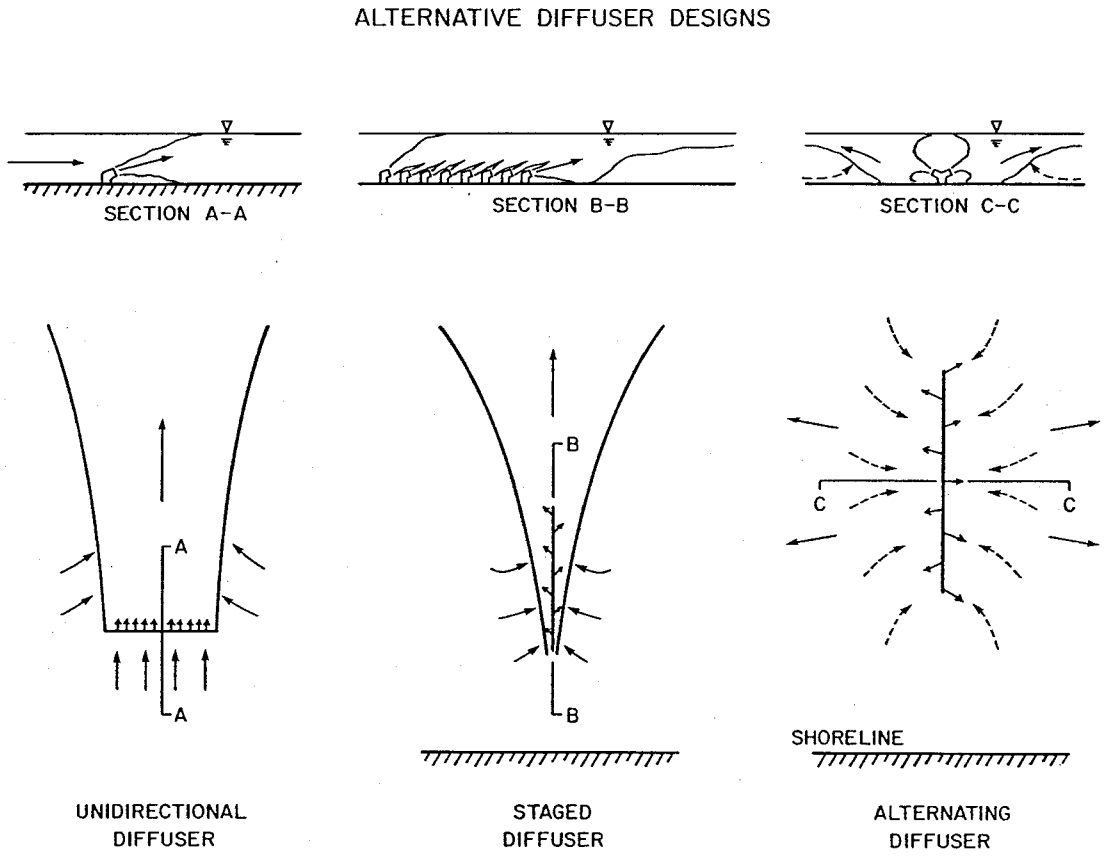

Figure 2.1 Different types of multiport diffusers.

The nozzles in a staged diffuser point in an offshore direction (as does the main diffuser pipe), or at a small horizontal angle ($\pm\alpha$) away from the diffuser axis. For example, $\alpha = \pm 25°$ for the staged diffusers for Units 2 and 3 of the San Onofre Nuclear Generating Station and for the diffuser at the Darlington Generating Station "A" (Ontario Hydro). Strong horizontal offshore momentum of the diluted thermal plume is generated by this nozzle arrangement, thus minimizing the shoreline impact. However, the large circulation generated may not be desirable in certain receiving water environments. The performance of staged diffusers increases typically with the strength of a longshore current (perpendicular to the diffuser).

An alternating diffuser introduces zero net horizontal momentum and therefore induces less large-scale net circulation of the environment. The dilution (or excess temperature) does not depend on the direction of the ambient current. In a quiescent ambient, however, the dilution is limited since there is no mechanism (e.g., offshore momentum) to carry the thermal plume away from the diffuser. Prototype examples using alternating diffusers for discharging cooling water include the Shoreham station (never operated) and the Northport stations in Long Island Sound. Stolzenbach et al. (1976), Adams and Stolzenbach (1977), and Paddock and Ditmars (1978) have commented on the relative merits of the different diffuser types under various ambient conditions.

The mixing processes involved in thermal diffusers in shallow water are very complicated, since the resulting flow and temperature fields are sensitive to the physical configurations. Studies on the fluid mechanical aspects require considerations of many factors, and a generalized treatment for all diffuser types has not yet been derived. The mean behaviors of unidirectional and alternating diffusers have been studied experimentally by Lantz and Lisauskas (1972), Jain et al. (1971), Lee et al. (1977) and Harleman et al. (1971, 1973). Predictive models (Adams, 1972; Lee and Jirka, 1979;

Jirka, 1982) have also been developed, but they will not be further elaborated here. Only previous investigations related to staged diffusers are reviewed in the following sections.

2.3 The Induced Flow Field and the Zonal Division

The earliest studies of staged diffusers have been the tests of various hydraulic models, which have been carried out as part of the design efforts for the outfalls of the cooling water recirculation systems for power-generating stations. Examples are the model studies for the San Onofre Nuclear Generating Station (Koh et al., 1974), the Perry Station (Acres American Inc., 1974) and the Darlington Generating Station "A" (Elsayed, 1981). Analytical studies of staged diffuser discharges, however, have appeared only recently, notably with Almquist and Stolzenbach (1980), Lee (1980), and Jirka (1982). Results from extensively studied turbulent buoyant jets and observations from the hydraulic model studies have led to a general acceptance that the overall flow field can be divided into three zones, based on the local flow and temperature characteristics. These are the near, the intermediate, and the far fields.

(i) The near field

The near field is the region directly above the diffuser and is characterized by initial jet mixing and jet interactions. Individual jets entrain ambient water as they rise toward the surface and grow to sizes comparable to the nozzle spacing, causing the jets to merge. Furthermore, recirculation eddies in the vertical direction may form because of the deflection of the jets by the surface, resulting in re-entrainment of diluted discharge into the jets. This recirculation (in a vertical plane) often occurs in shallow ambient water and is referred to as being unstable. The near field is, therefore, highly three-dimensional with respect to the velocity and temperature distributions.

(ii) The intermediate field

The intermediate field begins slightly beyond the diffuser where the thermal jets have reached the surface. The plume forms a continuous surface layer, which propagates beyond the end of the diffuser and behaves essentially as a large surface buoyant jet. In the case of a vertically mixed near field, restratification usually occurs some distance beyond the diffuser because of the discharge buoyancy. Entrainment of the ambient water at the bottom of the buoyant layer, hence mixing in the vertical direction, is reduced because of the presence of the stable density gradient. The flow structure is characterized mainly by horizontal motions and interfacial shear. Both the momentum and the buoyancy forces play important roles in the intermediate field. The surface thermal plume propagates downstream because of the residual momentum and, at the same time, spreads in the transverse directions because of the increasing significance of the buoyancy force. Eventually, gravitational spreading will dominate the mixing processes when the plume momentum has been dispersed or balanced by pressure gradients.

(iii) The far field

The far field is a zone of advection by the ambient current and of passive dispersion by the ambient turbulence. The transport and dispersion mechanisms in this region are entirely controlled by environmental factors. Net heat loss through the surface becomes more important.

A similar zonal classification has been adopted in studies of sewage discharge from multiport diffusers (Koh and Brooks, 1975; Roberts, 1979). However, the present study focuses on the mean behavior of the near and intermediate fields for thermal discharges from staged diffusers.

2.4 Turbulent Buoyant Jets and Multiport Diffusers

Various aspects of turbulent buoyant jets related to the staged-diffuser discharge in shallow water will be discussed in the following sections. Since the mixing processes and the fluid dynamics vary in the three flow regions, it is more convenient to review the analytical development of each zone separately.

2.4.1 Turbulent Jets and Plumes in Unconfined Environments

The near-field region is comprised of a number of round buoyant jets, at prescribed spacing, that are mixing with the surrounding ambient fluid and interacting among themselves (Figure 2.1). The use of the three-dimensional turbulent jet theory to model the initial jet mixing zone in the near field of a staged-diffuser thermal plume has been proposed by Stolzenbach et al. (1976); however, the merging of individual jets and the effect of the confined water depth cannot be described accurately by the basic mechanics of a single round jet.

Turbulent buoyant jets in a uniform, stagnant, and yet unconfined receiving environment have been studied by numerous investigators. The related theoretical and experimental works have been critically reviewed by Fan (1967), Koh and Brooks (1975), Jirka and Harleman (1973), and List (1982).

The gross behavior of turbulent jets along their trajectories has first been analyzed by Morton et al. (1956) and Priestley and Ball (1955) using integral techniques. Their analysis is based on the entrainment concept and a few assumptions pertaining to earlier laboratory observations and scaling arguments. These assumptions include similar cross-sectional velocity and density-deficiency profiles along the jet path, boundary-layer behavior (the length scale in the lateral direction is small compared to that in the longitudinal direction), the Boussinesq approximation (small relative density differences), and hydrostatic pressure distribution throughout the flow

field. Further assumptions of an unconfined, stagnant and uniform ambient condition simplify the analysis. By using similar profiles for the jet velocity and density, the governing equations (i.e., the conservation equations of mass, momentum and heat fluxes) can be integrated to obtain a set of ordinary differential equations. Using the entrainment hypothesis for closure and the discharge configuration (single jet) as the initial boundary conditions, the system of equations is then solved to yield the mean properties as explicit functions of the distance along the jet and the discharge parameters. Similar relationships can also be deduced from dimensional analysis for point sources. Detailed discussion of the integral method as applied to the analysis of jets and plumes has been given in Fischer et al. (1979).

Experimental results of Albertson et al. (1950) and Rouse et al. (1952) have demonstrated the linear expansion of the nominal boundaries of jets and plumes and the property of self-similarity. They have also indicated that the velocity and the tracer distributions are well fitted by Gaussian curves, which subsequently have become the most commonly used similarity profiles in jet and plume models.

The entrainment concept formulated by Morton et al. (1956) has assumed that the entrainment velocity (perpendicular to the direction of the jet axis) at the jet boundary (e^{-1} width) is proportional to the local centerline velocity. The proportionality constant is commonly referred to as the entrainment coefficient and has to be found empirically. For pure jets and plumes, most laboratory experiments (e.g., Albertson et al. (1950), Ricou and Spalding (1961) and Mih and Hoopes (1972) for jets; Rouse et al. (1952), and Lee and Emmons (1951) for plumes) confirm with slight variations that a constant entrainment coefficient for each flow configuration suffices.

Values commonly adopted for the entrainment coefficients (Fischer et al., 1979) are:

$$\text{round jet}: \ \gamma_{rj} = 0.057$$

$$\text{slot jet}: \ \gamma_{sj} = 0.068$$

$$\text{round plume}: \ \gamma_{rp} = 0.082$$

$$\text{slot plume}: \ \gamma_{sp} = 0.16.$$

Although the analysis for a buoyant jet essentially follows the same integral technique and also assumes Gaussian profiles, the entrainment coefficient is no longer a constant. Priestley and Ball (1955) have suggested that the entrainment coefficient is a function of the local Richardson number. This result has been confirmed by List and Imberger (1973) using dimensional reasoning coupled with experimental observations. Additional investigators (e.g., Koh and Brooks, 1975) have proposed other forms for the entrainment functions. Abraham (1965) replaced the entrainment assumption with a constant rate of spreading of the jet (which also has to be found empirically from laboratory studies) and obtained results similar to others.

The works discussed so far are for a stagnant and uniform environment where the jets or plumes rise continuously until they reach the water surface and are redirected in the horizontal direction as a surface spreading layer. In a stratified ambient environment, if the density gradient is sufficiently strong, the horizontally spreading layer may stay submerged. Morton et al. (1956), Brooks and Koh (1965) and Fan (1967) have used the constant entrainment coefficient to analyze the plane and round jets in linearly stratified receiving water bodies. Fan (1967) has conducted experiments of round jets in a stratified environment, whereas Wright and Wallace (1979) and Chen (1980) experimented on plumes.

More recent experimental studies of Roberts and Matthews (1987) and Wong and Wright (1988) on horizontal buoyant jets in stagnant but linearly stratified flu-

ids show that the entrainment is not significantly affected by the ambient density gradient until a collapse point, when the Froude number falls below a critical value. The critical point can be visualized as the bottom of the spreading layer. They have further observed that the entrainment continues for some distance beyond the collapse point. The resulting additional dilution, about 30% as observed by Roberts and Matthews (1987), is higher than suggested by Fischer et al. (1979) who have postulated that the entrainment terminated at the bottom of the spreading layer.

Turbulent buoyant jets in a cross-flow environment have been analyzed by Fan (1967), Hoult and Weil (1972), Abraham (1970), Hirst (1971), and later by Schatzman (1978, 1979). They used the same integral techniques and similarity assumptions, but with the addition of a drag term in the momentum equation to account for the unbalanced pressure in the windward and leeward sides of the jet. Fan (1967) performed experiments on round buoyant jets in a cross-flow and found that the entrainment coefficient was larger than that in a quiescent ambient. Furthermore, the entrainment coefficient was found to be decreasing with increasing densimetric Froude number, but the drag coefficient was increasing with increasing Froude number. Wright (1977a) proposed a model using dimensional analysis. He suggested four length scales based on the jet and ambient current characteristics and four flow regimes controlled by the relative magnitudes of the appropriate length scales. The model predictions agreed satisfactorily with his own experimental results (Wright, 1977b) and those of Fan (1967).

2.4.2 Merging of the Individual Jets

Previous studies on jet merging have focused on a row of round buoyant jets injecting fluid either vertically upwards or perpendicular to the diffuser axis as in a unidirectional diffuser (Figure 2.1). The mixing behavior after the individual jets have merged depends on the momentum and buoyancy fluxes per unit length of

the diffuser (Jirka and Harleman, 1973; Koh and Fan, 1970). Thus, the width of the "equivalent" slot orifice (B) for preserving the momentum flux is found to be (for equal discharge areas) the jet area per unit length, or

$$B = \frac{D_0^2 \pi}{4s}, \tag{2.1}$$

where s is the spacing of the individual jets of diameter D_0. The equivalent slot jet method is commonly accepted in the analysis of sewage discharge from multiport diffusers. Although the staged diffuser has different configurations other than unidirectional, the concept is also widely used in its theoretical development.

The concept of the equivalent slot jet is examined by a comparison of the average dilution produced by a multiport diffuser and by an equivalent slot diffuser (Cederwall,1971); the two are found to be close enough for practical purposes. However, experimental results of Liseth (1970) on sewage diffusers with horizontal discharges have shown that complete merging of the jets into a single, two-dimensional buoyant jet occurs at a depth-to-port spacing ratio (H/s) of 5 and that the center dilution is reduced in comparison with that of a single jet because of the merging.

For an unconfined flow field, a criterion for the merging of jets or the transition from round to slot buoyant jets was proposed by Koh and Fan (1970) to be when the jet width equals the port spacing or when the entrainment rate for the round jets equals that of the equivalent slot jet; the transition is based on conservation of momentum and buoyancy fluxes per unit length. Kannberg (1976) has carried out an experimental and analytical study on a similar problem. In a later numerical model study (Kannberg and Davis, 1977), Hirst's model (1971) for turbulent buoyant jets has been modified such that the transition occurs when the jet width of the initial round jet equals that of a two-dimensional jet. Comparisons with experimental data were claimed to have better agreement than the previous treatment of the same problem.

2.4.3 Effect of Shallow Water and Instability

In deep water bodies a buoyant jet will rise to the surface and will spread out horizontally as a surface buoyant layer in uniform ambient fluid, or will stay submerged as a subsurface layer in a stably-stratified environment. The thickness of the buoyant layer has been reported by numerous investigators. Rawn and Palmer (1929) have found the thickness to be 1/12 of the path length, while Frankel and Cumming (1965) have given an estimate of 1/4 of the water depth for a horizontal round buoyant jet. Hart (1961) has experimentally related the thickness to the jet diameter. Experiments by Liseth (1970) and Liu (1976), in which a manifold spanned the width of the test tanks, have resulted in surface thicknesses less than 30% of the depth while Bühler (1974) has reported a value of 40%. Roberts (1977) has found in experiments that line sources of pure plumes having a finite length in a large basin have field thicknesses that are 30% of the depth, in agreement with Koh's predictions (1976). Koh (1983) has proposed a model coupling the plume rise with the gravitational spreading and arrived at an explicit solution for two-dimensional plumes in uniform, as well as linearly stratified, environments. The predicted thicknesses are 30% and 40–45% of the depth, respectively.

In shallow water, however, a stable gravitational spreading layer as described above does not always exist. Instead, an unstable situation with internal recirculations over the depth has been observed in experiments by Iamandi and Rouse (1969), Murota and Muraoka (1967), Jirka and Harleman (1979), and Andreopoulos et al. (1986). The instability of the near-field region is caused by a combination of high discharge momentum and shallow water depth. Jirka and Harleman (1979) have presented an analysis on the stability of vertical plane buoyant jets by considering the dynamics of a stable near field consisting of three regions: the buoyant jet, the surface impingement, and the internal hydraulic jump regions. A stability criterion stating that

instability is attained when the inertia force (destabilizing) exceeds the buoyancy force (stabilizing) has been proposed and confirmed by the experimental results of Andreopoulos et al. (1986). In Jirka and Harleman's theory, this critical situation is achieved by decreasing the buoyancy flux until it is impossible to find the conjugate solution for the momentum equation of the internal hydraulic jump. By assuming that a two-dimensional flow section exists in the center portion of a multiport diffuser (i.e., the two-dimensional channel assumption), the criterion can be used to test for instability in multiport discharges. For the asymptotic case where the depth-to-equivalent-slot-width ratio is large ($H/B \geq 200$), the proposed instability criterion of Jirka (1982) approaches:

$$\frac{\ell_m}{H} \geq \frac{0.54}{(1 + cos^2\beta)^2} , \tag{2.2}$$

where ℓ_m is the momentum length scale based on the plane jet formulation ($m_0/b_0^{2/3}$), m_0 and b_0 are the discharge momentum and buoyancy fluxes per unit length of diffuser, respectively, β is the vertical discharge angle (from the horizontal plane), and H is the water depth. Most typical thermal discharges, according to this criterion, fall into the unstable range whereas the sewage discharges are always stable. Such a two-dimensional section, however, never exists in a staged diffuser flow field. Using stratified flow theory, Jirka (1982) has proposed another similar instability criterion for a staged diffuser:

$$\frac{\ell_m}{H} \geq 0.52 . \tag{2.3}$$

Although comparisons with experimental results and some existing thermal outfalls confirm the stability criterion, it does not predict the observed stratified near field in the case of the San Onofre model study (Koh et al., 1974).

From the available laboratory data on staged diffusers, Almquist and Stolzenbach (1980) have postulated that the unstable or vertically well-mixed condition occurs when $\ell_m/H \geq 2.0$. Cederwall (1970) and Argue and Sayre (1973) have proposed other stability criteria.

2.4.4 Surface Buoyant Jets

Restratification beyond the near field may occur and is governed by the overall larger-scale geometry rather than by the discharge characteristics alone. The behavior resembles that of a three-dimensional surface buoyant jet. There have been extensive experimental investigations on the dynamics of surface buoyant jets under various flow situations. A detailed review has been given by Chu and Jirka (1986). According to Baddour and Chu (1978), the flow field of a three-dimensional surface buoyant jet is composed of a turbulent core characterized by turbulent entrainment and surrounded by a gravitational spreading field where density-driven spreading dominates. Experimental results from many investigators, Wiuff (1978) in particular, indicate that the horizontal extent of the surface plume is large compared to the vertical extent. The experimental profiles of the velocity and buoyancy along the centerline in the longitudinal direction exhibit relatively rapid declines. The buoyancy profile also approaches a plateau value farther downstream. There have been efforts to delineate the mean and turbulent characteristics such as the extent of the turbulent core, the Richardson number at the end of the turbulent core and the plateau buoyancy from the experimental data, but the results are not conclusive.

Mathematical models have been developed for the treatment of buoyant jets using similar techniques including the integral method, entrainment hypothesis and assumed similarity profiles. Stolzenbach and Harleman (1971), Prych (1972), Koh and Fan (1970) and Wolanski and Koh (1973) have used the integral technique to model the buoyant spreading of surface discharges. Except for the formulations of the

lateral spreading equation and the entrainment functions, these mathematical models are alike. A problem that exists in the models of Prych (1972) and Stolzenbach and Harleman (1971) is the existence of singularities in a downstream location where the Froude number reaches a critical value. Neither model has suggested a method to solve the problem. There are a number of experimental studies to determine the entrainment at the bottom of the buoyant jet which is expected to be different from the submerged jets because of the presence of the density interface.

2.5 Laboratory Studies on Staged Diffusers

The majority of existing experimental data on staged diffusers come from seven hydraulic model studies—the San Onofre Nuclear Generating Station study (SONGS) (Koh et al., 1974), the Perry Station study (Acres American Inc., 1974), the Somerset alternate site study (Stolzenbach et al., 1976), the Campbell Station study (Roberge, 1976), the Charlestown site study (Brocard, 1977), the Jamesport Station study (Kirby and Brocard, 1979), and the Darlington Generating Station "A" (Elsayed, 1981). They have been performed to assist the determination of optimal diffuser configurations (in terms of cost-effectiveness) in compliance with the thermal standards under prevailing receiving water conditions. Consequently, each of the tests focus on a particular set of candidate configurations. The documented results are primarily surface isotherms covering the near and intermediate fields. These model studies provide useful primary information on the mean behavior of the induced thermal and flow field of staged diffuser discharges in coastal environments. A brief description for each of the hydraulic model studies is given.

(i) San Onofre Nuclear Generating Station study (1974)

The hydraulic model study was done in the Keck Hydraulics Laboratory at the California Institute of Technology with a length-scale distortion of 4:1 (horizontal and

vertical scales of 800:1 and 200:1, respectively). The study modelled two diffusers of 750 m (2462 ft) in length with 63 ports each (16 ports only in the model diffusers based on the 4:1 distortion ratio) on a sloping bottom. The horizontal and vertical discharge angles were $\pm 25°$ and $20°$, respectively. The prototype discharge flow rate was 52.4 m^3/s (1850 cfs) for each diffuser, and the initial temperature difference (ΔT_0) was 11.1 °C (16.7 °C in model). The diffusers were tested in both unidirectional and reversing current conditions. Maximum temperature rise and surface isothermal maps were reported along with selected vertical temperature profiles from a related undistorted sectional model study of scale 50:1. There were no velocity measurements involved. Major observations included a stratified near field and the decrease of maximum temperature rise with increased diffuser length and an increase of current strength under the unidirectional current conditions. The study optimized the length of the diffusers.

This study has the only distorted hydraulic model for staged thermal diffusers. The distortion provides proper modeling of the interfacial and bottom friction forces in the intermediate field. However, special care has to be exercised in the interpretation of the laboratory results in prototype dimensions. The plant has been in full operation for over five years with observed temperature increases below the model predictions (Ng and Koh, 1986).

(ii) The Perry Station study (1974)

The model was undistorted with a scale ratio of 75:1 and a sloping bottom topography. The model study was conducted for a proposed power station (Perry Nuclear Power Plant) which was to have an output of 2410 MW(e). The discharge flow rate was 72.5 m^3/s (2560 cfs), and the ΔT_0 was 16.1 °C. Surface temperature distributions were monitored under a variety of simulated current conditions and surface isotherm areas were reported. The study also included limited surface velocity measurements.

The results indicated that the near field was mixed vertically and that the near-field dilution was insensitive to both the clearance of the nozzles from the bottom and the small angle of inclination of the nozzles. Detailed results from this study are not available and therefore are not included in the later analysis.

(iii) The Somerset Alternate site study (1976)

This 100:1 undistorted model had a uniform bottom slope of 1/75. The model study was carried out for the Cayuga Station fossil-fueled power plant of 850 MW(e) production. The discharge flow rate was 21.0 m^3/s (740 cfs), and the ΔT_0 was 13.9°C. A staged diffuser of 122 m (400 ft) with 9 nozzles was chosen as the design configuration. Each nozzle (0.7 m in diameter) was oriented at 0° in the vertical plane and ±25° from the diffuser axis in the horizontal plane.

In addition to surface temperature, some indirect surface-velocity measurements were taken. The diffuser performance in terms of the near-field dilution was generally observed to increase with the diffuser length and the strength of the cross-flow. In low current conditions, however, the individual jet mixing dominated and the cross-flow effect diminished. The explanation for this was the additional diluting capacity of the cross-flow by interception, which in turn increased with both the diffuser length and the current strength. The performance depended little on the jet spacing, the number of nozzles, and the horizontal discharge angle.

(iv) The Campbell station study (1976)

The undistorted model had a scale ratio of 65:1 and consisted of 4 units. The study was conducted for a proposed expansion of the Campbell Electric Generating Station by the addition of Units 3 and 4 (each 800 MW(e)) to the existing Units 1 and 2 (combined capacity 647 MW(e)). The discharge flow rate was 19.0 m^3/s (668 cfs) for both Units 1 and 2, and 20.4 m^3/s (722 cfs) for each of Units 3 and 4. The discharge temperature difference was 16.2°C. The recommended configuration was

a three-diffuser system. The first diffuser (for Units 1 and 2) was 53 m (175 ft) in length with 8 nozzles each 0.74 m (2.44 ft) in diameter. The second and third diffusers (for Units 3 and 4) were identical with 10 nozzles each 0.69 m (2.26 ft) in diameter, discharging at ±20° from the diffuser axis and 10° up from the horizontal plane. The second and third diffusers each had a length of 69 m.

Surface temperature distributions, selected temperature profiles in the vertical direction, and velocity measurements on the surface and the bottom were recorded. Steady current conditions were simulated and surface isotherms were reported as in the other studies. It was found that a greater dilution resulted from a higher discharge velocity and that the performance improved with increasing diffuser length and current speed in the same manner as reported in the Sommerset study. Furthermore, an increase of the water depth did not seem to improve the dilution.

(v) Charlestown site study (1977)

This model had an undistorted scale of 90:1 and consisted of 2 units, each having an electrical output of 1200 MW(e). The total discharge flow rate was 54.0 m^3/s (1907 cfs) with an initial temperature difference of 20.6°C. The model was tested for both steady ambient-current condition and transient tidal-current condition. Results and observations indicated that the performance (in terms of maximum rise in temperature in the modeled region) improved with lengths of the diffuser and magnitudes of the ambient current. However, changes in both the vertical and horizontal discharge angles did not appreciably affect the diffuser performance. Results and observations were similiar to the Somerset study and the Campbell study. The final configuration selected was a diffuser 366 m (1200 ft) in length, with 34 nozzles (each 0.6 m in diameter) discharging at a vertical angle of 20° (from the horizontal plane) and a horizontal angle of ±20° from the diffuser axis. The diffuser was situated at a depth of 9 m to 10 m.

(vi) Jamesport Station (1979)

This 100:1 undistorted model consisted of 2 units, each having an electrical output of 1150 MW(e) and discharging 59.2 m^3/s (2089 cfs) at a ΔT_0 of 9.9°C. A staged diffuser of length 1308 m (4290 ft) with 127 nozzles having diameters from 0.3 m (1.0 ft) to 0.76 m (2.5 ft) was chosen. The discharge angle was 10° up from the horizontal and ±20° from the diffuser axis. Both surface and subsurface temperatures were measured at a better resolution than all previous hydraulic model studies. No velocity measurements, however, were available. The tests were performed with both steady longshore ambient current conditions and transient tidal cycles. Similar to the above studies, the diffuser performance improved with the increasing diffuser length. The heat-discharge-rate distribution along the diffuser was found to be an additional important parameter for performance.

(vii) The Darlington Station study (1981)

This 100:1 undistorted model study was conducted for the Darlington Generating Station "A" (4 units) in Lake Ontario. The total discharge rate was 121.3 m^3/s at 15.4°C above ambient temperature in the winter and 151.2 m^3/s at 12.35°C above ambient in the summer. The reference design selected was a single 900 m long diffuser with 90 ports (0.6 m in diameter) oriented ±25° from the diffuser axis and 20° up from the horizontal. The model diffuser was tested in various ambient-current conditions. Significant improvement in the mixing was observed when the discharge buoyancy flux became negligible in winter and a two-layer stratified flow did not develop. The detailed experimental result of the study, however, was received too late to be included in the analysis in later chapters.

Most of these early measurements were not designed for thorough examinations of the mixing mechanisms in the various flow regions. A more detailed experimental study with higher spatial resolutions in measurements was undertaken by

Almquist and Stolzenbach (1976) on staged diffusers under uniform and stagnant ambient conditions. Measurements were confined to the near-field region of the diffuser and only temperature was monitored. Normalized temperature rise along the diffuser axis and vertical temperature profiles at selected locations were reported. Long exposure photographs of the near field showed the resemblance of the entrainment flow pattern to that of a two-dimensional free jet. Beyond an initial three-dimensional region near the beginning of the diffuser (i.e., after the jet reached the surface), the induced flow structure was vertically mixed and justified the assumption that a two-dimensional flow field existed. These two observations formed the basis for the development of some predictive models to be discussed in the next section. It was also observed that a core region with relatively stable surface temperature excess existed in the two-dimensional section of the near field.

2.6 Predictive Models for Staged Diffusers

2.6.1 The Near Field

Several mathematical models have been developed for thermal discharges from staged diffusers to predict the induced flow and temperature distribution in the near field (Almquist and Stolzenbach, 1976, 1980; Lee, 1980; Jirka, 1982; Brocard, 1980; and Brocard et al., 1979). Jirka (1982) has presented a summary of the existing predictive models on multiport diffusers including not only staged diffusers, but also unidirectional and alternating types. Comparisons with published experimental data have been made in some cases for verification of the models. Figure 2.2 is a schematic diagram of the flow field and thermal field of Jirka (1982), which is common to all the models except for slight variations.

Almquist and Stolzenbach (1980) have proposed a model for staged diffusers in uniform and quiescent ambient water with $B \ll H \ll \ell_m$ (i.e., large ℓ_m, meaning

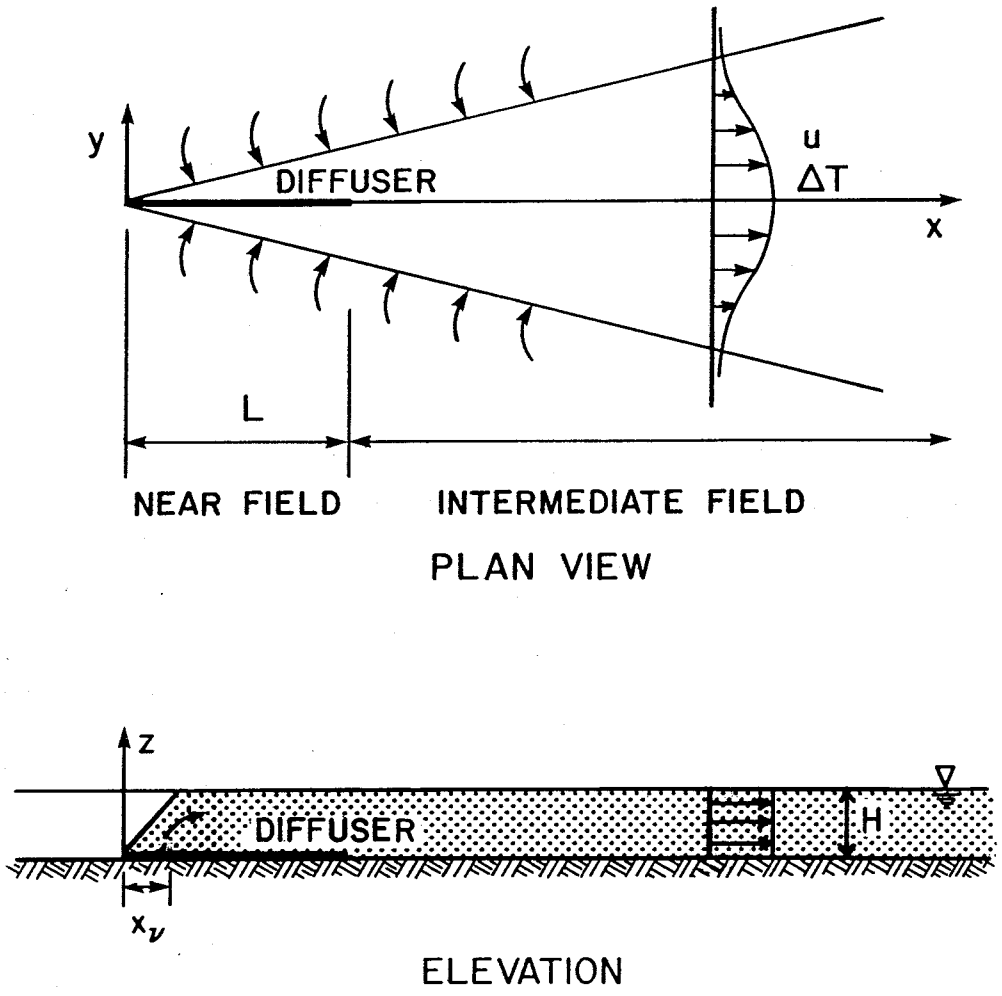

Figure 2.2 Postulated flow field and thermal field common to all theoretical models.

that discharge momentum flux is dominant compared to buoyancy flux). By modeling the diffuser as a line source of momentum (parallel to the axis of the diffuser) and using an entrainment hypothesis as in the case of a two-dimensional free turbulent jet, the governing equations—the conservation of mass and momentum—are integrated in the lateral direction to obtain an expression for the induced volume flux along the downstream direction of the diffuser. The derived governing equations are:

(1) conservation of momentum (M)

$$\frac{dM}{dx} = m_o \Longrightarrow M(x) = m_o x \; ; \tag{2.4}$$

(2) conservation of volume flux ($q_0 x + Q_e$, where Q_e is the entrained flow)

$$\frac{dQ_e}{dx} = \gamma M^{1/2} \qquad 0 < x < x_T \; , \tag{2.5}$$

$$\frac{dQ_e}{dx} = \gamma \frac{MH}{Q_e} \qquad x_T < x < L \; . \tag{2.6}$$

Hence,

$$Q_e = \frac{2}{3}\gamma m_0^{1/2} x^{3/2} \qquad 0 < x < x_T \; , \tag{2.7}$$

$$Q_e = \gamma^{1/2} m_0^{1/2} (Hx^2 - Hx_T^2 + \frac{4}{9}\gamma x_T^3)^{1/2} \qquad x_T < x < L \; , \tag{2.8}$$

where q_0 and m_0 are the discharge volume flux and momentum flux per unit length of the diffuser, and γ is the entrainment coefficient which takes the value of 0.2. x_T is the transition distance from the three-dimensional flow field to the two-dimensional (vertically mixed) flow field and has been found to be $(3/2\gamma)H$. The transition occurs when the nominal jet width b equals the depth. A volumetric dilution S_{bulk} is defined

as the ratio of the total volume flux to the discharge volume flux up to a distance x downstream:

$$S_{bulk} = \frac{q_0 x + Q_e}{q_0 x} . \tag{2.9}$$

It assumed an asymptotic value of

$$S_{bulk} = 1 + \gamma^{1/2} K \tag{2.10}$$

at large x, where $K = \sqrt{H/(q_0^2/m_0)} = \sqrt{4HL\cos\alpha\cos\beta/n\pi D_0^2}$. Therefore, the model predicts a constant dilution at some distance downstream of the transition. The model compares satisfactorily with their experimental results (Almquist and Stolzenbach, 1976) but poorly with the San Onofre model study as shown in Figure 2.3 (to be discussed subsequently).

Other major assumptions in the model are:

(1) Constant water depth.

(2) The induced flow field (and thermal field) is vertically well mixed, which leads to the use of the two-dimensional flow assumption except for a short three-dimensional region at the beginning where the jet has not reached the water surface. The transition is assumed to occur where the characteristic plume width was equal to the depth of water. This assumption has been supported by some laboratory model results (Section 2.4) and by the prediction of Jirka's instability criteria (1979, 1982), and forms the basis for all other predictive models. However, there is still some reservation about the vertically well-mixed flow field because the results of the San Onofre study have indicated a stratified induced flow condition despite the prediction of an unstable condition by the stability criterion (which, however, does not strictly apply to the geometry of a staged diffuser).

(3) The buoyancy effect is neglected by assuming that the temperature is a passive tracer and does not alter the dynamics of the mixing process, consistent with the fact that thermal discharges are almost always dominated by the discharge momentum flux rather than by buoyancy flux.

(4) Only side entrainment has been considered. The entrainment process has been claimed to be locally similar to a two-dimensional jet, and the dilution is due to side entrainment only. However, flow visualization photographs on the induced flow patterns clearly show entrainment from the back of the diffuser. It remains questionable to leave the back entrainment (additional momentum in the x-direction at $x = 0$) out of the formulation, since the models are based on integration along the diffuser axis.

(5) Self-similar profiles are assumed except in Jirka's model (1982). Top hat profiles have been used in the models of both Almquist and Stolzenbach (1980) and Lee (1980).

(6) Bottom friction has not been considered.

The two-dimensional jet entrainment hypothesis as used in the model may not be a reasonable assumption. Experimental observations by Roberts (1977) have suggested that water is entrained from the bottom and that the plume is directed outward at the surface as a buoyant layer. Such a complex three-dimensional flow pattern will be greatly oversimplified by a two-dimensional assumption.

Using the same entrainment hypothesis and assumptions, Lee (1980) has developed a model for staged diffusers parallel to the Almquist and Stolzenbach (AS) model while allowing a sloping bottom. Similar predictions to those of the AS model have resulted for the limiting case of constant water depth. Brocard (1980), on the other hand, has extended the AS model by adding a cross-flow entrainment term $\gamma_c V_a H$ to account for the increase in dilution that is due to a cross-flow; γ_c denoted the

cross-flow entrainment coefficient and V_a denoted the cross-flow velocity.

Jirka (1982) has presented a model for predicting the near-field dilution of a staged diffuser by using a lateral growth rate assumption instead of the entrainment hypothesis as used in other models. The diffuser is conceptualized as a line source of momentum with $(m_0/H)dx$ (depth averaged) in a distance dx per unit depth. Dilution is postulated to be caused by side-entrainment only. Assuming Gaussian velocity profiles, $u(x,y) \propto e^{-x^2/b^2}$, and since momentum is proportional to the square of the velocity profile, the total momentum profile at a distance x from the beginning of the diffuser can be found by the superposition of all the individual sources from 0 to x. A main assumption is that each individual source has a constant growth rate, κ, and is equal to that for a simple momentum jet (a value of 0.154 was used). The velocity profile at a downstream distance x will therefore be the square root of the total momentum profiles, assuming no bottom friction as in the other models. The temperature distribution can be found in an analogous manner.

The model predicts a gradual transformation from an initial Gaussian distribution to the final self-similar shape with the centerline values growing constantly. The three-dimensional region existing at the beginning of the diffuser is taken care of by a virtual source distance, x_ν, defined as H/κ, where κ is assigned the value 0.133. This value lies between those observed for two-dimensional and three-dimensional jet spreading. The virtual source distance enters into the derivation and has been found to be very important in the evolution of the profiles. A volumetric (bulk) dilution S_{bulk} is again defined and has an asymptotic value at a large distance

$$S_{bulk} = 0.67\frac{(m_0 H)^{1/2}}{q_0} . \tag{2.11}$$

This bulk dilution is about 50% larger than that predicted by the entrainment type models (Equation (2.10)).

Results from both Almquist and Stolzenbach's model and Jirka's model have been compared with the San Onofre hydraulic model study (Ng and Koh, 1986). Figure 2.3 is the centerline temperature excess measured from the SONGS model study in comparison with predictions from the two models. It indicates that the prediction from Jirka's model agrees very well with the physical model except at the end of the diffuser where the prediction slightly overestimates the ΔT. However, the AS model has predicted a much higher ΔT over the entire two-dimensional range. The lateral ΔT profile near the end of the diffuser is compared in Figure 2.4. The bell-shaped profile of the physical model spreads much wider than Jirka's prediction, possibly because of the angle of the SONGS jets ($\pm 25°$ to the axis), which resulted in a larger lateral growth rate. Another explanation for the discrepancies is the oversimplication of the induced flow field and thermal field, including the definite thermal stratification observed in the physical model.

In summary, the existing models are able to give reasonable predictions of the flow and temperature fields when the major assumptions are not violated. However, a more general model is needed to account for the density stratification, angled jets and cross currents, for example.

2.6.2 The Intermediate Field

Because of the density difference in the discharge, an unstable flow field may eventually restratify at some downstream distance, forming a surface flowing layer often referred to as a thermal plume. It behaves essentially like a surface buoyant jet with both momentum and buoyancy effects governing the mixing and spreading. Relatively little attention has been paid to this intermediate region. Jirka (1982) has suggested that after an adjustment distance of about 1.5 times the diffuser length, the flow field will be practically the same as that of a unidirectional diffuser. (The unidirectional diffuser has been modeled by Adams and Stolzenbach (1977) and Lee,

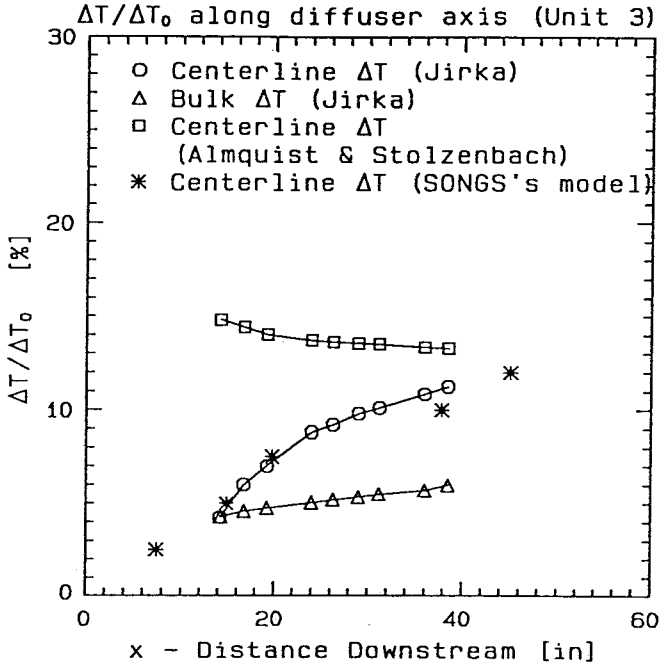

Figure 2.3 Comparison of theoretical models with observations from San Onofre physical model results—$\Delta T/\Delta T_0$ along the diffuser axis (based on model quantities).

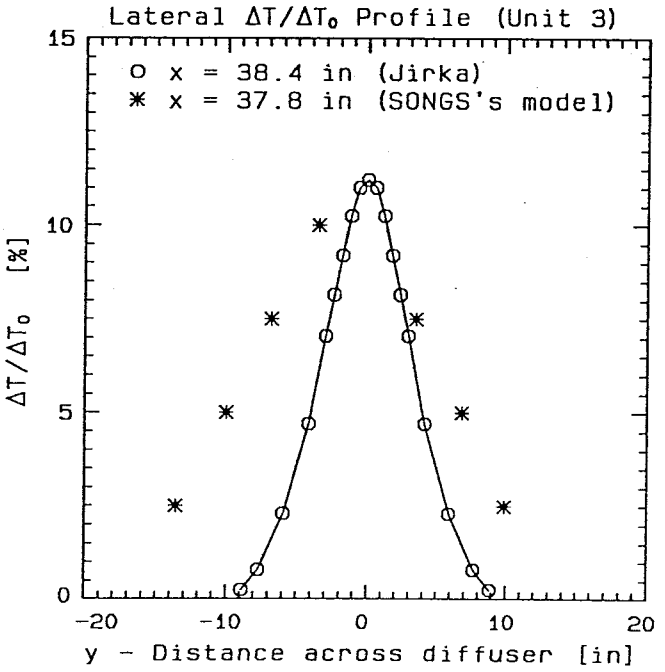

Figure 2.4 Comparison of theoretical models with observations from San Onofre physical model results—lateral $\Delta T/\Delta T_0$ profile near end of the diffuser (based on model quantities).

Jirka and Harleman (1977, 1979) using slip-stream analysis and an entrainment hypothesis.)

Brocard et al. (1979) has proposed a model for the complete trajectory of the flow using an integral technique. Their analysis uses entrainment assumptions as in the AS model and a lateral spreading relationship adopted from the analysis of Prych (1972) on surface buoyant jets. The governing equations are the three conservation equations and two trajectory equations for the path of the jet. The near-field analysis follows the same principles as the AS model, but allows a lateral entrainment term that is due to the current and an adjustment for the bottom shear stress. The intermediate field, on the other hand, is treated in a similar way as the three-dimensional surface buoyant jets by Prych (1972), Koh and Fan (1970), and Stolzenbach and Harleman (1971). Parabolic and Gaussian profiles are assumed in the vertical and lateral direction, respectively; however, the vertical profiles in the near field are modified to account for the momentum input from the bottom. Farther downstream in the far-field region where ambient turbulence is the dominating dispersion mechanism, the spreading relationship is replaced by a dispersion relationship derived from the dispersion coefficient and the "4/3 law." The model has showed generally good agreement with hydraulic model results (Campbell and Charlestown) in the higher ΔT region, but requires calibrations of several input coefficients. The transition from surface buoyant jet formulation to dispersion formulation is not detailed in the reports. The presence of singularities, as in the previous surface buoyant jet models, has not been resolved.

2.7 Summary

Laboratory data on staged thermal diffusers in shallow water come mainly from hydraulic model testings in the 1970's. Resolutions of the measurements are generally

too low for detailed analysis. Almquist and Stolzenbach (1976) conducted a slightly more detailed experimental study, but a systematic set of laboratory results is still lacking. Numerical models have been developed that are based either on the slot jet entrainment hypothesis or by integration of the profiles of hypothetical source elements along the diffuser. The models do not give sufficiently accurate predictions on the thermal and flow fields, but can provide guidelines in the preliminary configuring of diffusers. The biggest problem of the models is probably the assumption of vertically mixed profiles with no consideration of buoyancy and density stratification. The models do not give sufficiently accurate predictions on the thermal and flow fields, but can provide guidelines in the preliminary screening of diffuser configurations.

3. Physics of the Thermal Plume

3.1 Introduction

This chapter describes the physical processes taking place in the general flow field of thermal discharge from a staged diffuser in shallow water. The significance of the derived dimensionless variables and length scales in the different flow regimes are discussed. Relationships of mean properties with respect to distance from the discharge are proposed, using scaling arguments.

The problem under consideration is the thermal discharge from a submerged staged multiport diffuser in a laterally unconfined but shallow receiving water body. Figure 3.1 is the definition sketch of the staged diffuser. The staged diffuser consists of a number of nozzles n, each with jet diameter D_0 and separated by a center-to-center spacing, s. Each nozzle is oriented horizontally at an angle $\pm\alpha$ from the axis of the diffuser and at an angle β up from the horizontal plane. Cooling water at an elevated temperature of ΔT_0 is discharged from the diffuser at a total flow rate, Q_{T0}, which is distributed evenly among the nozzles. The ambient water has a uniform depth of $H+H'$, where H is the water depth above the discharge level and H' is the elevation of the nozzles from the bottom. At this stage ambient current is excluded for simplification. The discussion in the following sections will focus on the ideal case

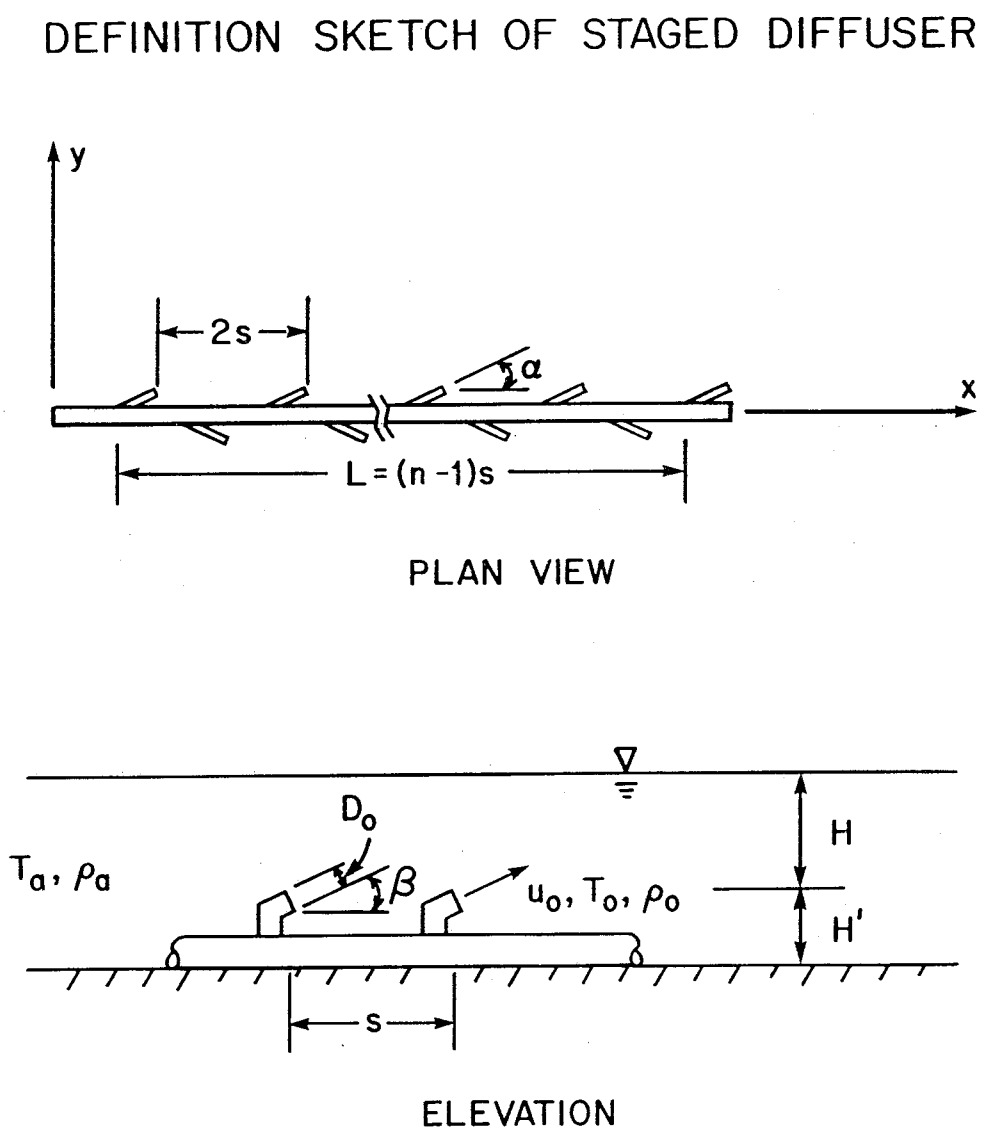

Figure 3.1 Definition sketch of staged diffuser.

of uniform ambient density, and the effect of stratification on the overall flow field will be considered in Appendix C.

3.2 The Hypothetical Flow Field

Figure 3.2 is a schematic diagram of the hypothetical flow field generated from the staged diffuser discharge. The flow structure is divided into two zones—the near field and the intermediate field—based on the inherent properties which vary with downstream distance.

(i) The near field

The near field is defined as the region in the immediate vicinity of the diffuser. Momentum and heat (buoyancy) fluxes are input to the receiving water body through the individual nozzles, thus keeping the near field in a development stage. This region is made up of a number of three-dimensional buoyant jets (momentum flux is dominant over buoyancy flux according to an order-of-magnitude analysis to be discussed in the next section) and is characterized by turbulent jet mixing and a certain extent of jet interaction (depending on the depth-to-spacing ratio). The entrainment pattern is highly three-dimensional and consequently yields complicated flow and temperature profiles because of the arrangement (geometry) and interference of the jets.

The flow field is further complicated by the shallow-water condition. Individual jets entrain ambient water along their upward paths through the water column. As the jets reach the surface, they are deflected by the air-water interface. In deep water, a surface layer that flows more or less horizontally away from the source will form, and there is little communciation between the jets and the layer. When the water depth is shallow, recirculating eddies may form (Jirka and Harleman, 1979), causing re-entrainment of diluted water back to the jets. The vertically mixed near field is referred to as being unstable. The existence and the extent of the instability depend

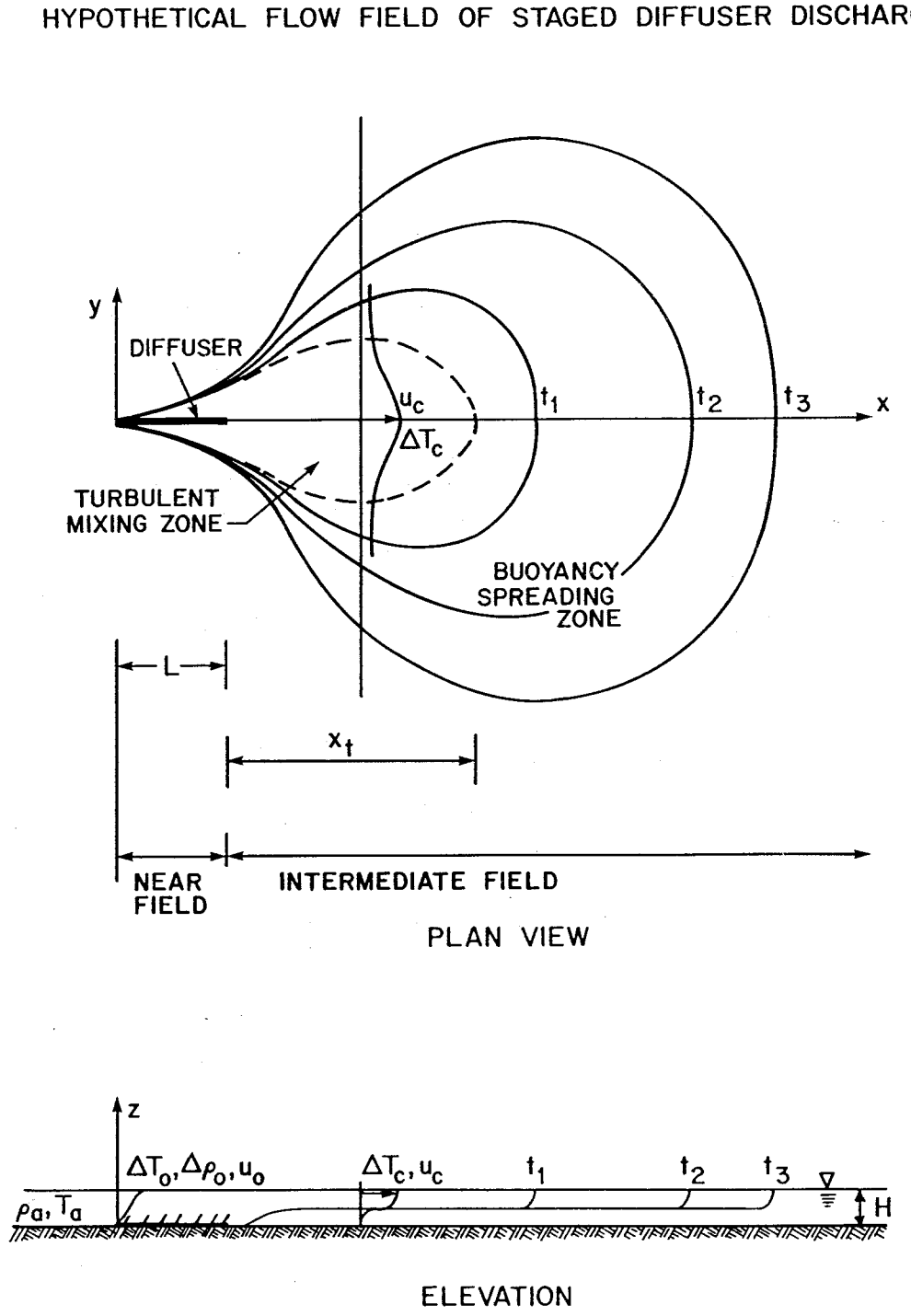

Figure 3.2 Schematic diagram of the plume at various times.

on the interplay or balance of the stabilizing buoyancy force and the destabilizing momentum force. Thus, a surface buoyant layer may not be well-defined because of the coupling of the dynamics of the entrainment flow toward the diffuser with the mixed flow away from the diffuser.

(ii) The intermediate field

Beyond the end of the diffuser where there is no further discharge of warm water, the thermal plume enters the intermediate regime. The flow field and temperature field will behave differently from the upstream region where the physical processes resemble those of a three-dimensional surface buoyant jet. The intermediate field has a more regular structure in terms of the induced velocity and temperature distributions compared to the near field. Because of the initial density difference between the discharge and the ambient, a surface layer usually forms either from the deflection of the jets (in the diffuser zone) by the water surface, or from stratification of an unstable near field. With the residual momentum flux carried over from the near field, the surface layer entrains ambient water and induces turbulent mixing as it flows downstream. At the same time, gravitational spreading takes place in the horizontal direction. The momentum mixing diminishes, while the buoyancy force becomes more significant with downstream distance. In other words, the fluid is in a deceleration state, and the flow field evolves gradually from a turbulent mixing zone with entrainment in both lateral and vertical directions to a gravitational spreading zone where activity is largely limited to the horizontal directions because of the stably stratified configuration with reduced shear stress.

The transition from turbulent mixing to horizontal spreading is, however, not only in the longitudinal direction. In the proximity of the centerline where velocity is the highest, momentum mixing is more significant, whereas at a lateral distance farther away from the diffuser axis, velocity decreases and buoyant spreading may

become more important. The intermediate field therefore can consist of an inner core dominated by momentum mixing, and a surrounding outer region dominated by buoyant spreading. The inner core is steady in the mean, whereas the outer zone extends downstream as well as grows laterally with time as in Figure 3.2. The lateral decay in temperature and velocity is expected to be more rapid in the inner steady zone but to be relatively small in the outer spreading region. As the plume grows in size radially, the plume fluid closest to the near field has the possibility of being re-entrained into the plume, forming recirculation eddies in the horizontal plane on both sides of the near-field boundary. The occurrence and extent of this inundated situation are governed by the relative balance of the inertia force and buoyancy force.

The thermal plume progresses downstream until the inertial forces diminish, and gravitational spreading becomes the sole dominating process. Ambient turbulence will eventually be effective in dispersing the thermal plume, and this flow region will be referred to as the far field. The following discussions include only the near field and the intermediate field.

3.3 Dimensional Analysis

The basic variables governing the performance of thermal discharges from staged diffusers in a quiescent ambient are:

diffuser variables: D_0, n, s, α, β;

discharge variables: u_0, T_0, ρ_0;

ambient variables: T_a, ρ_a, H, H', $(\partial\rho_a/\partial z)$;

and: g and ν.

The dependent variables in the system, denoted by ϕ_i, are the mean characteristics of the thermal plume at a given cross section and are functions of the independent

variables and the position of interest (x, y, z). The minimum surface dilution S_c, the lateral width and the depth of the plume, are some of the interesting and commonly studied variables. No comprehensive analytical relationship for the problem has yet been derived.

3.3.1 Assumptions and General Considerations

The number of independent variables can be reduced by adopting several assumptions common to buoyant jet analysis:

(1) The near-field region is fully turbulent ($Re \geq$ 20,000); thus the direct effect of viscosity can be neglected.

(2) The density changes caused by the discharge are small compared to the ambient density and are important only in the gravitational force term (the Boussinesq approximation); the four variables, ρ_0, ρ_a, $\partial\rho_a/\partial z$, and g are thus replaced by ρ_0, $\Delta\rho g$, and $g\partial\rho_a/\partial z$, where $\Delta\rho = \rho_0 - \rho_a$.

(3) The fluid density ρ and temperature T are related by a linear equation of state, $\rho = \rho_a(1 - \alpha_p(T - T_a))$, where α_p is the coefficient of thermal expansion. Therefore, only one of them may be considered as an independent variable. Further simplifications include the neglect of the slight heat transfer to the atmosphere in the regime considered, and the assumption of homogeneity of the ambient in the horizontal directions.

Previous analyses on buoyant jets have demonstrated the advantages of using flux variables in describing jet dynamics. The primary independent flux variables are the kinematic mass, momentum and buoyancy fluxes at the discharge and are defined as:

$$\text{volume flux } Q_{i0} = u_0(\pi D_0^2)/4; \tag{3.1}$$

$$\text{kinematic momentum flux } M_{i0} = u_0 Q_{i0}; \tag{3.2}$$

$$\text{kinematic buoyancy flux } B_{i0} = (\Delta\rho/\rho_a)gQ_{i0} \text{ or } g'Q_{i0}, \tag{3.3}$$

where the subscript ($i0$) represents flux from the individual nozzle, u_0 is the discharge velocity and D_0 is the initial diameter of the jets . Another set of flux variables can be defined for the entire diffuser:

$$Q_{T0} = nQ_{i0}; \tag{3.4}$$

$$M_{T0} = nM_{i0}; \tag{3.5}$$

$$B_{T0} = nB_{i0}. \tag{3.6}$$

Furthermore, according to Wright (1977), several length scales (three-dimensional) can be formed from the flux variables:

$$\ell_Q = Q_{i0}/\sqrt{M_{i0}}; \tag{3.7}$$

$$\ell_M = M_{i0}^{3/4}/B_{i0}^{1/2}; \tag{3.8}$$

$$\ell'_M = M_{i0}^{1/4}/\delta^{1/4}; \tag{3.9}$$

$$\ell'_B = B_{i0}^{1/4}/\delta^{3/8}, \tag{3.10}$$

where δ is defined as $-(g/\rho_a)(\partial\rho/\partial z)$. ℓ'_B can also be rewritten as $\ell'_B = {\ell'_M}^{3/2}/{\ell_M}^{1/2}$. Using the length-scale representations and applying the assumptions to simplify the problem, the overall flow field (the mean characteristics ϕ_i) can be described by the following dimensionless parameters (for steady state):

$$\phi_i = F(\ \ell_M/H,\ s/H,\ \ell_Q/H,\ \alpha,\ \beta,\ n,\ \ell'_M/H,\ H'/H,\ x/H,\ y/H,\ z/H\ ). \tag{3.11}$$

In the discharge configuration being considered, H' is assumed to be small (e.g., in the experiments, $H'/H \leq 0.13$), such that the variable can be dropped from the analysis.

3.3.2 The Near Field

The implications and significance of the dimensionless variables are discussed in this section.

To justify a three-dimensional formulation, the s/H ratio is discussed first. It is, in many cases, an index for jet merging. In other words, it is a criterion for using the equivalent slot-jet assumption in the analysis of multiport diffusers. Figure 3.3 illustrates two thermal jets, separated by a distance s, in a section of the staged diffuser. Each of the jets is assumed to be spreading at a rate equivalent to that of a three-dimensional pure jet. The commonly adopted value for the growth rate of the half-width is 0.127. This is equivalent to having a total jet-spreading angle of $2\beta_k$, where $\beta_k = 7.24°$. The possibility of recirculating eddies in the vertical plane in the shallow-water condition is neglected in this analysis. Merging of the jets is assumed if, geometrically, the boundaries of the two jets interact within the water column. This is equivalent to having the minimum perpendicular distance between the jets, represented by w_4 in Figure 3.3, approaching zero. Hence, a criterion for jet merging can be derived:

$$w_4 = (s - \frac{H}{\tan(\beta - \beta_k)} + \frac{H}{\tan(\beta + \beta_k)}) \sin(\beta + \beta_k) \leq 0 \,,$$

$$\Longrightarrow \qquad \frac{s}{H} \leq \frac{1}{\tan(\beta - \beta_k)} - \frac{1}{\tan(\beta + \beta_k)} \qquad (\text{for} \beta > \beta_k) \,. \tag{3.12}$$

The terms on the right-hand side of Equation (3.12) can be taken as a critical ratio $(s/H)_{cr}$ such that merging will occur when s/H of the diffuser is smaller than

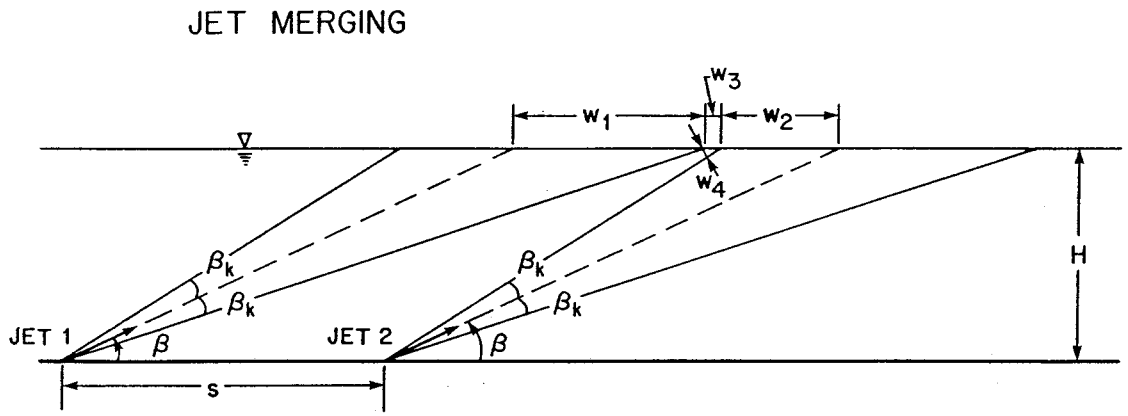

Figure 3.3 A section of the staged diffuser with $\alpha = 0°$, showing the geometry of two adjacent jets used for deriving critical spacing for jet merging (Equation (3.12)).

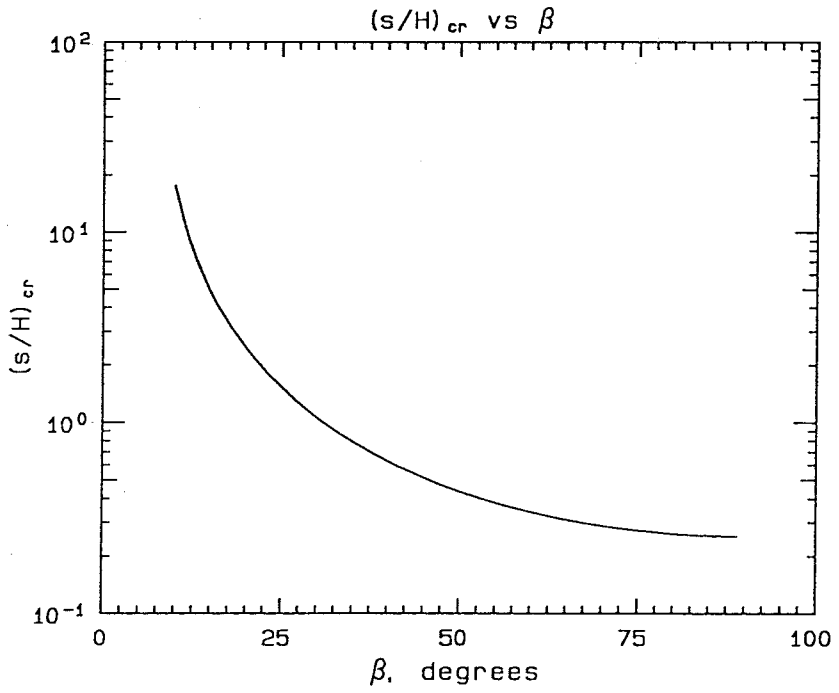

Figure 3.4 Critical s/H ratio versus β.

this critical value. Merging will always take place if $\beta \leq \beta_k$, including horizontal discharge, i.e., $\beta = 0°$. In other cases, the critical ratio decreases with an increasing discharge angle β for $\beta \geq 10°$ as shown in Figure 3.4.

Comparing the $(s/H)_{cr}$ and s/H ratios of the previous hydraulic model studies, both merging and non-merging conditions exist. Since the two-dimensional flow field assumption does not necessarily hold for the general case, the equivalent slot jet assumption cannot be used indiscriminately. A three-dimensional approach is thus proposed for subsequent analysis.

The second parameter to be discussed is ℓ_M/H. The momentum length scale ℓ_M is a measure of the distance over which the momentum force dominates over the buoyancy force. Hence, a decrease in the value of ℓ_M/H indicates an increasing tendency for plume-like flow to develop before the flow reaches the surface. Experimental results of Papanicolaou (1984) on vertical buoyant jets indicate that the limiting conditions for a pure jet and a pure plume are when $\ell_M/z \geq 0.94$ and $\ell_M/z \leq 0.19$, respectively, where z is the vertical distance above the source. For horizontal buoyant jets, Brooks (1980) shows that the asymptotic pure plume behavior occurs when $\ell_M/z \leq 0.03$. Reviewing the ℓ_M/H ratios in previous diffuser model studies shows that the range is from 1.2 to 2.8. However, for diffusers with an upward discharge angle β, the trajectory of the individual jets will be much longer than H. Assuming a straight trajectory, the effect of β can be taken into account by considering the ratio $\ell_M/(H/\sin\beta)$. This ratio is about 0.7 for the Darlington Station "A" diffusers and the Charlestown Station diffusers (both of which have $\beta = 20°$). For the Somerset site diffusers, which have $\beta = 0°$, the ℓ_M/H ratio is approximately 2.8. There are other thermal diffusers with $\ell_M/(H/\sin\beta)$ of around 0.3 to 0.4. These typical values suggest that momentum mixing is the dominant process in most cases (i.e., jet-like flow).

Further up the water column, the jets will be deflected by the buoyancy force. Fan and Brooks (1969) calculated the trajectory for turbulent buoyant jets. For thermal diffusers with a typical densimetric Froude number Fr_0 of about 35 (the range is from 30 to 70), the assumption of a straight-line trajectory is only reasonable for $\ell_M/z \geq 7$ in a horizontal discharge case. For inclined jets, β is an important variable in determining the critical ℓ_M/z ratio for the straight-line trajectory assumption. For example, the critical ℓ_M/z ratio is approximately 2.7 for $\beta = 15°$ and 1.6 for $\beta = 30°$. Comparing these critical ratios with the typical ℓ_M/H of 1.2 to 2.8 (this value does not include the reduction in the effective depth of water that is due to the surface layer), a limited amount of jet deflection is expected at the upper part of the water column.

The discussions on the s/H and ℓ_M/H ratios imply that the near field can be analyzed as a series of independent pure jets, neglecting the initial buoyancy flux. Furthermore, the typical range for the ratio ℓ_Q/H is from 0.02 to 0.1, and the typical ratio ℓ_Q/ℓ_M is approximately 0.025. The implication of small ℓ_Q/H and ℓ_Q/ℓ_M values is that the initial volume flux Q_{i0} is not significant dynamically. If buoyancy flux is neglected, $\ell_M \rightarrow \infty$ and will drop out. Only ℓ_Q remains from the dimensional analysis even though Q_{i0} is not important dynamically for a distance much larger than ℓ_Q. Defining a minimum surface dilution S_c in the diffuser region as a dependent variable, the controlling length scales in homogeneous ambient will then be H, ℓ_Q and s. Dimensional analysis results in:

$$S_c = F(\ell_Q/H, s/H, \beta, \alpha, n)\,, \tag{3.13}$$

where

$$S_c \equiv \frac{\Delta T_0}{\Delta T(z = H)}\,. \tag{3.14}$$

It is proposed that the near-field mean characteristics can be represented by the three-dimensional simple jet theory (Fischer et al., 1979) with an adjustment for jet merging controlled by s/H and n. For a certain α and H, the distance of the jet path (entrainment distance) is $H/\sin\beta$, assuming a linear trajectory. The minimum surface dilution S_c for diffusers with $\beta > 10°$ (taken arbitrarily) will be:

$$S_c = a_1(\frac{H/\sin\beta}{\ell_Q})f'(s/H,n)\ , \tag{3.15}$$

where a_1 is found empirically to be 0.18 ± 0.02 for a round jet. A minimum bulk dilution at the surface can also be defined as $S_{bulk} \equiv Q(H)/Q_{i0}$ at downstream distance x, and similarly,

$$S_{bulk} = (0.25 \pm 0.01)(\frac{H/\sin\beta}{\ell_Q})f'(s/H,n)\ . \tag{3.16}$$

The simple jet theory presented, however, is applicable only to situations where the surface effect is not important (i.e., in deep water), and there is no jet interference. In the case of shallow water, deflection of the jets by the water surface results in recirculating eddies and possibly an unstable flow field. The formation of a surface layer will decrease the initial surface dilution by reducing the depth of the entraining ambient. The thickness of this layer is also expected to be a function of the parameter ℓ_Q/H, the number of ports n, and the jet spacing-to-depth ratio s/H, which is an important parameter governing jet merging characteristics. The theory, however, does not include any dependency on the horizontal angle of discharge (α). However, a change in α obviously leads to a change in the horizontal extent of the flow field. It may also modify the instability relationship by increasing the stability of the flow.

The effect of ambient stratification is measured by the parameter ℓ'_M/H and ℓ'_B/H. ℓ'_M is a length scale for the momentum dominance of a round jet (of zero

buoyancy) over the effect of a stratified environment, whereas ℓ'_B is the length scale for buoyancy dominance of a pure plume in a stratified ambient. Again, order-of-magnitude analysis is used to determine the significance of the ambient stratification. For example, if the ambient is stably stratified with a 5.0°C temperature difference between surface and bottom ($H = 10\,\mathrm{m}$), the corresponding δ is approximately $1.07\mathrm{x}10^{-3}\mathrm{s}^{-2}$. Using SONGS discharge momentum flux ($M_{i0} = 3.29\,\mathrm{m}^4/\mathrm{s}^2$), buoyancy flux ($B_{i0} = 0.023\,\mathrm{m}^4/\mathrm{s}^3$) and water depth ($H = 10\,\mathrm{m}$) for illustration, ℓ'_M/H is about 0.75 and ℓ'_B/H is about 0.5. Both ratios are of unit order indicating that the density stratification does not become dynamically important in the initial mixing process. In other words, the stratification changes only the density or the temperature excess ΔT of the plume, but does not modify the dilution (i.e., the dynamics of the flow field).

Other quantities of interest are the characteristic growth rate of the plume, the characteristic width and the thickness of the plume at the end of the near field. Since momentum force is still the controlling factor, a similar functional dependency as for S_c on $\ell_Q/(H/\sin\beta)$, s/H and n should suffice.

3.3.3 The Intermediate Field

Shortly beyond the end of the diffuser, a surface buoyant layer will form and behave as a large surface buoyant jet. As discussed in Section 3.2, the intermediate field is comprised of a turbulent core region surrounded by a gravitational spreading field (Figure 3.2). Momentum mixing dominates the turbulent core with the ambient water being entrained from the sides as well as from the bottom of the layer. Because of the absence of further inputs of momentum and heat, the velocity and the temperature will decrease with distance until the end of the core region. The width of the plume, at the same time, will grow with distance, whereas the thickness may increase slightly (less compared to the growth of the width because of the buoyancy,

which keeps the layer flowing at the surface). In the gravitational zone, the motion is mainly in the horizontal directions; the buoyancy in the plume reduces activity in the vertical direction. The plume width-to-thickness ratio, as a result, will increase even further.

Depending on the discharge parameters and the ambient conditions, the extent of the turbulent mixing core region varies. Two limiting situations can be identified. The first condition is when momentum mixing dominates the region of interest, which is on the order of several diffuser lengths downstream. This will occur in shallow-water discharges with a large initial momentum flux, or $\ell_M/H \gg 1$. The other limiting case occurs in deeper water discharge with less initial momentum, $\ell_M/H \ll 1$. The gravitational spreading zone may move back to the diffuser region and, therefore, dominates the entire region of interest.

The surface buoyant jet problem has been studied using laboratory experiments and mathematical models (Section 2.4.4). The analysis, however, cannot apply to the present situation, even with modification. The first reason is that the initial conditions of the intermediate field of a staged diffuser are very different from that of an idealized surface buoyant jet. The beginning section of the intermediate field is basically the end of the diffuser zone (near field). The initial velocity and temperature distributions (referenced to the intermediate field) are expected to be more or less Gaussian in shape (confirmed for temperature later in the presentation of the present experimental results, Chapter 5), whereas in surface buoyant jet analysis, the initial discharge is always assumed to be uniform across the exit section. Even if the initial conditions (of the intermediate field of a staged diffuser) can be idealized as being uniform, the volume flux, Q_{I0}, at this section (a sum of the source volume flux and the total entrained volume flux in the near-field region) is too large to be neglected for some distance. In addition, the characteristic width of the surface layer, b_{I0},

at the beginning, is relatively large, and therefore the effect of the source geometry will remain for a long distance (compared to the distance of interest for thermal discharges). Hence, the mean characteristic ϕ_i is a function of many variables:

$$\phi_i = F(Q_{I0}, M_{I0}, B_{I0}, b_{I0}, h_{I0}, x, y) \,, \tag{3.17}$$

where the subscript $I0$ refers to the initial section of the intermediate field, M and B are the corresponding momentum and buoyancy fluxes and b and h are the characteristic width and thickness of the surface layer, respectively.

In the gravitational spreading zone further downstream, the flow field reduces to one that is similar to a continuous discharge of buoyancy. Buoyant discharge from a point source has been studied by Koh and Fan (1970) and Chen (1980). Analytical functions for buoyant spreading have been developed. However, the gravitational zone of a staged diffuser cannot be simplified as a point source because of the large plume width. Furthermore, at a greater distance away, heat transfer with the atmosphere will become more important, and the buoyancy of the plume will disappear.

The large number of significant independent variables involved in the problem makes the analysis of the intermediate field very difficult. In later chapters, efforts are focused on gaining a better qualitative understanding of this flow region from experimental observations.

3.4 Summary

On the basis of the experimental observations from previous laboratory studies on thermal discharge from multiport diffusers and surface buoyant jets, two distinct flow regions are postulated to exist in the flow field of a staged diffuser—the near field and the intermediate field. The near field is in the vicinity of the diffuser and is dom-

inated by three-dimensional jet mixing and jet interactions. Dimensional reasoning and scaling arguments are used to show that the simple jet theory (with modifications for n and s/H) can be used to describe the near-field mean characteristics. The intermediate field is a combination of a large surface buoyant jet and gravitational spreading plume. Even with simplifications, the large number of independent variables remaining in the problem make it very difficult to derive useful relationships for the flow-field characteristics at this stage.

4. Experimental Setup and Procedures

4.1 Objectives

The objective of the experiments is to measure the temperature distribution resulting from warm water discharged through staged diffusers in a large body of receiving water. Horizontal and vertical temperature profiles of the discharge plume at various distances from the beginning of the diffuser have been measured. The experiments also involve some indirect surface velocity measurements. A complete statement of the research objectives is given in Chapter 1.

4.2 Experimental Setup

The setup can be divided into five subsystems: the test basin, the warm-water supply and discharge system, the thermistor probes, the data acquisition system, and the photographic devices. The equipment has been designed to monitor the three-dimensional thermal field adequately.

4.2.1 The Test Basin

The experiments were performed in a 6.1 m (20.0 ft) wide, 11.0 m (36.0 ft) long, and 0.4 m (15.0 in) deep basin located in the subbasement of the W. M. Keck

Laboratory of Hydraulics and Water Resources (Figure 4.1). The walls of the basin were constructed of concrete blocks cemented together and mortared onto the laboratory floor. A plastic lining was shaped to cover the entire basin to prevent leakage. A survey of the basin floor revealed slight localized deviations (within 5.0 mm) from the mean level. No adjustment, was made however, in the experimental procedures or the data analyses that follow. Figure 4.2 is a photograph of the setup in the test basin.

The basin contained a false-bottom structure, consisting of a square plywood platform 5.4 m (17.75 ft) on a side, 7.6 cm (3.0 in) in height, with 1:3 sloping edges on the four sides, as shown in Figure 4.3. The finished level of the structure was 8.9 cm (3.5 in) high with the top 1.3 cm (0.5 in) being covered and levelled with sand of 1.0 mm nominal diameter. The sand layer provided a level "false" bottom, even if the plywood might warp after extended immersion in water. The structure served to conceal the main pipe of the diffuser, leaving only the nozzles in the water column (to minimize H'). This was done to avoid the ambiguity of deceptive increases in the measured dilution that were due to the additional amount of water below the jet level. Such considerations are particularly important in shallow water experiments, since the expected range of water depth is comparable to the size of the diffuser pipe (5.1 cm in diameter).

Two carriages were mounted on rails along the side walls of the basin. One carriage was used for equipment mounting (the instrument carriage), while the other served as an observation deck. The instrument carriage also had rails along its length to accommodate a traversely running probe carrier, which supported thermistor probes, depth probes and other accessories. While the two longitudinally running carriages were moved manually, the probe carrier was driven by a 1/4 horsepower motor equipped with a 100:1 speed reducer to increase the torque output and

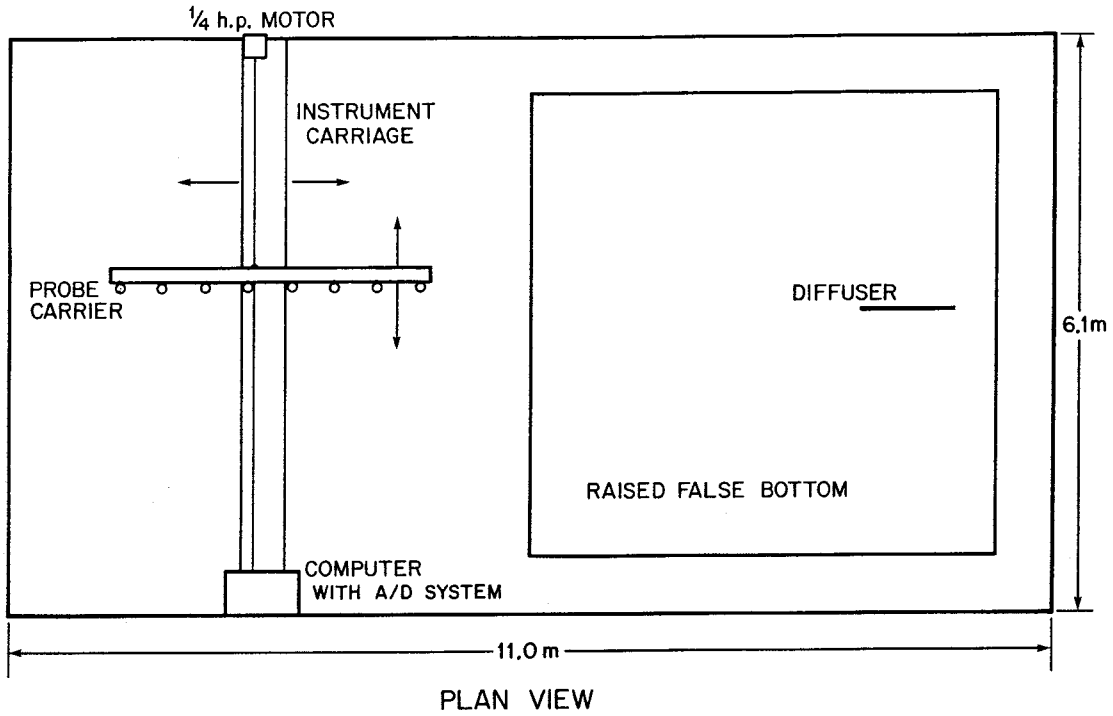

Figure 4.1 Schematic diagram of the test basin layout.

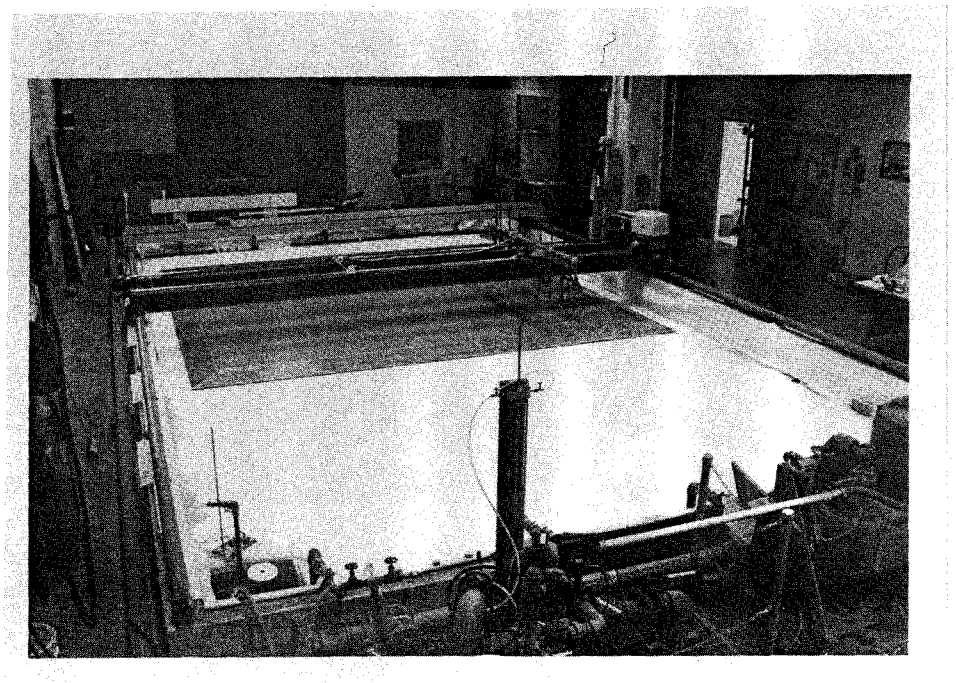

Figure 4.2 Photograph of the test basin.

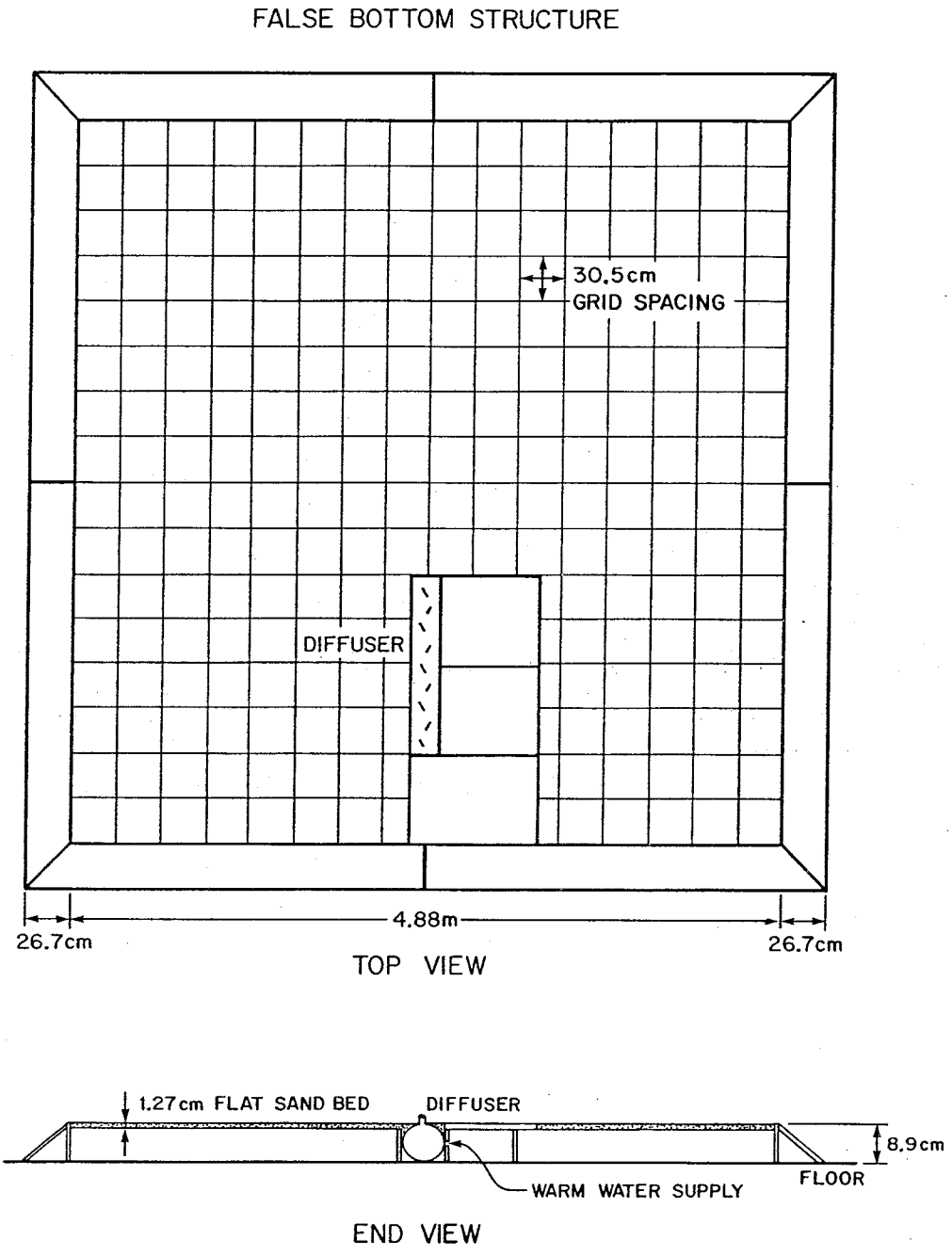

Figure 4.3 Schematic diagram of the false bottom structure.

a Minarik speed controller to control remotely the speed of movement. The position of the carriages was measured by potentiometers. Attached to each carriage was a wheel (30.5 cm and 25.4 cm in diameter for the instrument carriage and the probe carrier, respectively) connected to the potentiometer. When the carriage moved, the wheel rotated and changed the resistance of the potentiometer. The resistance output was then calibrated to give the position of the carriage. Samples of the calibration curves for the lateral and longitudinal positions are presented in Appendix B. The horizontal position of the probe carrier could be located to within ± 0.29 cm.

4.2.2 The Warm Water Supply and Discharge System

The arrangement of the warm water supply system is shown in Figure 4.4. It consisted of a 175-liter storage tank, a heater to maintain water at a designated temperature, and a flow meter (Fischer & Porter Co., model 10A1027) of 70.6 cm^3/s (1.12 gpm) capacity to monitor the discharge flow rate. The warm water was circulated (with a Jabsco centrifugal pump) from the storage tank through a 1.27 cm (O.D.) hose to the diffuser for discharge. A dye bottle was connected to the outlet of the supply tank just downstream of the pump to color the effluent for flow visualization. Upstream of the inlet to the diffuser, a by-pass pipe was installed to drain away unusable discharge water, particularly that which had not yet attained the prescribed temperature prior to the start of the experiments.

Concealed in a precut slot in the false bottom structure, the diffuser was made of two concentric Plexiglas cylinders of 98.0 cm in length, 0.32 cm in wall thickness, and 5.1 cm and 3.8 cm in respective external diameters. The endplates were sealed with O-rings to keep the air space between the two cyclinders watertight for insulation. There were 16 aligned fittings at 6.0 cm spacing on the diffuser, capable of housing up to 16 nozzles of variable sizes and discharge angles. Located at the midsection of the diffuser was the inlet for warm water, and 24.0 cm from it was a special fitting for

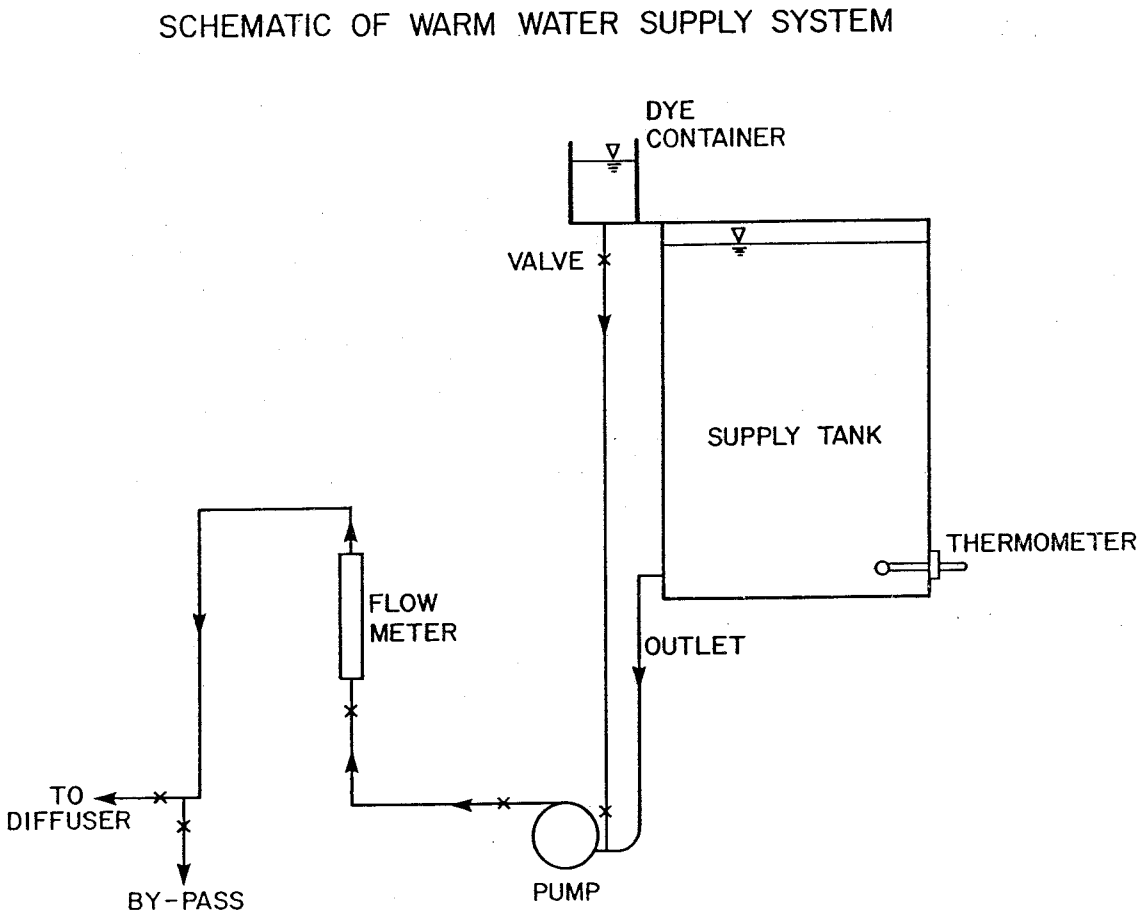

Figure 4.4 The warm water supply and discharge system.

a single thermistor, which would monitor the water temperature inside the diffuser. A baffle plate (same length as the diffuser) with distributed holes 0.6 cm in diameter was placed inside the inner cylinder for a more evenly distributed flow among the nozzles. Dimensions of the diffuser with an enlarged section of a nozzle are shown in Figure 4.5a. Figure 4.5b is a photograph of the diffuser unit.

The nozzles were made of brass and were capped by sharp-edged orifices, which controlled the diameter of the discharge jet and could be replaced with other sizes. Friction-type joints with O-rings to guard against leakage were used in all connections to facilitate changes in the diffuser configuration (e.g., the number, size, and orientation of the jets).

While the sizes of the jets were predetermined, the diameters of the orifices had to be decided by trial and error processes to account for the jet contraction. The initial sizes of the orifices were estimated using the coefficient of contraction in the range of velocity ratios between the nozzles and the jets. Water was then discharged through the orifices (with the initial diameters), and the sizes of the jets at the contraction were measured with a caliper. The sizes of the orifices were then adjusted accordingly until they produced the designated jet sizes.

4.2.3 The Thermistor Probes

Temperature was measured with thermistors. A total of 160 thermistors assembled into eight probes were used to monitor the temperature of the discharge plume, with an additional thermistor inside the diffuser for detecting the discharge temperature. The experiments employed standard negative-temperature coefficient (NTC) thermistors 0.25 cm in diameter with a nominal temperature constant (T.C.) of 22 seconds. By transferring a thermistor rapidly from water of higher temperature to lower temperature and vice versa, however, the actual T.C. was found to be around 0.5 second.

a)

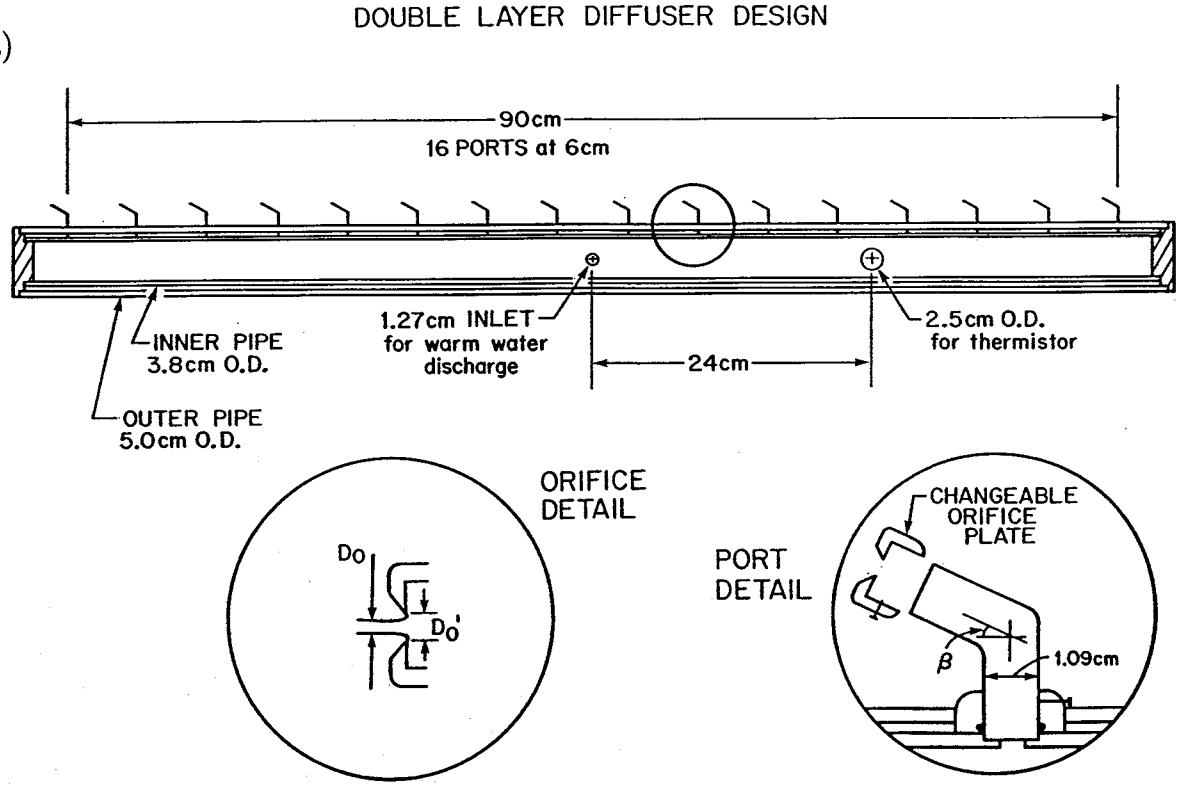

b)

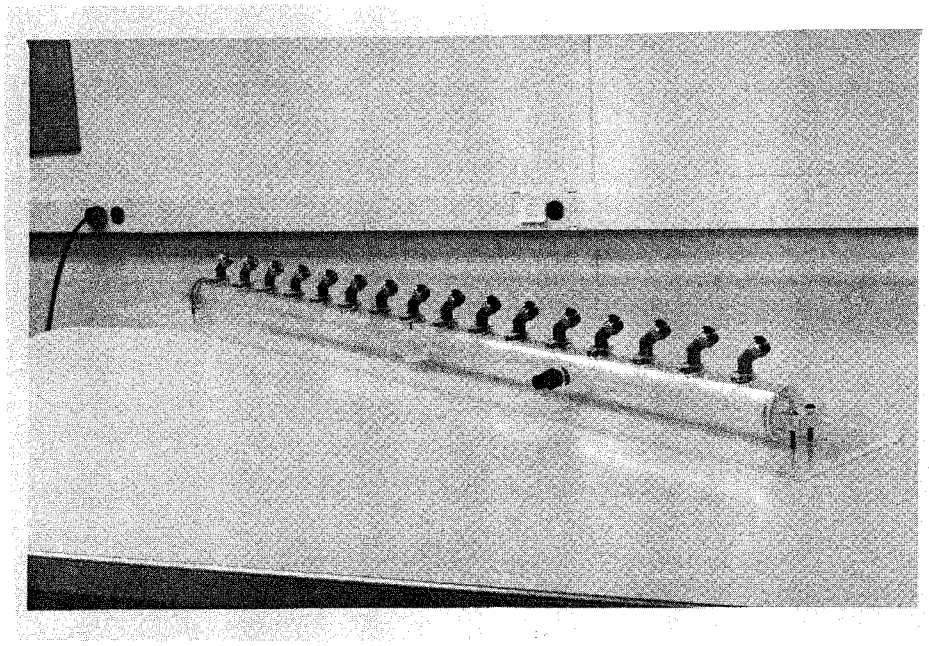

Figure 4.5 Staged multiport diffuser. a) Schematic diagram; b) Photograph.

The thermistor probe is depicted schematically in Figure 4.6, and in a photograph in Figure 4.7. Figure 4.8 is a photograph of the thermistor (to be placed inside the diffuser) for monitoring discharge temperature. The body of a thermistor probe was machined from a lucite block 0.5 cm x 1.5 cm x 17.75 cm to form an airfoil cross section to minimize the form drag in water. Twenty holes of 0.5 cm at 0.75 cm spacing were drilled in each probe to hold the thermistors. A slot was cut along the full length of the body to make room for the conductor wires, which ran from the thermistors to the top of the probe and ended in a snap connector. An acrylic cement (Weld-On #40 of Industrial-Polychemical Services) was used to fill the holes and the slots to retain the airfoil shape after assembly.

A brass rod crimped to a mounting bracket at one end was screwed to the top cover plate of the probe at the other end. The whole unit was then mounted onto the probe carrier described in Section 4.2.1.

4.2.4 The Data Acquisition System

Experimental data were collected by an IBM PC (with 512K random access memory) equipped with an analog and digital I/O board (DT 2811, manufactured by Data Translation, Inc.). The I/O board provided 12-bit resolution of the input voltage and allowed 16 single-ended or 8 differential input channels for A/D (analog/digital) conversions at a throughput rate of 20kHz. In the experiments, 161 channels for the thermistors and 2 additional channels for longitudinal and lateral position tracking were needed. Therefore, 2 multiplexer units, each capable of multiplexing 8 channels into 128 channels were introduced into the system to sample all the inputs. Figure 4.9 is the circuit diagram of one channel (out of 8) in a multiplexer unit.

The raw signals from the thermistors and the potentiometers were in units of resistance and were converted to voltages before being transmitted to the A/D converter. This was achieved by connecting all the raw signals (in resistance) to bridge

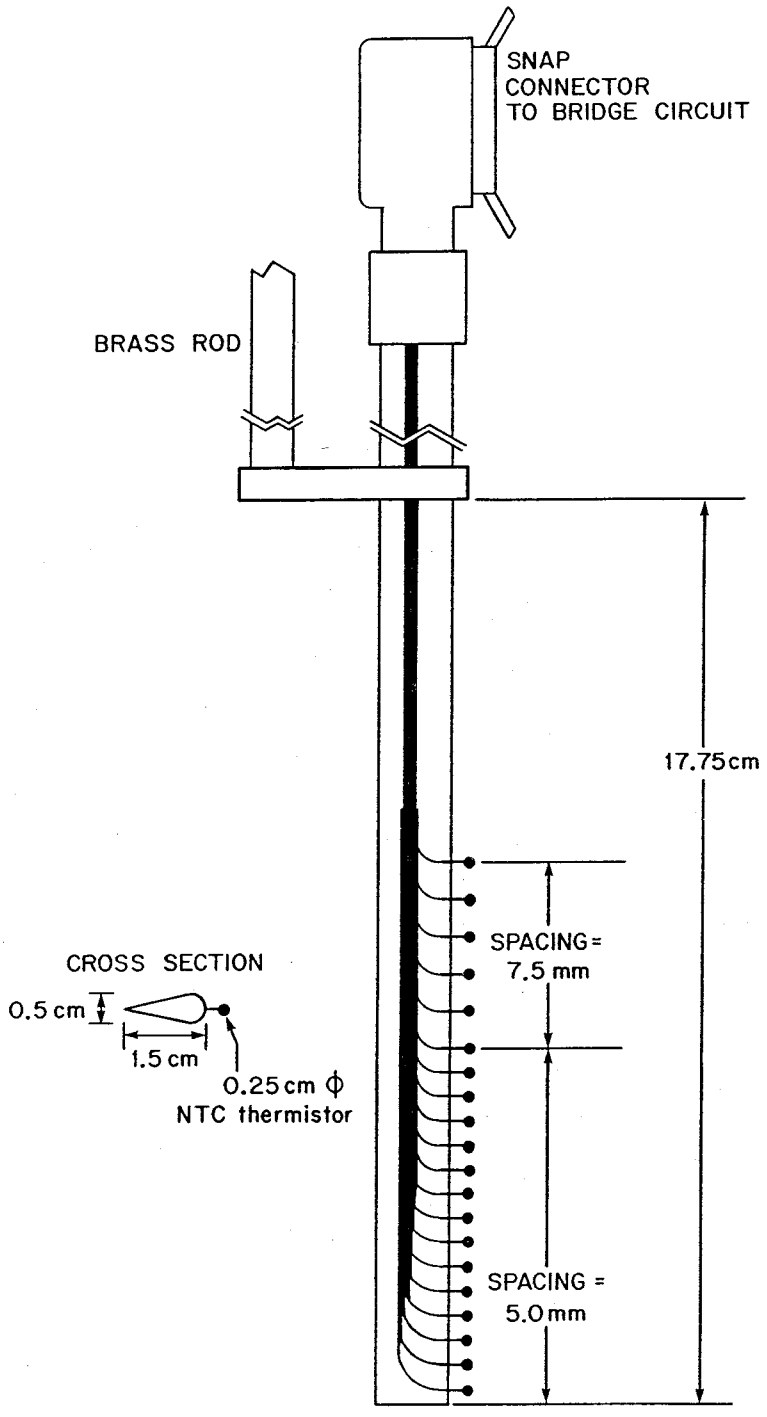

Figure 4.6 Schematic diagram of a thermistor probe.

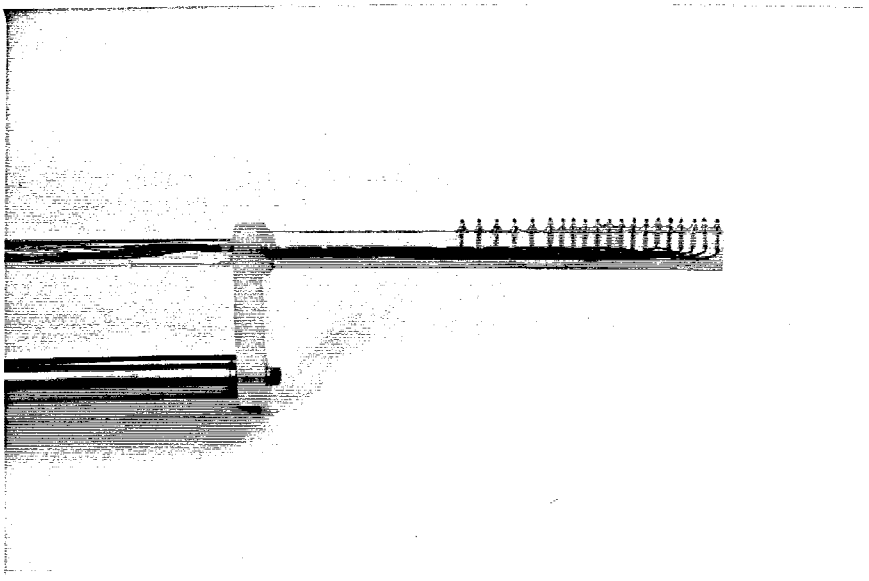

Figure 4.7 Photograph of a thermistor probe.

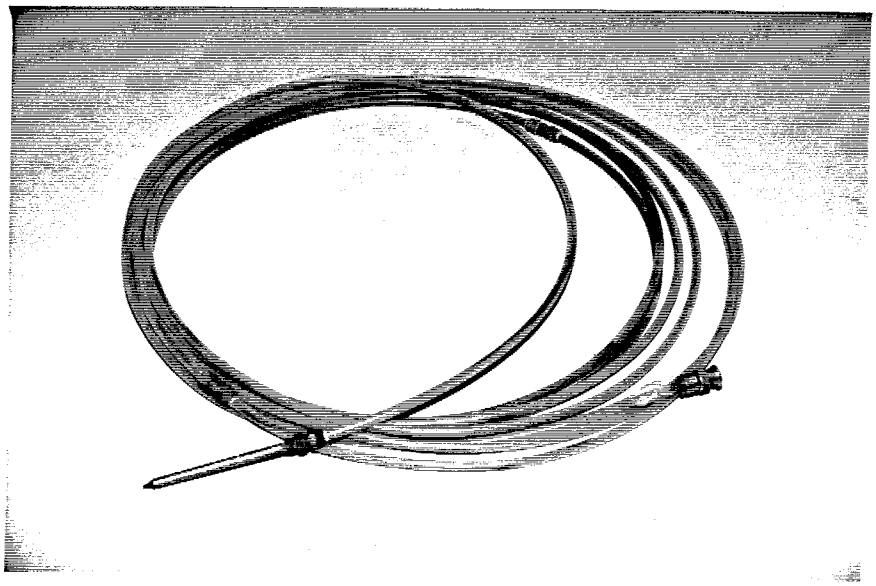

Figure 4.8 Photograph of the thermistor for monitoring discharge temperature inside diffuser.

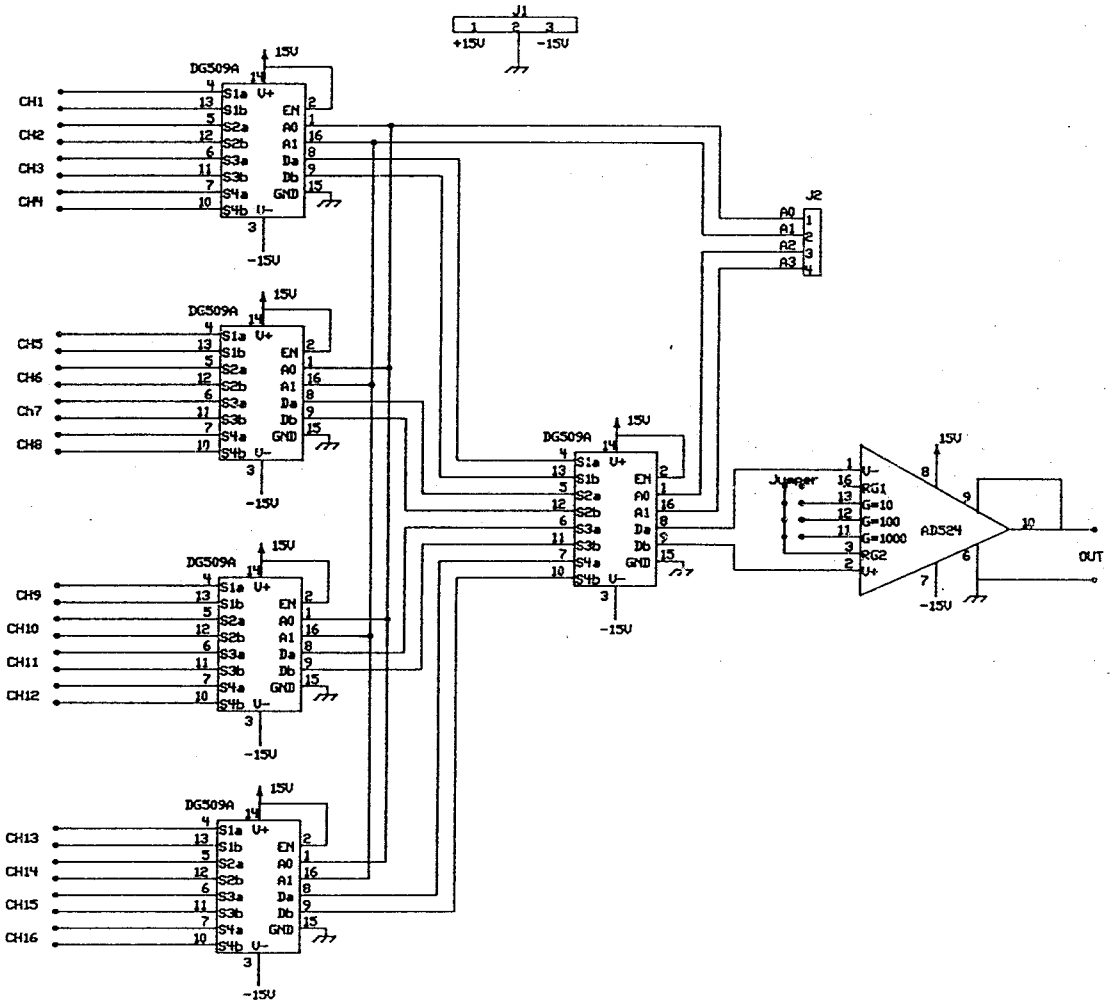

Figure 4.9 Circuit diagram of a multiplexer unit.

circuits, one for each individual thermistor and potentiometer. Since there were 20 thermistors in each probe, it was more convenient to arrange the 20 bridge circuits into a compact unit referred to as a bridge box. Figure 4.10 is an example of two bridge circuits (out of 20) for the thermistor probe. All components are connected by shielded cables to minimize noise.

A computer program written in Turbo Basic language (Borland) issued a software trigger to initiate the conversion and collection procedures at the start of an experiment. The same program was responsible for signalling the end of the data acquisition procedures and storing the digital data to files in convenient formats for future retrieval and analysis. Figure 4.11 illustrates the signal flow-path and the interconnection of components of the data acquisition system. A sample data collection program is listed in Appendix A.

4.2.5 The Photographic Equipment

A Nikon F camera mounted about 3.7 m above the water surface was used to obtain the overhead pictures of the advancing thermal plume. The camera was equipped with a 28 mm wide-angle lens and could be triggered through the use of a motor drive. Color films of ASA-400 film speed were used. Kriegrocine red B concentrate dye (Special-T/California) was mixed with the discharge to differentiate the plume from the ambient water and to enhance visualization .

An array of grid lines at 30.5 cm apart were set up on the sand surface of the false-bottom structure to provide a reference system for the physical dimensions of the growing plume. Photographs were taken at predetermined time intervals to give an estimate on the frontal celerity of the plume. In some experiments, paper particles were added to enhance the indirect measurement of surface velocity at selected locations.

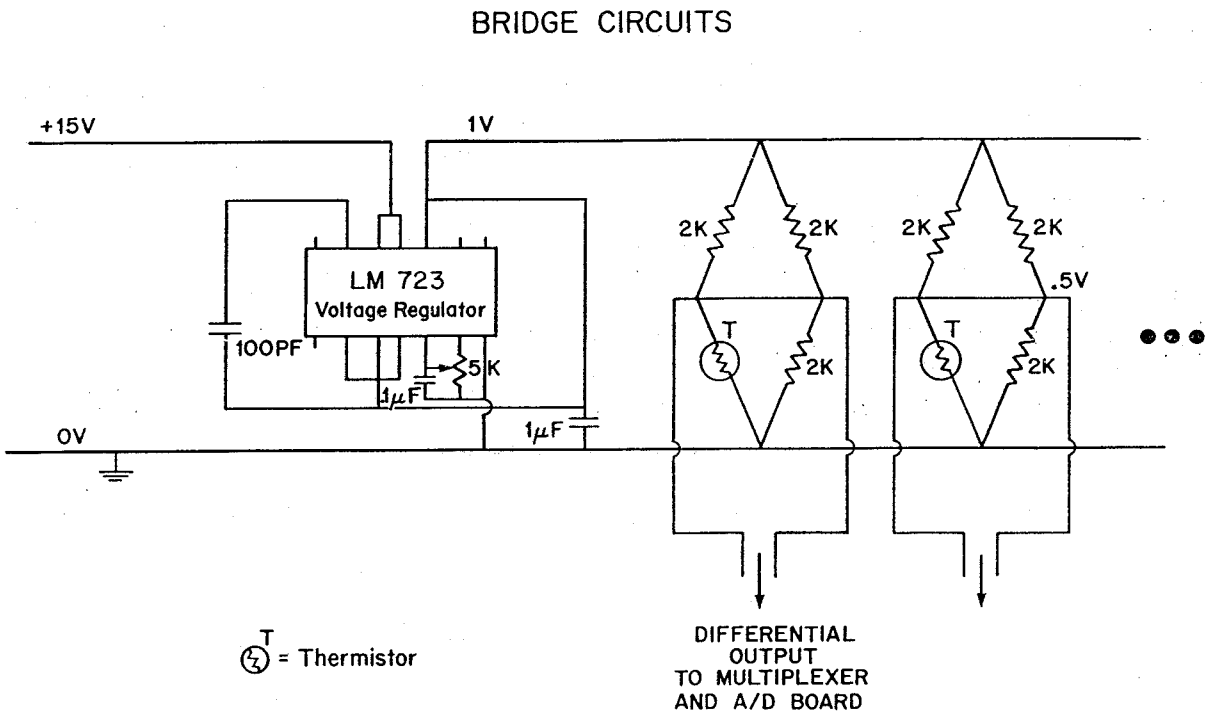

Figure 4.10 Diagram of two bridge circuits for the thermistor probes.

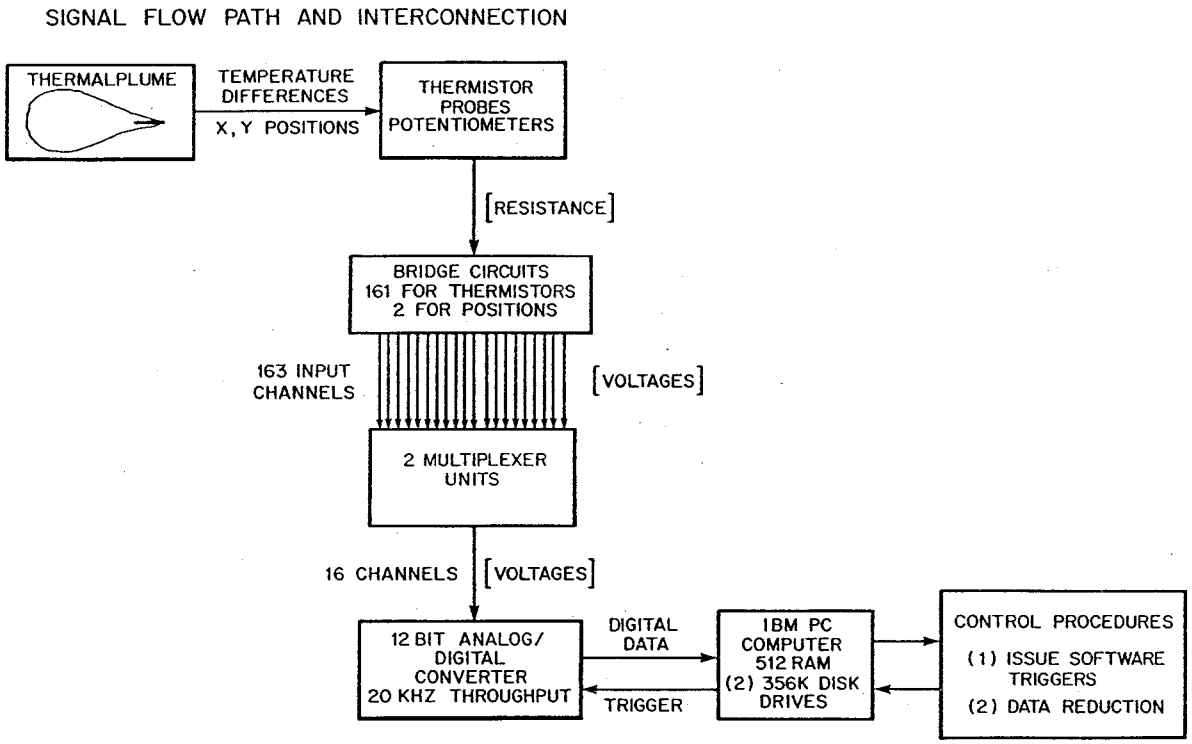

Figure 4.11 Signal flow path and the interconnection of components of the data acquisition system.

4.3 Experimental Constraints

There are several constraints concerning the experimental setup that should be addressed. The first constraint is the time duration allowed for each experiment. The duration is taken as the time interval between the start of the discharge and the time when the plume reaches the basin's walls, or the time when the plume recirculates back to the diffuser regime. This is directly governed by the size of the test basin and the discharge characteristics. A simple estimate can be made by considering the gravitational spreading velocity $v \propto \sqrt{g'h}$ and the horizontal dimensions of the basin, which are 11.0 m and 6.1 m. For a typical g'_0 of approximately 4.0 cm/s^2 (corresponding to an initial temperature difference of 16°C), a dilution of the order of 10 and a plume thickness of around 1 cm in the experiments, two estimates resulted: 30 minutes in the longitudinal and 8 minutes in the lateral direction. In practice, it was found that the duration was mostly between 20 minutes and 40 minutes. This time constraint limited the number of operations and hence the amount of information that could be acquired in one single experiment. Therefore, measurements were designed to be completed within the above time period or, when necessary, the procedures were separated into two independent operations for running the test twice.

The maximum possible sampling rate offered by the data acquisition system can be another constraint. It is stated in Section 4.2.4 that the A/D board provides a throughput rate of 20 kHz. The ultimate sampling rate, however, is limited by the clock speed of the system computer and the software, and is much lower than 20 kHz. Using the previously described system, the gross rate was found to be approximately 200 samples per second (i.e., 2 samples per second for 100 input channels to be monitored). This sampling rate did not generally present a problem when dealing with mean characteristics of the thermal field, but required extra caution in cross-scanning experiments when the probes were moving at a certain scanning rate across

the test basin. In the latter situation, the scanning rate was carefully selected to be slow enough to provide sufficient resolution for the cross-sectional temperature profiles and yet fast enough to complete the scanning before recirculation occurs. A number of tests had been carried out by moving the probes across the tank at different scanning speeds while sampling at the maximum possible rate. By comparing the time series obtained and their energy spectrums, it was concluded that speeds ranging from 0.6 cm/s to 0.8 cm/s provided good resolution and an acceptable vibrational level.

Another constraint is that each thermistor probe has been designed to measure temperature only over a water depth of 10.75 cm. Hence, for experiments requiring more extended coverage, the probes were positioned to monitor the upper 10.75 cm of the water column. The surface portion was sampled because more activities were expected in the surface layer than in the bottom; this was because of the stratification of the thermal plume, especially in deep-water discharge cases. An alternative was to conduct the experiment in two parts; one sampled the top portion of the water column, while the other sampled the bottom.

A final constraint to be addressed is the environmental factors over which there is little control. The relative humidity in the laboratory and the equilibrium temperature of water in the test basin are important since they govern the amount of heat loss in the system. Although it is impossible to control these environmental conditions with the facilities available in the laboratory, one can estimate the heat loss by monitoring the air temperature, water temperature and relative humidity. A serious limitation, nevertheless, existed because of the lack of precise control over the discharge temperature at the diffuser; only the water temperature in the supply tank could be controlled. However, as the warm water flows from the supply to the discharge end, heat energy is continuously dissipated to the surrounding because of an inevitable temperature gradient. Since the amount of heat loss varied according

to the ambient and supply conditions, it was very difficult to make a precise adjustment for it. Therefore, the water temperature at the storage tank was targeted at 2.0°C to 3°C (depending on individual experimental conditions) higher than the desired discharge temperature to compensate (approximately) for the heat loss. The final discharge temperature deviated slightly from the target value but was monitored throughout each experiment by the thermistor located inside the diffuser. In practice, it was difficult to duplicate experiments with identical, initial, elevated discharge temperatures (ΔT_0). The variation in ΔT_0 from target values ranges from 0.1°C to 1.5°C.

4.4 Experimental Procedures

In this study, experiments were performed under quiescent ambient conditions, with either a homogeneous or stratified water column. The experimental procedures are similar except for the preparation of the appropriate ambient density gradient. The details of preparing the stratification in the receiving water are explained in Appendix C, while this section describes the general procedures.

Typically, there were two groups of measurements conducted, and the experimental procedures for them varied accordingly. The first group measured temperature along the axis of the diffuser; the second measured the lateral temperature profiles by scanning across the diffuser. The two sets of measurements had to be carried out in separate experiments because of the limited time available before recirculation became significant. For most experiments, this duration was approximately 20 minutes, a time period too short to measure with sufficient resolution the temperature distribution over the entire basin. The sampling objective was to obtain a maximum amount of information on the temperature field within the constraints of time and the capacity of the A/D and computing system to process the real-time data.

Measurements along and downstream of the diffuser axis provided significant representations of the thermal field. Therefore, most of the experiments focused on the centerline measurements, and are referred to as the *centerline* experiments. However, this type of measurement alone would not reveal sufficient details of the three-dimensional temperature field necessary for understanding the complicated mixing processes and entrainment patterns. The *cross-scanning* experiments were therefore designed to get cross-sectional temperature profiles for selected cases. It should be noted that the centerline measurements produced time-averaged values, since the probes were fixed in one particular position for a predetermined period of time (usually 1 minute). The scanning measurements, however, were instantaneous with respect to both time and space.

Prior to all experiments, the test basin was filled with water to a predetermined level. The water depth was checked using two depth probes mounted on the probe carrier. The 8 thermistor probes were mounted on the same carrier at a 30.5 cm spacing. The elevations of the probes were adjusted so that the first thermistor (from the bottom) in each probe was about 1 cm above the nozzles to avoid collision when the carrier moved. The carriages and the carrier were secured in their initial positions, which were different for the centerline and scanning experiments. The basin water was then allowed to sit undisturbed for a minimum of three hours until the ambient turbulence and residual currents died off. At least 20 minutes before the start of an experiment, the electronic system was switched on to ensure that stability was established by the time measurements began. Shortly before each experiment, the ambient temperature was recorded with both thermistor probes and a thermometer to provide a background reference. The relative humidity was also recorded using a psychrometer. The discharge water was heated to a prescribed temperature, i.e., 16.0°C above the ambient plus an adjustment for the heat loss as explained in the previous section. The warming of discharge water was accomplished by recirculating

water between the storage tank and the heater unit until the designated temperature was reached. A red-dye solution was prepared in a dye bottle to be added to the discharge water.

During an experiment, warm water was continuously pumped from the storage tank to the diffuser. The volumetric flow rate was regulated by two valves and monitored with the flow meter. The first few liters of warm water exiting through the diffuser had an irregular temperature because of cooler water already residing in the diffuser. Just before the start of the experiment, flow was initiated through a by-pass drain installed before the inlet of the diffuser to discard the partially cooled initial flow of water. A thermometer was used to monitor the water temperature at the by-pass drain until it turned relatively stable. The by-pass drain was then shut off and the warm water was redirected to the diffuser, thus signalling the start of the experiment.

(i) Centerline experiments

The aforementioned operations applied to both centerline and scanning experiments, but the measurement procedures were different for each. In the centerline experiments, the lateral position of the probe-carrier was always aligned with the axis of the diffuser. The arrangements are best illustrated by the diagram in Figure 4.12. The instrument carriage bearing the probe carrier and the scanning mechanism was initially positioned such that the first thermistor probe in the row of eight probes was 2.0 cm upstream of the first nozzle in the diffuser with 16 or 4 jets, and at 1.5 cm downstream of the nozzle in single jet cases. The eight probes were spaced 30.5 cm apart along a line as indicated by numbers 1 through 8. Each experiment was completed with seven more measurement positions, giving a total of 64 vertical profiles at different positions along the diffuser plume. The computer began to collect data at the start of the discharge. The probes were kept stationary in their positions during

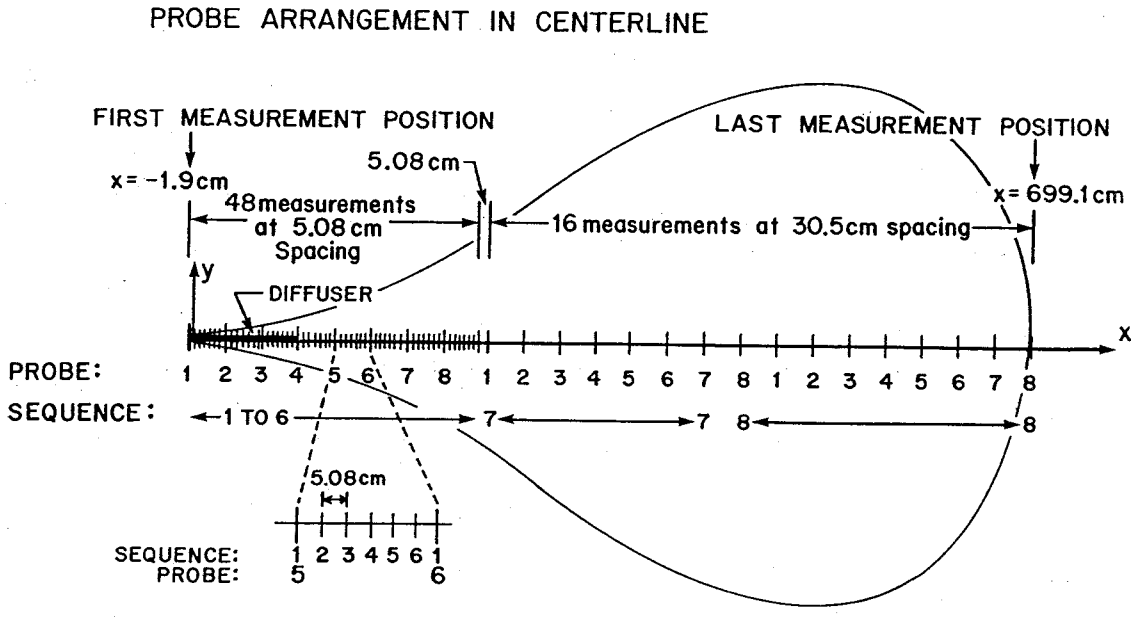

Figure 4.12 Probe arrangements for centerline experiment.

the data acquisition period, which was normally five minutes for the first probe position, and one minute for all the others. The first measurement period was assigned five minutes in order to provide time for the plume to develop fully. When the measurement for a position was finished, the carriage was moved 5.08 cm downstream. Once again, the computer triggered another data collection and conversion cycle with the probes in their new positions. This procedure was repeated until the 7th and the 8th positions, when the probes were moved 256.0 cm downstream instead of 5.08 cm. Throughout the course of the experiment, the flow rate and the temperature at the storage tank were closely monitored.

(ii) Scanning experiments

A different strategy was employed for the cross-scanning experiment. Figure 4.13 is a schematic diagram illustrating the probe positions and scanning sequences for the cross-scanning experiments. The initial position of the probes was not on the centerline, but was approximately 180.0 cm away in the lateral direction. The initial longitudinal position was chosen such that the first probe in the carriage was 5.4 cm downstream of the center point of the diffuser. Again, each probe was 30.5 cm apart. Contrary to the centerline case, measurements did not take place until the plume had grown to a definite shape and the front had passed the last thermistor probe. The scanning mechanism was then turned on to drive the probe-carrier across the warm-water plume, and at the same time, the data acquisition routine was activated. It took about ten minutes for the carriage to cover the full width of the tank, but only half of the width was necessary because of the approximate symmetry of the plume. For most experiments, six minutes were allowed for scanning and measurements to ensure coverage of at least half of the plume. When measurements of the first position were completed, the procedures for scanning and the data acquistion were repeated at 283.0 cm downstream of the first position, with the probes then moving in the

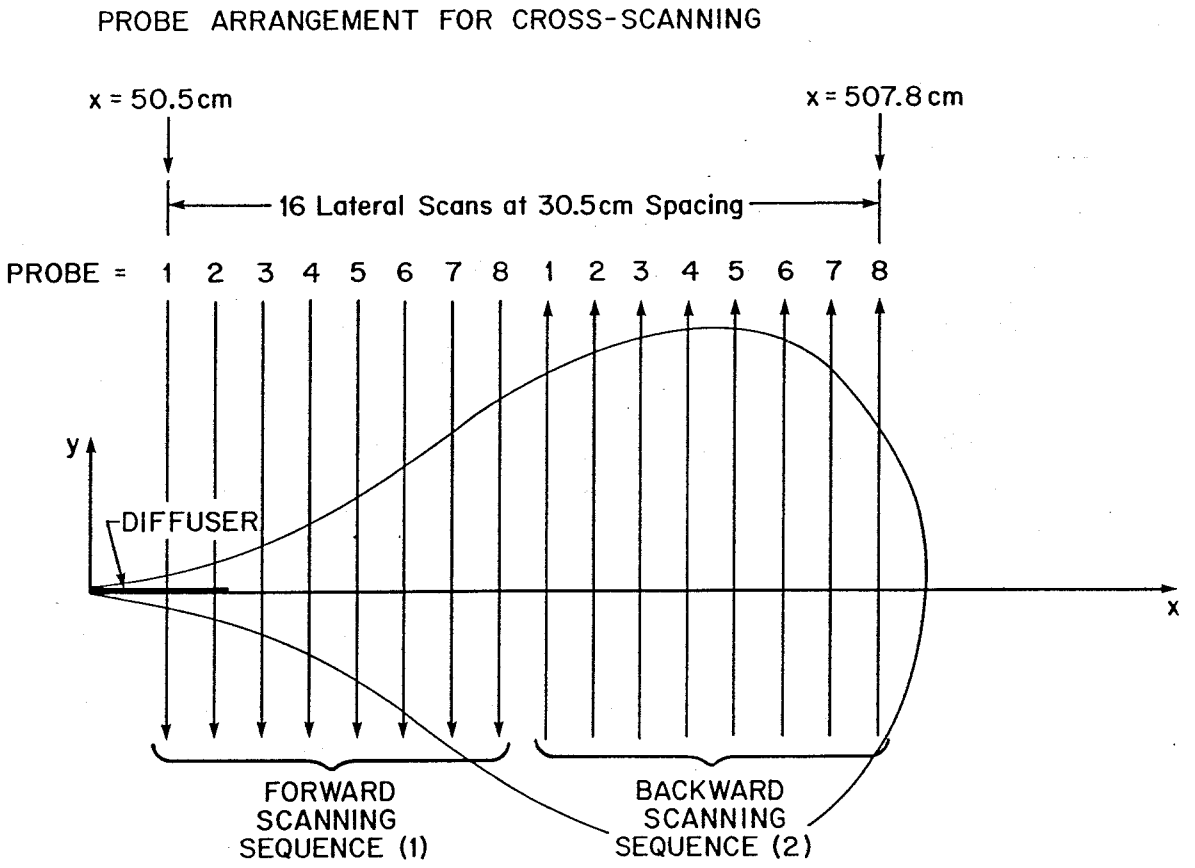

Figure 4.13 Probe arrangements for scanning experiments.

reverse direction.

In some cases, photographs of the diffuser plume were taken at specified time intervals during the time lapse between the start of the discharge and the start of measurements. The series of photographs gave estimates on the speed of the advancing front and the geometry of the thermal plume.

4.5 Data Reduction

At the end of each experiment, the acquired data were retrieved from the virtual disk of the IBM PC and transferred to floppies in ASCII format. The remaining data processing was carried out with IBM AT and PS2 computers. Since the raw data were in digital form, they had to be converted to temperature or position values for analysis. Calibration curves were prepared for the conversions. The thermistors were calibrated individually by immersing the probes into a water bath of known temperature. The probes were left undisturbed for a few minutes to obtain stable readings. The computer was then activated to read signals for two minutes; thus a time averaged value for each thermistor was obtained. This procedure was repeated for a range of water temperatures likely to be encountered in the experiments. Second-order regression analysis of the calibration data yielded zero-, first-, and second-order constants of the regression equation. Since the thermistors had slightly varying characteristics among themselves, a separate curve was required for each one. The calibration for potentiometers was done in a similar fashion for relative lateral and longitudinal positions. A first-order regression was found to be sufficient. Samples of the calibration curves and their associated regression equations are included in Appendix B.

From deduced positions and temperatures (i.e., the ambient, the discharge, and the plume) one could calculate the normalized temperature excess resulting from the

diffuser discharge under a particular set of experimental conditions. Relevant parameters including the discharge Froude number, discharge buoyancy and momentum fluxes, and various length scales could also be found.

4.6 Experimental Uncertainties

Sources of experimental uncertainties need to be addressed. An emphasis is placed on temperature measurements. The analog-to-digital converter (A/D) had a resolution of 12 bits, which provided 4096 levels of difference. According to calibrations, this was designed to represent a temperature difference of 26.0°C (the difference varied slightly among thermistors). Hence the resolution of the A/D converter in temperature units was approximately 0.006 °C. The noise associated with the electronic system contributed to part of the uncertainty. The time history of the raw data often reflected fluctuations about certain mean values, with standard deviations ranging from 0.004°C to 0.006°C while stationary and from 0.006°C to 0.014°C while scanning. The calibration procedures introduced another uncertainty. The thermometer used for the calibration was graduated at 0.1°C and was estimated to be accurate within 0.025°C . The root mean-square value of the random errors for temperature difference, ΔT, amounted to 0.026°C (stationary) and 0.029°C (scanning). The fluctuation of the water temperature in the supply tank was of the order ± 0.5°C during the time duration of each experiment.

For the potentiometric measurements of position, the 12 bits A/D board provided a resolution of 0.25 cm. Results from a number of tests indicated that the standard deviations for the two potentiometers were 0.066 cm and 0.14 cm for the lateral and horizontal positions, respectively.

Other errors were introduced during the course of the experiment. One source was the self-warming of the thermistors; this factor was 1 milliwatt/°C, according to

the manufacturer's specifications. The current that generated from the bridge circuit and flowed through the thermistors was about 0.25 milliwatt, hence the reading was 0.25 °C higher than it should have been. This is a systematic error in the temperature measurements, and will cancel itself in the calculation of ΔT.

Another problem came from the thermistor probes. Although the cross-sectional area of the probes was shaped to be aerodynamic, its disturbance to the flow field could still be great, especially at locations where the principal axes of the flow were at an angle to the airfoils. Furthermore, the flow generated a wake region behind each probe, and the next probe lying in that wake would be very likely affected, thus giving an incorrect temperature readings. In cross-scanning experiments, the vibration of the probes upon moving also induced an additional amount of energy for mixing, thus affecting the accuracy of the results. The speed of the carriage was therefore reduced to the slowest viable rate to minimize the problem. The nominal speed of the scanning was 0.8 cm/s, whereas the fluid velocity of the plume was on the order of 5 cm/s near the diffuser, to around 1 cm/s at a few diffuser lengths downstream. The measurements at the downstream end were therefore more seriously affected.

Finally, the amount of heat transfer through the air-water interface is not taken into account in the data-reduction process. The rate of heat transfer can be estimated from $K_h/(\rho C_p h)$, where K_h is the surface heat exchange coefficient, ρ is the fluid density, C_p is the specific heat capacity and h is the depth of the mixed layer. Results from a previous Keck Laboratory study on heat transfer from the test basin show K_h has a value of 16 $(w/m^2)/°\mathrm{C}$ ±20%. If a value of 3 cm is assumed for the mixed layer (the water depth is from 4 cm to 12 cm), $K_h/\rho C_p h$ will be $1.27\text{x}10^{-4}\,\mathrm{sec}^{-1}$. The characteristic time for the temperature decay that is due to heat transfer only is thus 2 hr 11 min. This is much longer than the duration of each experiment (approximately 20 min). A calculation using the laboratory-determined

value for K_h $(16\,(w/m^2)/^\circ\mathrm{C})$ has been performed to estimate the total amount of heat transfer to the atmosphere within an appropriate time required to complete individual experiments. This compares the observed rate of temperature decrease in several experiments having different initial conditions to the estimated rate of temperature decay that is due solely to heat loss. The rate of temperature drop that is due to heat loss only is found to be approximately 1/6 to 1/12 of the total rate of heat reduction.

5. Experimental Results–Homogeneous Ambient

5.1 Scope of Experiments

The objectives of the study are, through the use of experimental techniques, to further the understanding of the mixing and entrainment processes taking place in thermal discharges from staged diffusers, and to establish quantitative relationships regarding mean characteristics of the plume. To accomplish the objectives, a variety of discharge and ambient configurations were investigated. While the majority of the experiments were conducted in homogeneous ambient conditions, several exploratory experiments have been carried out for a stratified ambient. This chapter presents the results of the uniform ambient experiments. The stratified experiments are described in Appendix C.

Physical variables that characterize submerged thermal discharges and ambient conditions include the number of ports n, jet diameter D_0, port spacing s, total discharge flow rate Q_{T0}, initial temperature excess ΔT_0, horizontal and vertical orientations of the jets α and β, and the depth of water above the level of the discharge H. The initial buoyancy of the discharge is $g' = \Delta\rho g/\rho$ per unit mass, as determined from ΔT_0 and the ambient temperature.

The independent variables can be reduced to a set of dimensionless parameters:

$$L/H,\ s/H,\ \ell_M/H,\ \alpha,\ \beta,\ \ell_Q/H,$$

where ℓ_M denotes the discharge-momentum length scale per jet, defined as $M_{i0}^{3/4}/B_{i0}^{1/2}$ where M_{i0} and B_{i0} are the discharge momentum and buoyancy fluxes of the individual port; $L = (n-1)s$ denotes the length of the diffuser; ℓ_Q is a length scale of the jet size and is defined as $Q_{i0}/M_{i0}^{1/2}$, where Q_{i0} represents the discharge from each port. The discharge Froude number $Fr_0 = u_0/\sqrt{g_0' D_0}$ can also be written as $(\pi/4)^{1/4}(\ell_M/\ell_Q)$.

In practice, most submerged thermal outfalls are located in shallow water, and the discharges are momentum- rather than buoyancy-dominated. The overall ranges of the relevant dimensionless parameters in the prototypes are shown in Table 5.1. The experimental parameters were chosen in order to cover a range of plume configurations, i.e., from shallow to deep water, multiports to single port, and strongly to moderately momentum-dominated discharges. The studied ranges and their significances are shown in Table 5.2. To achieve these ranges, the experimental controls shown in Table 5.3 were used (with occasional variations).

Table 5.1 Range of typical diffuser parameters.

Parameter	Typical Range
Fr_0	20–80
L/H	1–30
s/H	1–5
ℓ_M/H	1–12
ℓ_Q/H	0.05–0.10
n	10–63

Table 5.2 Studied range of dimensionless diffuser parameters.

Parameter	Studied Range
Fr_0	5–90
L/H	0.5–6
s/H	0.5–6
ℓ_M/H	0.5–12.5
ℓ_Q/H	0.018–0.33

Table 5.3 Experimental values of variables.

Experimental Variable	Experimental Value
Number of ports n	16 4 1
Diameter of jet D_0 (at *vena contracta*)	0.25 cm (n=16) 0.52 cm (n=4) 0.75 cm (n=1) 1.03 cm (n=1)
Orifice Diameter D_0' (see Section 5.6)	0.335 cm (n=16) 0.559 cm (n=4) 0.759 cm (n=1) 1.014 cm (n=1)
Port spacing s	6.0 cm 24.0 cm
Discharge flow rate Q_{T0}	20.3 cm^3/s 28.8 cm^3/s 40.7 cm^3/s 57.5 cm^3/s
Depth of water above discharge level H	2.00 cm 4.00 cm 8.00 cm 12.00 cm
Horizontal orientation of nozzle α	0° ±25°
Vertical orientation of nozzle β	25°
Initial temperature difference ΔT_0	16.0°C

In determining the control values, reference was made to the 1974 San Onofre diffuser model study (Koh et al., 1974), which consisted of two diffusers, each with 16 ports having a 0.25 cm jet diameter and a spacing of 6.0 cm. The nozzles were oriented upward at 20° from the horizontal and at ±25° from the diffuser axis. The bottom topography in the model showed a continuously changing slope from 4.05% near the shoreline to 1.05% in the diffuser region, then increasing to 5.2% farther offshore. (Note: Because the model was distorted 4:1, prototype slopes are four times less.) The water depth was 4.0 cm at the beginning of the diffuser, which was closer to the shore. The total discharge flow rate for each diffuser was 28.8 cm^3/s. The SONGS model configuration was repeated in the present study, but only one diffuser was used. Other discharge flow rates at 20.3 cm^3/s, 40.7 cm^3/s, and 57.6 cm^3/s were selected to produce discharge momentum fluxes at half, two, and four times, respectively, of the original experiment.

The initial temperature difference ΔT_0 and the vertical orientation of the nozzles were held constant in all experiments. Because of the fluctuation of heat losses from the warm water supply system to the surroundings (an experimental difficulty explained in Section 4.2.2), it is difficult to have precise control over the discharge temperature. The final values of ΔT_0 varied from 14.0°C to 17.0°C.

In general, only one of many control variables, excluding the number of ports and the diameter of jets, was varied in each experiment. A relationship was established between n and the corresponding D_0 such that, for a chosen discharge flow rate Q_{T0}, the total initial momentum and buoyancy fluxes were preserved in experiments with diffusers of different n. Since $M_{i0} \propto u_0^2 D_0^2$ and $B_{i0} \propto g_0' u_0 D_0^2$, and g_0' is supposed to be a constant in all the experiments (because of constant ΔT_0), it follows that for

different numbers of ports n_1 and n_2,

$$n_1 u_{01}^2 D_{01}^2 = n_2 u_{02}^2 D_{02}^2$$

and

$$n_1 u_{01} D_{01}^2 = n_2 u_{02} D_{02}^2$$

for constant M_{T0}, B_{T0} and Q_{T0}. Therefore,

$$D_{01} = \sqrt{\frac{n_2}{n_1}} D_{02} \,. \tag{5.1}$$

Among the large number of independent variables in the system, the depth of water, the number of ports, the diameter of jets, and the discharge rate were expected to be most significant in controlling the plume behaviors, and were studied in greater detail. Variables such as s and α were kept unchanged at 6.0 cm and 0°, respectively, for most experiments, and varied only occasionally for qualitative comparison purposes. A tabulation of the performed experiments and the related physical and dimensionless parameters is presented in Appendix D.

5.2 Results of Two Sample Experiments

The thermal plumes from the 55 experimental configurations displayed similar overall features but varying details, according to different testing conditions. In this section, the complete results from a centerline experiment (**0816cl**) and a scanning experiment (**1122scan**) are presented and discussed with an emphasis on the mean characteristics of the thermal structures. Comparisons with other experiments are made when significant modifications in the plume behavior are observed. The two

experiments, 0816cl and 1122scan, had nearly identical initial discharge and ambient conditions, except for environmental factors such as air temperature, humidity, and the equilibrium temperature of water in the test basin. In addition, the temperature excess at the discharge ΔT_0 differed by 0.6°C in the two experiments. The physical variables and the relevant parameters of the two experiments are shown in Table 5.4. All the variables have been defined in Section 3.1, Section 3.3.1 and in the List of Symbols.

Table 5.4 Variables and relevant parameters of the two experiments: 0816cl and 1122scan.

Variable/Parameter	Centerline Expt. (0816cl)	Scanning Expt. (1122scan)
n	16	16
D_0 [cm]	0.25	0.25
s [cm]	6.0	6.0
α [°]	0	0
β [°]	25	25
H [cm]	4.0	4.0
Q_{T0} [cm^3/s]	28.8	28.8
ΔT_0 [°C]	16.1	16.7
Fr_0	35	34
$M_{i0}(M_{T0})$ [cm^4/s^2]	65.8(1052.5)	65.8(1052.5)
$B_{i0}(B_{T0})$ [cm^4/s^3]	8.1(129.3)	8.5(135.4)
ℓ_M [cm]	8.13	7.94
ℓ_Q [cm]	0.22	0.22
ℓ_M/H	2.04	2.00
ℓ_Q/H	17.10	17.10
Re_0	1260	1260

5.2.1 The Centerline Experiment–0816cl

Vertical profiles of time-averaged temperature were measured at 64 stations along the axis of the diffuser, 48 of which were at 5.08 cm apart and the rest at 30.48 cm apart. At a vertical spacing of 5.0 mm, six thermistors were used to cover the top 2.75 cm of the water column of which the total depth is 4.0 cm. The arrangement of the measurement positions has been given previously in Figure 4.12.

All measurements and observations were taken along the diffuser axis.

Just before the experiment was started, ambient temperatures were measured at eight locations equally spaced at an interval of 30.48 cm from the beginning of the diffuser. The mean-temperature profiles of Figure 5.1 suggest a reasonably homogeneous water column with 20.21 °C near the surface and 20.23 °C at the lower levels (x/L is the longitudinal distance normalized by the diffuser length, which is 90.0 cm for the 16-port diffuser, based on 15 spaces at 6.0 cm; $x = 0$ is taken at the beginning of the diffuser).

Figures 5.2a to 5.2d are samples of the time series for the temperature near the surface (0.25 cm below water surface) measured at four stations located directly above, near the end and beyond the diffuser. All four of the series exhibit similar transient structures. Initially, when the plume is still upstream of the thermistor probes, the temperature is equivalent to the ambient value. Upon the arrival of the plume, a transition period begins with an abrupt increase in temperature. The curves gradually levell off at the end of the transition, which is followed by a pseudosteady period when the temperature fluctuated about a relatively stable mean value.

Despite the similarities among the time series, the temperature rise and the fluctuations decrease with distance downstream. This is expected; as the plume progresses beyond the end of the diffuser, there is no further supply of heat flux and momentum flux, but the thermal and turbulent energies continue to disperse or decay similarly to the diffuser region.

(i) Longitudinal profiles of normalized temperature excess $\Delta T/\Delta T_0$

The time-averaged value in the pseudosteady-state period is extracted from each temperature record (a total of 384) to describe the thermal characteristics along the axis of the diffuser. Figures 5.3a, 5.3b and 5.3c illustrate the longitudinal profiles of the normalized, time-averaged temperature excess $\Delta T/\Delta T_0$ at different levels. The

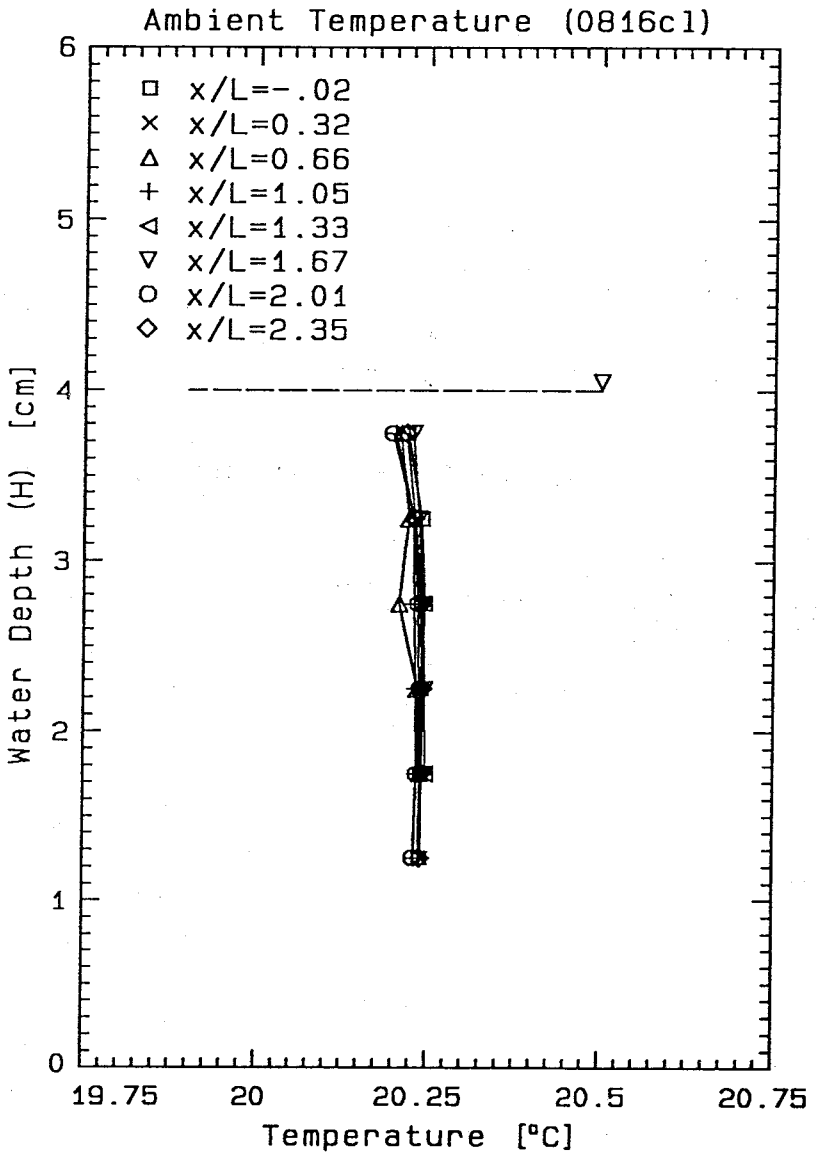

Figure 5.1 Mean ambient temperature profiles (before startup) of centerline experiment–0816cl.

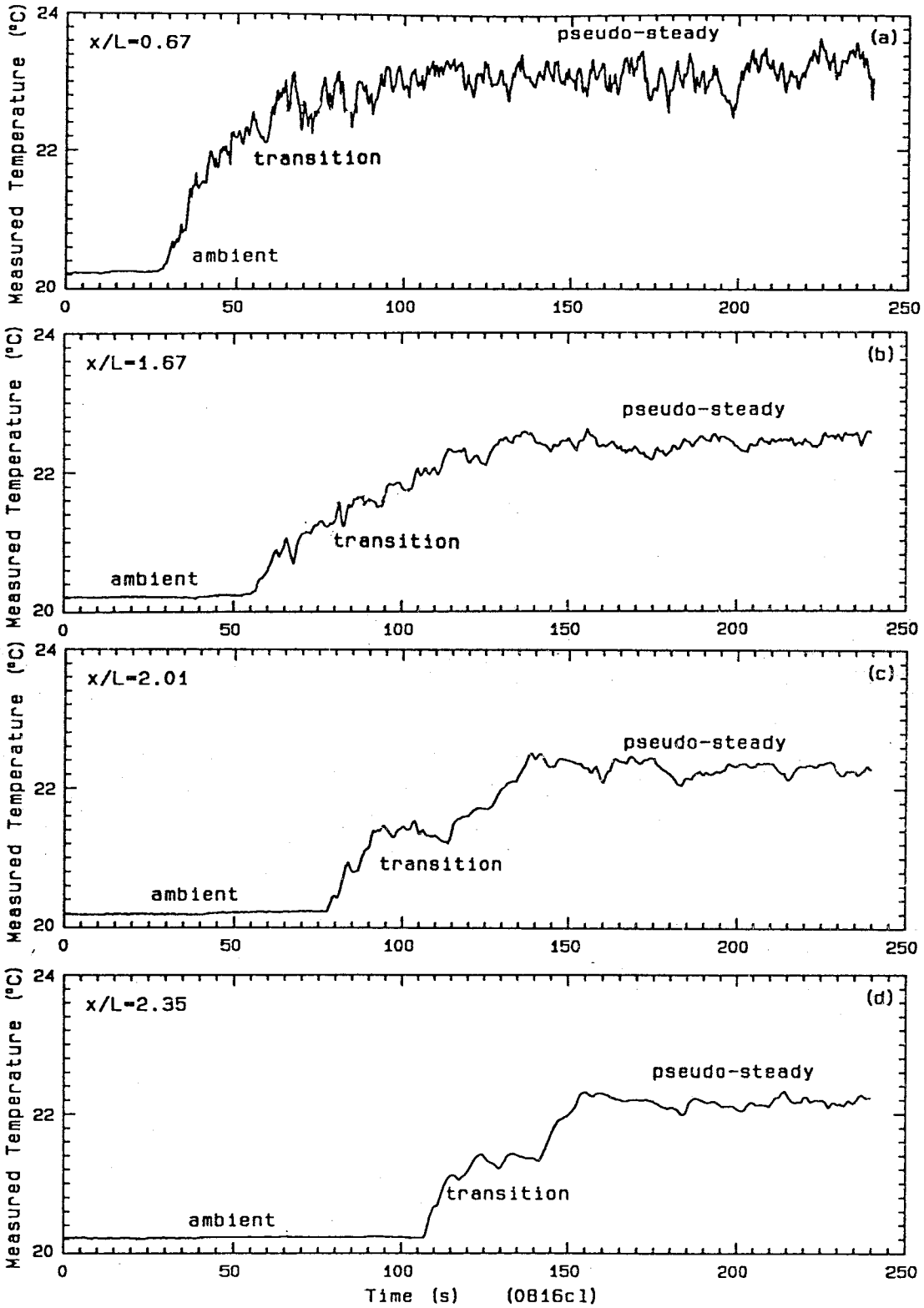

Figure 5.2 Sample time series for the near-surface temperatures measured at four stations. a) $x/L = 0.66$; b) $x/L = 1.67$; c) $x/L = 2.01$; d) $x/L = 2.35$.

temperature structure directly above the diffuser is distinguished by a number of peaks and troughs. Such irregularities are signatures of the individual jets and are magnified in the profiles near the bottom.

Merging of the jets may have occurred near the surface; however, because of the shallow water depth, the potential travel distance of each jet is too short for it to lose its identity. Accordingly, there should be 16 peaks of temperature rise corresponding to the 16 ports of discharge. The spacing of the measuring stations (5.08 cm in the diffuser region), however, is not sufficient to resolve the detailed structures of individual jets. Instead, the profiles reflect the general complexities exhibited in this near-field region. Further observation indicates that the last peak of temperature is located slightly beyond the end of the diffuser. The extra distance corresponds to that required for the last jet to reach the water surface and is found to be 8.6 cm for the experimental configuration.

The temperature drops drastically immediately downstream of the diffuser. For instance, the near-surface $\Delta T/\Delta T_0$ decreases from a peak value of 22% to 13% in a distance of one diffuser length (L), i.e., 90.0 cm. It continues to decline afterward but at a much slower rate of 5% in $4L$. The mid-depth profile shows an even more abrupt drop at the end of the diffuser from 28% to 8% in less than $0.1L$. Instead of decreasing further, the profile rebounds to 9% at $1.6L$; afterward it continues to decrease at a rate of $1.0\%/L$ until $x = 5.0L$. The bottom profile also displays a temperature drop in the corresponding position, but the $\Delta T/\Delta T_0$ stays below 2% after $2.0L$. This indicates that the plume has detached from the bottom and drifted downstream, behaving essentially as a surface buoyant jet. The temperature reversal (or the rebound) in the lower levels is evidence for circulation caused by the last jet when it hits the water surface and is deflected back down the water column. This action thickens the surface layer for a short distance and also induces eddies that draw

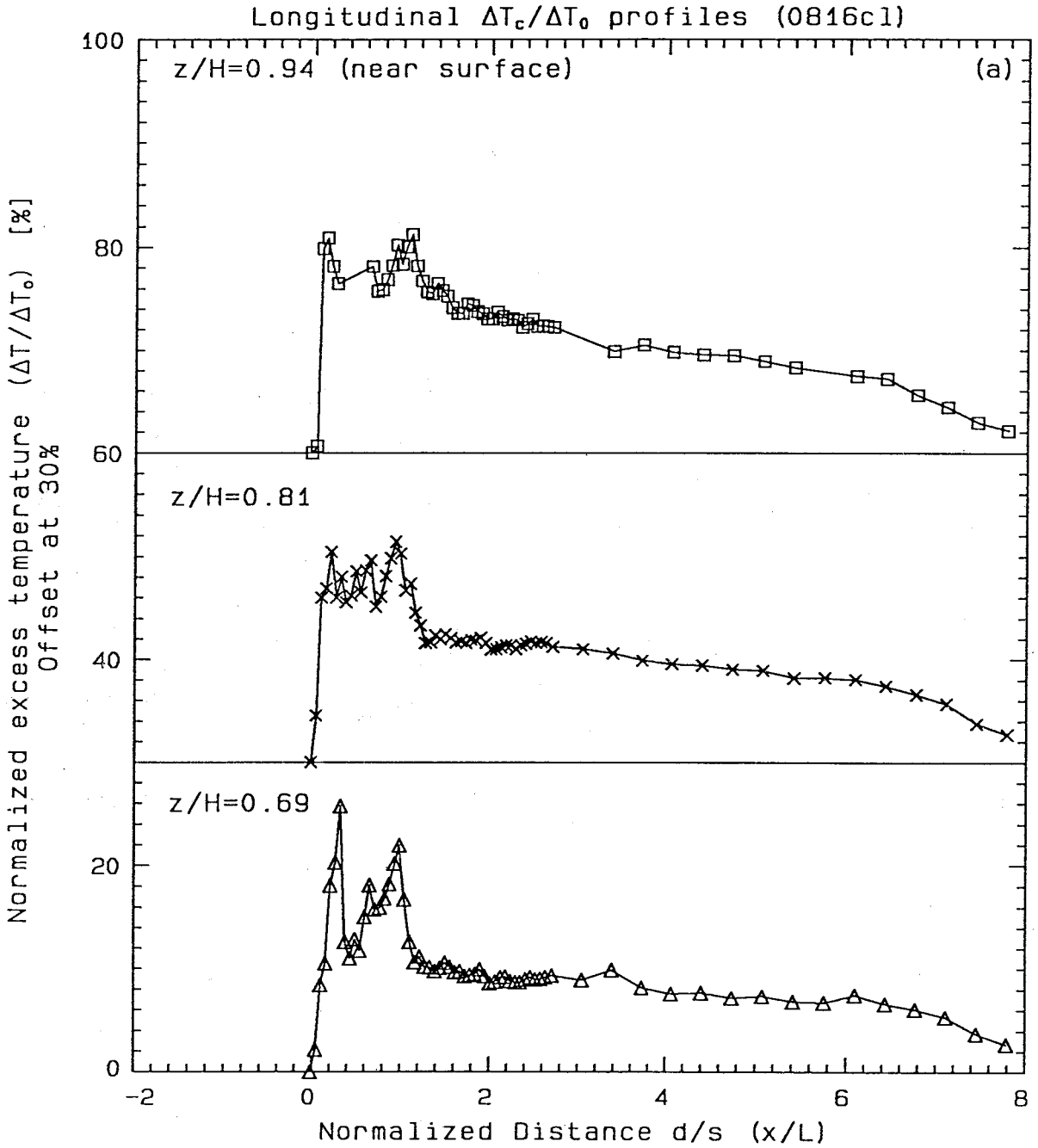

Figure 5.3a Longitudinal profiles of $\Delta T_c/\Delta T_0$ at near-surface levels.

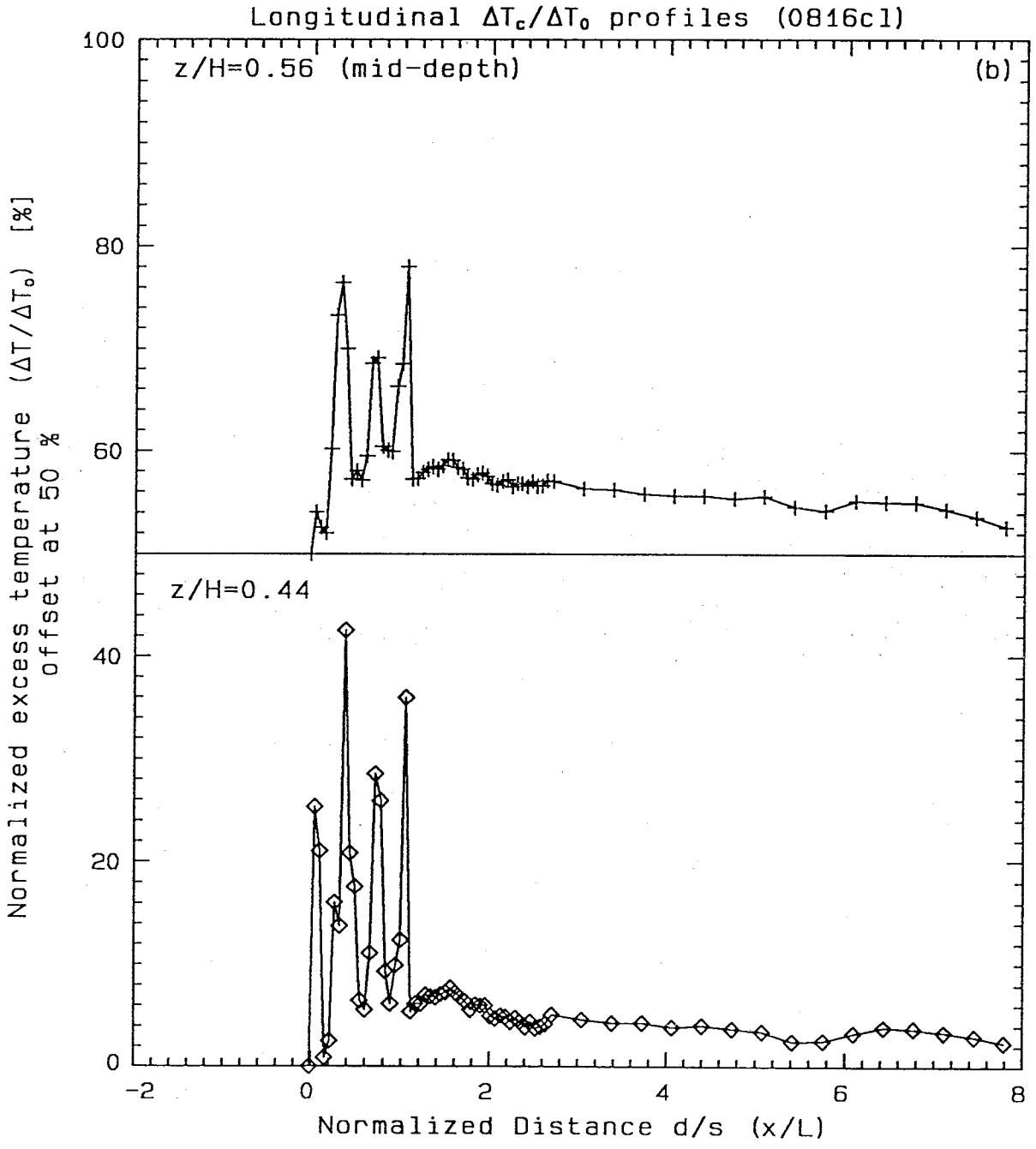

Figure 5.3b Longitudinal profiles of $\Delta T_c/\Delta T_0$ at midlevels.

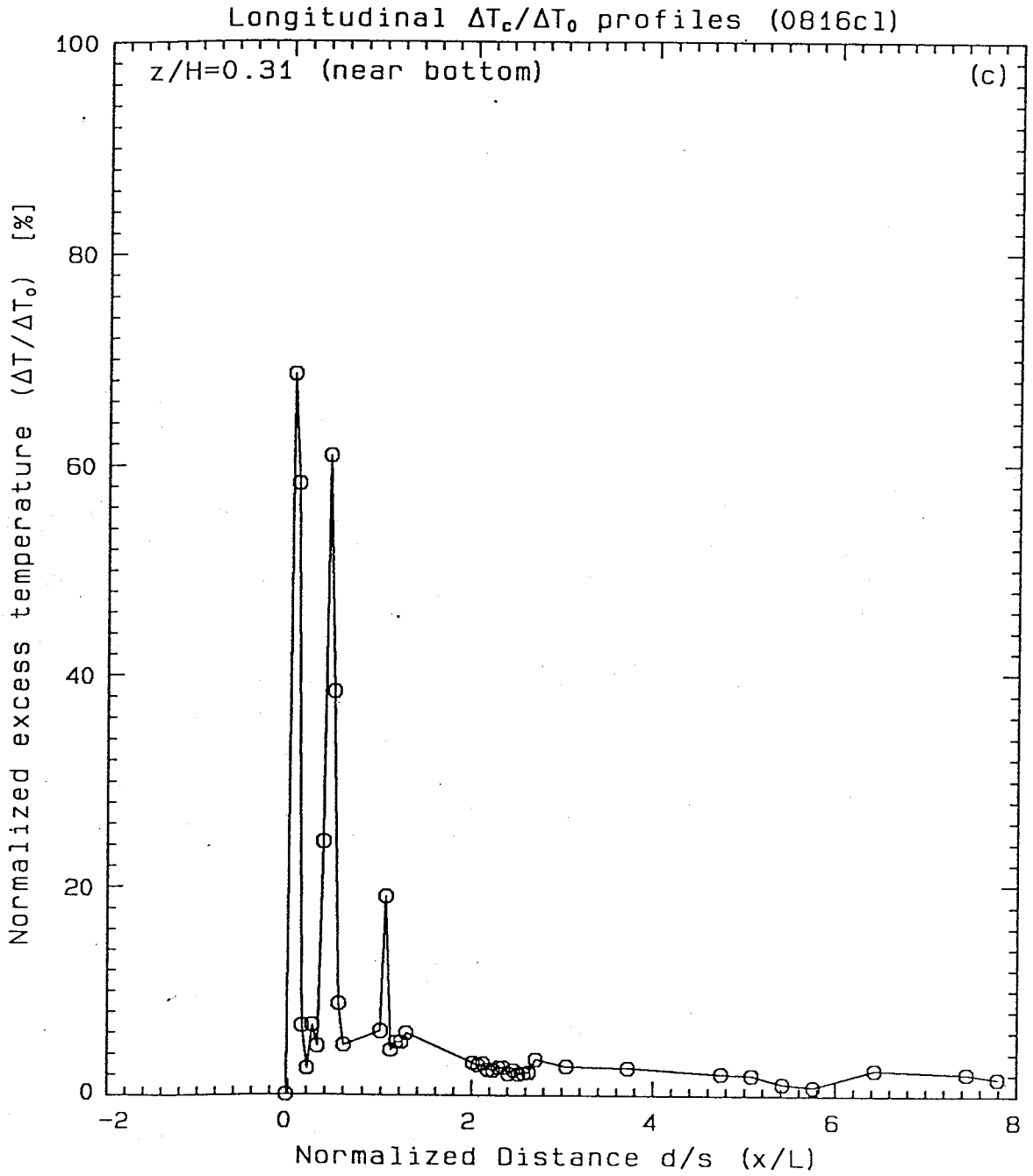

Figure 5.3c Longitudinal profiles of $\Delta T_c/\Delta T_0$ at bottom level.

the warmer water from the surface to the lower part of the water column, resulting in an increase of $\Delta T/\Delta T_0$.

The extent and magnitude of the temperature reversal depend on the depth of water as well as the momentum flux of the jet. Because of faulty thermistors, part of the bottom profiles are missing; it is uncertain whether the rebound has extended all the way to the lowest level. At the downstream end where the stations are in the proximity of the edge of the advancing plume, there is another rapid drop in the surface profile. It marks the front edge of a pseudosteady-state zone. The $\Delta T/\Delta T_0$ in this region, however, should not be interpreted as mean values because of the unsteady characteristics of gravitational spreading.

(ii) Vertical distribution of normalized temperature excess $\Delta T/\Delta T_0$

Figures 5.4a to 5.4d provide more quantitative information on four profiles at $x/L = 0.66$ (diffuser region), $x/L = 1.05$ (end of diffuser), and $x/L = 2.01$ and $x/L = 2.35$ (both downstream of diffuser). For example, in Figure 5.4b the temperature rise is high both at the level of $0.44H$ and at levels near the surface. This indicates that at the lower level the probe has caught the jet in front of it, while near the surface the probe has encountered the flow from all preceding jets. Profiles (c) and (d) resemble each other closely; both decrease in a simple manner from 12.3% near the surface to 2.5% near the bottom. In fact, it is noticed that beyond a certain distance, the vertical $\Delta T/\Delta T_0$ profiles from the stations downstream essentially collapse to a single curve (within an experimental uncertainty of 2.0%). In experiment 0816cl, this occurs at $1.8L$ from the end of the diffuser. Such a resemblance in temperature structures, nevertheless, ceases as the x-value progresses to the unsteady zone at the plume front.

(iii) Vertical isothermal maps

Figure 5.5 shows the isotherms ($\Delta T/\Delta T_0$) constructed from the 64x6 matrix

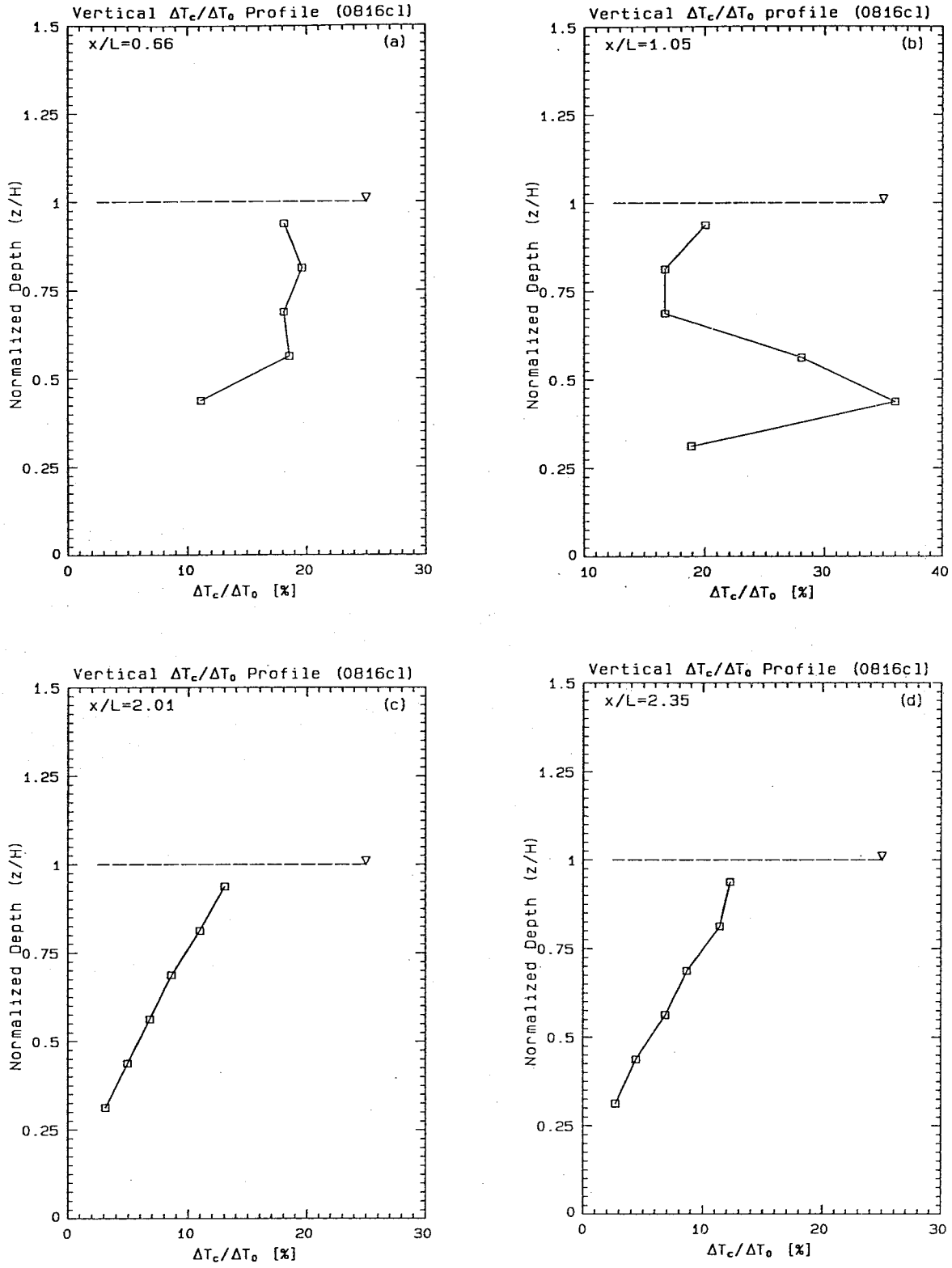

Figure 5.4 Vertical profiles of $\Delta T_c/\Delta T_0$ at four stations.
a)$x/L = 0.66$; b)$x/L = 1.05$; c)$x/L = 2.01$; d)$x/L = 2.35$.

of mean temperature along the diffuser axis. In the vicinity of the diffuser, the contours are condensed and steep. Some jet structures are revealed; however, the individual jets cannot be identified because of the limited resolution of measurement, as discussed previously. In general, this near-field region is dominated by complicated interactions of jets among themselves and with the water surface. It is potentially unstable (especially with large efflux of momentum) with some portion of the diluted warm water being circulated back to the jet efflux.

After a short distance, the contours detach from the bottom, e.g., lifting past $z/H = 0.31$ for 7.5% at $1.2L$ and 5.0% at $1.5L$, and apparently form a stratified surface layer. Since the temperature gradient and the concomitant density gradient down the water column are continuous and smooth, the surface layer in this context is loosely defined as the portion of the diluted plume water that has a $\Delta T/\Delta T_0$ greater than, for instance, 2.0%. The layer gets thinner as it advances downstream, as indicated by the sloping of the 5.0% and 7.5% contours, at a very gentle rate of approximately 1:600 for the 5.0% contour (the horizontal and vertical scales are greatly distorted at a ratio (horizontal/vertical) of approximately 120).

At the downstream end close to the edge of the front, the contours resume steeper angles and are shaped like the front of a density current. Since the flow is unsteady in this region, the values should not be considered as time averages. Nevertheless, it qualitatively marks the boundary between the frontal head and the external flow. The general flow pattern near the head of the front has been studied by Simpson (1982) and confirmed by Imberger (1983) with field data.

(iv) Fluctuation characteristics

Besides the mean properties, the variances obtained from the temperature records (again referring to the pseudosteady period) deserve some attention as they are indices of the fluctuation energy in the thermal and flow fields. Figures 5.6a to 5.6c are

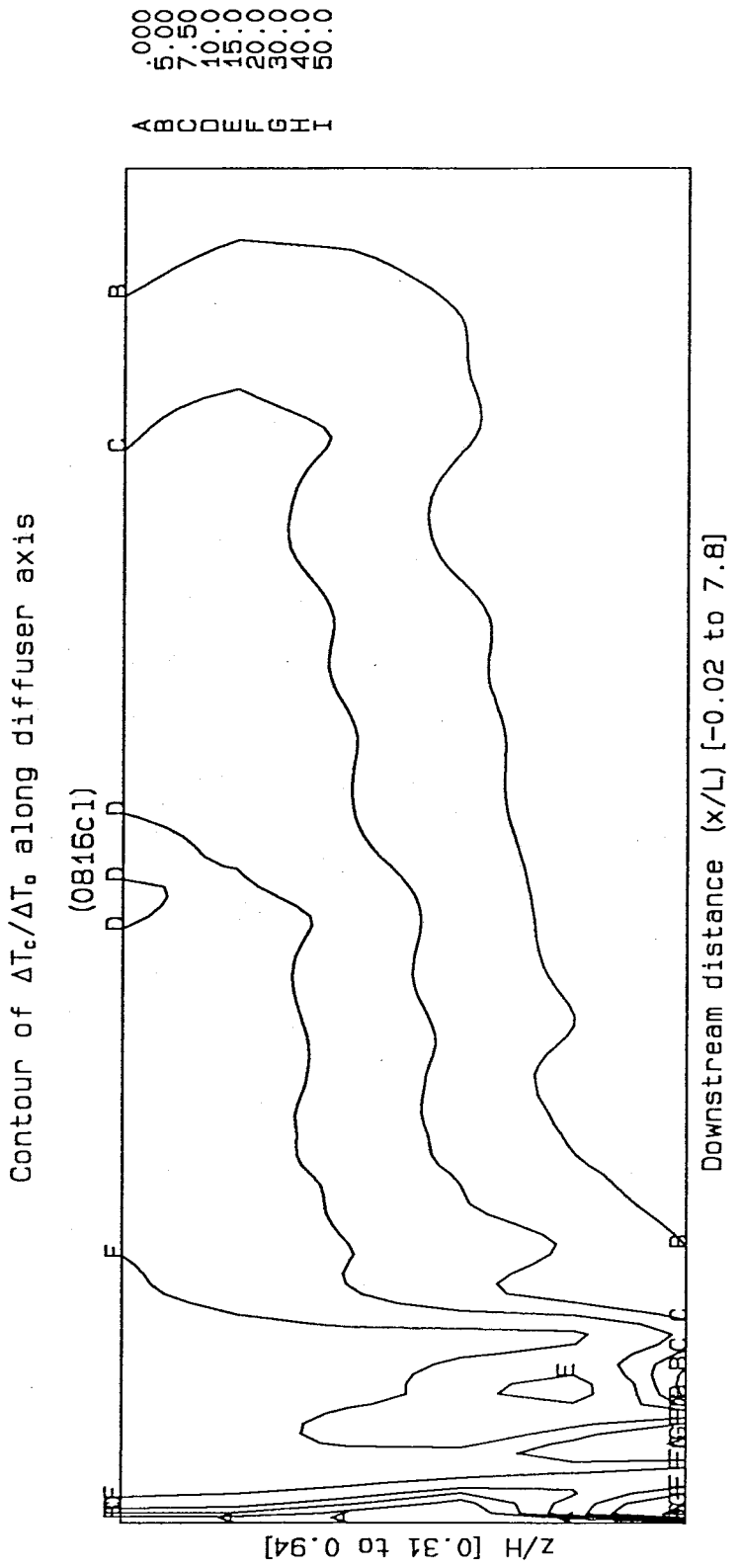

Figure 5.5 Contour map of $\Delta T_c/\Delta T_0$ in the vertical plane along the diffuser axis. Vertical domain shown is $0.31 < z/H < 0.94$. Contour intervals are indicated by letter code (in %).

variances of the measured temperature along longitudinal distance at various levels. The variances demonstrate patterns similar to that of the mean $\Delta T/\Delta T_0$ with a number of irregularities in the diffuser region, and have higher values closer to the discharge level. Unlike the mean profiles, the variances do not decrease thereafter in a smooth manner, but rather the fluctuations continue until about $2.2L$, suggesting some turbulent activities (e.g., momentum mixing). Eventually, the variances decrease to insignificant values, indicating that there is essentially no fluctuation in the thermal field (at all levels) downstream of $2.2L$. A contour map of the variances shown in Figure 5.7 depicts a complicated diffuser zone, features of the liftoff and the surface flowing layer, and an inactive downstream region.

Spectral analysis was performed for the near-surface temperature records at longitudinal positions $0.99L$, $1.67L$, and $2.35L$, to study the frequency distributions of the thermal energy. The spectra in logarithmic scales are shown in Figures 5.8a to 5.8c. In addition to the decrease in the variance (the area under the curve) with downstream distance, the energy spectrum apparently shifts from high frequencies to low frequencies. In other words, the smaller eddies either dissipate at a faster rate, or merge into the larger ones.

5.2.2 The Scanning Experiment–1122scan

Figure 4.13 shows the arrangement of the probe measuring positions during the cross-scanning experiment which produces 16 continuous lateral temperature profiles at each of 6 depths (5.08 cm spacing down the water column), at a spacing of 30.5 cm in the downstream direction. The mean ambient temperature in Figure 5.9 shows more variations (0.1 °C in 2.37L) than that of experiment–0816cl, but is still considered to be fairly homogeneous.

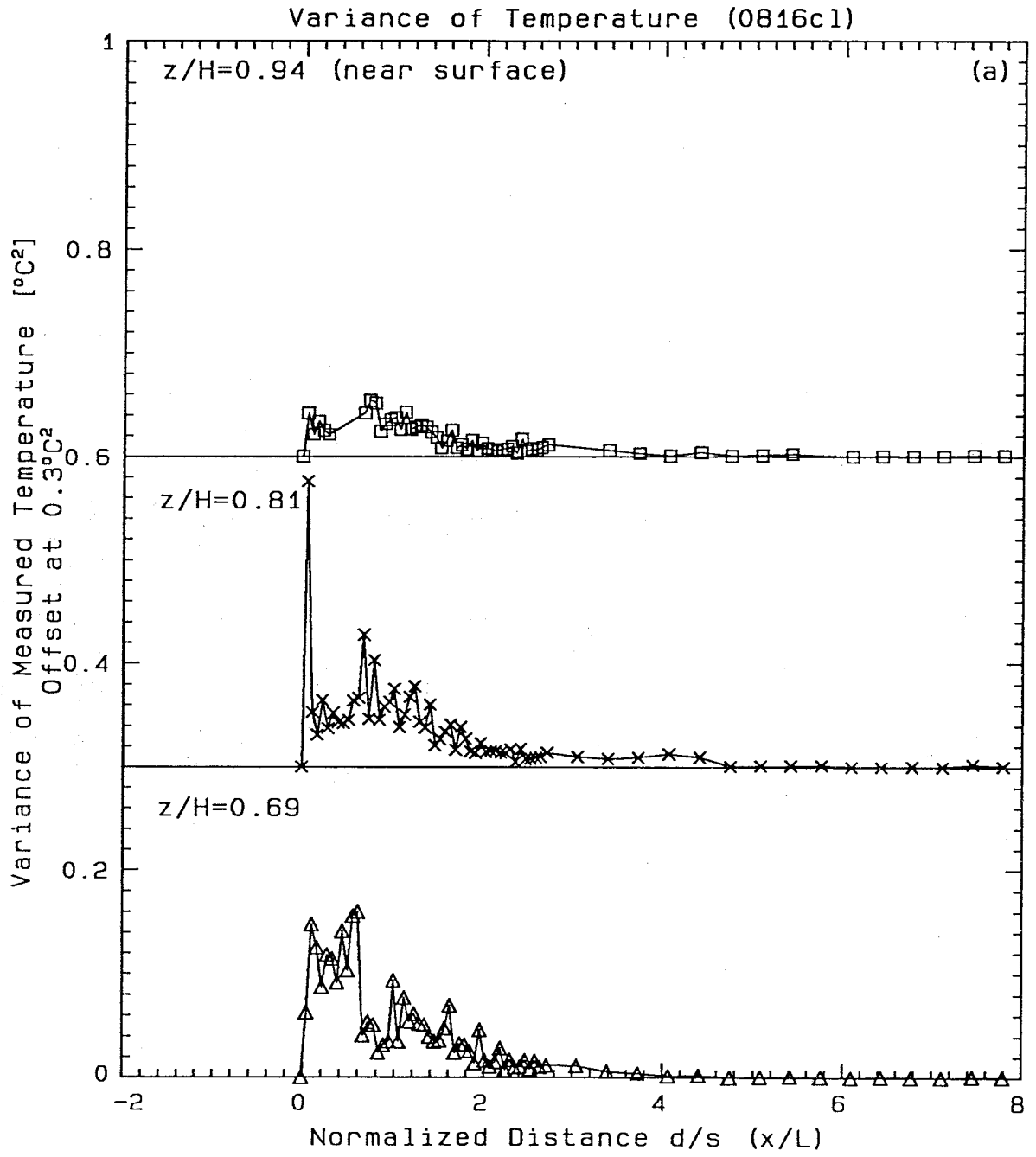

Figure 5.6a Longitudinal profiles of variance of measured temperature at near-surface levels.

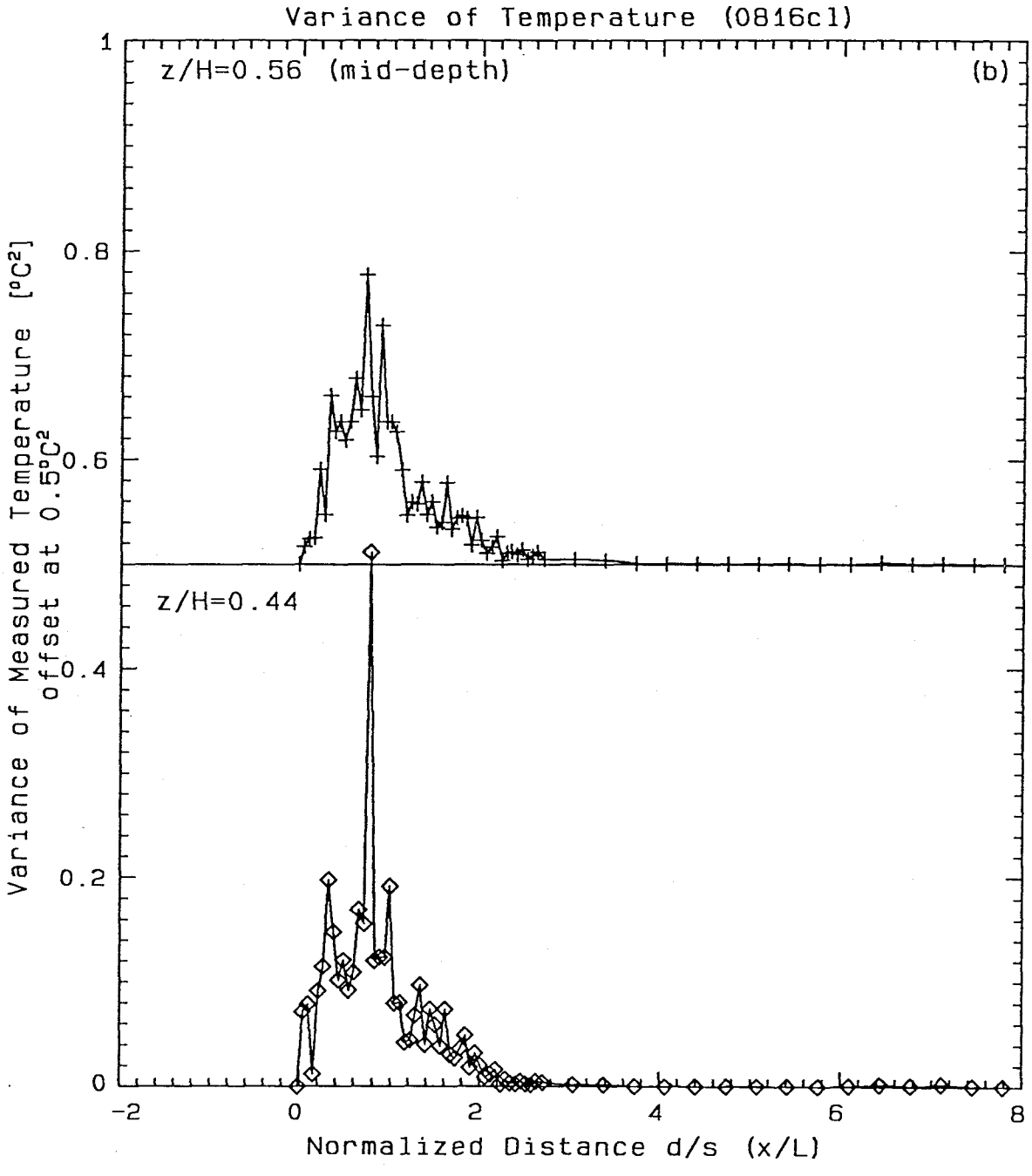

Figure 5.6b Longitudinal profiles of variance of measured temperature at midlevels.

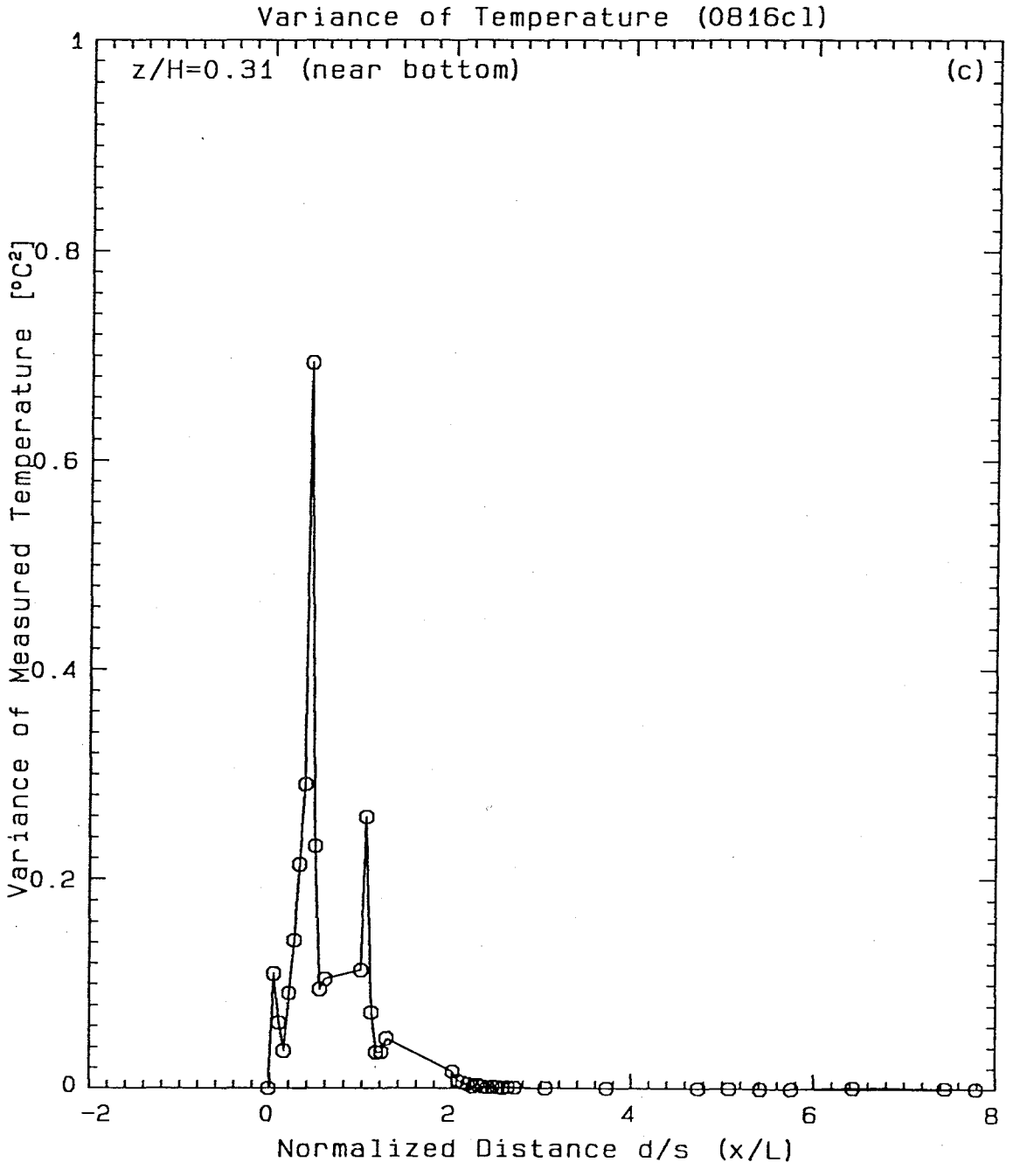

Figure 5.6c Longitudinal profiles of variance of measured temperature at bottom level.

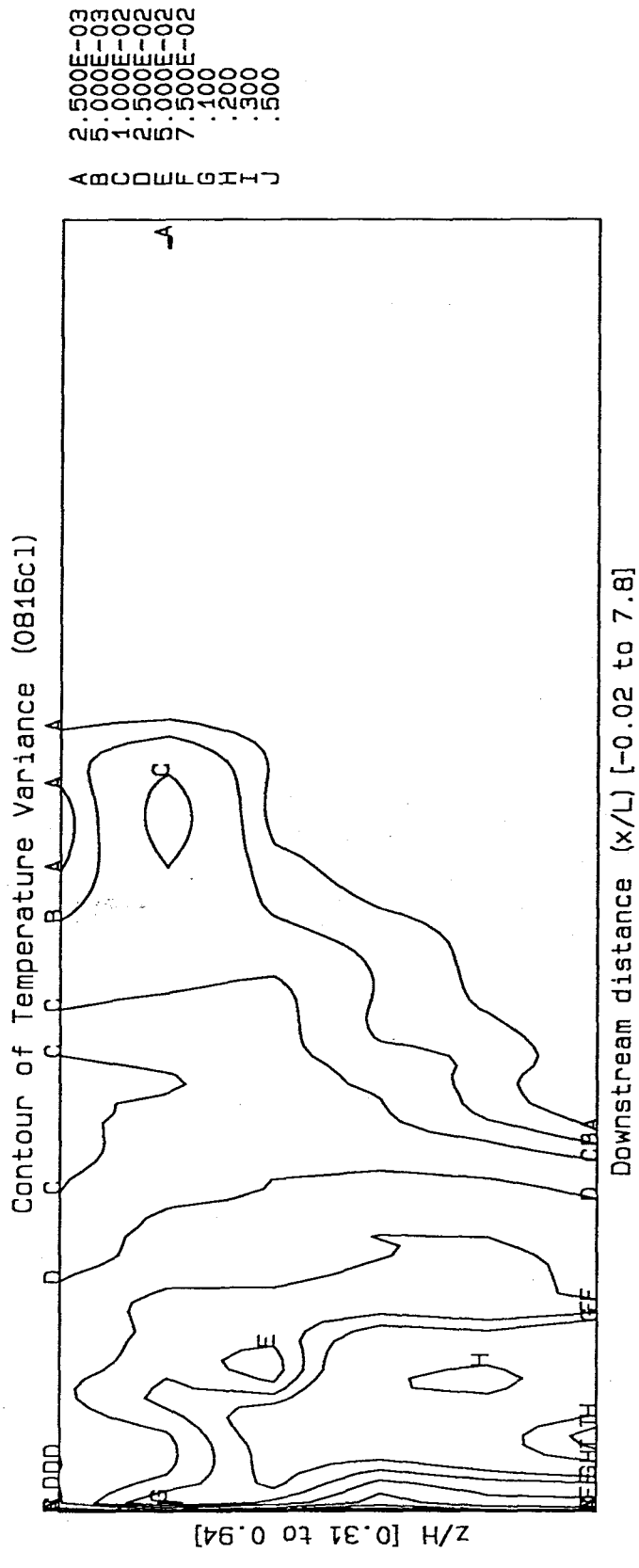

Figure 5.7 Contour map of the variance of the measured temperature in the vertical plane along the diffuser axis. Vertical domain shown is $0.31 < z/H < 0.94$. Contour intervals are indicated by letter code (in $°C^2$).

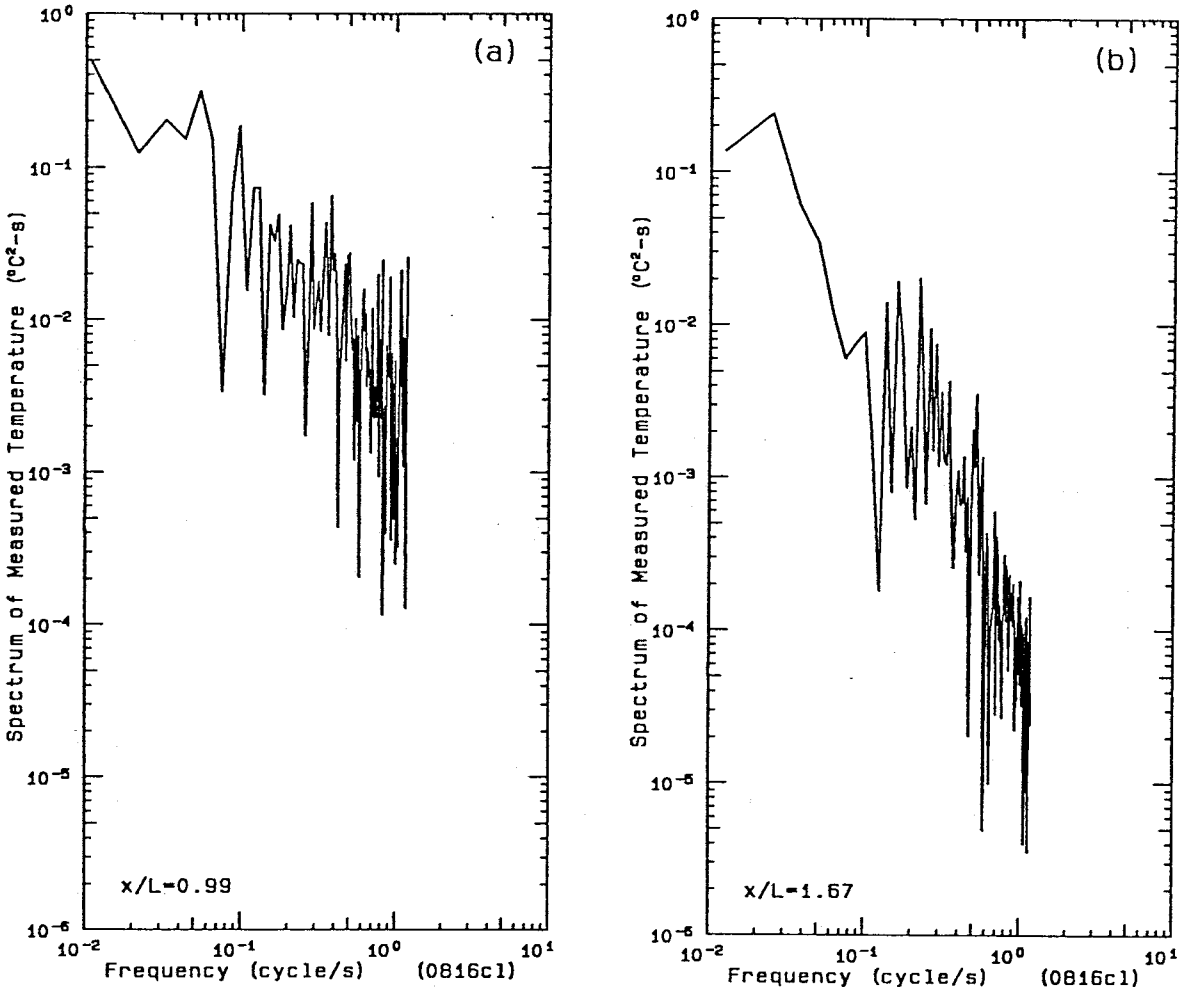

Figure 5.8 Energy spectra of the near-surface temperature. a) $x/L = 0.99$; b) $x/L = 1.67$.

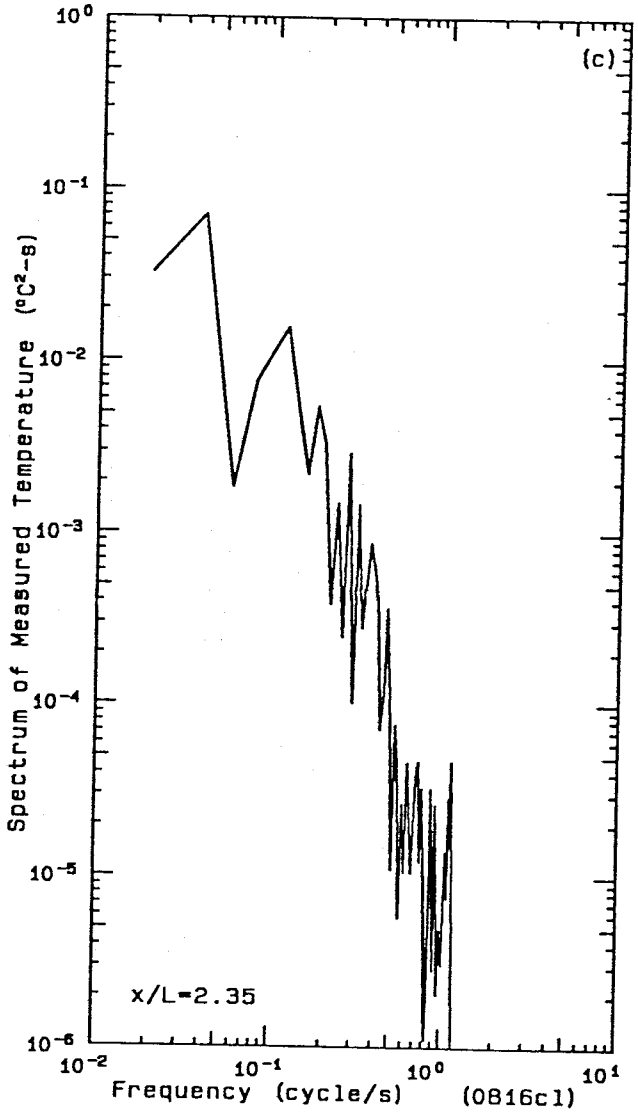

Figure 5.8 Energy spectra of the near-surface temperature.
c) $x/L = 2.35$.

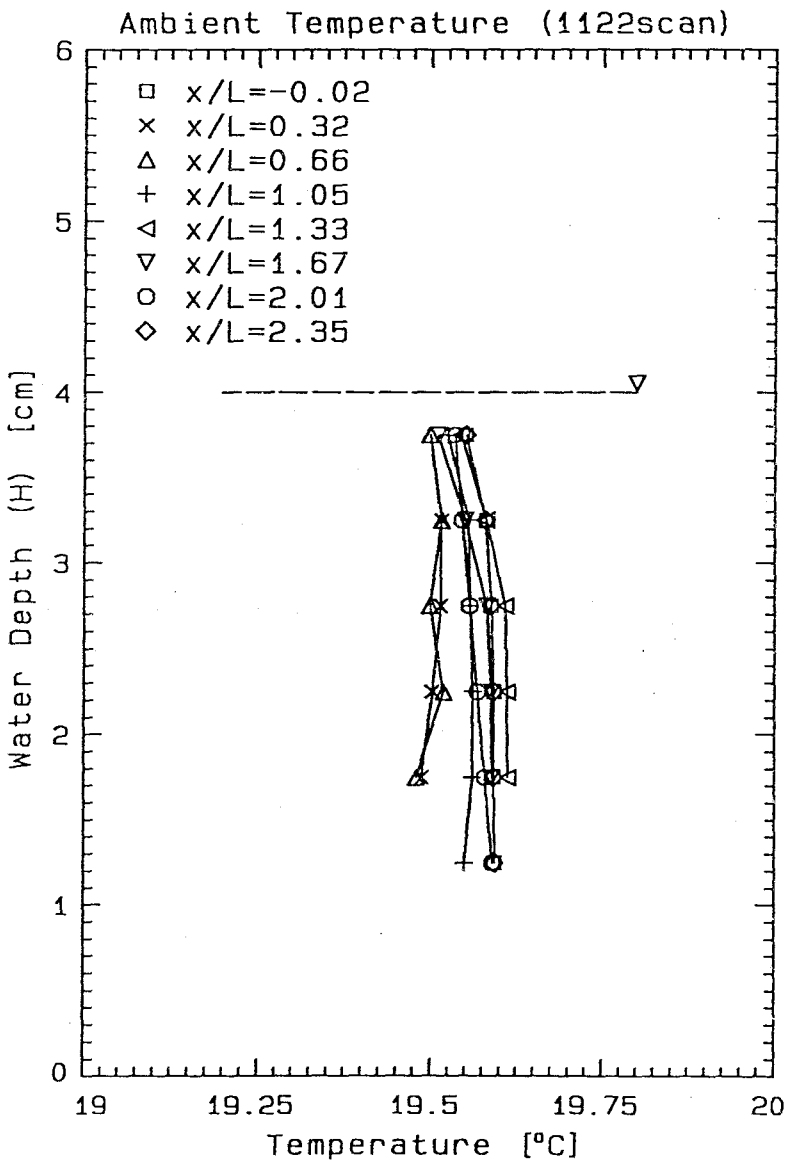

Figure 5.9 Mean ambient temperature profiles before startup of the scanning experiment–1122scan.

(i) Lateral profiles of normalized temperature excess $\Delta T/\Delta T_0$

In contrast to the centerline experiments, the temperature measurements are instantaneous with respect to both time and space. Furthermore, by assuming symmetry about the diffuser axis, only half (or slightly over half) of the plume has been surveyed in each scan. Samples of the profiles at different downstream locations are given in Figures 5.10a to 5.10d. While the peak temperature decreases, the lateral extent of the plume increases with distance downstream. The growth of the half-width of the plume is shown in Figure 5.11. The half-width is defined as the distance from the diffuser axis to the position where $\Delta T/\Delta T_0 \leq e^{-1}$ of the peak values (the supposed centerline values).

In Figure 5.10, it is observed that the profiles are not perfectly symmetric; the windward side (the side facing the moving probes) often has a steeper slope of temperature increase than the leeward side. This may be attributed to the response characteristics of the thermistors; however, the time constant, found to be about 0.5 s, should not cause such discrepancies. A more plausible explanation is that the probes mobilize a small amount of water as they move to scan across the basin, thus changing the thermal characteristics as well as the dynamics of the plume. The significance of the disturbance grows with downstream distance as the velocity of the plume decreases to smaller values compared to the speed of the probes. The scanning speed of the thermistor probes has therefore been carefully chosen to minimize this adverse effect (Section 4.3).

(ii) Isotherms in vertical planes across diffuser axis

Figures 5.12a to 5.12h illustrate the contour maps of $\Delta T/\Delta T_0$ in the transverse vertical planes along some of the scannings. The influence of the diffuser in the lateral direction grows with downstream distance in agreement with the previous discussion and is surprisingly uniform in the vertical direction until $1.92L$ (Figure 5.12e). As

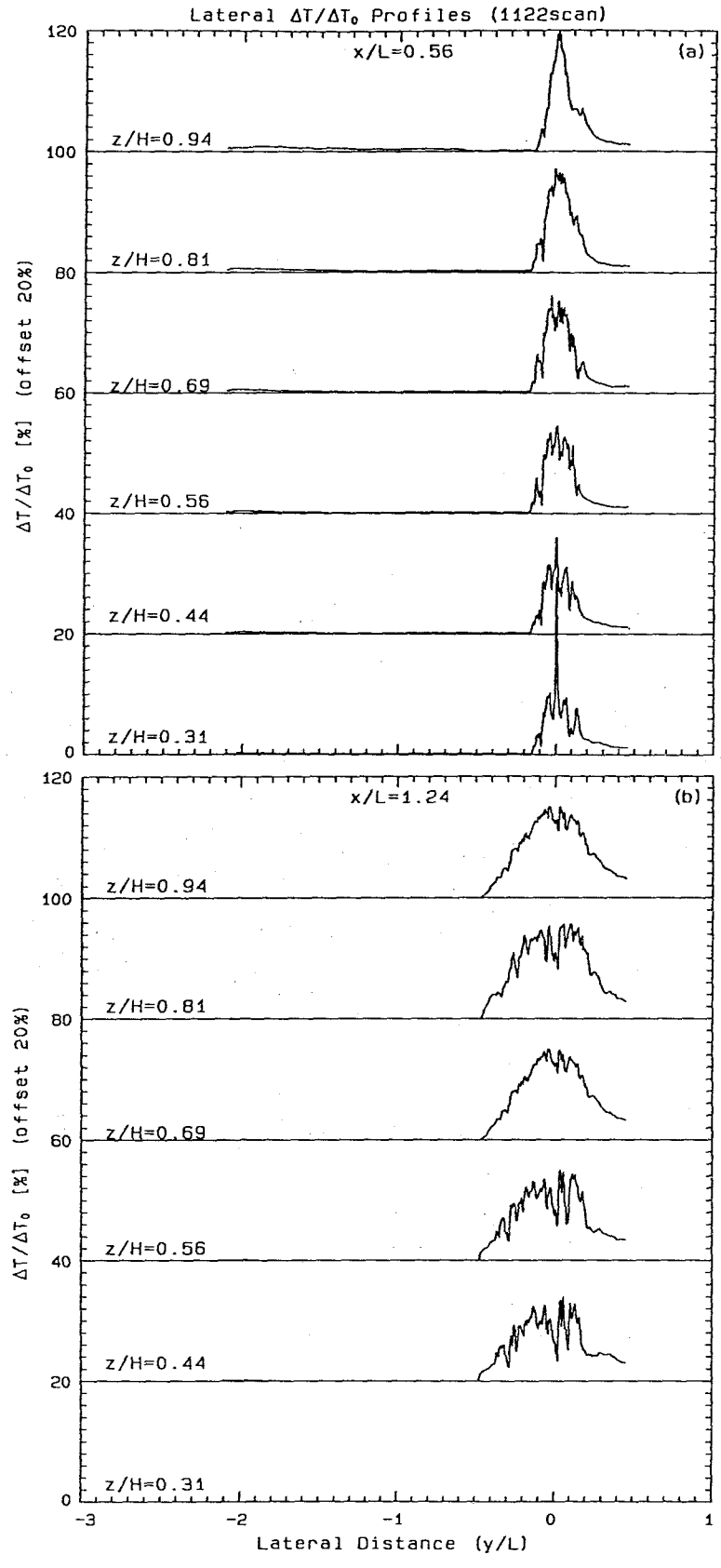

Figure 5.10 Lateral profiles of $\Delta T/\Delta T_0$. a) $x/L = 0.56$; b) $x/L = 1.24$.

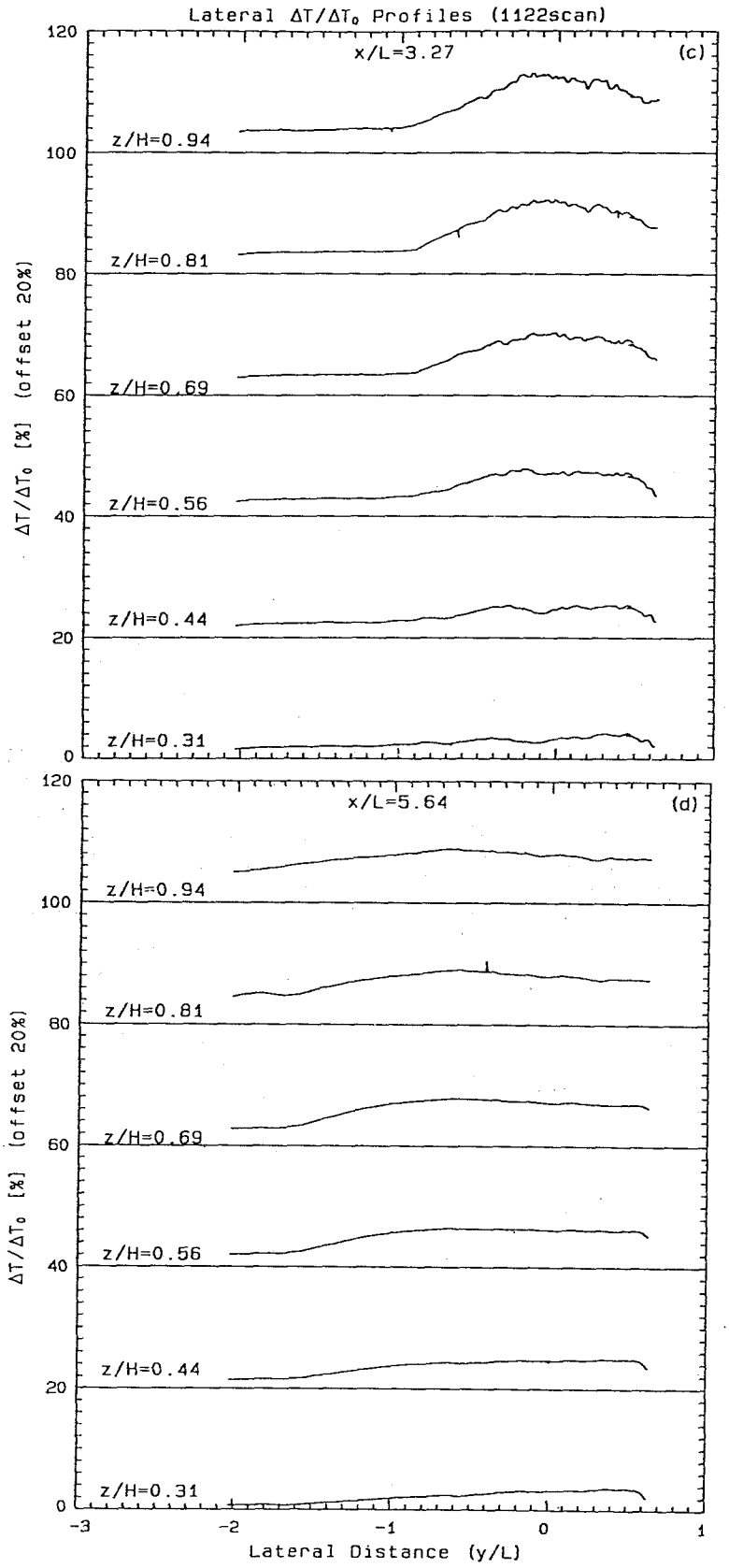

Figure 5.10 Lateral profiles of $\Delta T/\Delta T_0$. c) $x/L = 3.27$; d) $x/L = 5.64$.

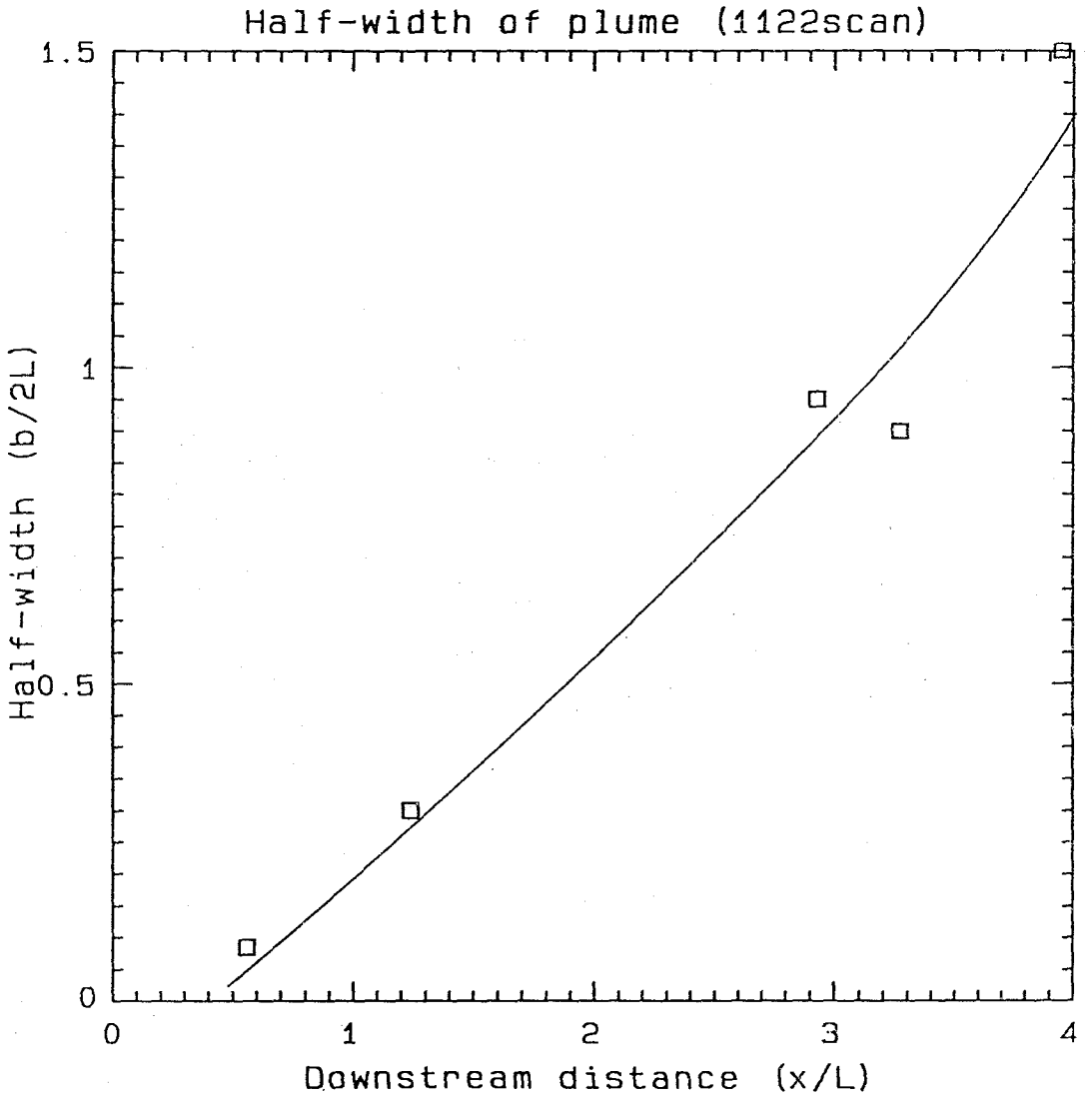

Figure 5.11 Growth of plume half-width with downstream distance.

indicated by the almost vertical inclinations of the 2.5% and 5.0% contours, the water column appears to be fairly well mixed. The contours begin to show signs of a stably stratified region at $2.26L$ (Figure 5.12f), where fluctuations are high but smooth out with travelled distance. At $2.26L$ and beyond, the top portion of the 2.5% contour extends farther away from the diffuser axis than does the bottom portion, which indicates the lateral spreading of a surface layer. This is confirmed by Figure 5.12g at $2.93L$, where the 2.5% contour lifts off from the bottom. The front advances laterally further until $3.27L$ (Figure 5.12h), where the 2.5% contour extends beyond the course of the scanning.

(iii) Isotherms of near-surface $\Delta T/\Delta T_0$ distribution

Figures 5.13a and 5.13b show the isothermal maps of the near-surface ($z/H = 0.94$) $\Delta T/\Delta T_0$ from $0.56L$ to $2.93L$ and from $3.27L$ to $5.64L$, respectively. Two maps are illustrated because of a time lapse of about seven minutes between the two set of measurements. Figure 5.13a corresponds to the plume at $t = 5$ min 30 sec from the start of the discharge, whereas Figure 5.13b corresponds to $t = 12$ min 12 sec. Since part of the thermal field is dominated by unsteady processes, the plume has grown to a different size between the first (forward) and the second (backward) scanning. Hence, a single plot of the time-lagged data sets may be misleading. In Figure 5.13a, where only the latter half of the diffuser zone is included, the unsteadiness can easily be identified from the shape of the contours. The 2.5% and 5.0% contours suggest that the width increases at an approximately constant rate until it reaches $1.6L$ where the plume widens drastically. The contours turn toward the diffuser axis after some distance, reflecting a radial spreading pattern. The isotherms in Figure 5.13b do not reveal as clearly the radial pattern seen in Figure 5.13a. The temperature also has much less variation in Figure 5.13b, about 5.0% over the entire area.

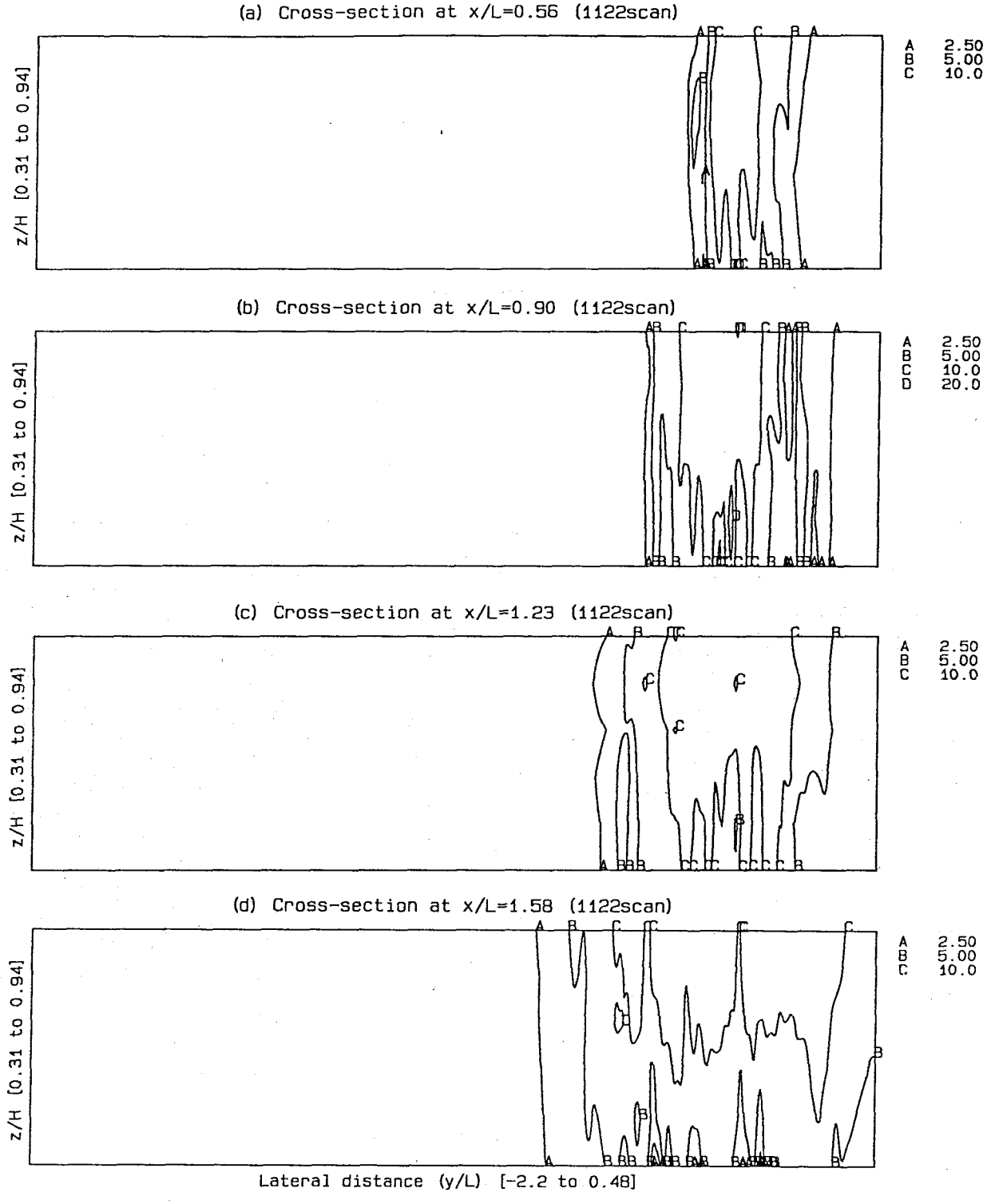

Figure 5.12 Contour map of $\Delta T/\Delta T_0$ in the vertical planes across the diffuser axis. Vertical domain shown is $0.31 < z/H < 0.94$. Contour intervals are indicated by letter code (in %). a)$x/L = 0.56$; b)$x/L = 0.90$; c)$x/L = 1.23$; d)$x/L = 1.58$.

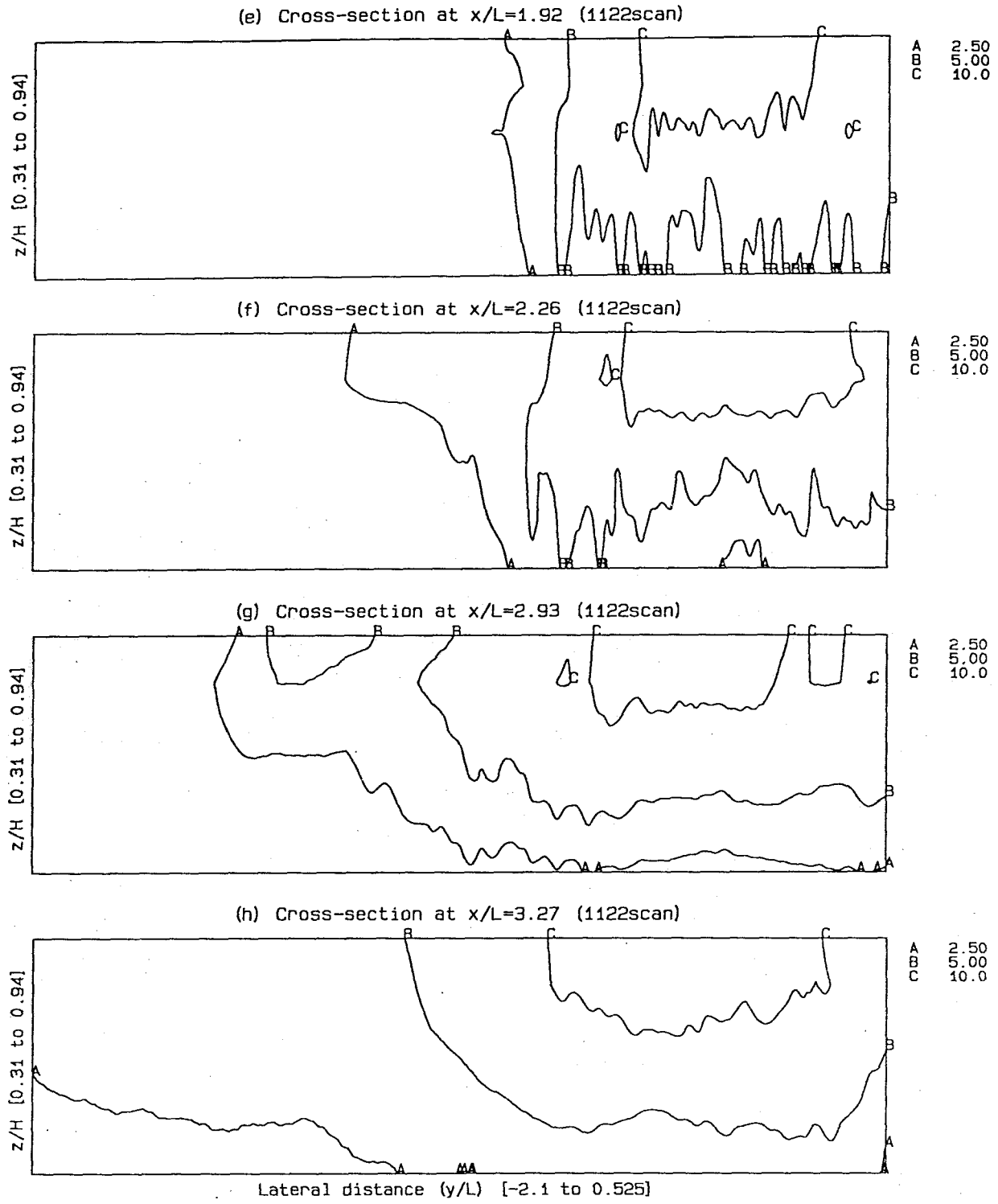

Figure 5.12 Contour map of $\Delta T/\Delta T_0$ in the vertical planes across the diffuser axis. Vertical domain shown is $0.31 < z/H < 0.94$. Contour intervals are indicated by letter code (in %). e)$x/L = 1.92$; f)$x/L = 2.26$; g)$x/L = 2.93$; h)$x/L = 3.27$.

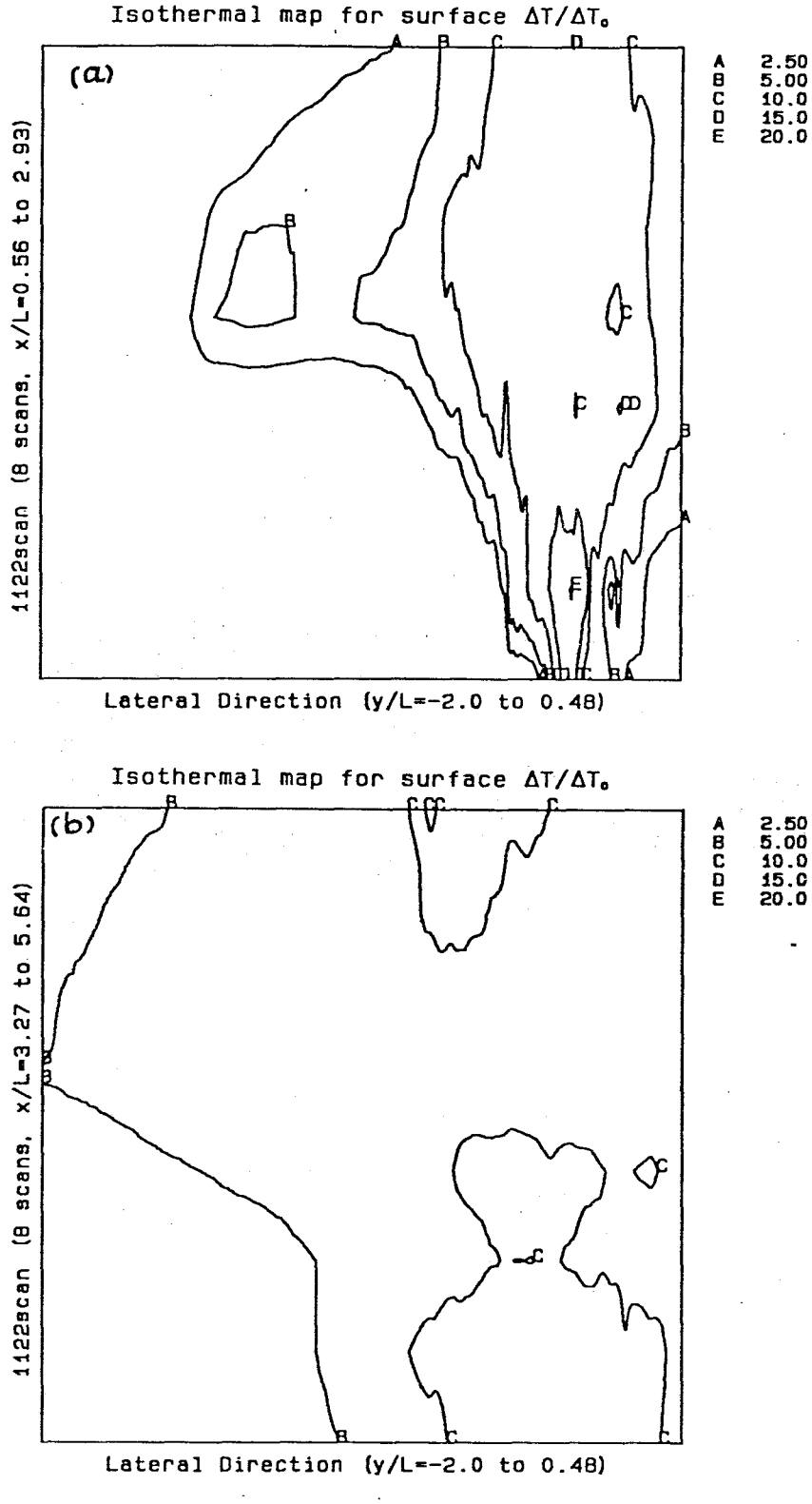

Figure 5.13 Contour map of near-surface $\Delta T/\Delta T_0$ ($z/H = 0.94$). a) $0.56 \leq x/L \leq 2.93$; b) $3.27 \leq x/L \leq 5.64$.

5.2.3 Photographs of Plume Growth

Overhead photographs of the plume (enhanced with dye), as shown in Figures 5.14a to 5.14d, were taken at various times after discharge to study the growth of the plume and the frontal propagation. Figure 5.15 illustrates the tracings of the plume boundary from the whole sequence of overhead photographs. As clearly demonstrated, the frontal region propagates downstream and spreads radially with time. The width of the plume above the diffuser attains steady state about 3 min 15 sec after the start of the discharge. It grows linearly with distance until the spreading process begins to dominate.

5.3 Summary of Plume Development

The discussion of the results of the two model experiments support the hypothetical zoning of the flow field as proposed in Chapter 3. The overall structure of the thermal plume can be divided into three zones: near field (the diffuser zone), intermediate field (the turbulent mixing zone and the gravitational spreading zone), and the far field, which is not included in this discussion.

(i) Near field—the diffuser zone

The region directly above the diffuser is dominated by the mixing process of a number of three-dimensional jets and is very complex because of the interactions among jets. The water column is partially mixed and is potentially unstable (when a shallow water condition is combined with a large discharge momentum flux) with recirculation of diluted warm water back to the jet efflux. The width of the plume increases more or less linearly with distance downstream. The temperature across the diffuser shows a bell-shaped distribution, but is rather irregular in the longitudinal direction, reflecting the influence of the individual jets. The resolution of the mea-

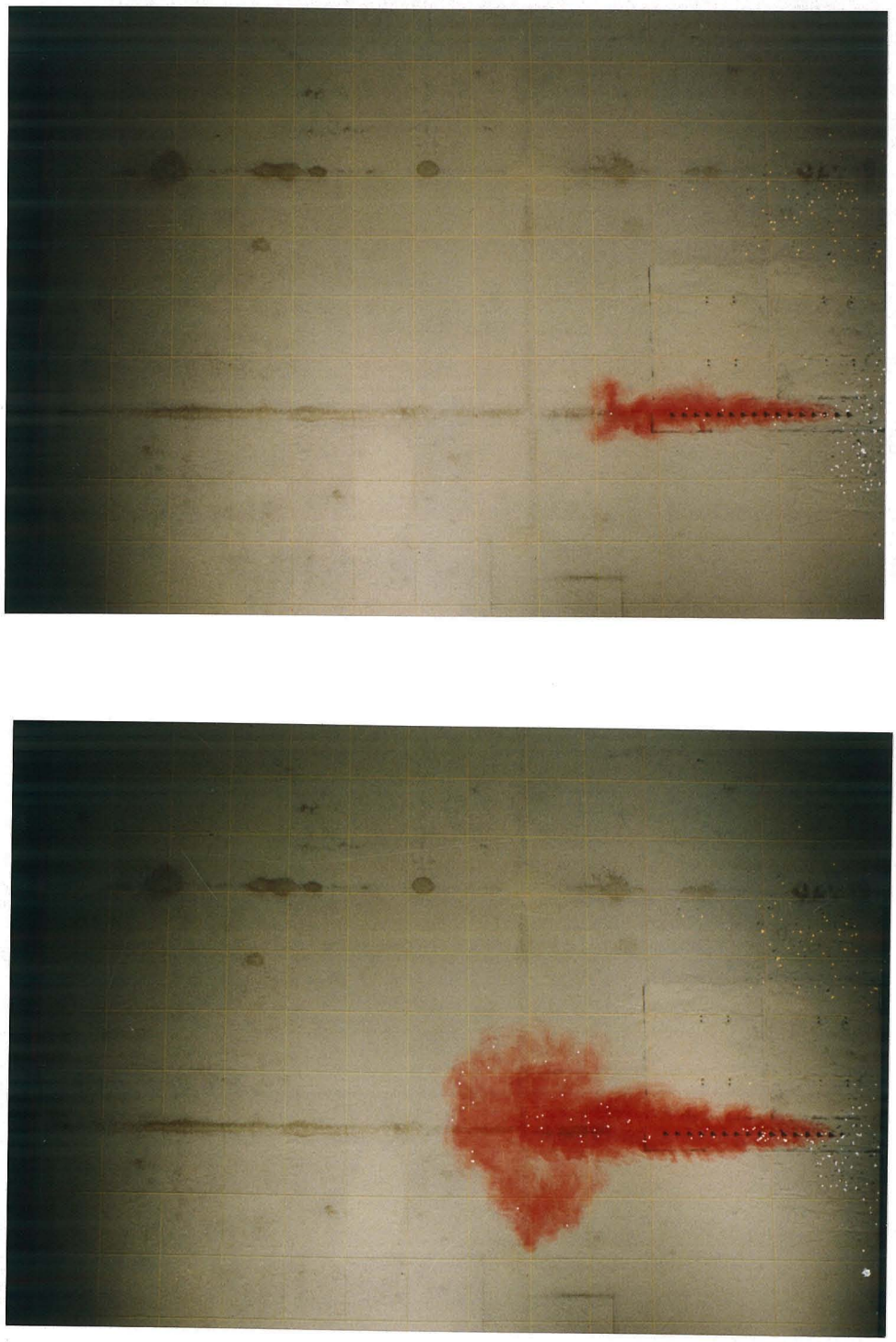

Figure 5.14 Overhead photographs of the diffuser plume after discharge. a) t = 0.5 min; b) t = 1.0 min.

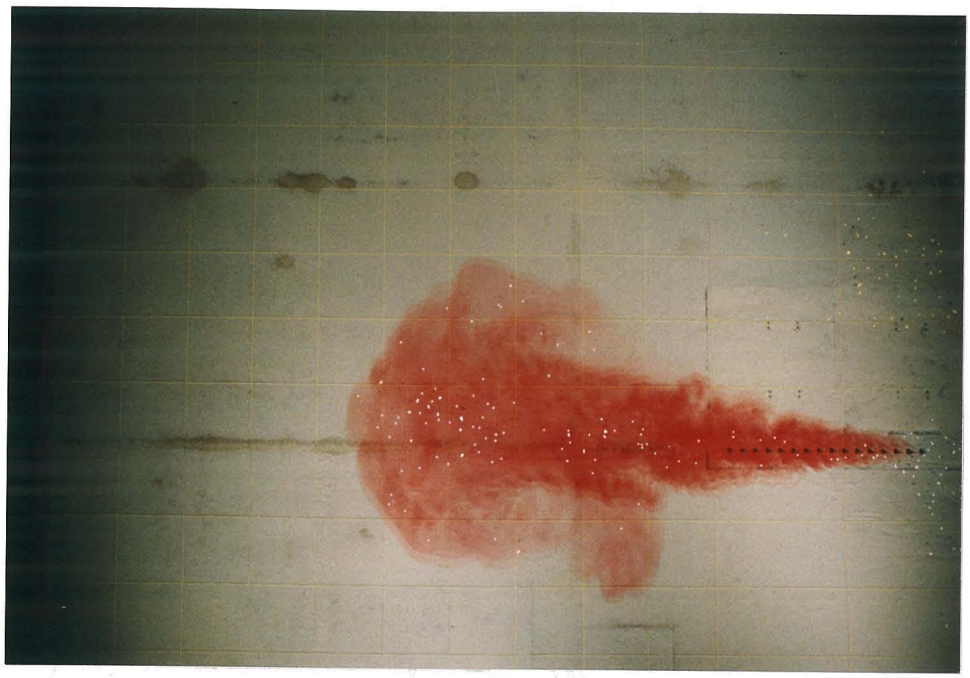

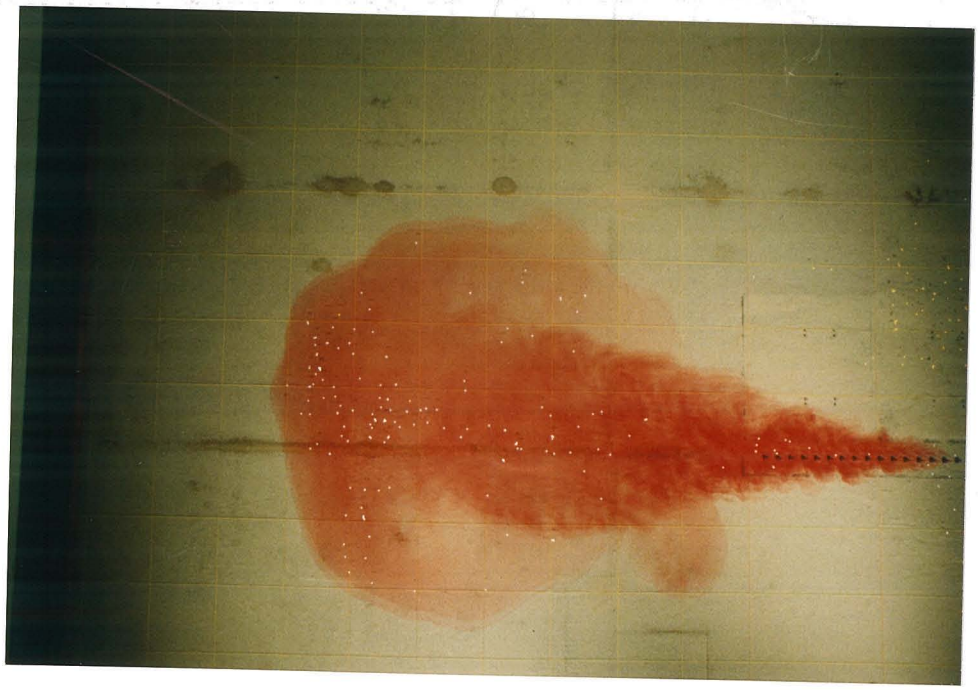

Figure 5.14 Overhead photographs of the diffuser plume after discharge. c) t = 1.5 min; d) t = 2.0 min.

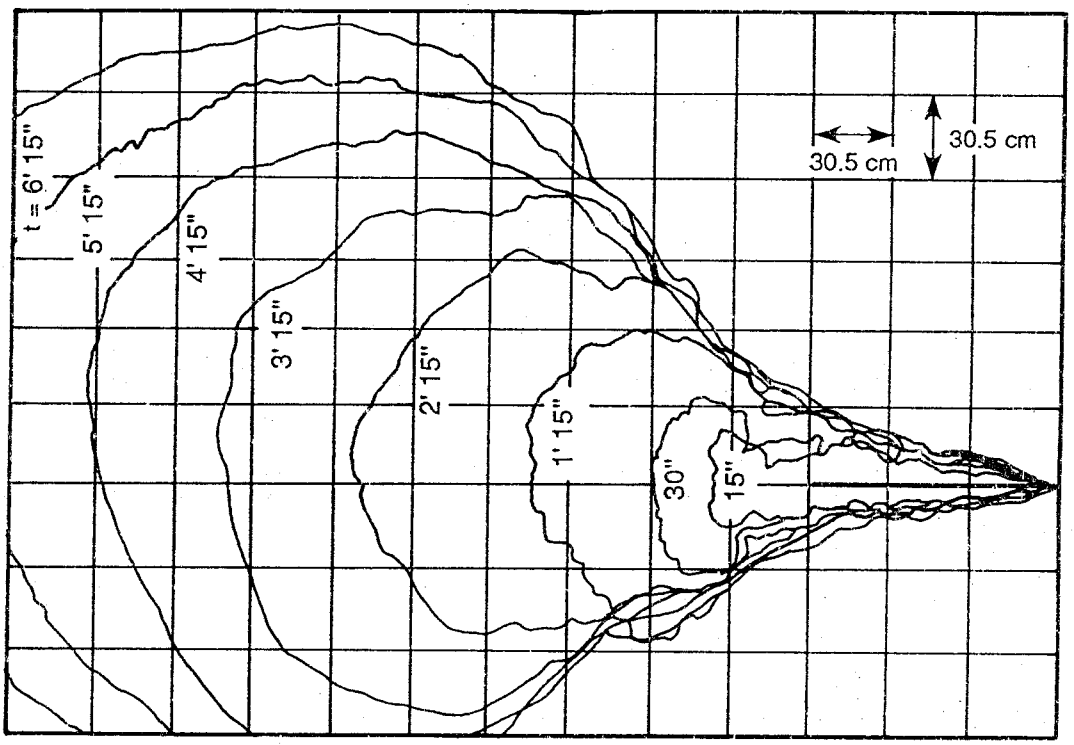

n = 16, D_ϕ = 0.25 cm $\alpha = 0°$, $\beta = 25°$

Q_{TO} = 28.8 cm^3/s, H = 4 cm

Figure 5.15 Dye tracings of diffuser plume boundaries.

suring stations, however, is not adequate for a detailed investigation of the thermal structure in this zone.

(ii) Intermediate field—the turbulent mixing zone

At a short distance from the diffuser, the plume lifts off from the bottom and drifts downstream as a buoyant surface layer. Since momentum and heat fluxes are not replenished beyond the diffuser, the buoyancy force becomes progressively more important with distance downstream. The temperature declines exponentially at the beginning of the surface buoyant jet zone when turbulent mixing still dominates, but approaches a plateau value at some farther distance when the inertial force diminishes.

(iii) Intermediate field—the gravitational spreading zone

Farther downstream, the turbulent mixing energy is largely reduced because of the dispersion of momentum through interfacial friction loss. Hereafter, the plume is in the gravitational spreading zone where the driving force is the density difference between the plume and its immediate surrounding. The plume propagates forward with the residual momentum from the buoyant jet zone and simultaneously spreads radially. Because of the nature of the spreading process, the plume characteristics, such as the temperature distribution and the size of the cloud, are unsteady. In the inner region of this zone, the temperature stays relatively stable and steady provided that heat loss is not a significant factor (discussed in Section 4.6). This region will extend laterally as well as in the downstream direction with time; however, the area of growth in the experiments is limited by the size of the test basin.

5.4 Comparison with Other Experiments

The plume characteristics are governed to various extents by the control factors. This section is devoted to a study of such behavioral dependencies on four

of the physical variables. Selected experiments, one for each variable, have identical configurations as experiments 0816cl and 1122scan except for the variable under examination.

5.4.1 Significance of the Initial Horizontal Orientation of the Jets "α"

The comparison between cases of $\alpha = 0°$ and $\alpha = \pm 25°$ (experiments 0827cl and 0828scan) is aided by Figures 5.16a to 5.16c, which illustrate the distributions of $\Delta T/\Delta T_0$ along the diffuser axis at various levels. In the diffuser zone, the staggered diffuser (with $\alpha = \pm 25°$) produces temperature profiles of steady increase at all levels, while the unidirectional diffuser produces irregular ones. This is attributed to the fact that for the staggered diffuser, the nozzles are pointing away from the thermistor probes and therefore the measured temperature excess on the centerline is lower. Soon after the end of the diffuser, the two sets of profiles essentially collapse together until farther downstream where the plumes are no longer steady.

The vertical profiles shown in Figures 5.17a to 5.17c confirm these findings of the differences in the diffuser zone and the similarities in the surface buoyant jet zone. However, in Figure 5.17d ($x/L = 2.35$), the profile is more uniform in the $\alpha = 25°$ case; the difference between near-surface and near-bottom $\Delta T/\Delta T_0$ is 6% (compared to 10% in the $\alpha = 0°$). Detailed lateral temperature profiles are not available for comparison on the horizontal extent of the plume; however, the tracings of the plume boundaries given in Figure 5.18 show, in the 25° case, a wider plume with a slower speed of propagation. Both of these features are expected since the jets are discharging at an angle away from the diffuser axis, thereby expanding the lateral reach of the plume; furthermore, the forward momentum and therefore the speed of propagation is only a component in the downstream direction of the total discharge momentum.

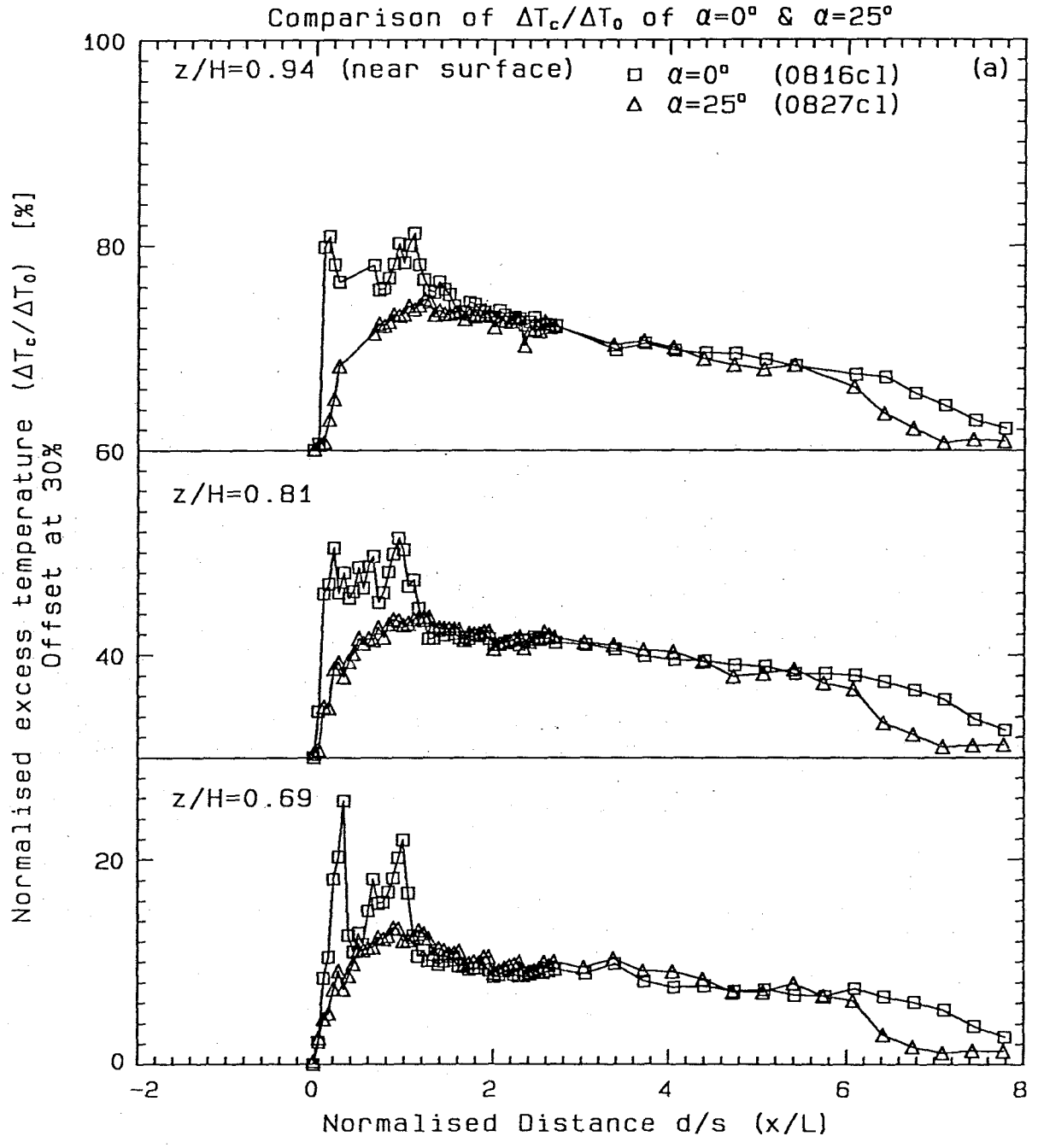

Figure 5.16a Comparison of longitudinal profiles of $\Delta T_c/\Delta T_0$ at near-surface levels of 2 cases: $\alpha = 0°$ (experiment–0816cl) and $\alpha = 25°$ (experiment–0827cl).

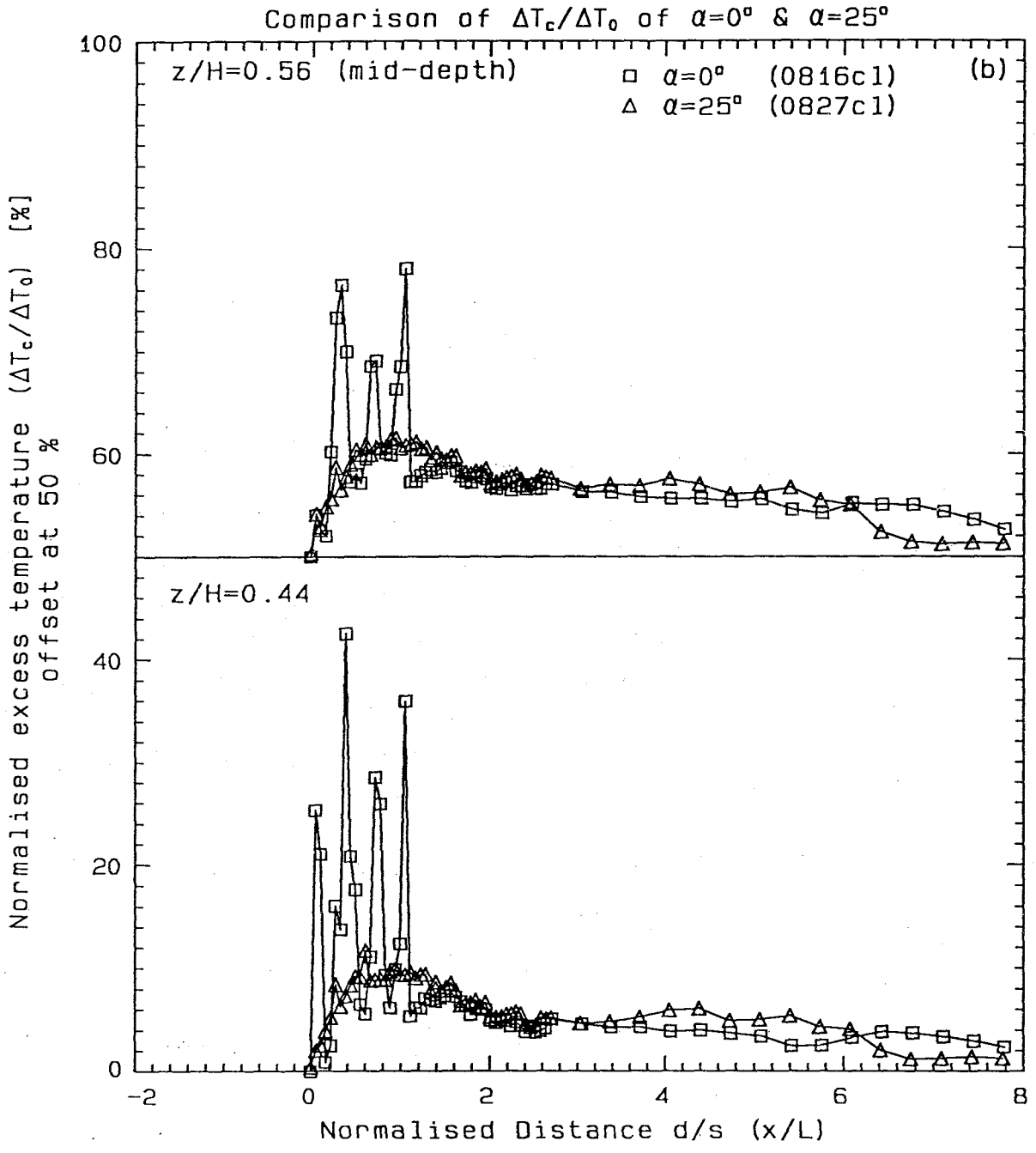

Figure 5.16b Comparison of longitudinal profiles of $\Delta T_c/\Delta T_0$ at midlevels of 2 cases: $\alpha = 0°$ (experiment–0816cl) and $\alpha = 25°$ (experiment–0827cl).

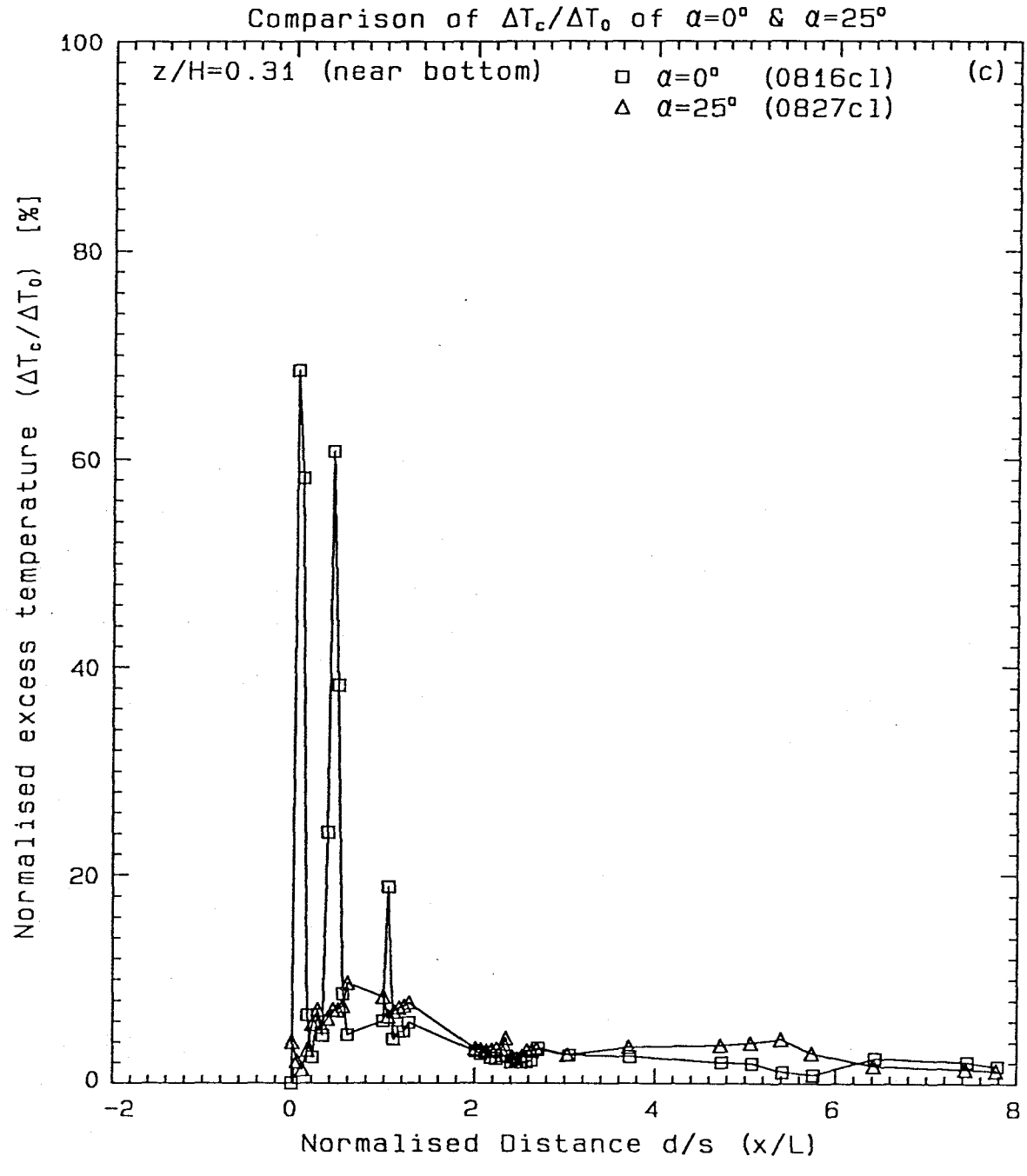

Figure 5.16c Comparison of longitudinal profiles of $\Delta T_c/\Delta T_0$ at bottom level of two cases: $\alpha = 0°$ (experiment–0816cl) and $\alpha = 25°$ (experiment–0827cl).

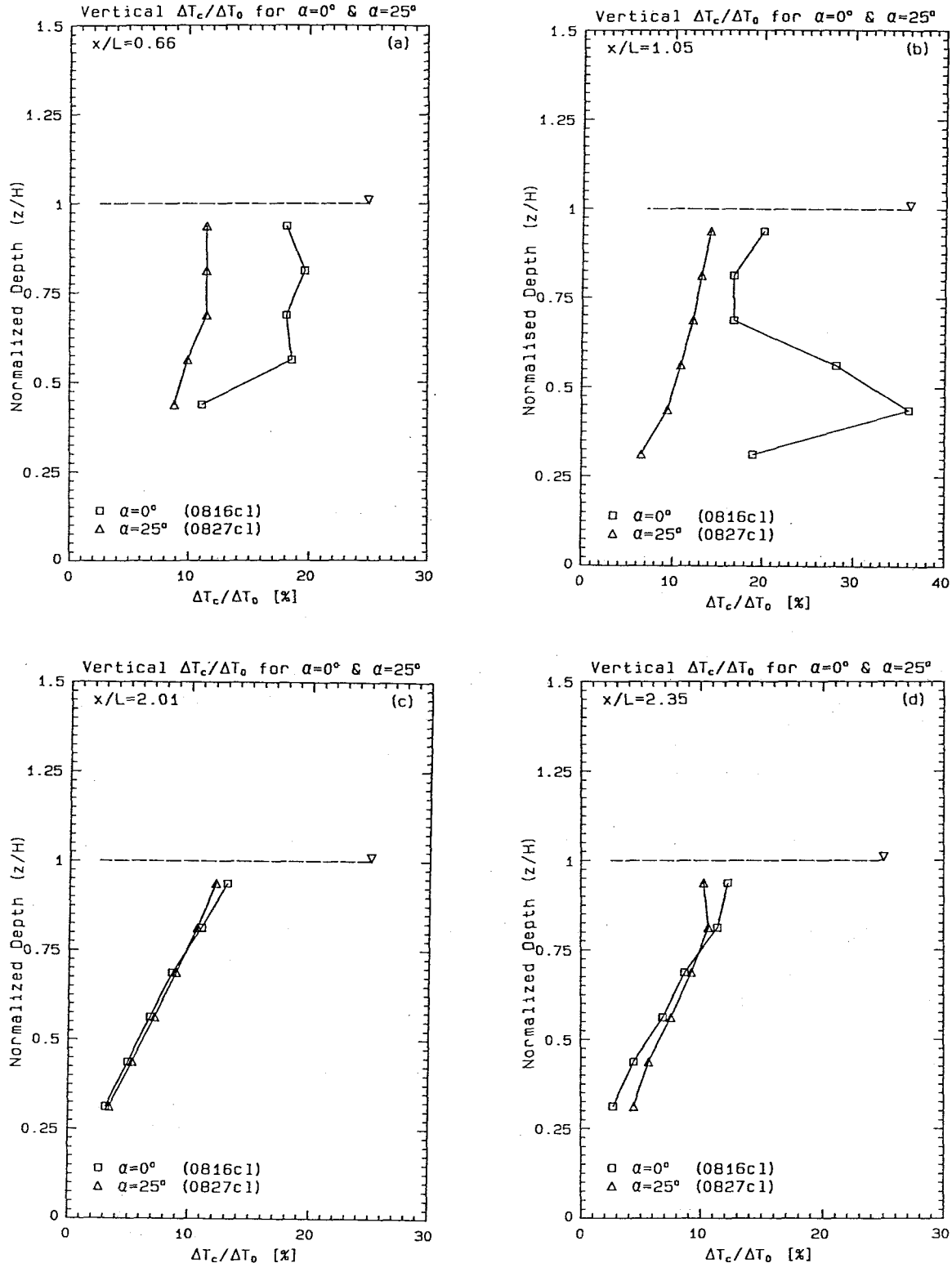

Figure 5.17 Comparison of vertical profiles of $\Delta T_c/\Delta T_0$ of 2 cases: $\alpha = 0°$ (experiment–0816cl) and $\alpha = 25°$ (experiment–0827cl). a) $x/L = 0.66$; b) $x/L = 1.05$; c) $x/L = 2.01$; d) $x/L = 2.35$.

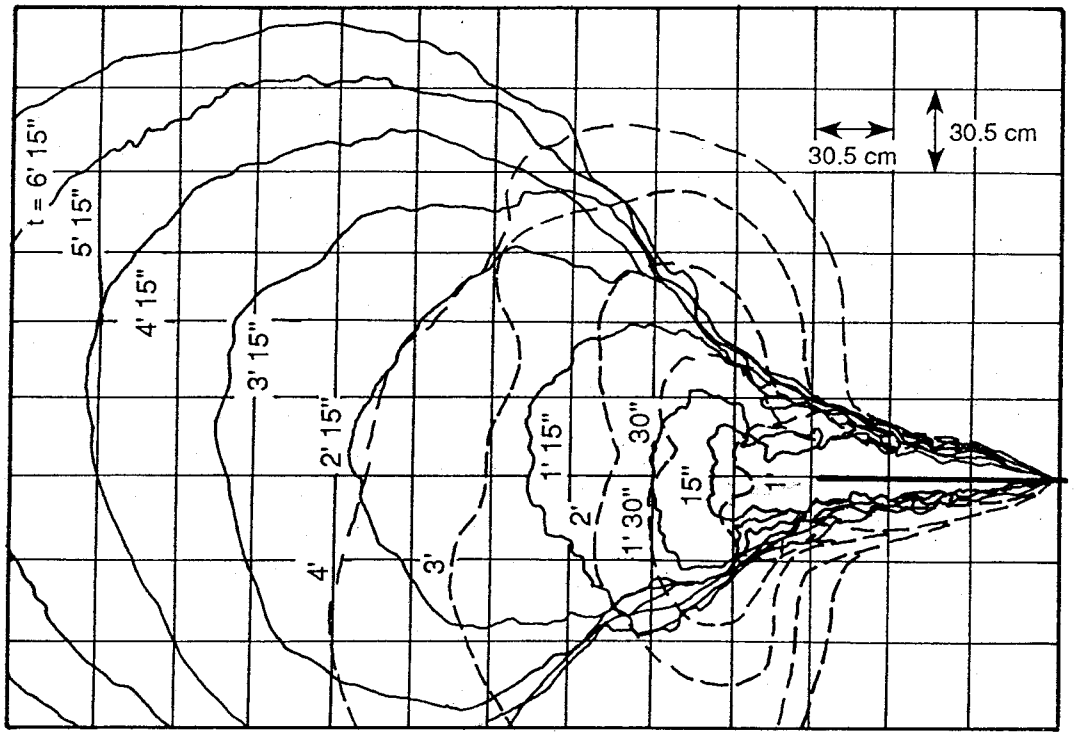

Figure 5.18 Comparison of plume boundaries at various times for $\alpha = 0°$ (experiment–1122scan) and $\alpha = 25°$ (experiment–0828scan).

5.4.2 Significance of the Water Depth "H"

The depth of water is definitely one of the most important controlling factors on the behavior of plumes, as noted in the $\Delta T/\Delta T_0$ profiles in Figures 5.19a to 5.19c for experiments with $H = 8$ cm (experiment 0714cl) and $H = 4$ cm (experiment 0816cl). The temperature excess decreases in all regimes with increasing water depth. The vertical profiles in Figures 5.20a to 5.20d provide an interesting comparison; the distributions of $\Delta T/\Delta T_0$ for the two depths differ by a factor of about 2, especially downstream of the diffuser as seen in Figures 5.20c and 5.20d. A contour map of $\Delta T/\Delta T_0$ in the vertical plane along diffuser axis for the $H = 8$ cm case (Figure 5.21) clearly exhibits the existence of the liftoff and the surface layer structures. To show the horizontal extent of the plume, a surface isothermal map is constructed from the scanning measurements of the $H = 8$ cm experiment (1123scan), as presented in Figure 5.22. The map covers a longitudinal distance from $0.56L$ to $2.93L$, but not the unsteady region from $3.27L$ to $5.64L$. It shows, when compared to the surface isothermals for the $H = 4$ cm case (Figure 5.13a), a much wider plume, as indicated by the 2.5% and 5% contours, and a more uniform thermal distribution. Because of the additional depth of water available for mixing in the diffuser zone, the jet velocity at the surface is smaller than for the case of shallow water discharge. This results in a more slowly propagating plume and therefore a radial spreading zone much closer to the diffuser; it is so close in fact that the surface buoyant jet zone is virtually nonexistent (the inundated condition). The tracings in Figure 5.23 illustrate both the differences caused by the change of the water depth and the absence of the surface buoyant jet zone in the $H = 8$ cm case.

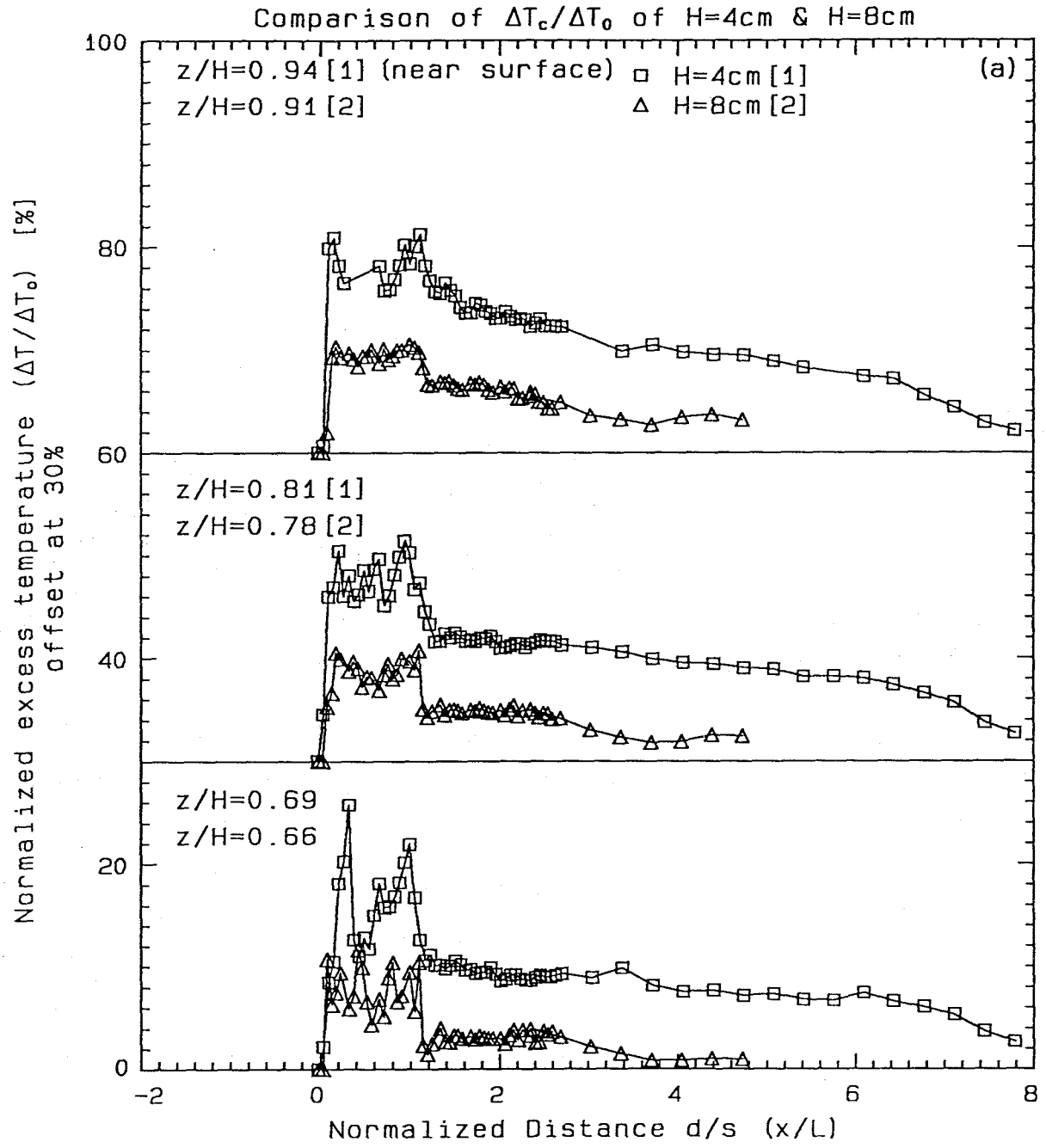

Figure 5.19a Comparison of longitudinal profiles of $\Delta T_c/\Delta T_0$ at near-surface levels for 2 cases: $H = 4.0$ cm (experiment–0816cl) and $H = 8.0$ cm (experiment–0714cl).

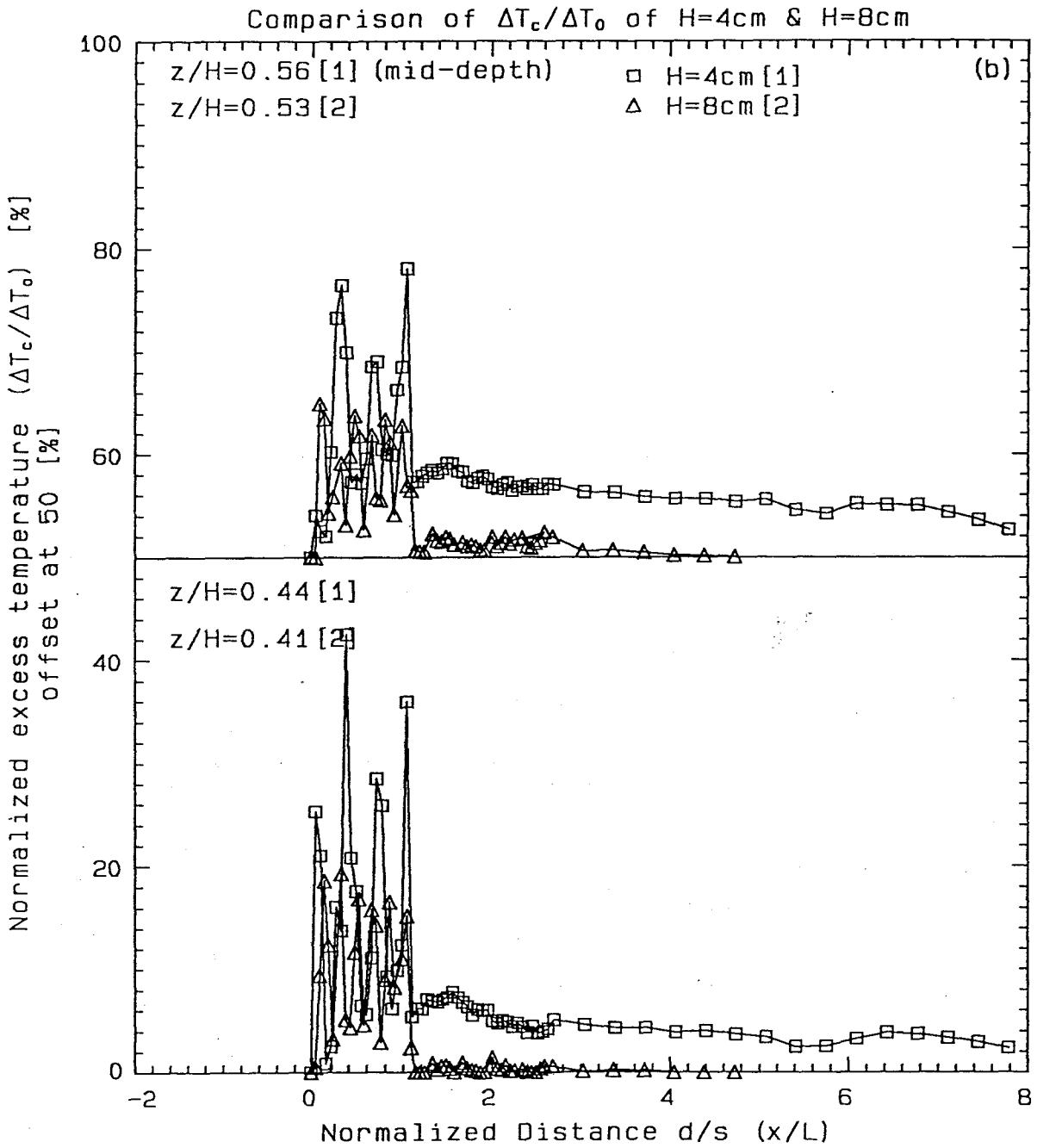

Figure 5.19b Comparison of longitudinal profiles of $\Delta T_c/\Delta T_0$ at midlevels for 2 cases: $H = 4.0$ cm (experiment–0816cl) and $H = 8.0$ cm (experiment–0714cl).

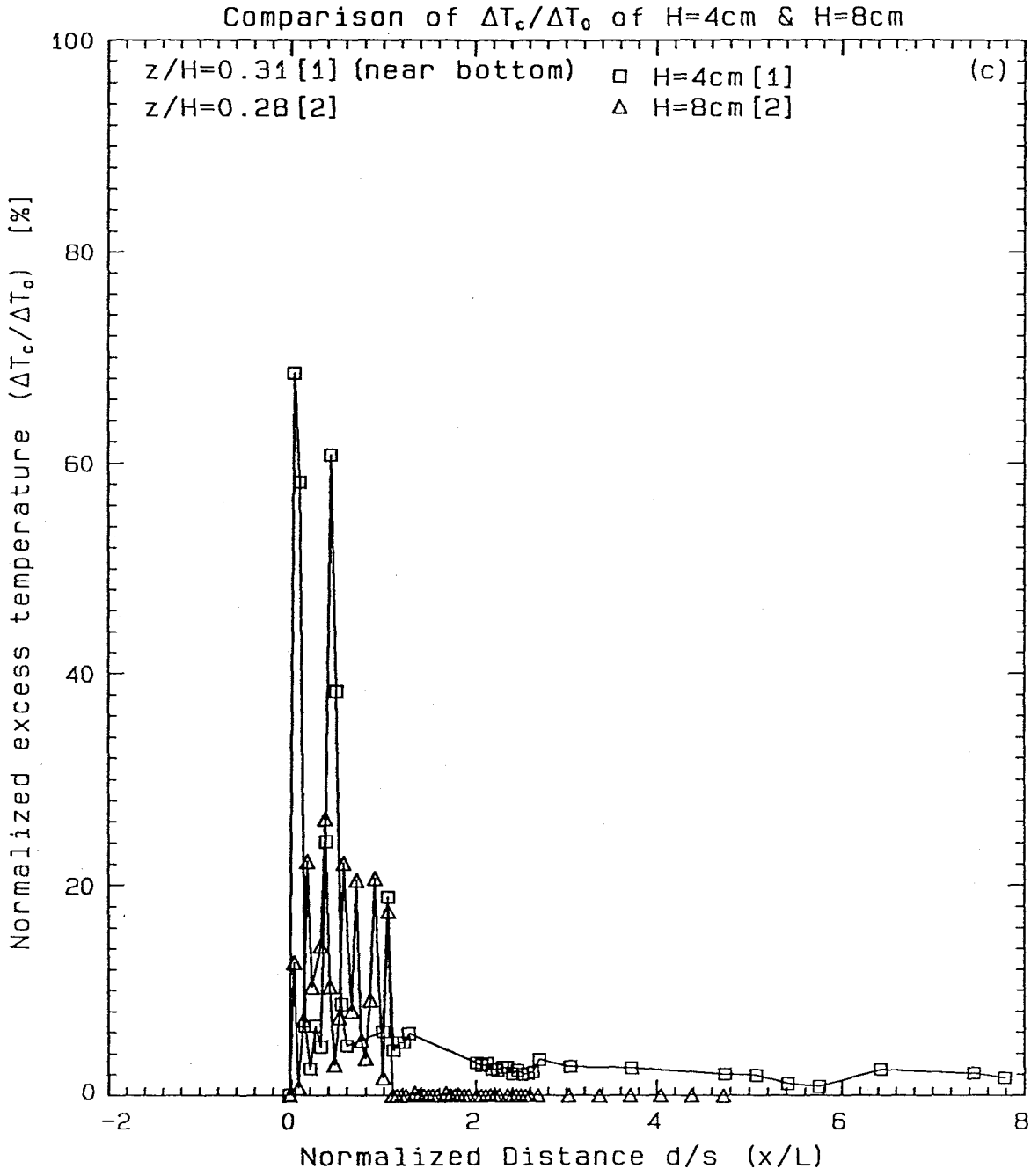

Figure 5.19c Comparison of longitudinal profiles of $\Delta T_c/\Delta T_0$ at bottom level for 2 cases: $H = 4.0$ cm (experiment–0816cl) and $H = 8.0$ cm (experiment–0714cl).

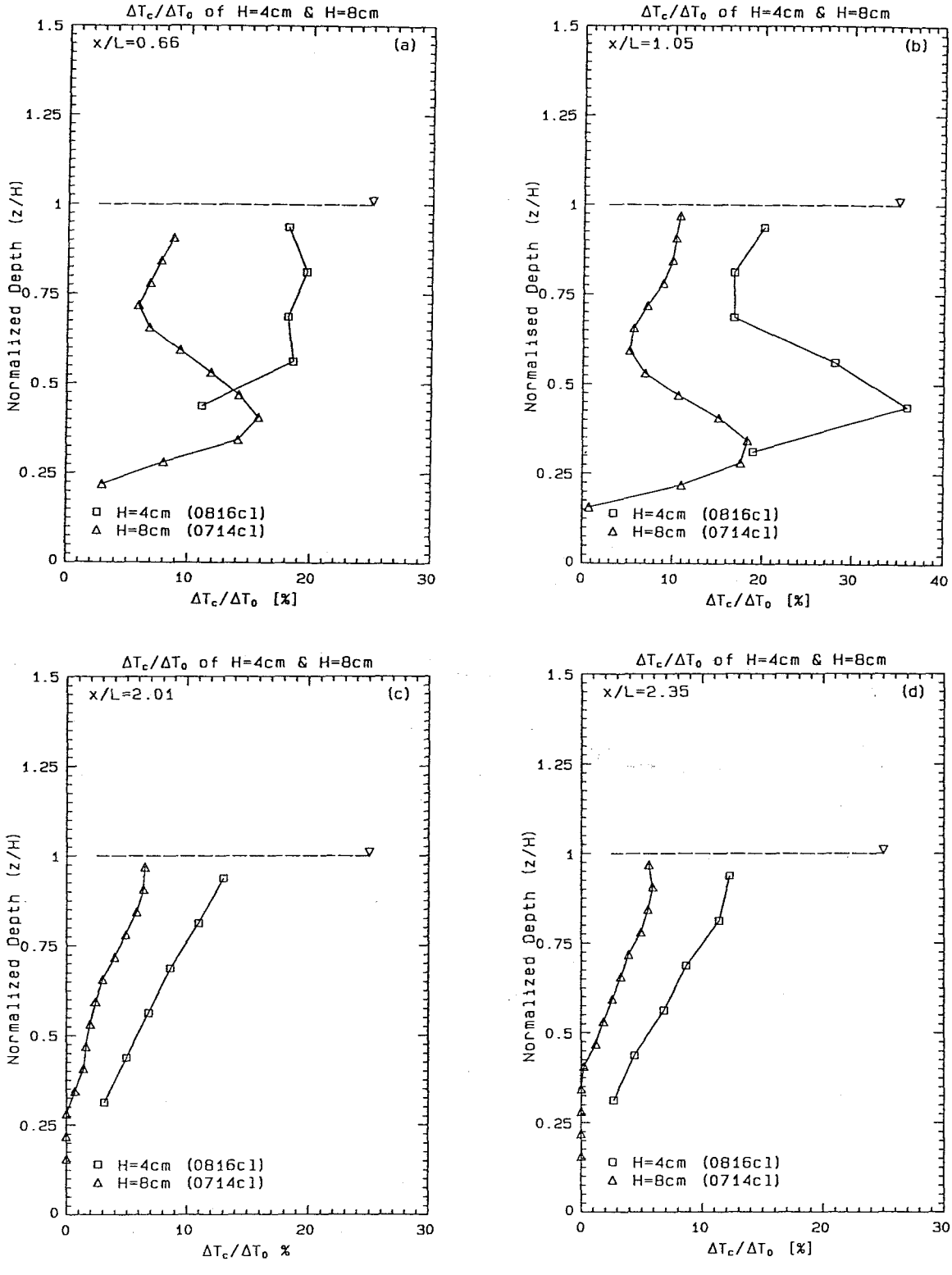

Figure 5.20 Comparison of vertical profiles of $\Delta T_c/\Delta T_0$ for $H = 4.0$ cm (experiment–0816cl) and $H = 8.0$ cm (experiment–0714cl) cases. a) $x/L = 0.66$; b) $x/L = 1.05$; c) $x/L = 2.01$; d) $x/L = 2.35$.

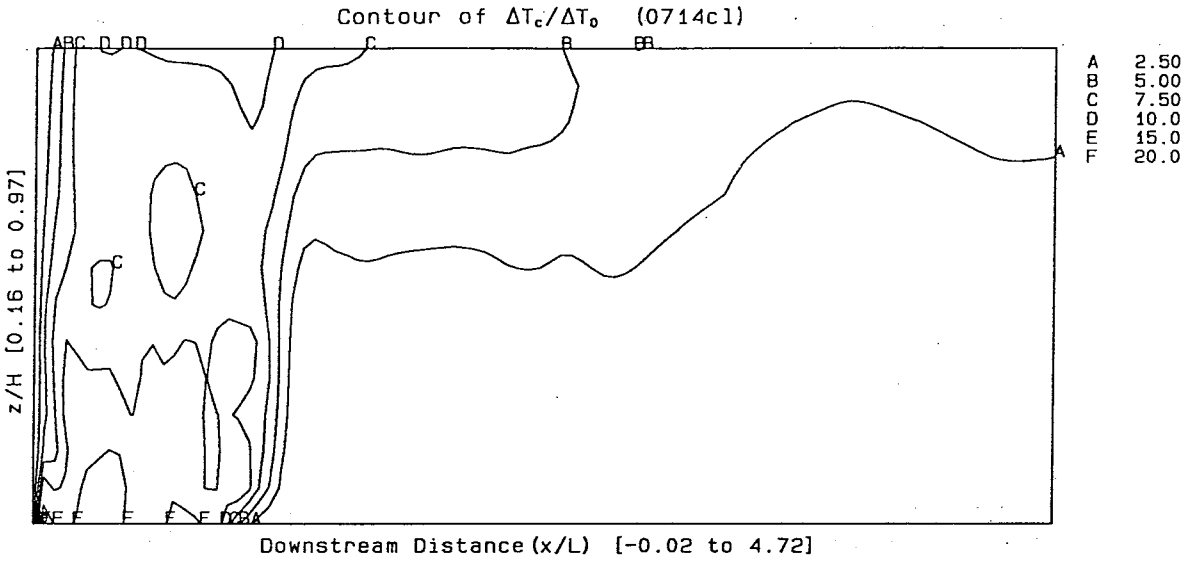

Figure 5.21 Contour map of $\Delta T_c/\Delta T_0$ for $H = 8.0$ cm (experiment–0714cl) in the vertical plane along the diffuser axis. Vertical domain shown is $0.16 < z/H < 0.97$. Contour intervals are indicated by letter code (in %).

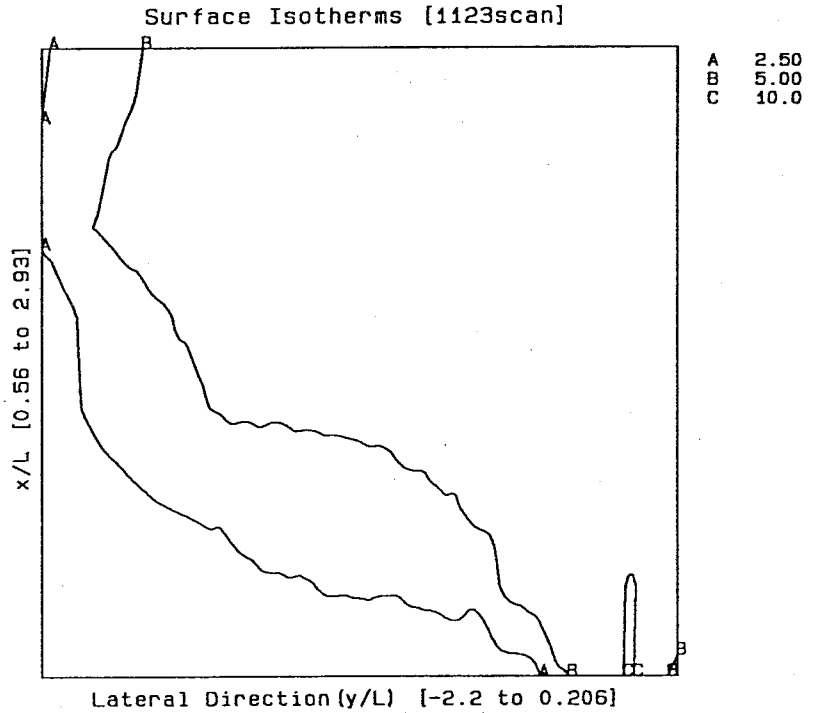

Figure 5.22 Contour map of near-surface $\Delta T/\Delta T_0$ for $H = 8.0$ cm (experiment–1123scan). Contour intervals are indicated by letter code (in %).

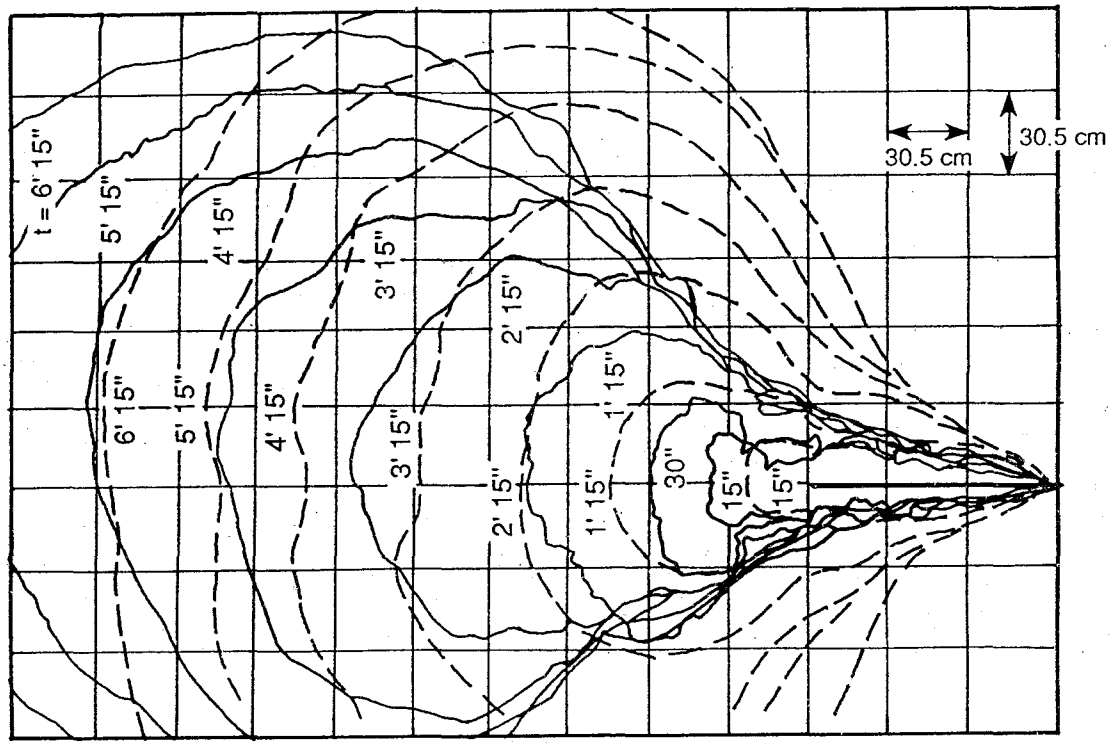

Figure 5.23 Comparison of tracings of plume boundaries at various times for $H = 4.0$ cm (experiment–1122scan) and $H = 8.0$ cm (experiment–1123scan).

5.4.3 Significance of the Discharge Flow Rate "Q_{T0}"

The distribution of $\Delta T/\Delta T_0$ along the diffuser axis in separate experiments with discharge rates 28.8 cm^3/s (experiment–0816cl) and 57.5 cm^3/s (experiment–0628cl) are compared in Figures 5.24a to 5.24c. The profiles agree reasonably well in the diffuser region, at least for the upper half of the water column. In the surface buoyant jet zone, the temperature curve for the 57.5 cm^3/s discharge has a different rate of decay from the 28.8 cm^3/s case; the temperature of the former case is lower near the surface but higher near the bottom. At certain levels (e.g., $0.69H$ and $0.56H$) the profiles collapse into one for most of the distance.

Figures 5.25a to 5.25d show that the plume of the larger Q_{T0} experiment extends to deeper levels and has a more uniform vertical distribution in the surface buoyant jet zone, even though there are little differences in the diffuser region. The increase in momentum flux (by four times) apparently induces a better mixed (vertically) downstream area, and the plume stays attached to the bottom (see contour map in Figure 5.26) even though the flow rate and buoyancy flux are each doubled. The width of the plume at a distance from the diffuser, however, does not necessarily become larger with increasing discharge rate because the extra momentum will drive the plume faster and also farther downstream before the gravitational process takes over. This is clearly illustrated in Figure 5.27 (constructed from measurements of scanning experiment–1122scn2), the isothermal map of surface $\Delta T/\Delta T_0$ for $Q_{T0} = 57.5$ cm^3/s, and Figure 5.28, the comparison of the plume boundaries at various time intervals for the two cases.

5.4.4 Significance of the Jet Diameter "D_0" and the Number of Nozzles "n"

A 4-port discharge system with $D_0 = 0.52$ cm is compared to the one with 16 ports ($D_0 = 0.52$ cm). The efflux from the individual jets of the former is therefore

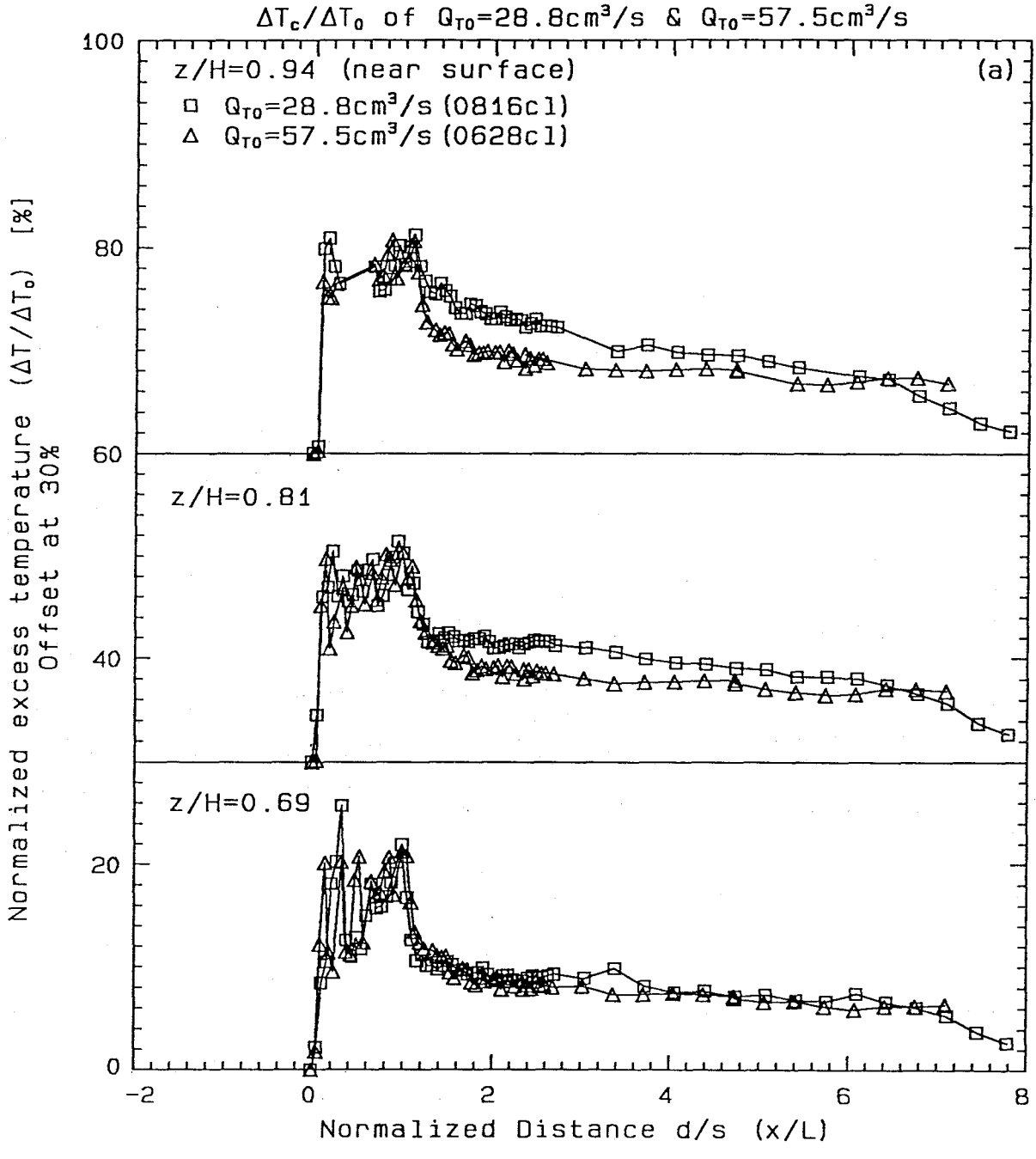

Figure 5.24a Comparison of longitudinal profiles of $\Delta T_c/\Delta T_0$ at near-surface levels for $Q_{T0} = 28.8\,\mathrm{cm}^3/\mathrm{s}$ (experiment–0816cl) and $Q_{T0} = 57.5\,\mathrm{cm}^3/\mathrm{s}$ (experiment–0628cl).

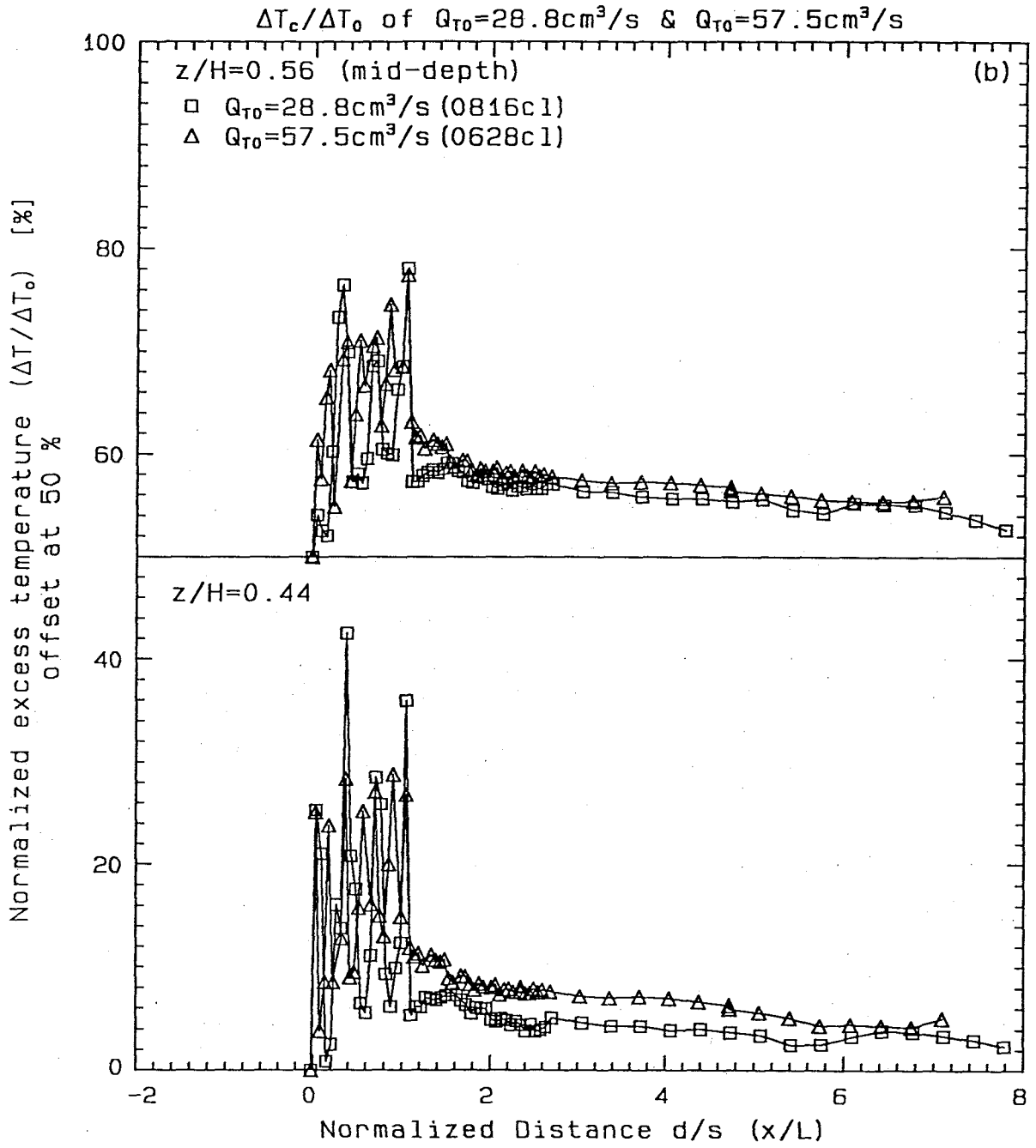

Figure 5.24b Comparison of longitudinal profiles of $\Delta T_c/\Delta T_0$ at midlevels for $Q_{T0} = 28.8$ cm^3/s (experiment–0816cl) and $Q_{T0} = 57.5$ cm^3/s (experiment–0628cl).

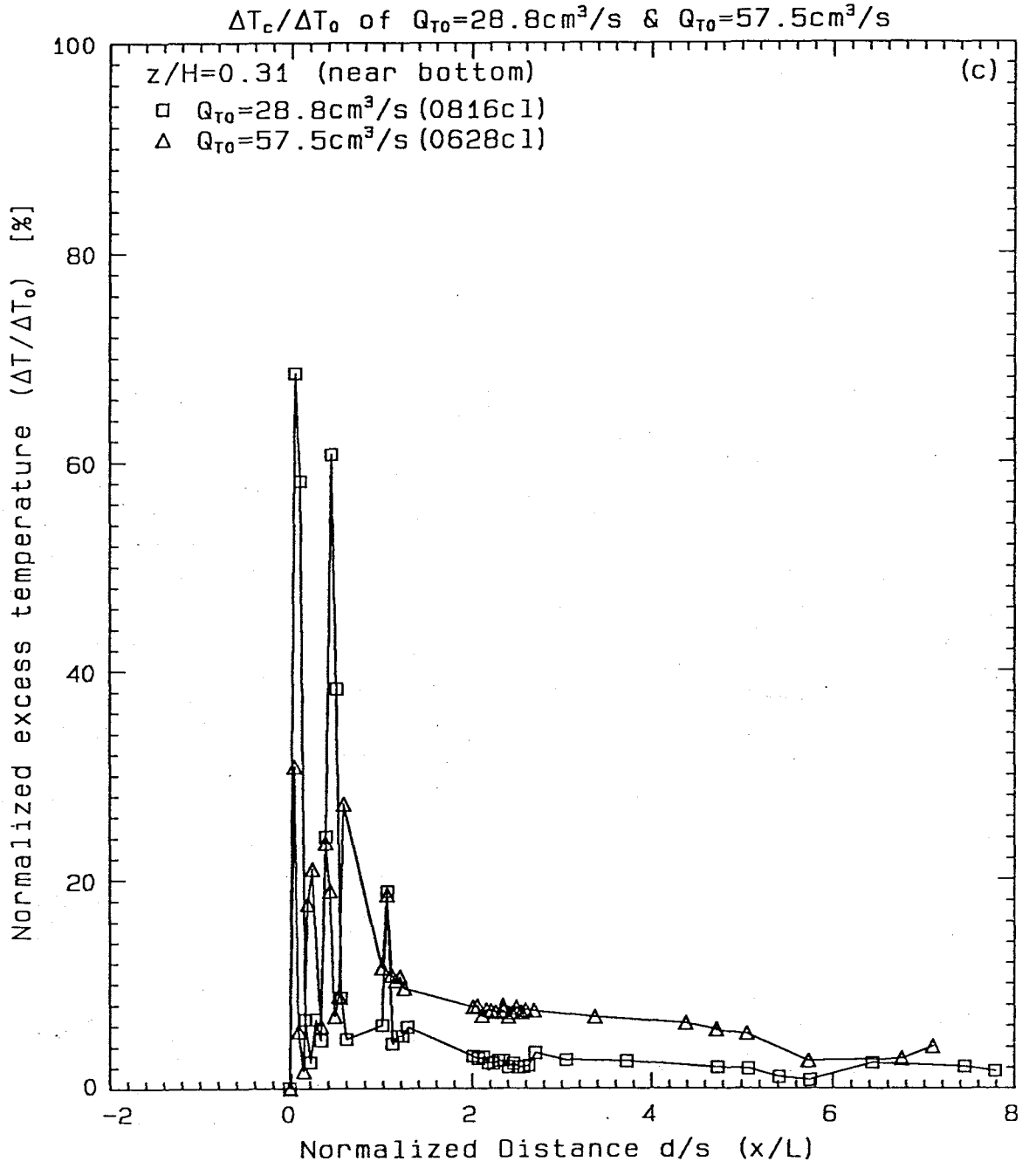

Figure 5.24c Comparison of longitudinal profiles of $\Delta T_c/\Delta T_0$ at bottom level for $Q_{T0} = 28.8\,\mathrm{cm}^3/\mathrm{s}$ (experiment–0816cl) and $Q_{T0} = 57.5\,\mathrm{cm}^3/\mathrm{s}$ (experiment–0628cl).

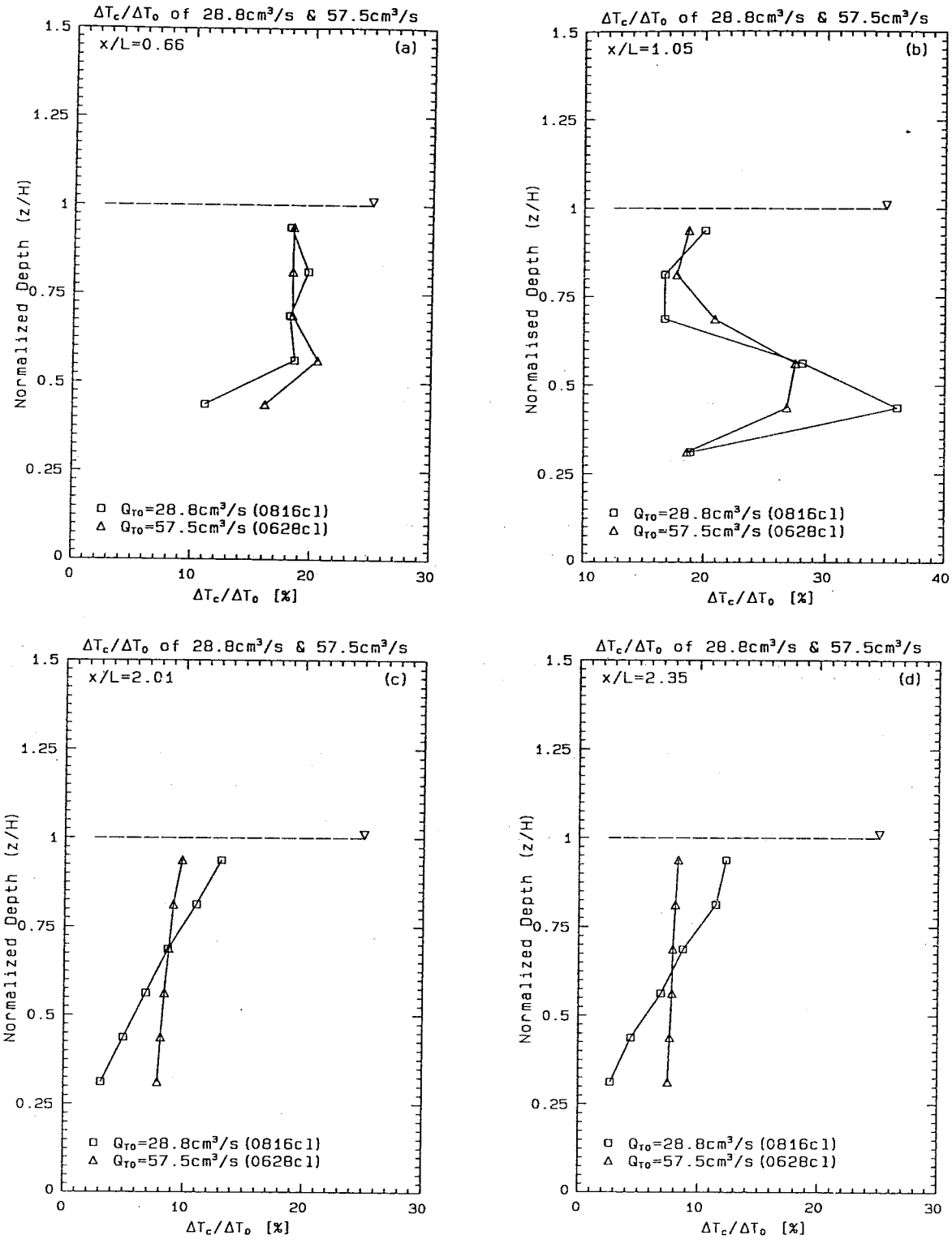

Figure 5.25 Comparison of vertical profiles of $\Delta T_c/\Delta T_0$ for $Q_{T0} = 28.8\ \mathrm{cm}^3/\mathrm{s}$ (experiment–0816cl) and $Q_{T0} = 57.5\ \mathrm{cm}^3/\mathrm{s}$ (experiment–0628cl). a) $x/L = 0.66$; b) $x/L = 1.05$; c) $x/L = 2.01$; d) $x/L = 2.35$.

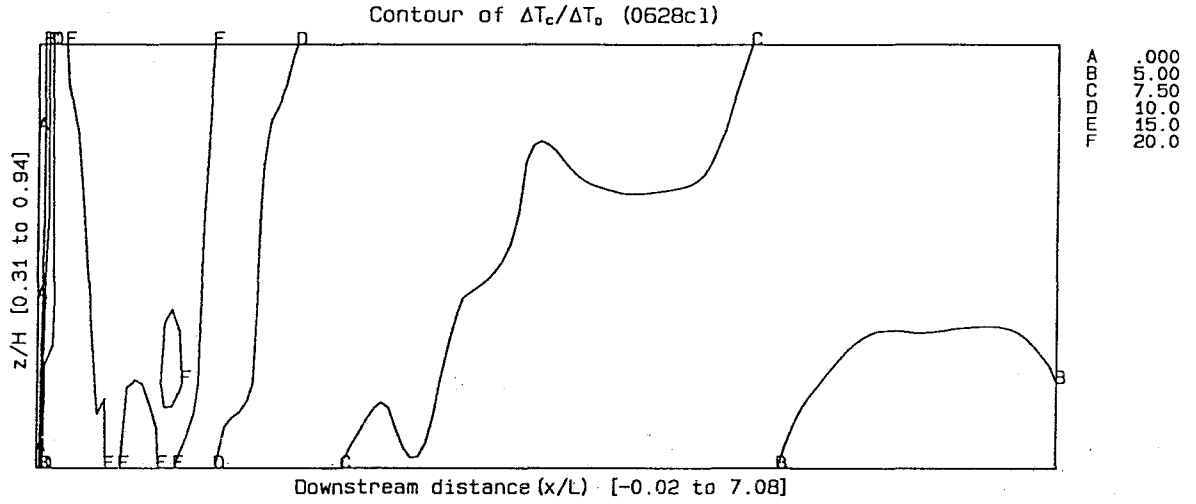

Figure 5.26 Contour map of $\Delta T_c/\Delta T_0$ in the vertical plane along the diffuser axis for $Q_{T0} = 57.5\ \mathrm{cm}^3/\mathrm{s}$ (experiment–0628cl). Vertical domain shown is $0.31 < z/H < 0.94$. Contour intervals are indicated by letter code (in %).

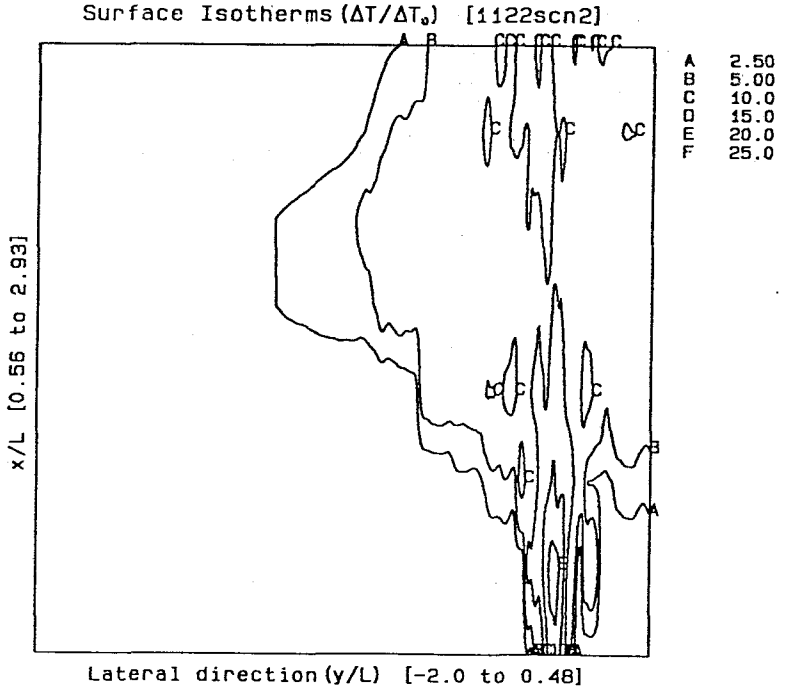

Figure 5.27 Contour map of near-surface $\Delta T/\Delta T_0$ for $Q_{T0} = 57.5\ \mathrm{cm}^3/\mathrm{s}$ (experiment–1122scn2). Contour intervals are indicated by letter code (in %).

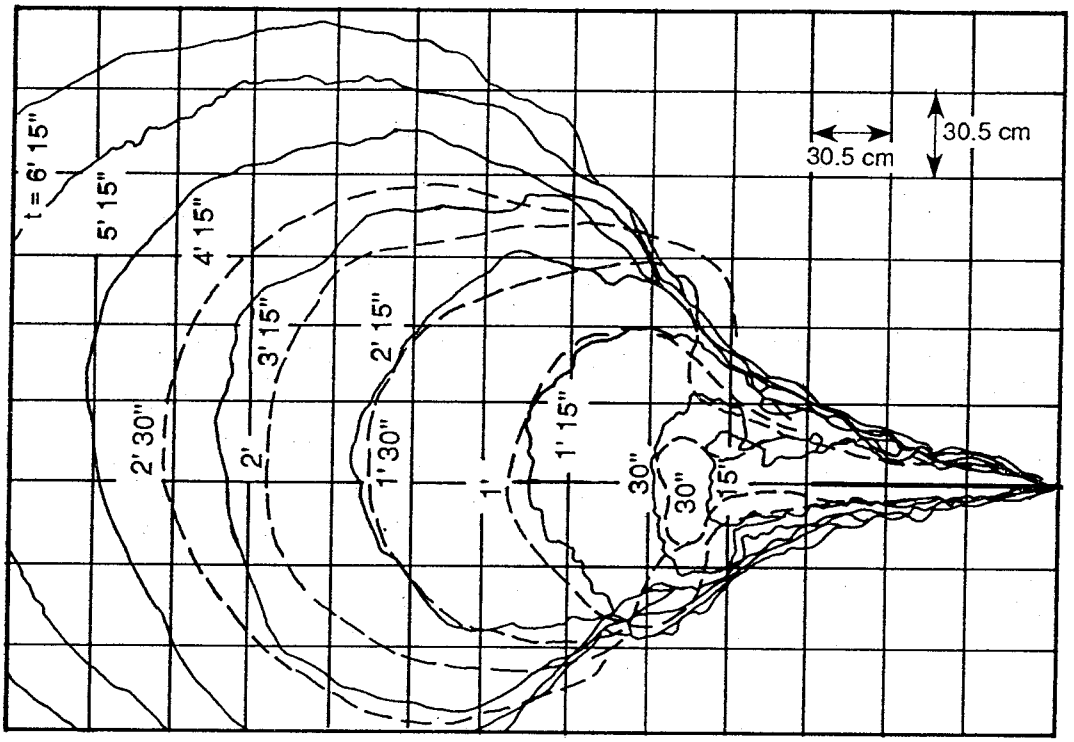

Figure 5.28 Comparison of tracings of plume boundaries at various times for $Q_{T0} = 28.8$ cm^3/s (experiment–1122scan) and $Q_{T0} = 57.5$ cm^3/s (experiment–1122scn2).

greater since the total discharge rate and momentum flux are the same in both cases. The spacing is kept the same, so the diffuser length for the 4-port system is reduced to $(n-1)s = 3s$ (instead of $15s$). Figures 5.29a to 5.29c show the longitudinal profiles of $\Delta T/\Delta T_0$ for the two cases (experiment–0922cl2 with $n = 4$ and experiment–0816cl with $n = 16$). The comparison is obscured because of the difference in the diffuser length (18.0 cm for $n = 4$ vs 90.0 cm for $n = 16$). For proper comparison, the downstream distance has to be normalized by a common length. The length of the long diffuser $L_{n=16}$, which is equivalent to 90.0 cm, is used as the common normalization factor, and $x/L = 0$ is referenced from the beginning of the diffuser. The peak $\Delta T/\Delta T_0$ is higher for the 4-port discharge than for the 16-port discharge. However, for the $n = 4$ case, the temperature in the region immediately after the diffuser zone declines much faster and the temperature excess remains lower for the rest of the downstream region. The deviation is less obvious in levels below $0.56H$ and minimal beyond the diffuser zone. The higher peak of $\Delta T/\Delta T_0$ in the $n = 4$ experiment can be explained by its larger ℓ_Q/H value. Furthermore, the faster drop of temperature excess in the surface buoyant jet zone reflects more dilution, which is probably caused by the higher residual momentum in the plume, even though the total initial momentum flux is the same for the two cases. This is because the discharge momentum flux per jet is four times smaller in the 16-port diffuser and the jets are distributed over a longer distance (five times compared to the 4-port case). The residual momentum from the jets near the beginning of the long diffuser has more or less dissipated by the time the plume reaches the intermediate-field region.

The higher momentum also induces a more uniform water column compared to the $n = 16$ experiment. Figure 5.30 shows the isothermal contours of $\Delta T/\Delta T_0$ along the diffuser axis of the 4-port discharge. After the diffuser zone, which is characterized by steep and intensive contours similar to the 16-port case, the 5.0% contour remains close to the bottom for some distance before it starts to rise to the surface. This is an

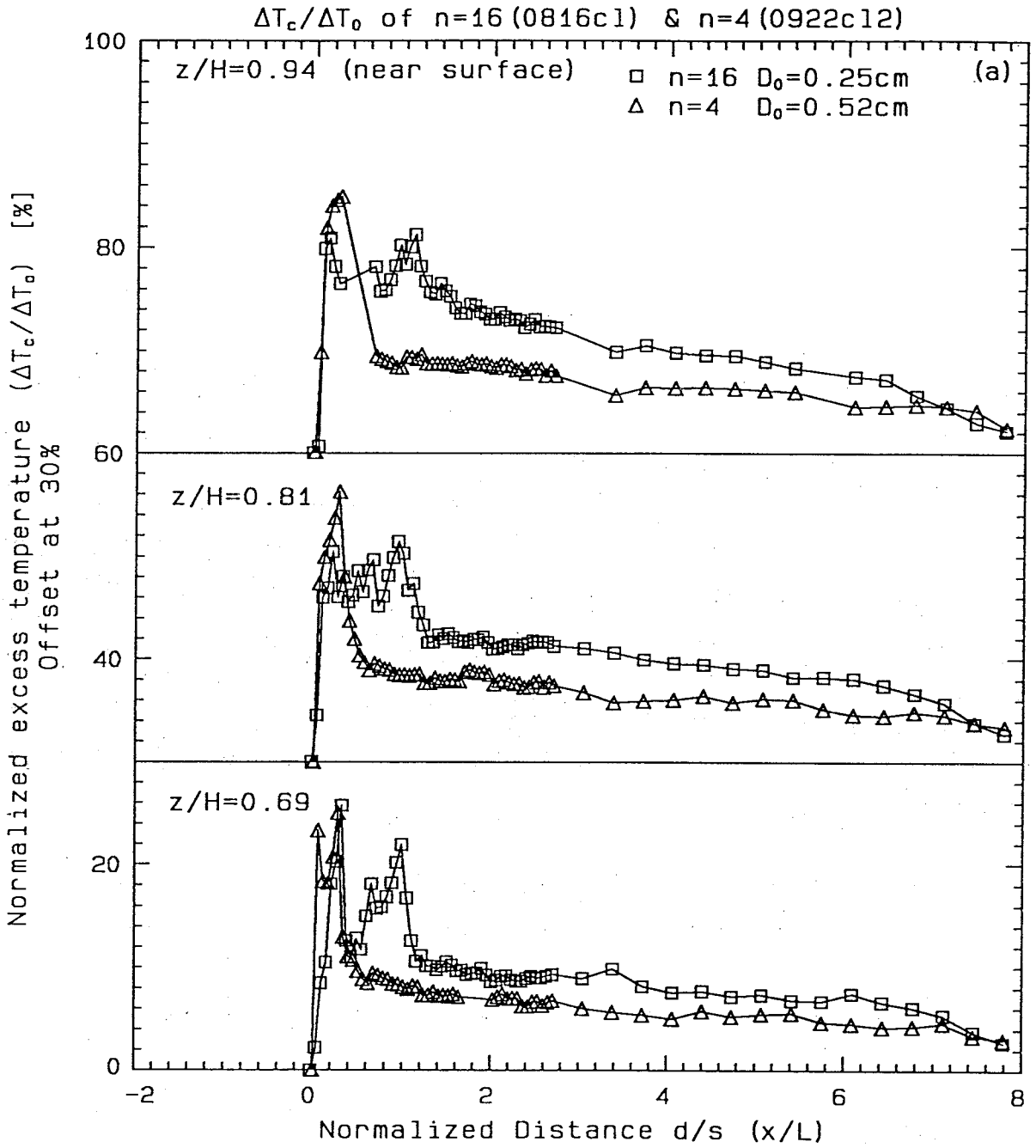

Figure 5.29a Comparison of longitudinal profiles of $\Delta T_c/\Delta T_0$ at near-surface levels for $n = 16$ (experiment–0816cl) and $n = 4$ (experiment–0922cl2). ($x/L = 0$ at beginning of diffuser and $L = 90$ cm is used as the normalizing factor for both cases.)

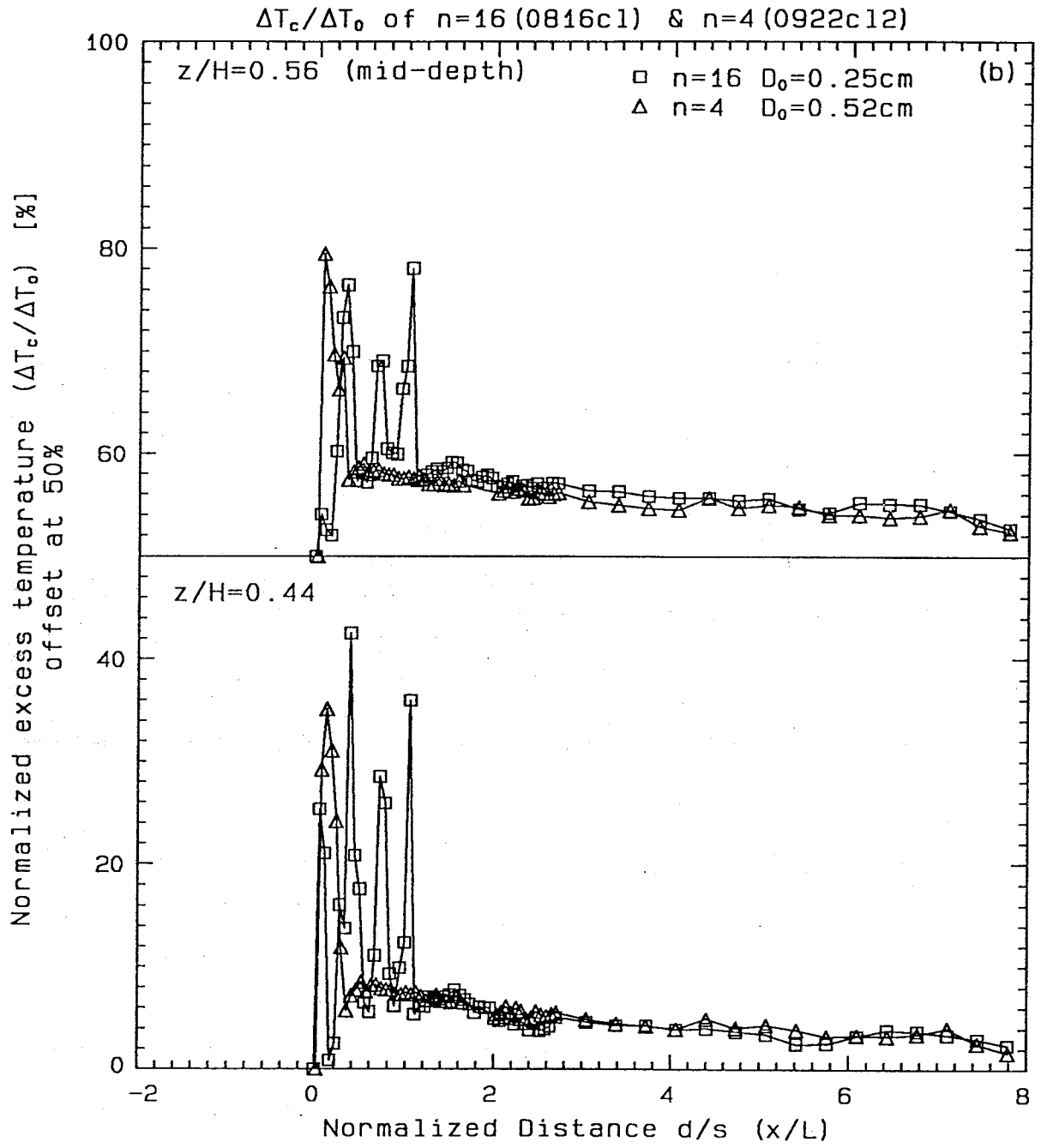

Figure 5.29b Comparison of longitudinal profiles of $\Delta T_c/\Delta T_0$ at midlevels for $n = 16$ (experiment–0816cl) and $n = 4$ (experiment–0922cl2). ($x/L = 0$ at beginning of diffuser and $L = 90$ cm is used as the normalizing factor for both cases.)

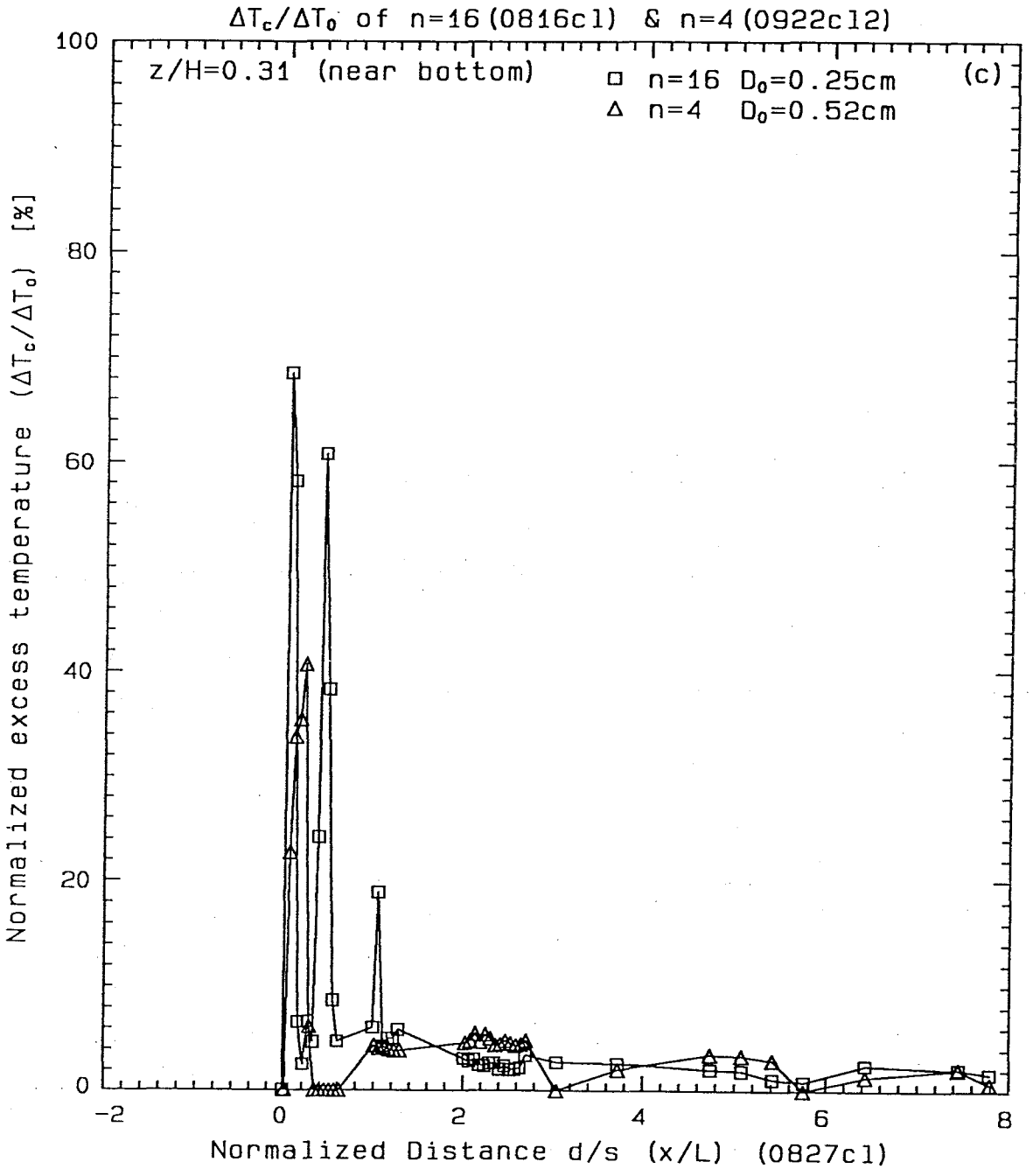

Figure 5.29c Comparison of longitudinal profiles of $\Delta T_c/\Delta T_0$ at bottom level for $n = 16$ (experiment–0816cl) and $n = 4$ (experiment–0922cl2). ($x/L = 0$ at beginning of diffuser and $L = 90$ cm is used as the normalizing factor for both cases.)

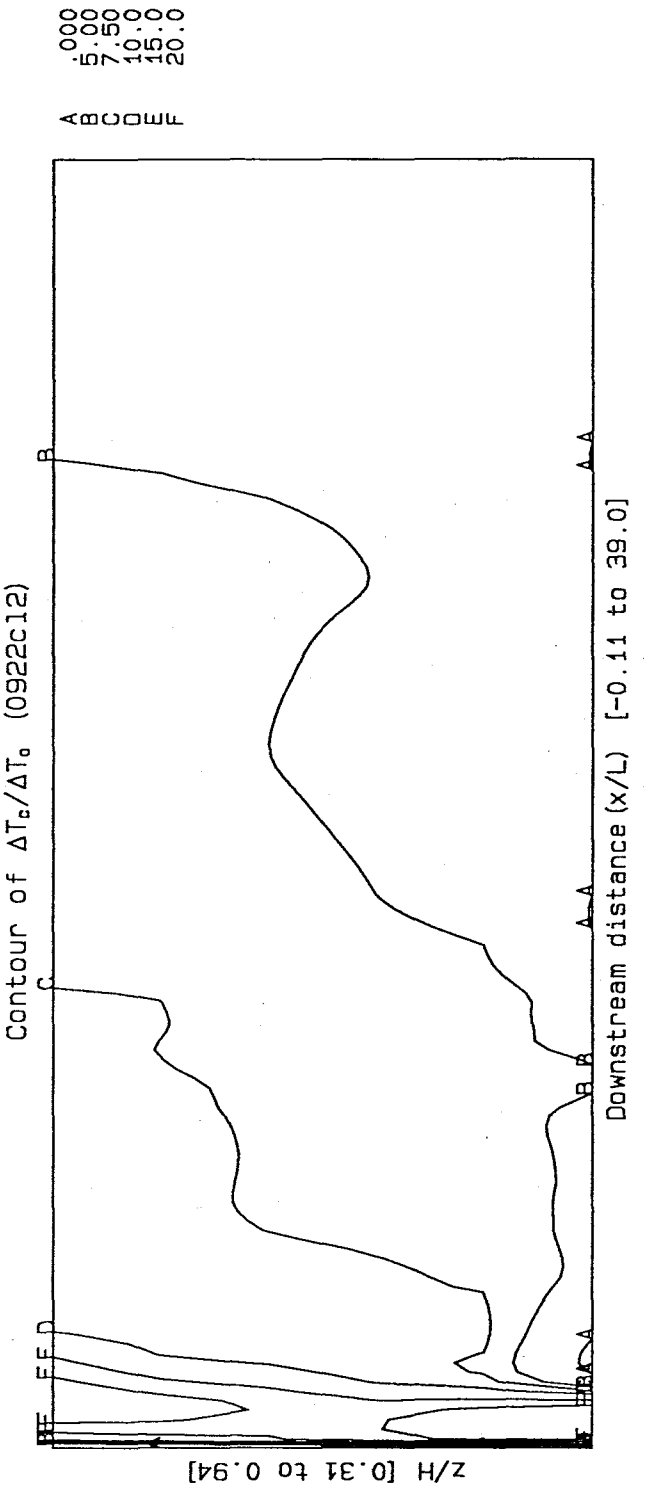

Figure 5.30 Contour map of $\Delta T_c/\Delta T_0$ in the vertical plane along the diffuser axis for $n = 4$ (experiment–0922cl2). $L = 18$ cm is used as the normalizing factor. Vertical domain shown is $0.31 < z/H < 0.94$. Contour intervals are indicated by letter code (in %).

indication of a vertically mixed plume, which eventually stratifies farther downstream, with the dissipation of the destabilizing momentum.

An additional experiment using a single-port discharge with a jet diameter of 1.03 cm was performed with the same momentum flux and discharge. The temperature distributions at near-surface, mid-depth, and near-bottom levels from all three experiments ($n = 1$ (experiment–1101cl), $n = 4$ (experiment–0922cl2) and $n = 16$ (experiment–0816cl)) are compared in Figures 5.31a and 5.31b; the downstream distance is referenced from the middle of the respective diffuser. For the single-port case, the midpoint is considered to be the position of the jet itself. The downstream distance for all cases is normalized by the length of the 16-port diffuser, $L_{n=16} = 90.0$ cm as in the previous comparison figures for $n = 4$ and $n = 16$ experiments. The peak $\Delta T/\Delta T_0$ definitely increases with a decreasing number of ports. The profiles of the single-port and 4-port cases agree very well at the upper levels (surface to $0.56H$), while the profile of the 16-port case has higher values near the surface, but coincides with the other two curves at level $0.56L$. At the bottom level, the single-jet case in turn has the highest $\Delta T/\Delta T_0$. The same profiles are shown again in Figures 5.32a and 5.32b, with the reference point moved to the end of the diffuser; for the case of $n = 1$, the end of the diffuser is defined as the position of the jet itself. Similar conclusions can be drawn from the comparison.

5.5 Key Results

From the discussion above, it is evident that the results of each experiment describe plume behaviors pertaining only to the specific testing conditions. A systematic method of treatment is therefore required to unify the results from all the experiments and to provide key representations of the thermal structure under various circumstances. Among the large volume of test results, some have more practical

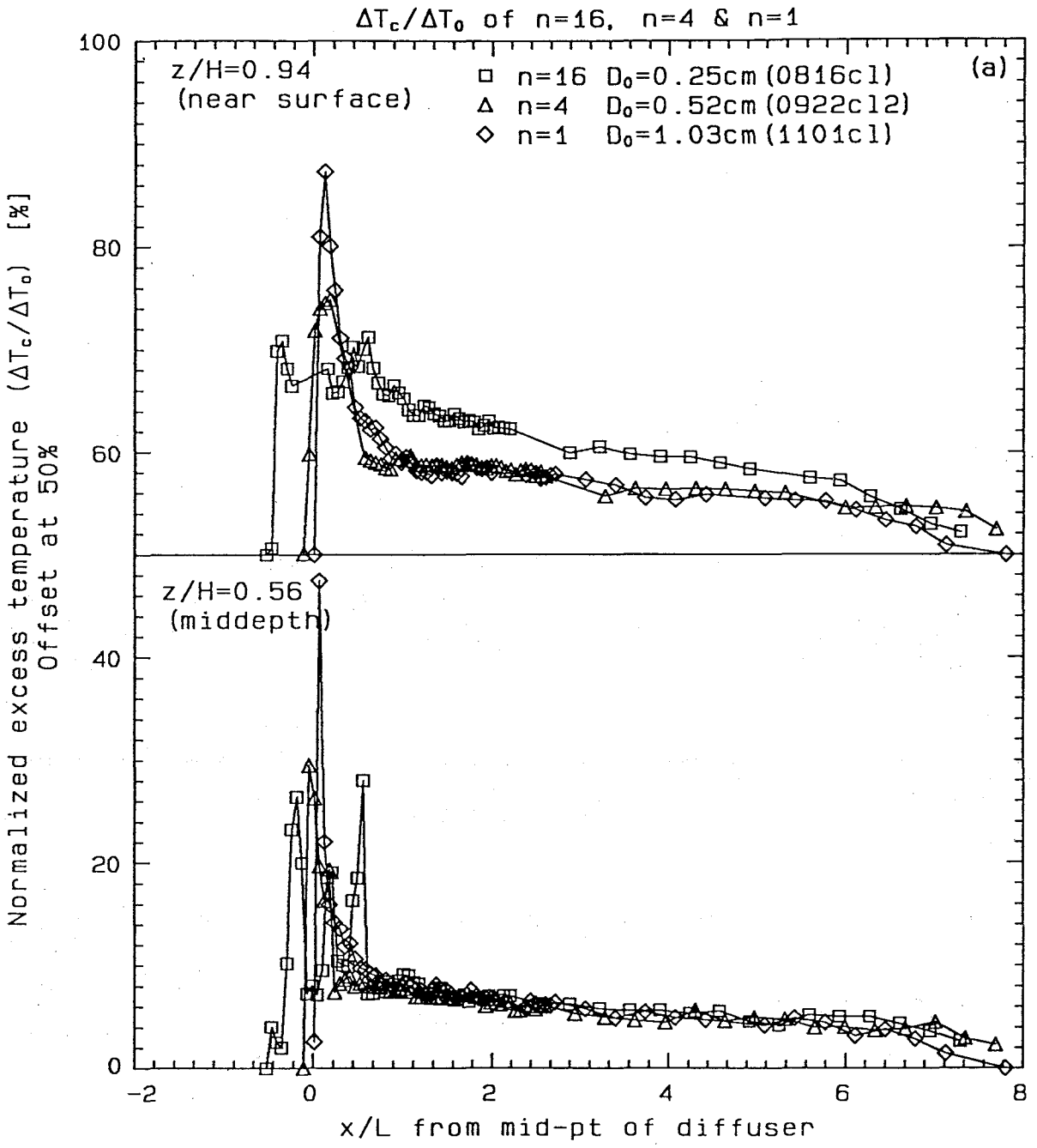

Figure 5.31a Comparison of longitudinal profiles of $\Delta T_c/\Delta T_0$ at near-surface and midlevels for $n = 16$ (experiment–0816cl), $n = 4$ (experiment–0922cl2) and $n = 1$ (experiment–1101cl). x/L is referenced from the midpoint and $L = 90$ cm is used as the normalizing factor for all cases.

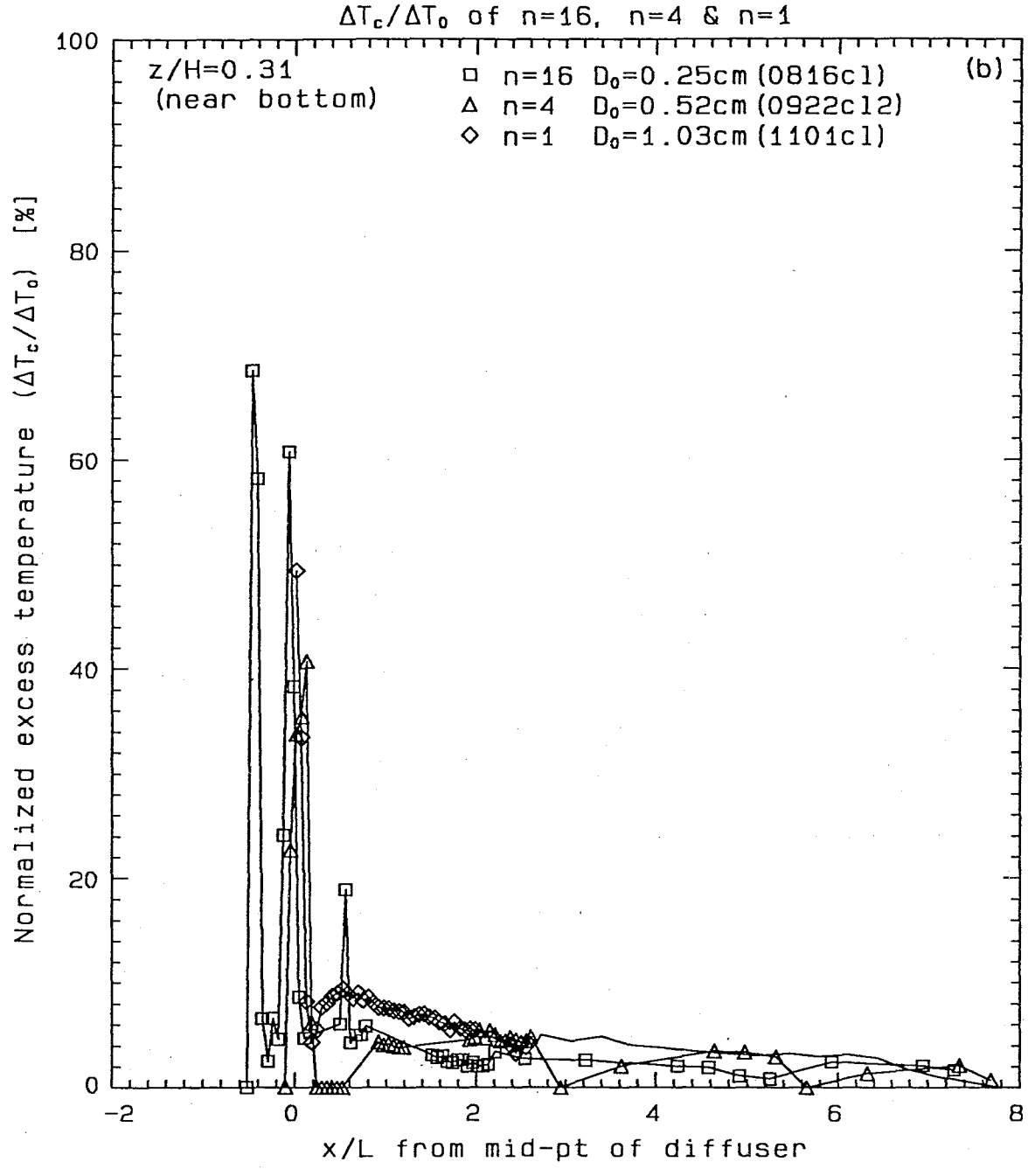

Figure 5.31b Comparison of longitudinal profiles of $\Delta T_c/\Delta T_0$ at bottom level for $n = 16$ (experiment–0816cl), $n = 4$ (experiment–0922cl2) and $n = 1$ (experiment–1101cl). x/L is referenced from the midpoint and $L = 90$ cm is used as the normalizing factor for all cases.

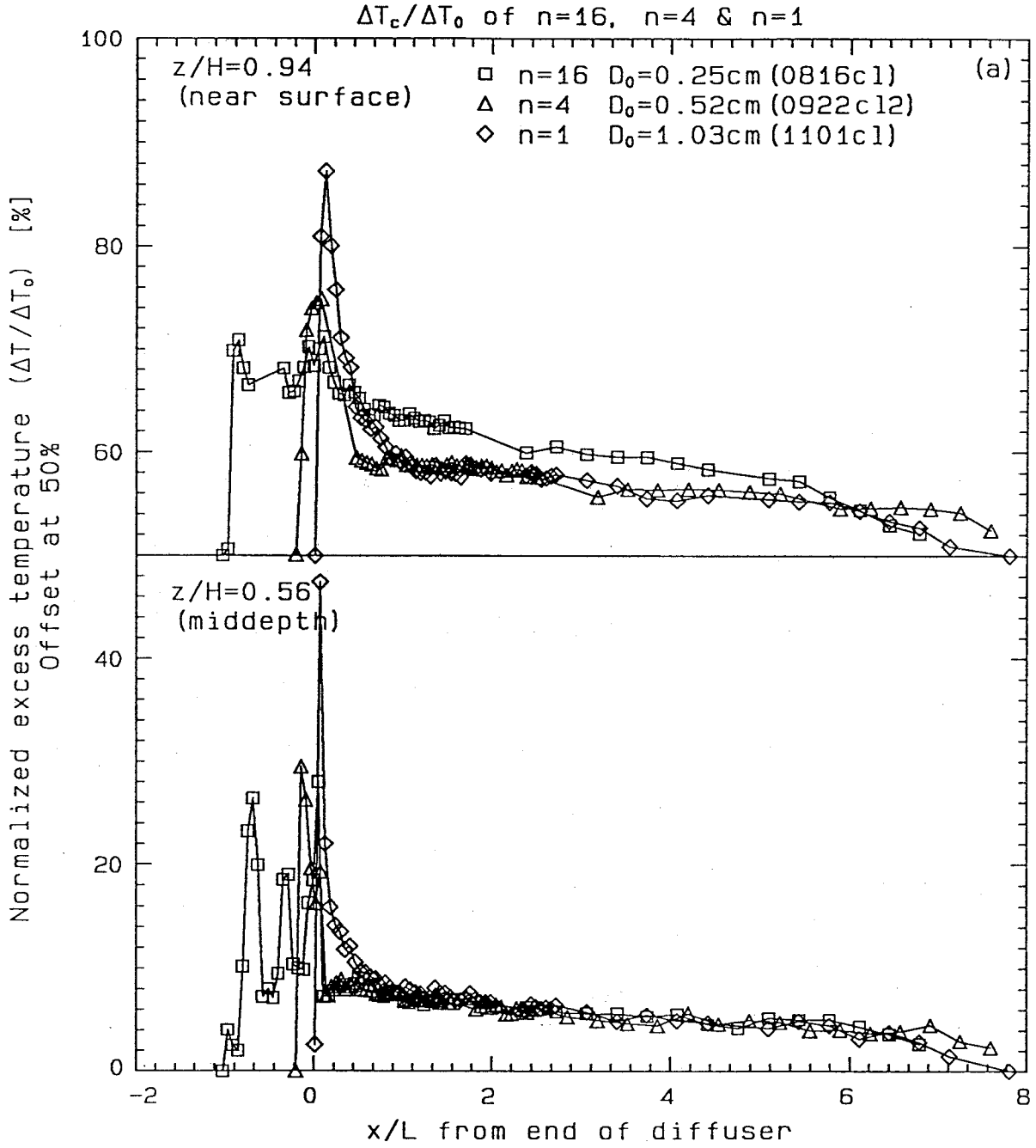

Figure 5.32a Comparison of longitudinal profiles of $\Delta T_c/\Delta T_0$ at near-surface and midlevels for $n = 16$ (experiment–0816cl), $n = 4$ (experiment–0922cl2) and $n = 1$ (experiment–1101cl). x/L is referenced from the end of diffuser and $L = 90$ cm is used as the normalizing factor for all cases.

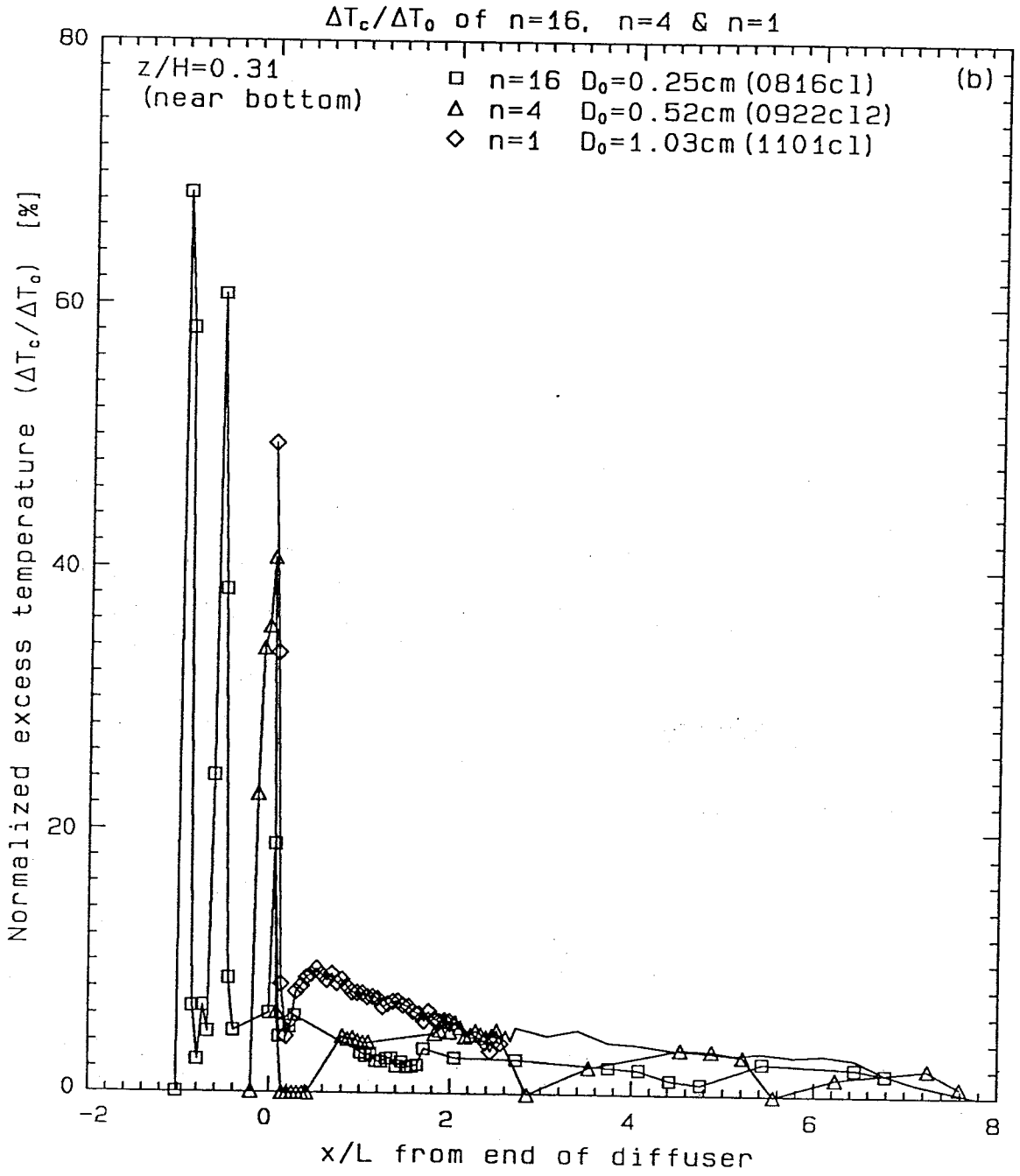

Figure 5.32b Comparison of longitudinal profiles of $\Delta T_c/\Delta T_0$ at bottom level for $n = 16$ (experiment–0816cl), $n = 4$ (experiment–0922cl2) and $n = 1$ (experiment–1101cl). x/L is referenced from the end of diffuser and $L = 90$ cm is used as the normalizing factor for all cases.

interest, while others are crucial in understanding the underlying physics concerning mixing in diffuser discharges. Referred to as the **key results**, these critical quantities are identified for each set of experimental results and are used for model comparison, verification of hypotheses and development of empirical relationships. These results, together with the corresponding experimental conditions, are presented in tables in Appendix D. Details are analyzed and discussed in Chapter 6.

A total of 27 key results are chosen as defined in Figure 5.33 and below. In the following, "surface" is defined as the level at 0.25 cm below the mean water surface; "bottom" is defined as the level at the centerline of the nozzles; and "end of the diffuser zone" is defined as the longitudinal position at which the last jet in the diffuser reaches the water surface. This corresponds to $x \approx 90 + (H/\tan\beta)$ (cm) for $n = 16$; $x \approx 18 + (H/\tan\beta)$ (cm) for $n = 4$; and $x \approx H/\tan\beta$ (cm) for $n = 1$.

(i) Near field

- T_{peak}—peak surface $\Delta T/\Delta T_0$ along diffuser axis
  (from centerline experiments)
- ϵ—lateral growth rate of total plume width at surface
  (from time lapse photographs)
- T_{s1}—centerline surface $\Delta T/\Delta T_0$ at end of the diffuser zone
  (from centerline experiments)
- T_{b1}—centerline bottom $\Delta T/\Delta T_0$ at end of the diffuser zone
  (from centerline experiments)
- h_1—thickness of the surface layer at end of the diffuser zone, defined as the depth from surface to $\Delta T/\Delta T_0 = T_{b1} + e^{-1}(T_{s1} - T_{b1})$
  (from centerline experiments)
- b_1—width of plume at end of the diffuser zone, taken as the total width of the surface temperature profiles with $\Delta T/\Delta T_0 \geq e^{-1}T_{s1}$
  (from scanning experiments)

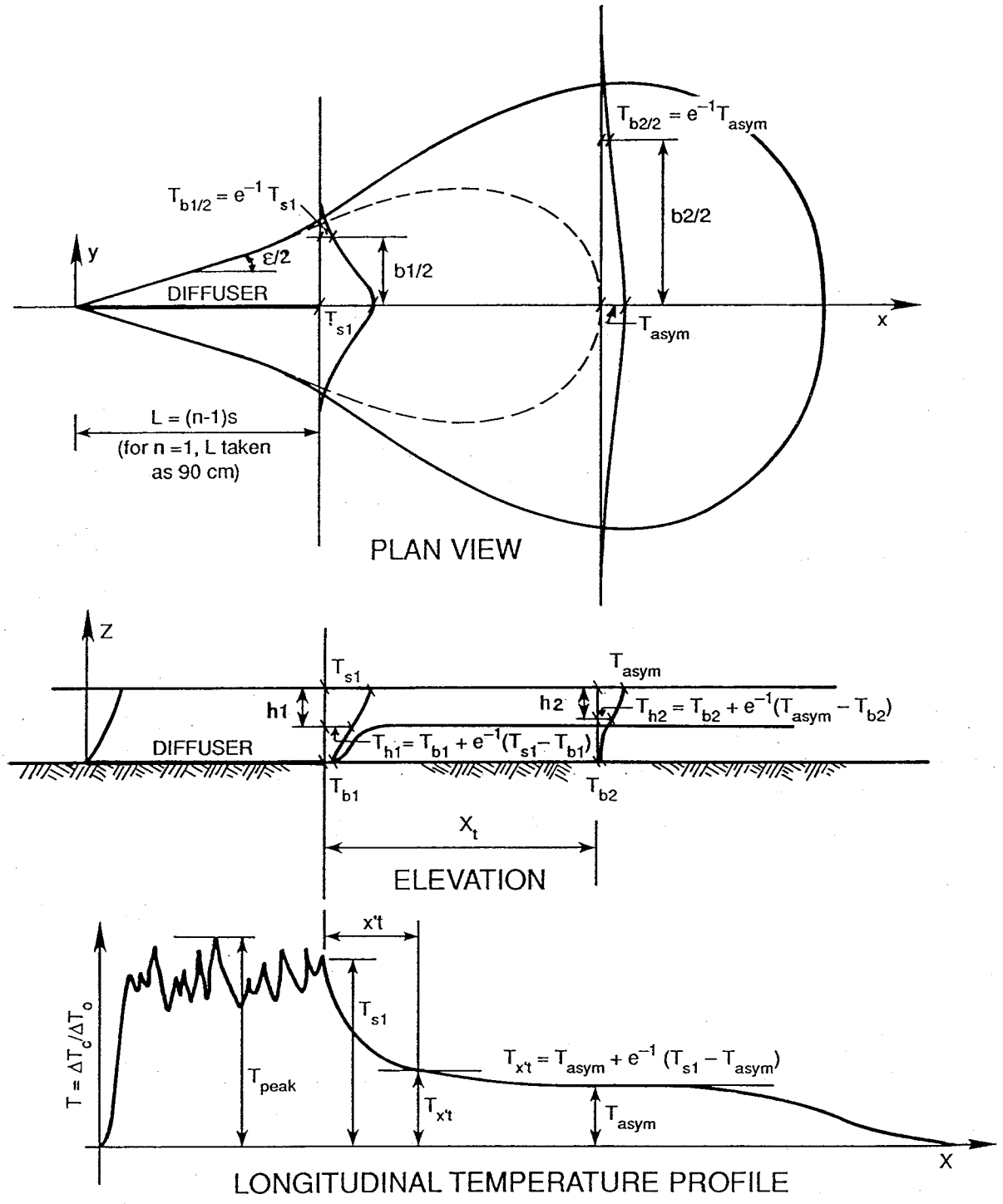

Figure 5.33 Definition diagram of the **key results** in homogeneous experiments. For the case of only one jet ($n = 1$), L is arbitrarily taken as 90 cm.

(ii) Intermediate field—surface buoyant jet zone

- T_{asym}—asymptotic value of surface $\Delta T/\Delta T_0$ beyond surface buoyant jet zone
  (from centerline experiments)
- T_{b2}—the bottom $\Delta T/\Delta T_0$ corresponding to T_{asym}
  (from centerline experiments)
- x_t—the "transition distance" from end of the near field to the corresponding longitudinal position of T_{asym}
  (from centerline experiments)
- b_2—the total plume width at x_t
  (from scanning experiments)
- h_2—the thickness of the surface layer at x_t
  (from centerline experiments)

(iii) Intermediate field—gravitational spreading zone

- V_t—propagation velocity of the center of the radially spreading plume
  (from time lapse photographs)

(iv) Overall

- T_{kL}—surface $\Delta T/\Delta T_0$ along diffuser axis at kL downstream of end of diffuser, for $k = 1/2, 1, 2, 4$. The length L is taken as the diffuser length for the 16-port experiments (90.0 cm = 15 spacings) and for the 4-port experiments (18.0 cm = 3 spacings). For the single-jet experiments the length L was arbitrarily taken as 90.0 cm for data presentation.
  (from centerline experiments)

- T_{mH}—surface $\Delta T/\Delta T_0$ along diffuser axis at mH downstream of end of diffuser for m = 4, 8, 16, 32, 64, 128
  (from centerline experiments)
- $x_{0.1}$—distance downstream from end of diffuser with $\Delta T/\Delta T_0 \geq 10\%$
  (from centerline experiments)
- $x_{0.2}$—distance downstream from end of diffuser with $\Delta T/\Delta T_0 \geq 20\%$
  (from centerline experiments)
- $A_{0.1}$—surface area with $\Delta T/\Delta T_0 \geq 10\%$
  (from scanning experiments)
- $A_{0.2}$—surface area with $\Delta T/\Delta T_0 \geq 20\%$
  (from scanning experiments)

The key results for the two experiments (0816cl and 1122scan) are summarized in Table 5.5; for experimental input variables, see Table 5.4 or Tables D.1a and D.1b. The complete listing for the 91 experiments (55 centerline experiments and 36 scanning experiments) is presented in Appendix D. These results will be discussed in Chapter 6.

5.6 Further Notes on Jet Diameter

After the completion of the data analysis and the preparation of the thesis, a further confirmation of the jet diameters was undertaken. The jet diameters (D_0) reported in Table 5.3 were based on visual measurements of the contracted jets discharging in air using a calipers and a micrometer. These values were used throughout the thesis and in the analyses.

The confirming tests were made by measuring the flow rate Q discharging in air from a single straight nozzle (orifice diameter D_0') with a head of water E_T (depth of water above the center level of the orifice) in the supply tank. The discharge

Table 5.5 Summary of the key results of experiments 0816cl and 1122scan ($L = 90$ cm, $H = 4$ cm; input variables given in Table 5.4).

Key Results	Values
T_{peak}[%]	21.2
ϵ	0.52
T_{s1}[%]	21.0
T_{b1} [%]	4.3
h_1[H]	0.33
b_1 [L]	0.51
T_{asym} [%]	13.0
T_{b2}[%]	3.0
b_2 [L]	0.60
h_2 [H]	0.35
x_t [L]	1.01
V_t [cm/s]	0.48
$T_{L/2}$ [%]	15.0
T_L [%]	13.5
T_{2L} [%]	11.0
T_{4L} [%]	9.0
T_{4H} [%]	18.0
T_{8H} [%]	15.8
T_{16H} [%]	14.0
T_{32H} [%]	13.0
T_{64H} [%]	10.3
$x_{0.1}$ [L]	2.33
$x_{0.2}$ [L]	0.12
$A_{0.1}$ [L^2]	2.81
$A_{0.2}$ [L^2]	0.08

coefficient C_D can be calculated according to:

$$C_D = \frac{Q}{(\pi D_0'^2/4)\sqrt{2gE_T}} \,. \tag{5.2}$$

Jet diameters can therefore be estimated from the observed discharge coefficient since the coefficient of contraction $C_c=(D_0/D_0')^2$ is related to C_D by:

$$\frac{1}{C_c^2} = \frac{1}{C_D^2} - K_e(\frac{D_0'}{d})^4 \,, \tag{5.3}$$

where K_e is the entrance loss coefficient to the short nozzle (1.06 cm diameter) ahead of the orifice and d is the diameter of the pipe. The calculations of C_D and C_c have been carried out for the three orifices with diameters of 0.335 cm, 0.559 cm and 1.014 cm. The estimated contracted jet diameters are 0.28 cm, 0.47 cm and 1.01 cm, respectively, corresponding to calculated contraction coefficients of 0.69, 0.69 and 1.00 for the three orifice sizes. (A value of 0.4 is used for K_e in all cases.)

Although the jet diameters determined by these two methods agreed within a few hundredths of a centimeter, the calculated values of ℓ_Q and ℓ_M would differ by up to 10% and 15%, respectively. However, these differences are within the range of other uncertainties and are believed not to change the conclusions.

6. Discussion of Experimental Results

6.1 Introduction

The overall behavior of the thermal plume observed in this study has been described in Chapter 5. This chapter will examine in detail the changes in plume behavior by varying source and ambient parameters. Attention is focused on the more important characteristics such as the minimum initial dilution and the asymptotic dilution beyond the diffuser region. Controlling parameters in the near- and intermediate-flow regimes will be identified, and they will be used to devise a systematic way to summarize and describe the important plume behaviors.

The results of the present study will be compared with those from previous laboratory studies and with predictions from existing mathematical models. Comparison with the thermistor chain field data collected for SONGS is also included. The possibility of extrapolating the obtained set of experimental results to a wider range of discharge and ambient conditions will be examined. The definitions of the key results of the near field and intermediate field are given in Figure 5.33.

6.2 The Near Field

The longitudinal temperature profiles along the diffuser axis at near-surface level will be discussed first by comparing with predictions from mathematical models. Other near-field key results to be examined include the peak surface-temperature increases (T_{peak}), the lateral growth rate of the total width of the plume (ϵ), the width of the plume (b_1) and the thickness of the surface buoyant layer at the end of the diffuser zone (h_1).

6.2.1 Near-surface Temperature Increase along the Diffuser Axis ($\Delta T_c(x)/\Delta T_0$)

The mathematical models proposed by both Jirka (1982) and Almquist and Stolzenbach (1980) give predictions of the temperature increase along the centerline of a diffuser in the near-field region. The models are based on the equivalent slot diffuser concept and the integral technique, and are reviewed in Chapter 2. The governing parameter in both theories is K, which is equivalent to $\sqrt{4HL/n\pi D_0^2}$ in Jirka's model, where H is the depth above nozzle centerline. In Almquist and Stolzenbach's model, K is defined as $\sqrt{(4HL\cos\alpha\cos\beta)/n\pi D_0^2}$. For $\alpha = \beta = 0°$, this gives the same value as Jirka's definition of K. An asymptotic dilution has been formulated in the two mathematical models and will be compared with the present experimental results as well as with other laboratory results described in Section 6.2.5. In the following set of Figures 6.1a through 6.1f and 6.2a through 6.2f, the Figure 6.1 graphs are at the top of the pages while the Figure 6.2 graphs are on the bottom to facilitate model comparison for the same data sets.

Figure 6.1a shows the comparison of the surface $\Delta T_c(x)/\Delta T_0$ profiles in the diffuser region of the present study with Jirka's model ($\Delta T_c(x)$ = centerline excess temperature). The extent of agreement between the laboratory data and the model

varies with testing conditions. While Jirka's model predicts a universal profile (of the temperature excess multiplied by K versus the longitudinal distance normalized by x_ν, the virtual source distance, which is taken as $7.5H$), the experimental results spread over a range of values. The profiles are truncated at the end of the diffuser. Profiles from experiments of the same ℓ_Q and H, however, agree closely. (The variable ℓ_Q is defined as $Q_{i0}/\sqrt{M_{i0}}$ and is equivalent to $\sqrt{A_0}$ or $\sqrt{\pi/4}D_0$; for diffusers of equal volume and momentum fluxes, $D_0\sqrt{n}$ is a constant, thus giving $D_0 \sim 1/\sqrt{n}$.) This indicates that ℓ_Q/H is a potentially important parameter in the near field, supporting the argument of the simple jet hypothesis.

The discrepancy between the prediction and the measurements can be partly explained by the model assumptions, which include a vertically-mixed flow field and the slot jet approach. Furthermore, the diffuser configuration for the model development differs from that for the experiments; the former is composed of a series of jets discharging horizontally (i.e., $\beta = 0°$), while the latter has jets discharging at an upward angle of $\beta = 25°$. The figure is based on $x_\nu = 7.5H$ as specified by Jirka; however, if x_ν is adjusted to smaller values (being expected because of the upward jet angle), then the measured profiles would have been stretched out to higher values of x/x_ν.

Figure 6.1b shows the comparison of Jirka's model with the result of the hydraulic model study of the SONGS diffusers (Koh et al. 1974). It presents a very good agreement with the model, although the diffuser configuration is similiar to that of the experiments of the present study for which $\alpha = \pm 25°$ (horizontal angle of the jets from the diffuser axis).

Figures 6.1c through 6.1f are similiar comparisons of the results from the various laboratory studies with Jirka's prediction. The agreement between predictions and measurements varies with different experiments, but is not particularly satisfactory.

Among the laboratory results, Jirka's prediction has the best agreement with the SONGS study, the Somerset study, and the Charlestown study. In general, Jirka's model describes reasonably well the overall trend of increasing temperature along the diffuser.

Subsequent comparisons are made between the laboratory results and the model of Almquist and Stolzenbach (1980), as shown in Figures 6.2a to 6.2f. The mathematical model proposed a universal curve for the volumetric dilution S (modified after $(S-1)(\gamma^{1/2}K)^{-1}$, where γ is an entrainment coefficient taken as 0.2; K is the diffuser parameter as defined in Section 6.2.1) along the diffuser axis, which is different from the centerline initial dilution obtained in experiments. Hence, for the purpose of comparison, the mathematical model is adjusted to give an equivalent centerline dilution S_c in terms of the flux-averaged dilution S by the relation:

$$S_c = (\frac{\lambda^2}{1+\lambda^2})^{1/2} S \,, \tag{6.1}$$

where λ is the spreading ratio of heat versus momentum and self-similar Gaussian profiles for the lateral temperature and velocity distributions are assumed. The centerline dilution for the experimental results is defined as the reciprocal of $\Delta T_c/\Delta T_0$.

In all cases, Almquist and Stolzenbach's theory does not predict accurately the dilution for the beginning portion of the diffuser region. As in the case of Jirka's theory, this model is developed for horizontally discharged jets parallel to the diffuser axis. There is a transition distance (approximately $7.5H$ from the beginning of the diffuser as proposed by the model), where the thermal plume has not yet reached the surface. The predicted dilution is depth-averaged, whereas the measurements are obtained at near-surface level, resulting in a large discrepancy within the transition distance. More realistic predictions are obtained at considerable distance downstream (but still within the diffuser region), where the plume has more fully developed over the depth.

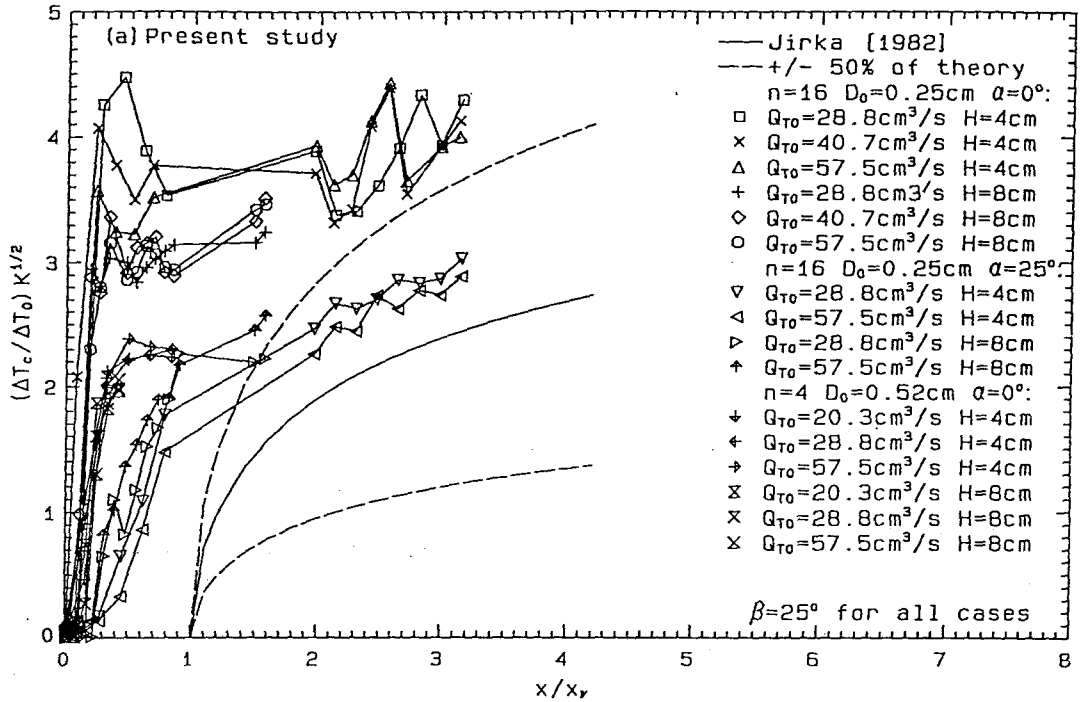

Figure 6.1a Comparison of measured longitudinal profiles of temperature increase with Jirka's model for the near field—the present study.

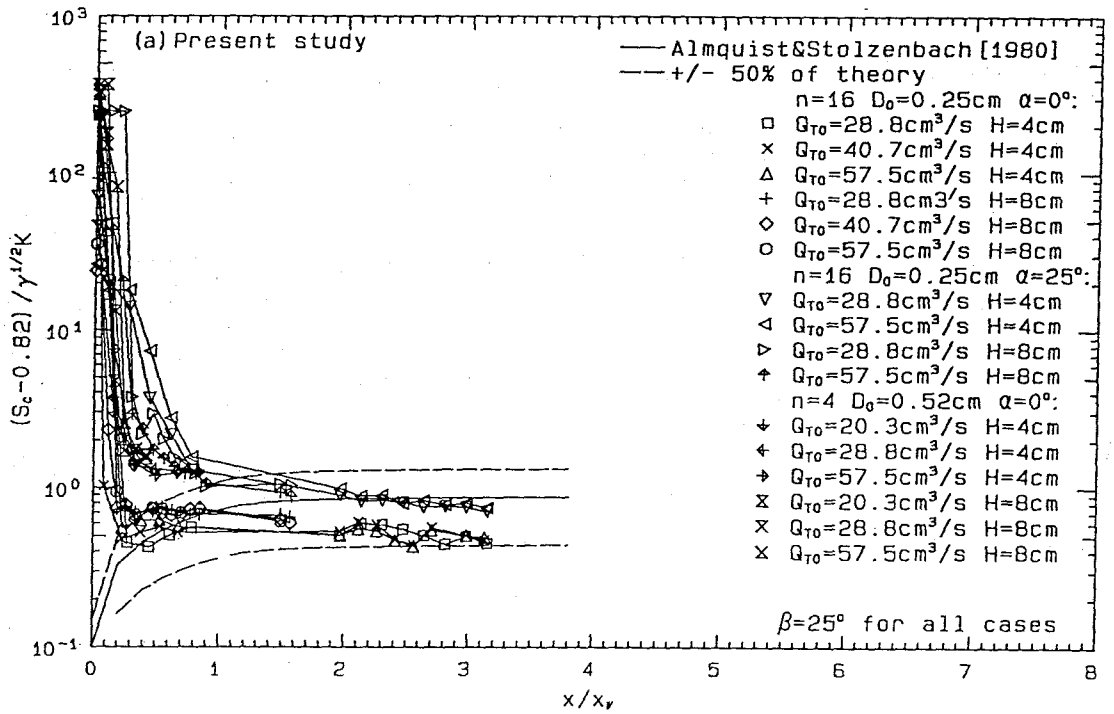

Figure 6.2a Comparison of measured longitudinal profiles of dilution with Almquist and Stolzenbach's model for the near field—the present study.

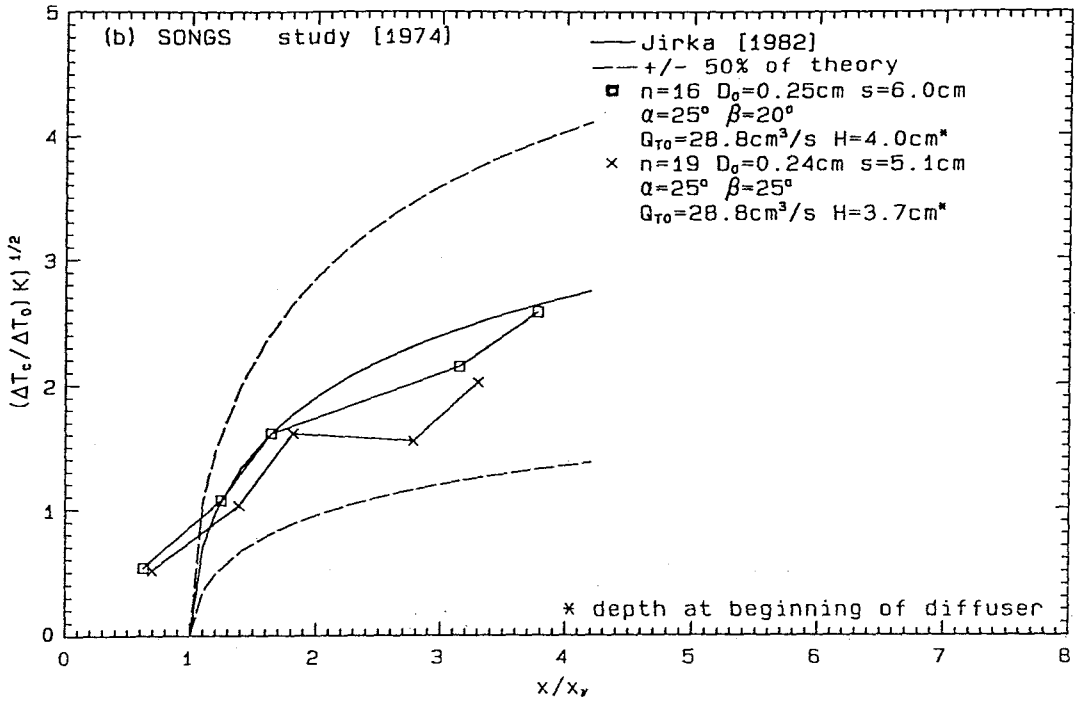

Figure 6.1b Comparison of measured longitudinal profiles of temperature increase with Jirka's model for the near field—SONGS hydraulic model study.

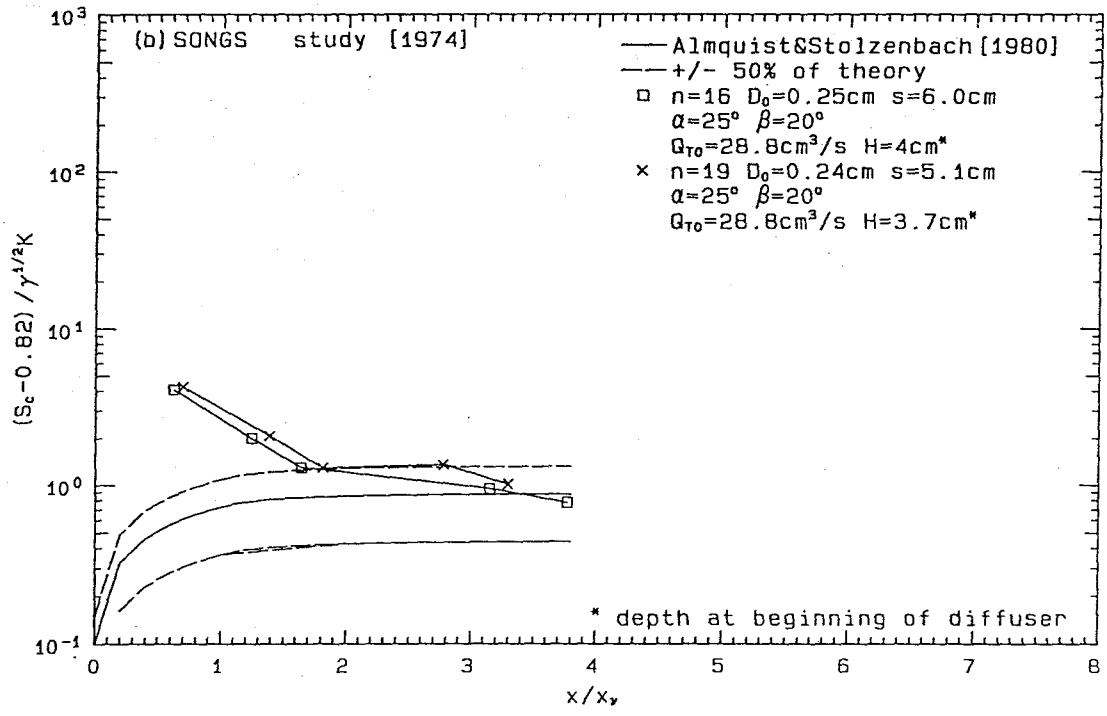

Figure 6.2b Comparison of measured longitudinal profiles of dilution with Almquist and Stolzenbach's model for the near field—SONGS hydraulic model study.

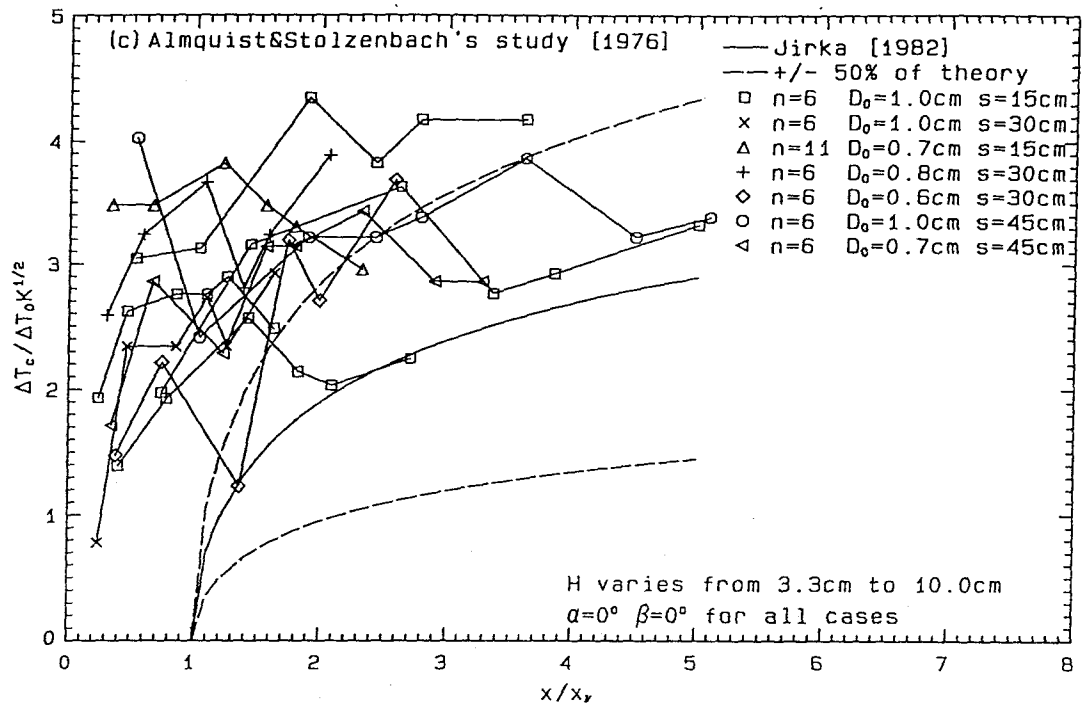

Figure 6.1c Comparison of measured longitudinal profiles of temperature increase with Jirka's model for the near field—Almquist and Stolzenbach's experimental study.

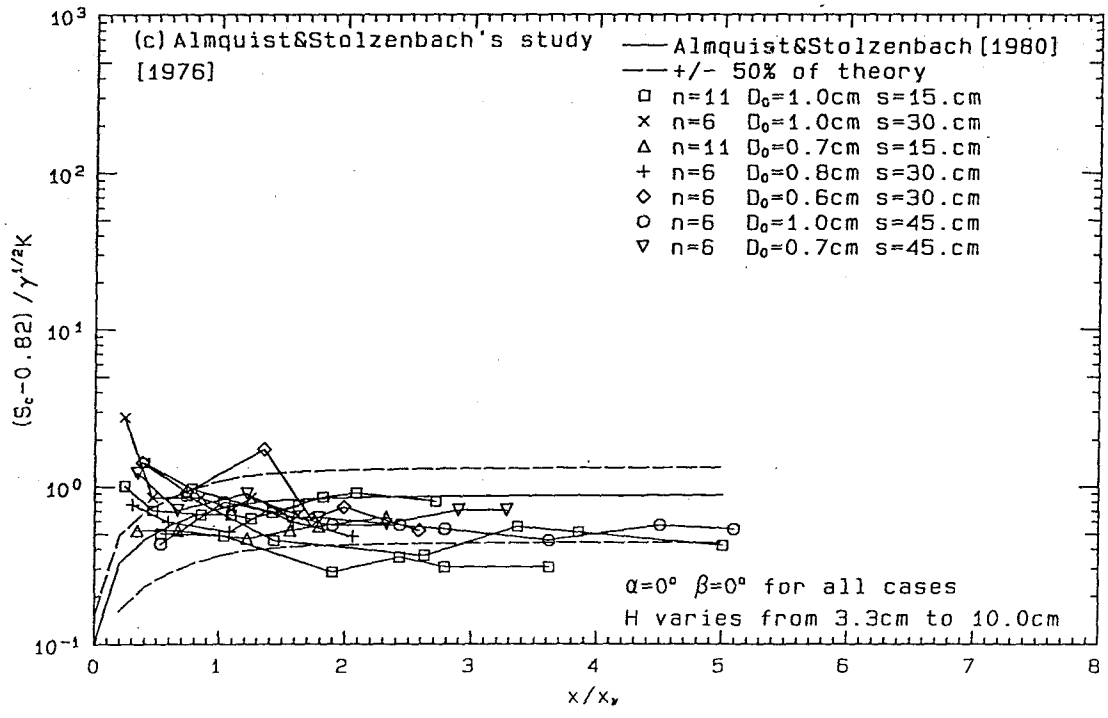

Figure 6.2c Comparison of measured longitudinal profiles of dilution with Almquist and Stolzenbach's model for the near field—Almquist and Stolzenbach's experimental study.

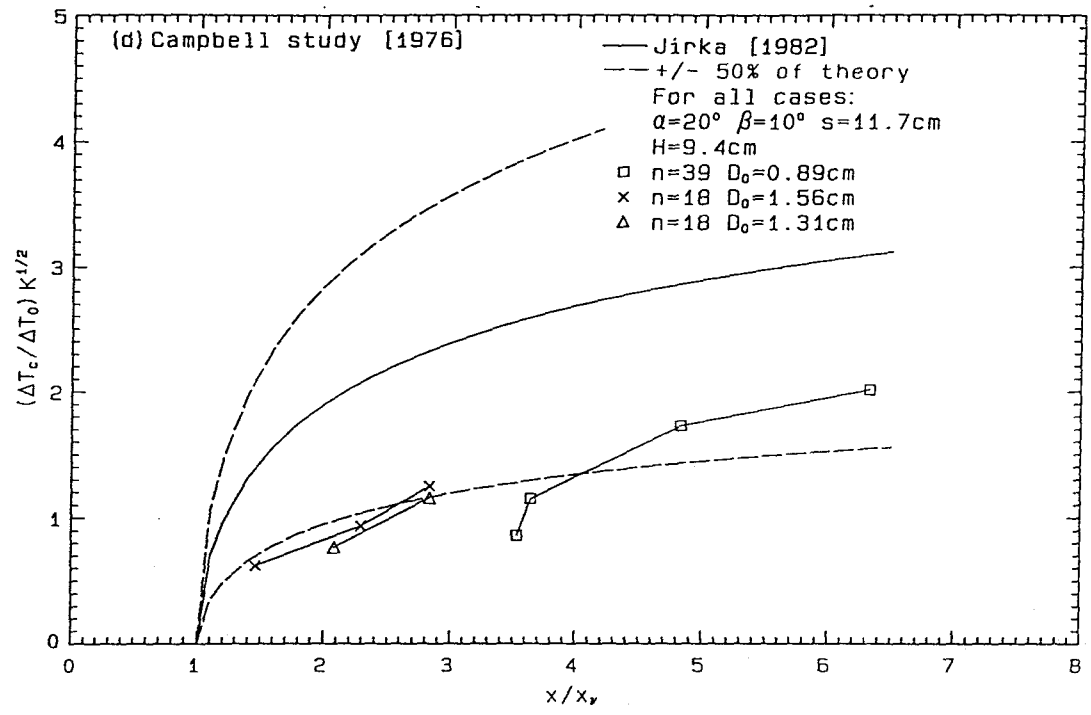

Figure 6.1d Comparison of measured longitudinal profiles of temperature increase with Jirka's model for the near field—Campbell Station hydraulic model study.

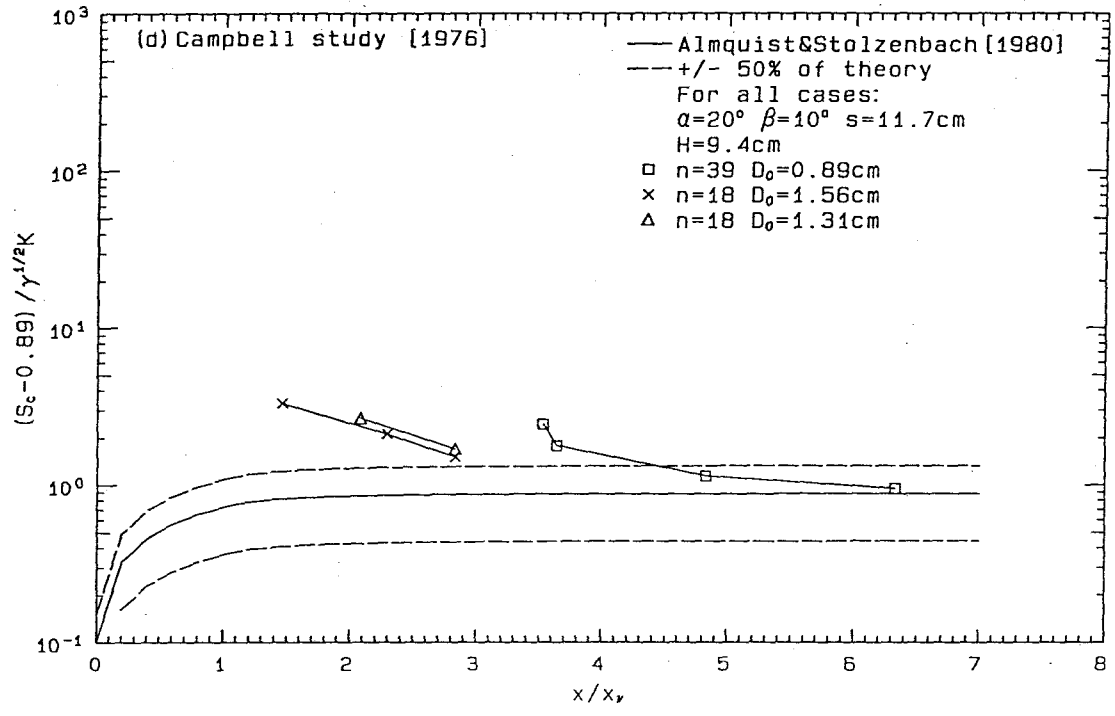

Figure 6.2d Comparison of measured longitudinal profiles of dilution with Almquist and Stolzenbach's model for the near field—Campbell Station hydraulic model study.

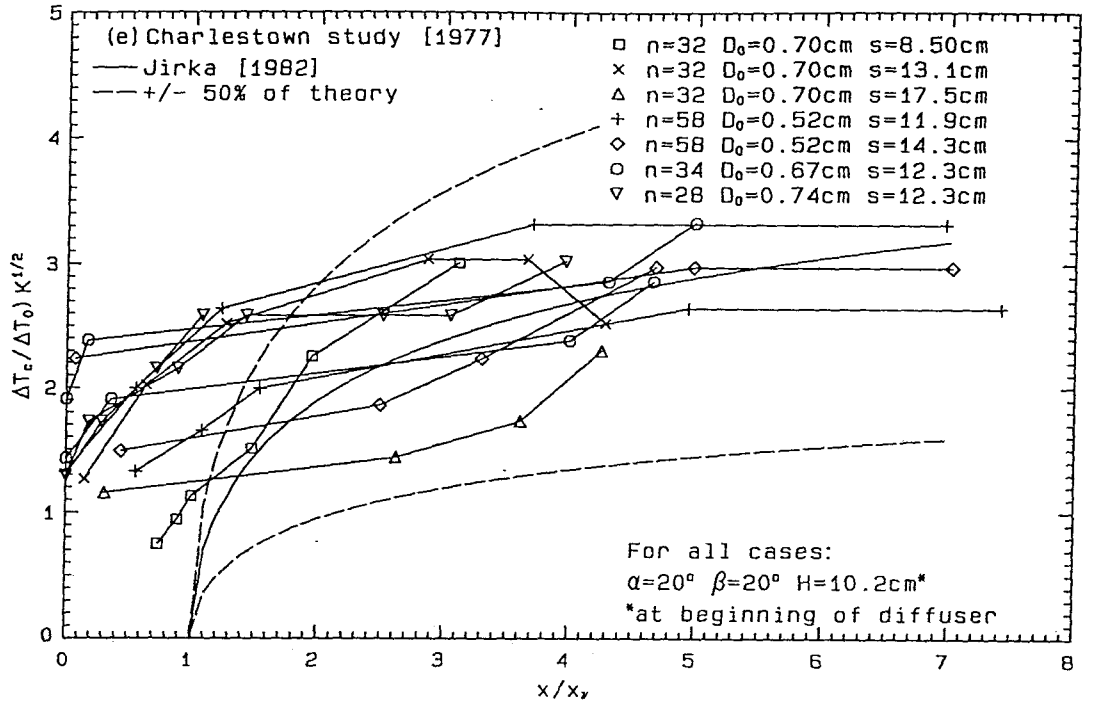

Figure 6.1e Comparison of measured longitudinal profiles of temperature increase with Jirka's model for the near field—Charlestown Station hydraulic model study.

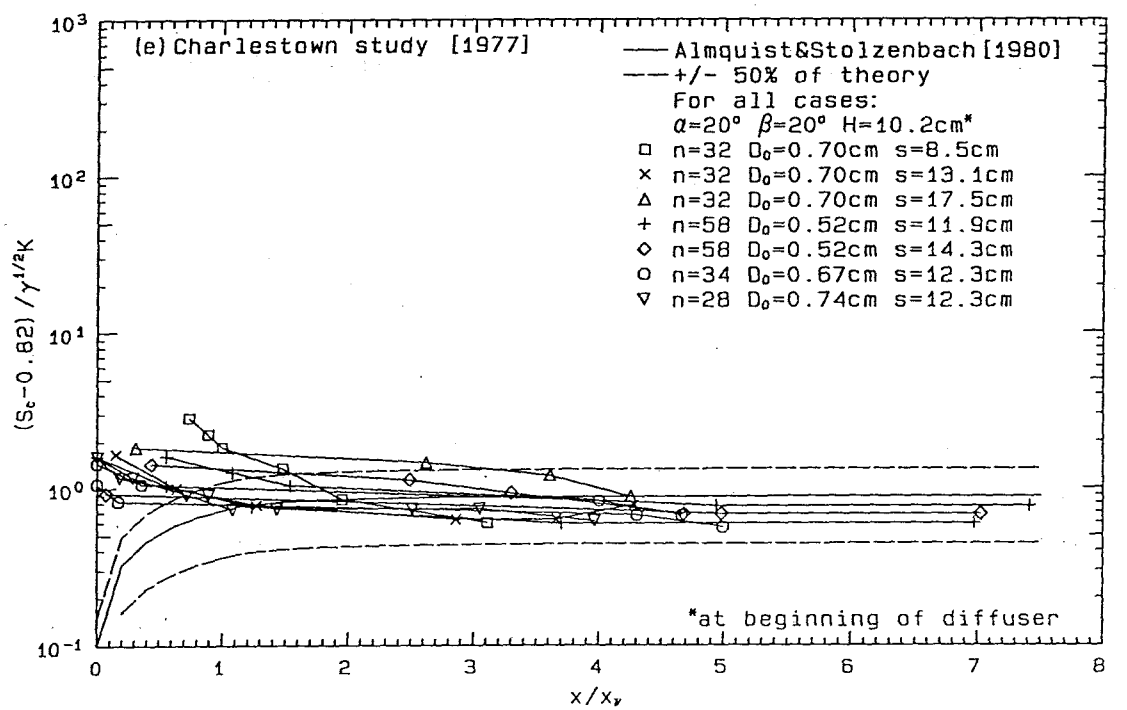

Figure 6.2e Comparison of measured longitudinal profiles of dilution with Almquist and Stolzenbach's model for the near field—Charlestown hydraulic model study.

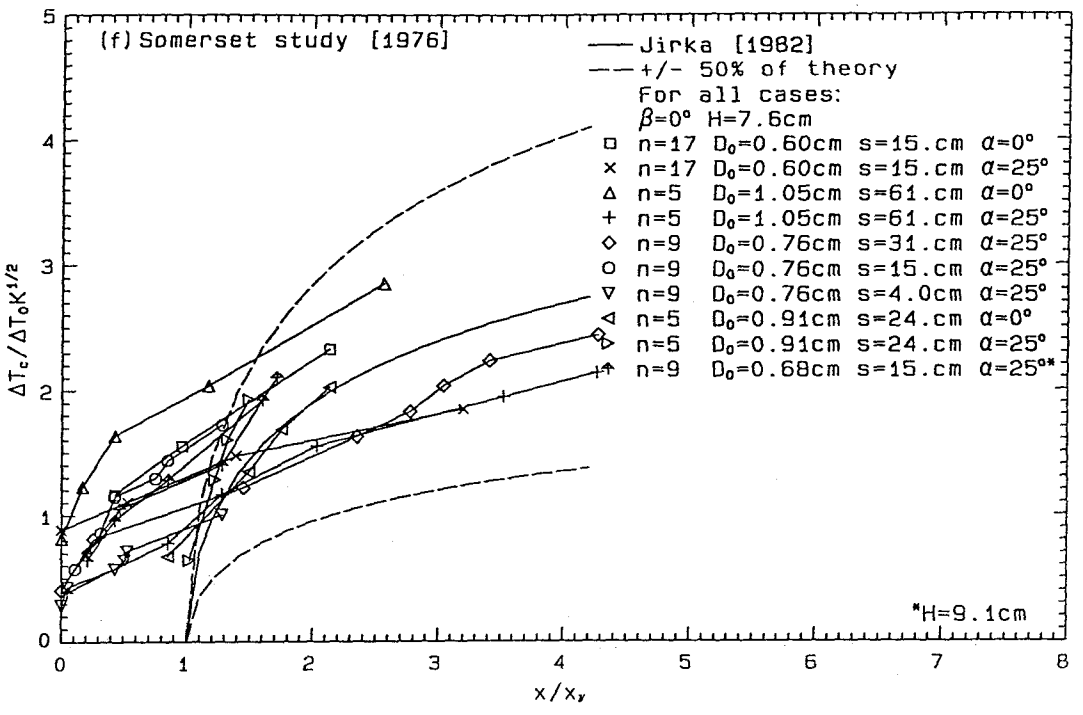

Figure 6.1f Comparison of measured longitudinal profiles of temperature increase with Jirka's model for the near field—Somerset alternate site hydraulic model study.

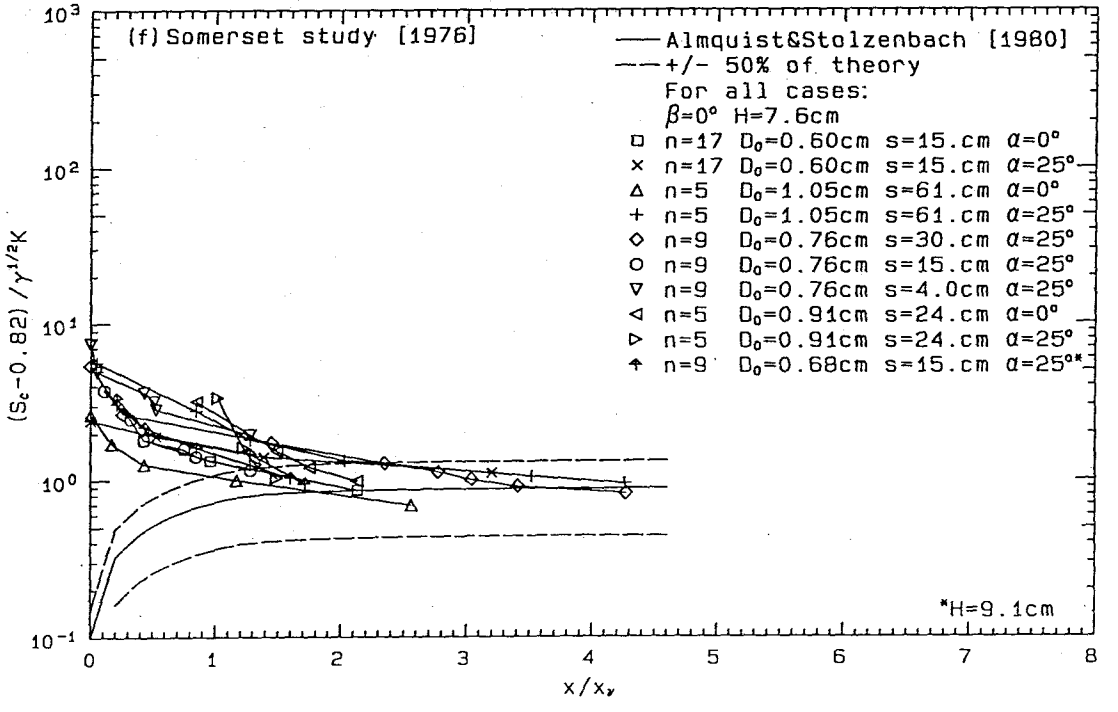

Figure 6.2f Comparison of measured longitudinal profiles of dilution with Almquist and Stolzenbach's model for the near field—Somerset alternate site hydraulic model study.

The model suggests an asymptotic dilution depending solely on the diffuser parameter K at large distance. Slight differences in the receiving water conditions, such as sloping bottoms in some of the laboratory models versus the idealized flat bottom assumption in the theory, also contribute to variations between the measurements and the predictions.

Although neither existing mathematical model provides accurate predictions of the temperature profiles, each gives reasonable descriptions on the overall behavior and the ranges of dilution at the downstream end of a staged multiport diffuser. This makes them useful as guidelines in the preliminary stage of future thermal diffuser design.

6.2.2 Normalized Peak Temperature Increase (T_{peak})

The normalized peak temperature rise T_{peak} (defined as the maximum centerline $\Delta T_c/\Delta T_0$, which should also be the peak value anywhere in quiescent receiving water, even for the case with $\alpha = \pm 25°$ as found from experimental observations) at the surface is chosen as the characteristic representation of the temperature distribution in the near-field region. A definition diagram of the peak temperature rise and other important plume characteristics is illustrated in Figure 5.33. A minimum initial dilution based on this peak temperature increase is defined as $\Delta T_0/\Delta T_{peak}$. The hypothesis that the near-field peak-temperature rise or the minimum initial dilution can be described by the simple jet theory has been discussed in Chapter 3. According to the three-dimensional turbulent jet theory,

$$\frac{\Delta T_c}{\Delta T_0} = c_1 \left(\frac{\ell_Q}{D_T}\right)^{\xi_1}, \tag{6.2}$$

$$c_1 = 5.6 \pm 0.1,$$

$$\text{and } \xi_1 = 1.$$

c_1 is an empirically determined coefficient, and D_T is the distance along the trajectory of the jet from the source. For all the experimental results, D_T is taken as $H/\sin\beta$, equivalent to the distance travelled by the individual jet to reach the water surface. However, when $\beta = 0$ or is very small, D_T is essentially undefined (according to the above definition). In subsequent discussions, Equation (6.2) is considered to be valid for $\beta \geq 10°$, an arbitrarily assigned value. The temperature increase is controlled, therefore, by the governing parameter ℓ_Q/H.

The measured values of T_{peak} (i.e., $\Delta T_{peak}/\Delta T_0$) versus $\ell_Q/(H/\sin\beta)$ of the present study, along with the prediction of the simple jet theory are shown in Figure 6.3. In addition, two lines representing $\pm 20\%$ of the simple jet prediction are given. The experimental values of T_{peak} agree fairly well with the simple jet theory; this confirms the hypothesis that ℓ_Q/H is the governing parameter and that the individual jet characteristics are most significant in the near field for this data set. However, there is a slight but consistent shift from the theory prediction for different groups of data. The discrepancy is found to be dependent mainly on the number of ports, n (or in other words, $\ell_Q = \sqrt{\pi/4}D_0 \sim n^{-1/2}$ for fixed total discharge).

For the data plotted in Figure 6.3, the following linear relationships were fitted for each subgroup with the same value of n:

$$T_{peak} = \frac{\Delta T_{peak}}{\Delta T_0} = c_2\left(\frac{\ell_Q}{H/\sin\beta}\right)^{\xi_2}, \tag{6.3}$$

with

$$n = 1 \ : \ c_2 = 4.69,$$

$$n = 4 \ : \ c_2 = 6.0,$$

$$n = 16 \ : \ c_2 = 9.4,$$

and $\xi_2 = 1$, for all cases of n.

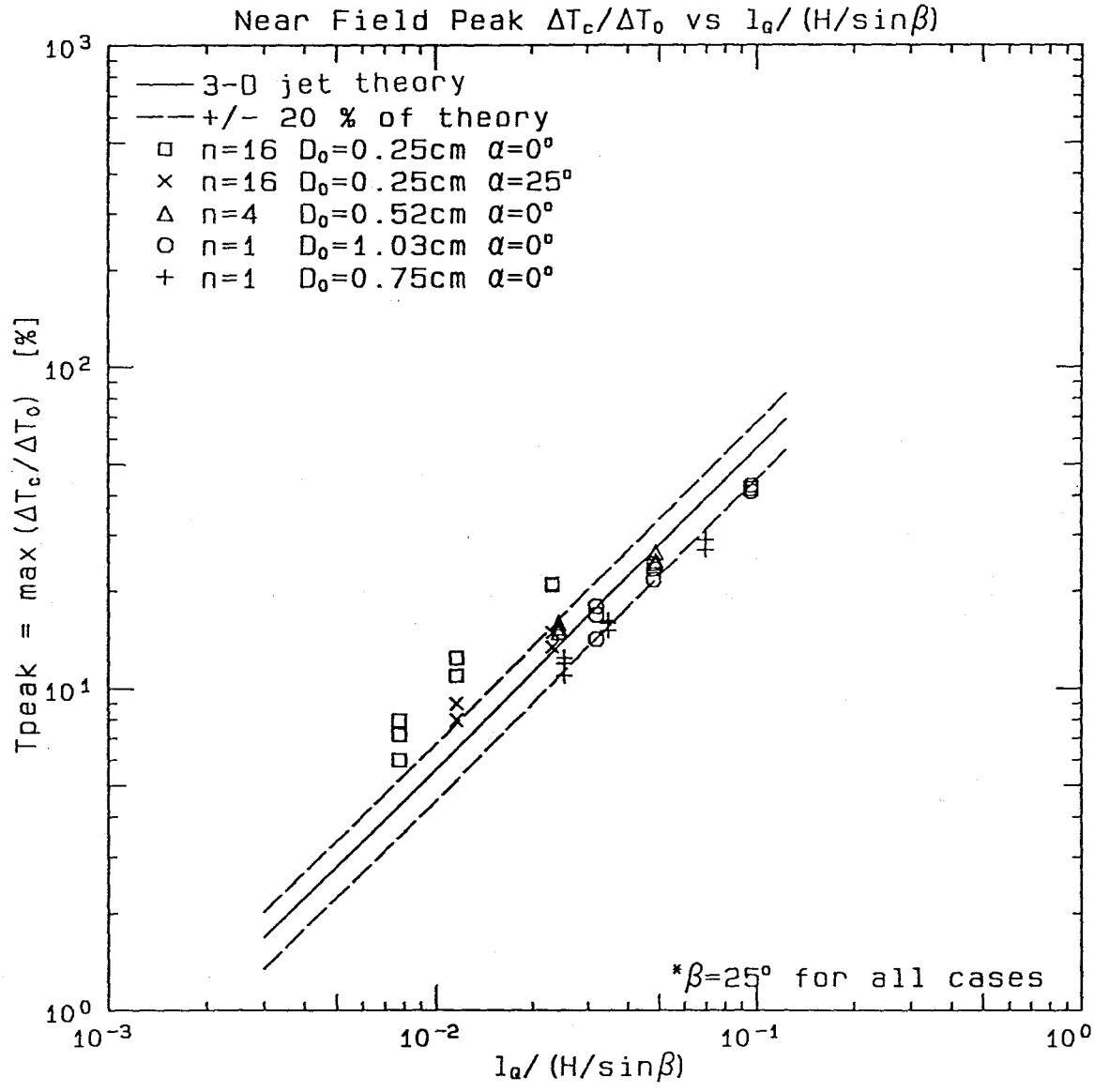

Figure 6.3 Comparison of normalized near-field peak temperature increase with the simple jet theory.

A good overall approximation is found to be:

$$T_{peak} = \frac{\Delta T_{peak}}{\Delta T_0} = 4.7 n^{1/4} \left(\frac{\ell_Q}{H/\sin\beta} \right) . \tag{6.4}$$

Figure 6.4 shows the measured values of T_{peak} versus $n^{1/4}\ell_Q/(H/\sin\beta)$. There is much less scatter of the data than in Figure 6.3.

The deviation of the experimental data from the simple jet theory can be explained by the nonlinear interaction among individual jets and the possible existence of a surface-blocking layer. The interaction of jets is largely a function of the jet spacing and water depth, i.e., s/H. However, the significance of the ratio s/H on the plume behavior is not studied in the experiments. Dilution is more or less inhibited in the blocking layer because the jets are entraining the diluted water in the layer rather than the ambient water. The formation and perseverance of this layer is expected to be governed by the relative strength of the stabilizing (buoyancy) and destabilizing (momentum) forces.

The observation that the difference between the experimental data and the theory is a function of n or ℓ_Q suggests that the thickness of the blocking layer depends on ℓ_Q, also. It should be noted that n and D_0 are chosen such that the momentum and buoyancy fluxes are preserved in experiments of equal volumetric flow rates, with the exception of the group of experiments for $n = 1$ and $D_0 = 0.75$ cm. As the number of ports increases, the fluxes per individual jet decrease. For thermal discharges, where the momentum flux is the dominant factor of the mixing process in the near field, the stability of the surface-blocking layer is expected to decrease with an increase of discharge momentum flux per jet. In the extreme case of $n = 1$ and for the most shallow water discharge ($H = 2$ cm), the jet physically shoots out of the ambient water and then falls back. The re-entry induces additional mixing by the generation of large-scale eddies in the water column. As a result, the observed minimum dilutions

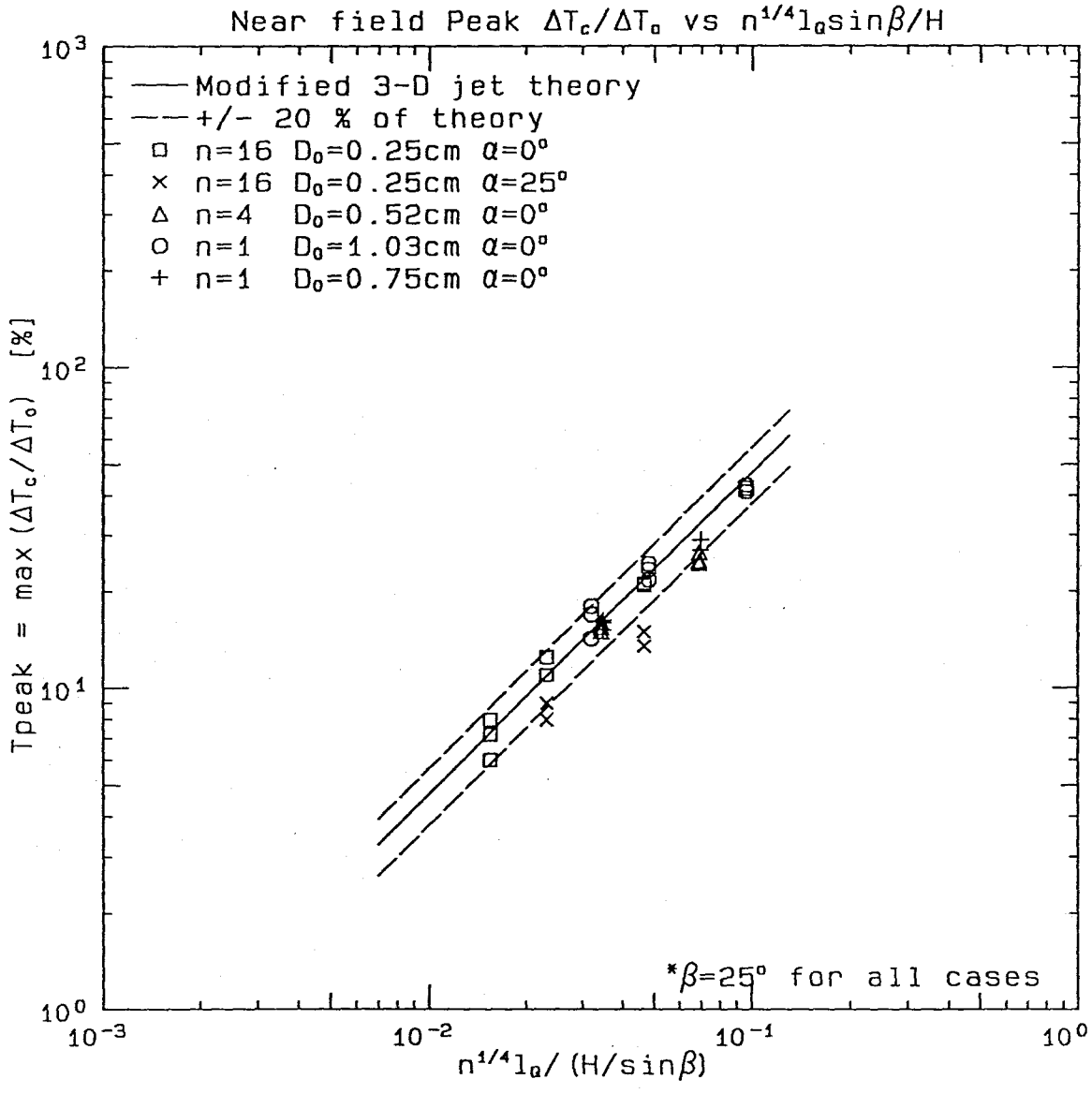

Figure 6.4 Comparison of normalized near-field peak temperature increase with $n^{1/4}\ell_Q/(H/\sin\beta)$.

of the single-port experiments are higher than theoretical predictions.

The combined effects of the surface-blocking layer and jet interactions can be described, apparently, by modifying the dilution relationship (Equation (6.4)) of the simple jet model with an empirically determined factor, $n^{1/4}$. As a result, the improvement in the initial dilution by increasing the number of ports is less than that predicted by the simple jet theory ($S \propto n^{1/4}$ in the experiments versus $S \propto n^{1/2}$ in the simple jet theory).

6.2.3 Thickness of the Surface Layer at the End of the Diffuser (h_1)

The term "blocking layer" can be misleading since such a layer is not well defined in the diffuser zone. In experiments with shallow-water depth and strong-discharge momentum fluxes that cause instability, the layer is nonexistent. Even in the stable configurations where there is no interaction of the diluted water and the jet, the discrete inputs of warm water along the diffuser makes it difficult to define a characteristic layer thickness. The thickness of the blocking layer fluctuates because of both the input manner and the interactions among individual jets. Therefore, the simple jet model gives better predictions for cases with wider jet spacing and in deeper ambient water. Shortly beyond the diffuser zone, the surface layer is much better defined.

In the following discussion, the thickness of the layer at the end of the diffuser zone is taken as the characteristic thickness of the surface-blocking layer in the near field. The thickness h_1 is defined as the distance from the water surface to the position where

$$\Delta T_{\text{surface}} - \Delta T(h_1) = e^{-1}(\Delta T_{\text{surface}} - \Delta T_{\text{bottom}}) \,. \tag{6.5}$$

Thus, it is a length scale of the vertical temperature distribution in the water column, rather than the physical thickness of the surface layer. The normalized thickness, h_1/H, is plotted against the governing parameter of the near field, ℓ_Q/H, in Figure 6.5. An approximate equation is obtained:

$$\frac{h_1}{H} = (0.9 \pm 0.05)(\frac{\ell_Q}{H})^{1/3} , \tag{6.6}$$

for the experimental range of $0.015 < \ell_Q/H < 0.25$.

6.2.4 Lateral Spreading Rate of the Plume (ϵ)

The average rate of spreading of the total plume width, ϵ, is measured from the overhead photographs taken during the experiments (definition diagram in Figure 5.33). The width of a plume is taken as the width of the visual boundary of the dye cloud.

In cases of deep receiving water and small volume flux (or momentum flux) per individual jet, the plume width in the near field may become unsteady, and grows slowly with time at a particular location. The unsteadiness is an indication that the effect of gravitational spreading at the end of the intermediate field propagates back to the diffuser zone. Eventually, the plume water will be re-entrained by the diffuser, creating an unsteady near field, equivalent to a submergence of the source in an open channel discharge. The experimental data indicate that this unsteady condition will occur when $\ell_M/H \leq 1.025$, where $\ell_M = M_{i0}^{3/4}/B_{i0}^{1/2}$. Under such conditions, the spreading rate of the plume is undefined and will not be included in the discussion. Figures 6.6a to 6.6d show overhead photographs of the unsteady near field of a plume with the experimental conditions: $n = 16$, $D_0 = 0.25$ cm, $H = 12$ cm and $Q_{T0} = 20.3\ \mathrm{cm}^3/\mathrm{s}$, at various times after starting the heated water discharge .

Figure 6.7 plots the measured ϵ versus $\sqrt{n}\ell_Q/H$ of the present study. For small

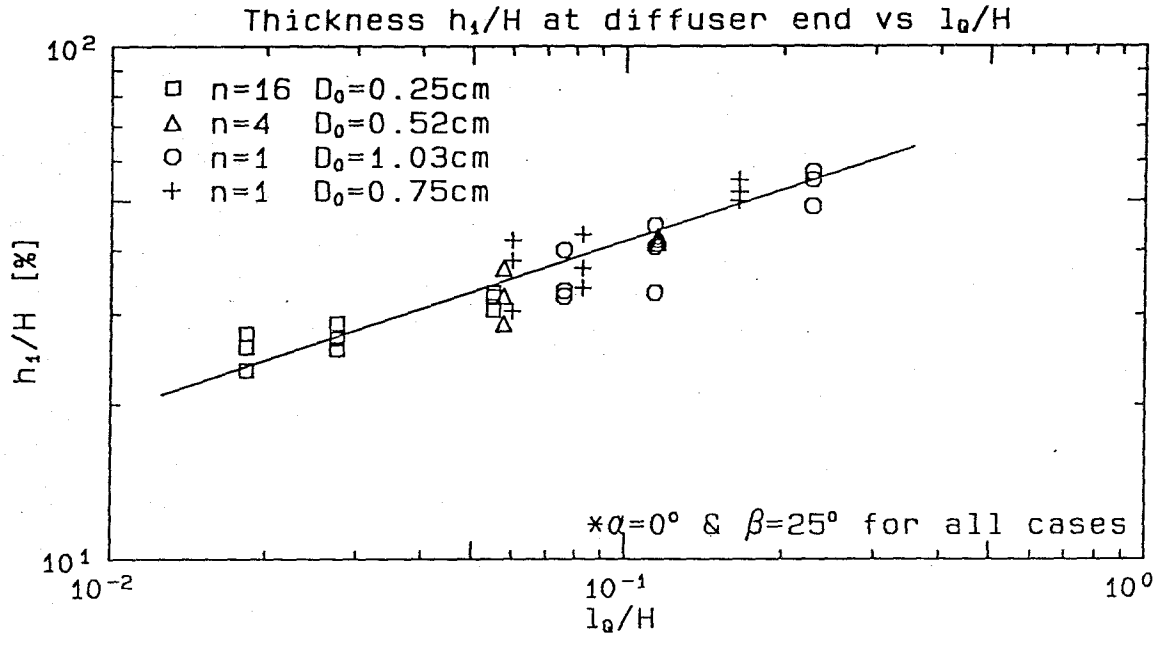

Figure 6.5 Normalized thickness of the surface layer, h_1/H, at the end of the diffuser.

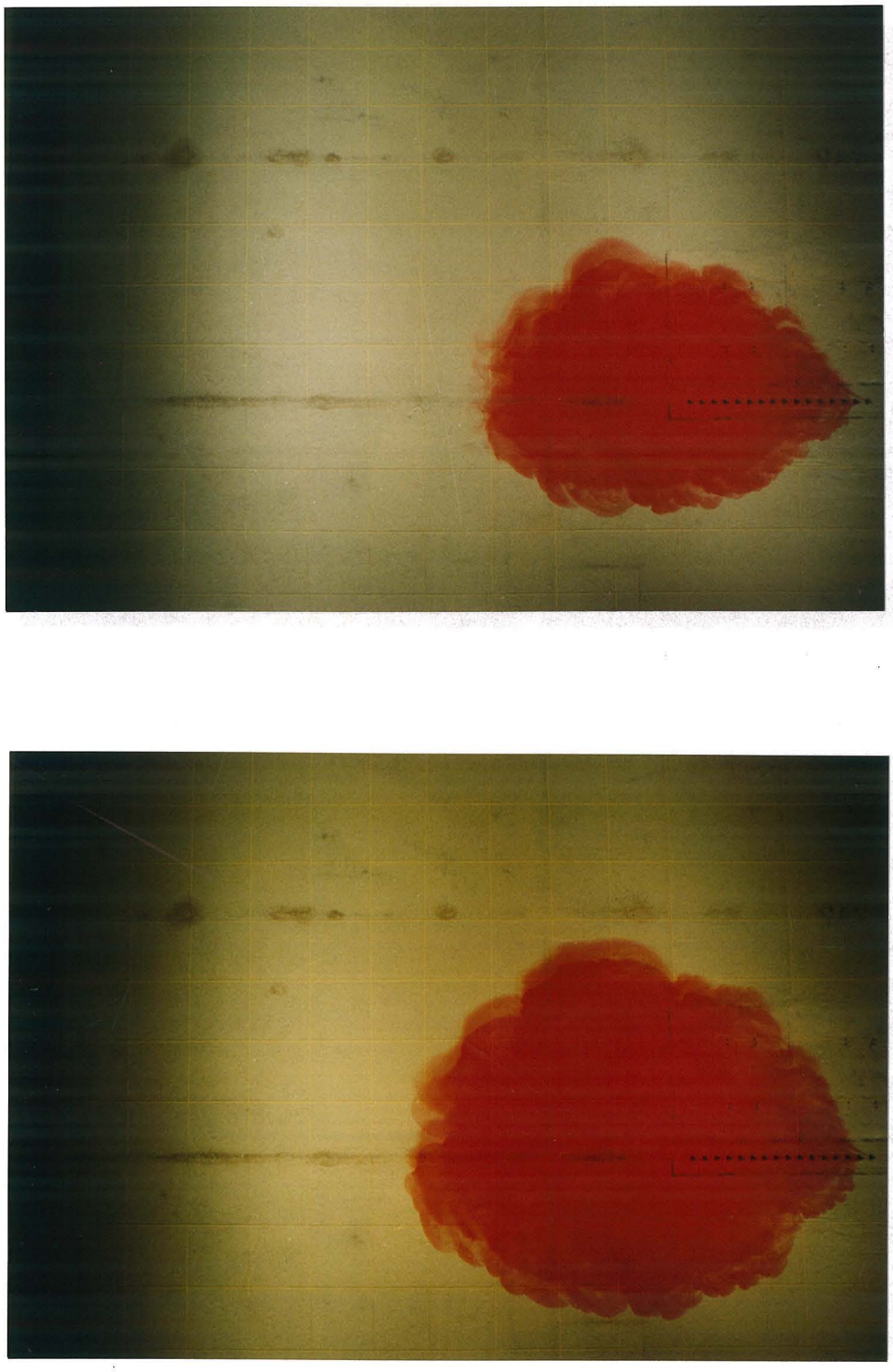

Figure 6.6 Overhead photographs of the thermal plume with discharge condition: $n = 16$, $D_0 = 0.25\,\text{cm}$, $Q_{T0} = 20.3\,\text{cm}^3/\text{s}$ and $H = 12\,\text{cm}$. a) $t = 2$ min 50 sec; b) $t = 3$ min 50 sec.

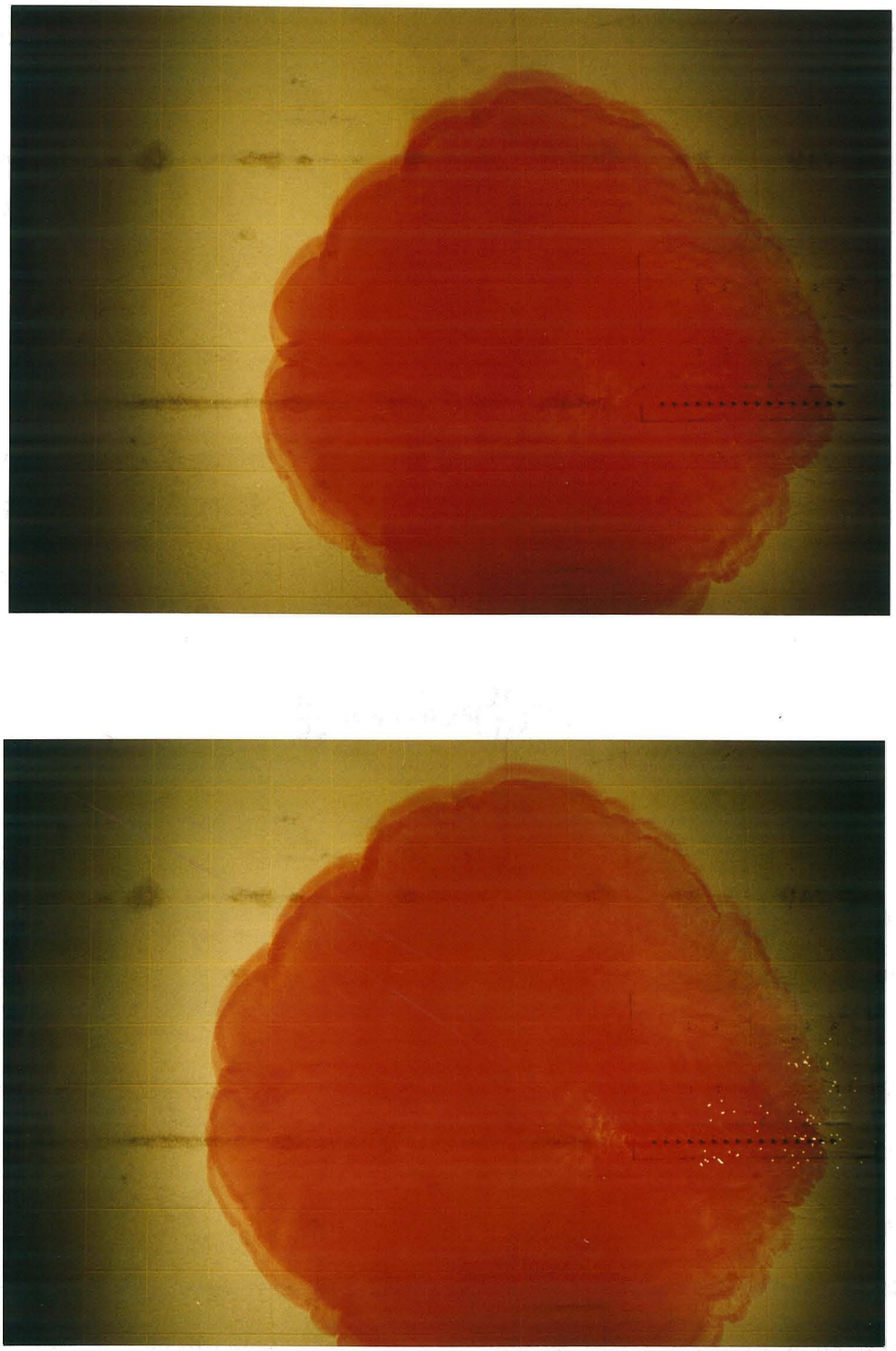

Figure 6.6 Overhead photographs of the thermal plume with discharge condition: $n = 16$, $D_0 = 0.25\,\text{cm}$, $Q_{T0} = 20.3\,\text{cm}^3/\text{s}$ and $H = 12\,\text{cm}$. c) $t = 5$ min 50 sec; d) $t = 7$ min 50 sec.

$\sqrt{n}\ell_Q/H$, corresponding to a deep ambient condition, the spreading rates of the plume among experiments with various n or ℓ_Q agree closely. However, for large $\sqrt{n}\ell_Q/H$ (i.e., a shallow-water depth condition) there is a higher degree of scattering. This indicates that the size of the individual jet has an influence on the growth of the plume. An approximate curve to fit the data can be represented by:

$$\epsilon = 0.31(\frac{\sqrt{n}\ell_Q}{H})^{-1/3} . \tag{6.7}$$

This formulation of the near-field spreading rate presents an alternative to the one proposed by Lee (1980) who derived the spreading rate as a function of the entrainment coefficient (γ) and K for $\alpha = 0°$:

$$\frac{db}{dx} = \gamma + 0.25(\frac{H}{B})^{-1} . \tag{6.8}$$

6.2.5 Comparison with the Modified Simple Jet Model

The simple jet hypothesis requires a finite vertical discharge angle in order to define the distance travelled by individual jets until they reach the water surface. Since the laboratory studies of the Somerset site (Stolzenbach et al., 1976) and Almquist and Stolzenbach (1976) were conducted on diffusers with horizontal discharges, the simple jet model cannot be compared to the results of these studies.

Figure 6.8 compares the minimum dilutions measured in this study and in some previous laboratory studies with the prediction of the modified simple jet model. The comparison is, in general, satisfactory and justifies the use of the simple jet model as an aid to predict the performance of a staged diffuser in early design stages.

The model of Almquist and Stolzenbach (1980) predicted an asymptotic centerline value for dilution in the near field to be attained after a certain distance

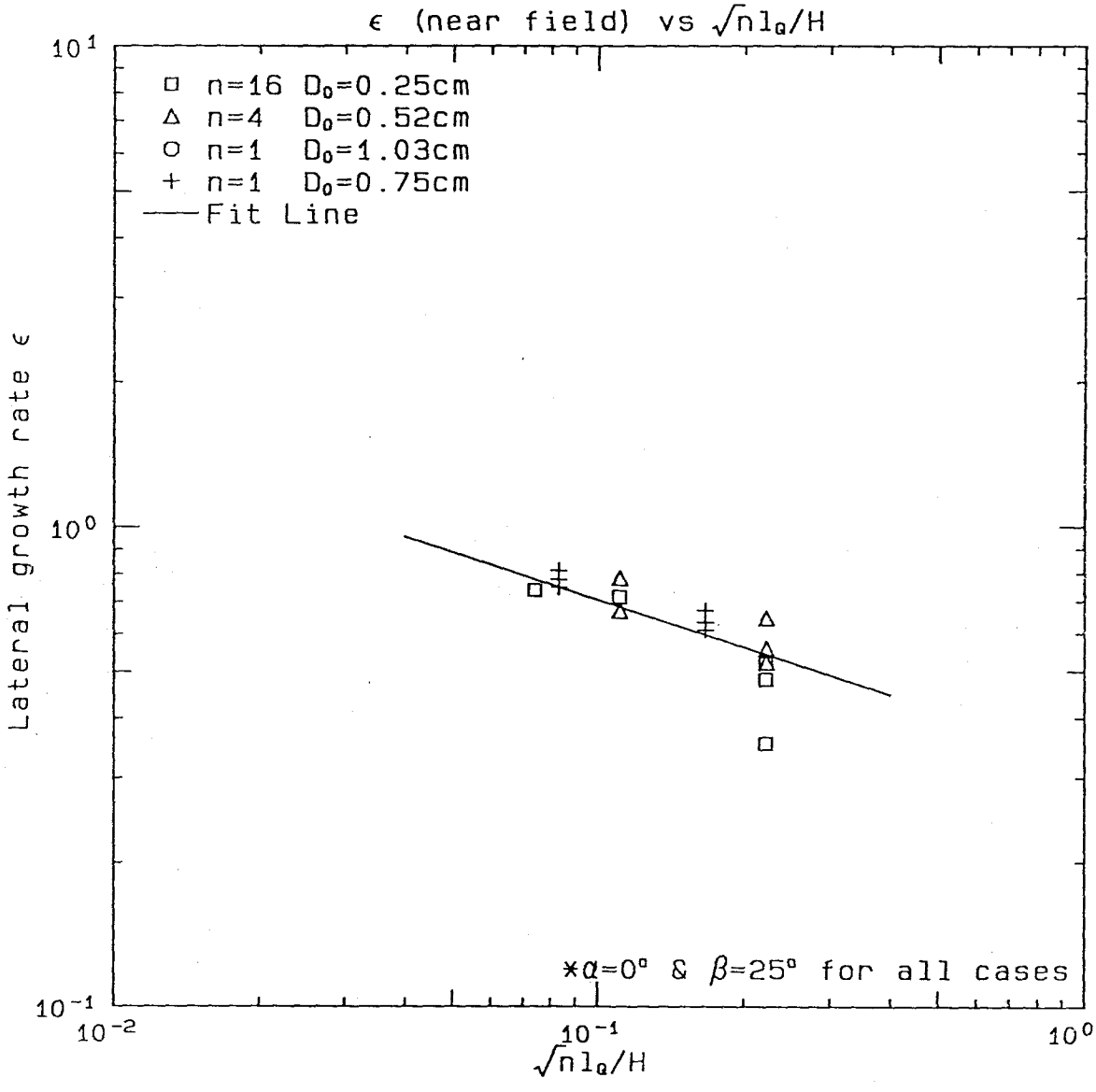

Figure 6.7 Average lateral growth rate of the total plume width, ϵ.

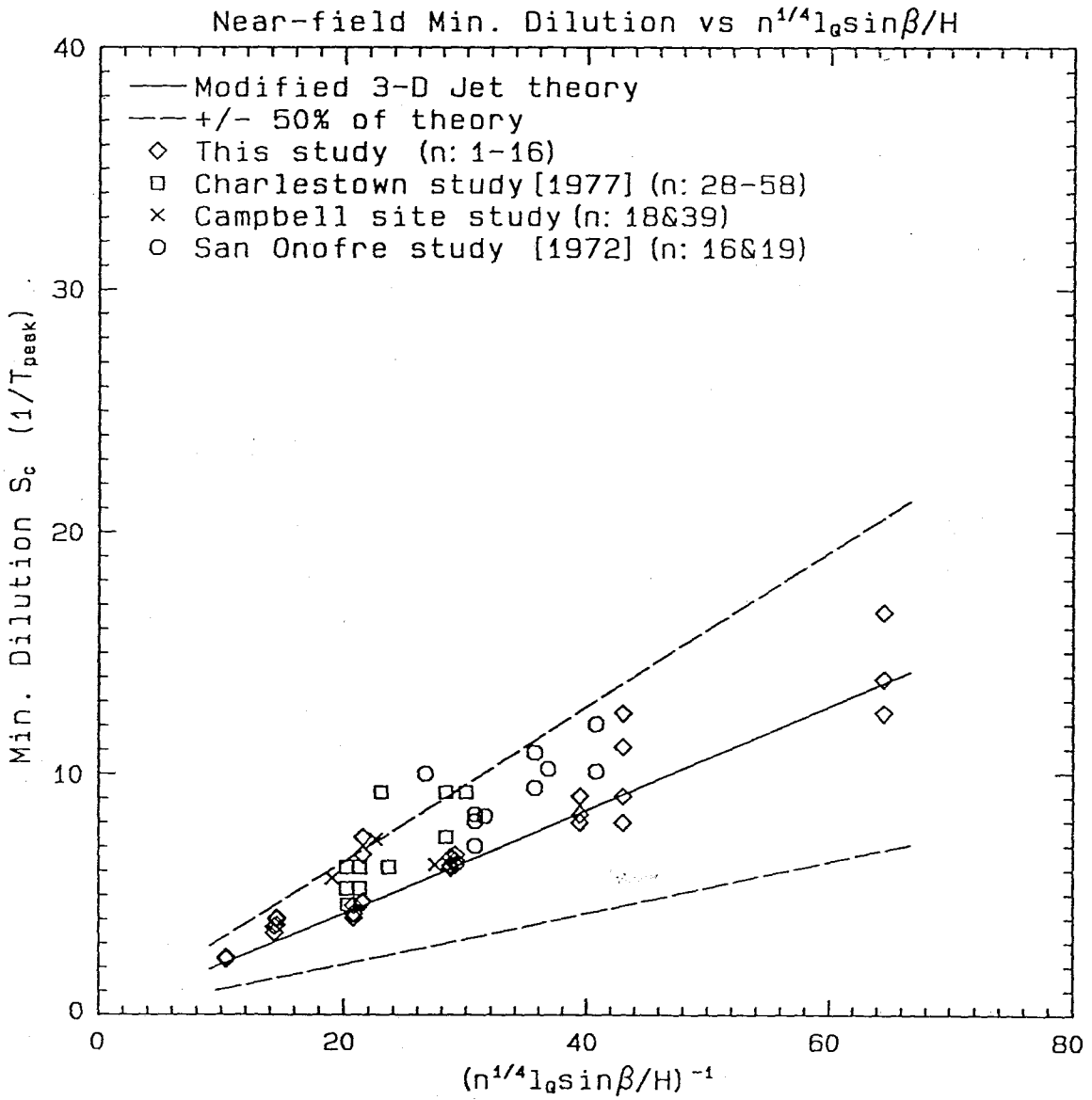

Figure 6.8 Comparison of various laboratory results with the modified simple jet model.

(Equation (2.10)) or in terms of K:

$$S_a = 0.82 + 0.37K \,, \tag{6.9}$$

where

$$K = \sqrt{\frac{4HL\cos\alpha\cos\beta}{n\pi D_0^2}} \,.$$

In Figure 6.9, this asymptotic near-field dilution is compared with the minimum initial dilution from the present study as well as from various previous experimental studies. The overall trend of the laboratory results agrees with that predicted, with experimental deviations from the theory of up to about $\pm 50\%$.

Jirka (1982) also derived an asymptotic dilution for the near field of a staged diffuser, Equation (2.11) which can be rewritten as:

$$S_a = 0.67K \,, \tag{6.10}$$

where $K = \sqrt{4HL/n\pi D_0^2}$. This dilution prediction is also compared with various experimental results as shown in Figure 6.10.

6.3 The Intermediate Field

The intermediate-field key results to be discussed are the temperature rise at the end of the surface buoyant jet region (designated as the asymptotic temperature rise T_{asym}) and the dilution achieved in this turbulent mixing zone, S_2. Beyond the surface buoyant jet regime, the temperature rise is approximately constant except near the initial front, where the temperature is unsteady. The transition distance x_t

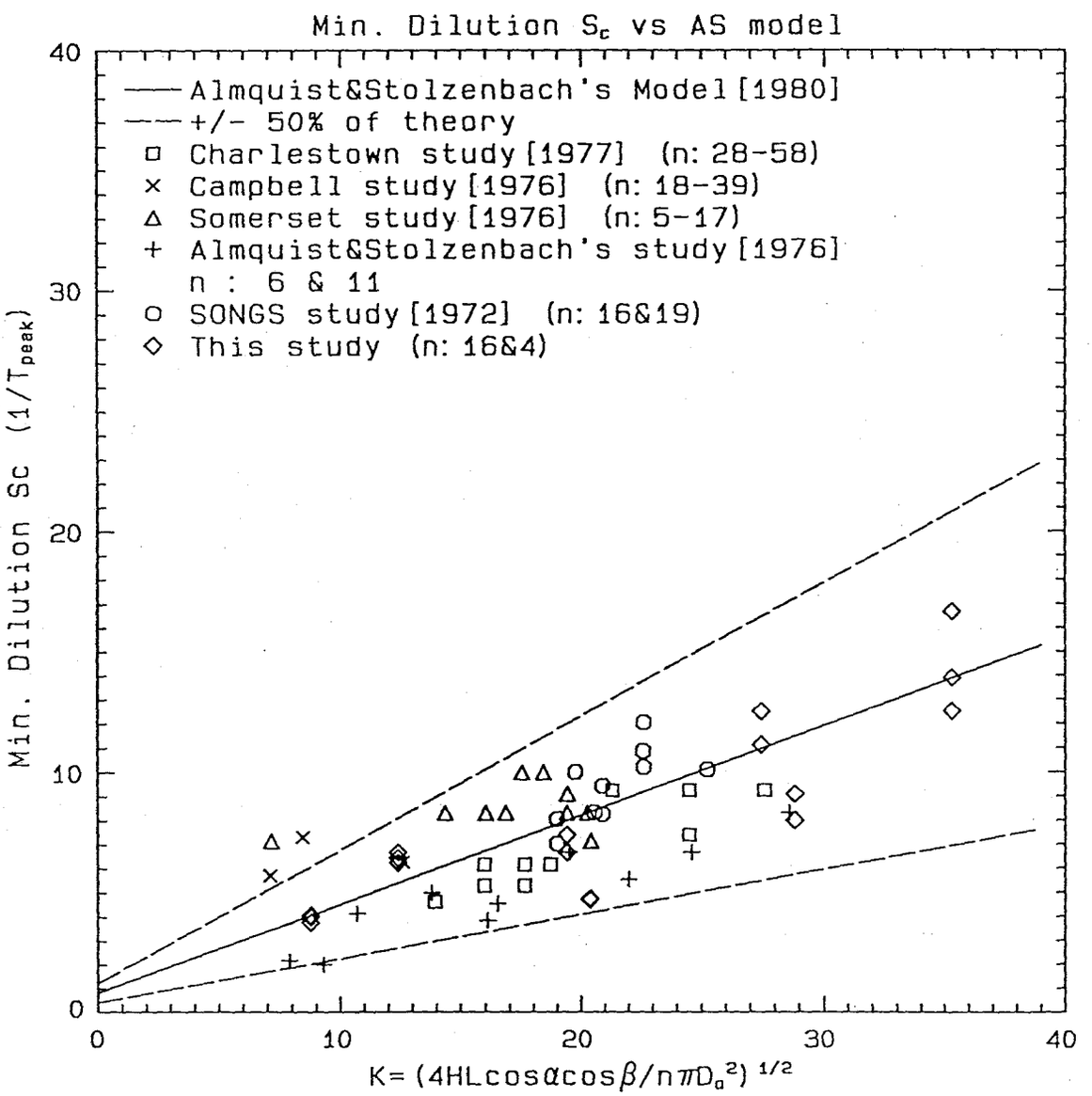

Figure 6.9 Comparison of various laboratory results with the model of Almquist and Stolzenbach (1980).

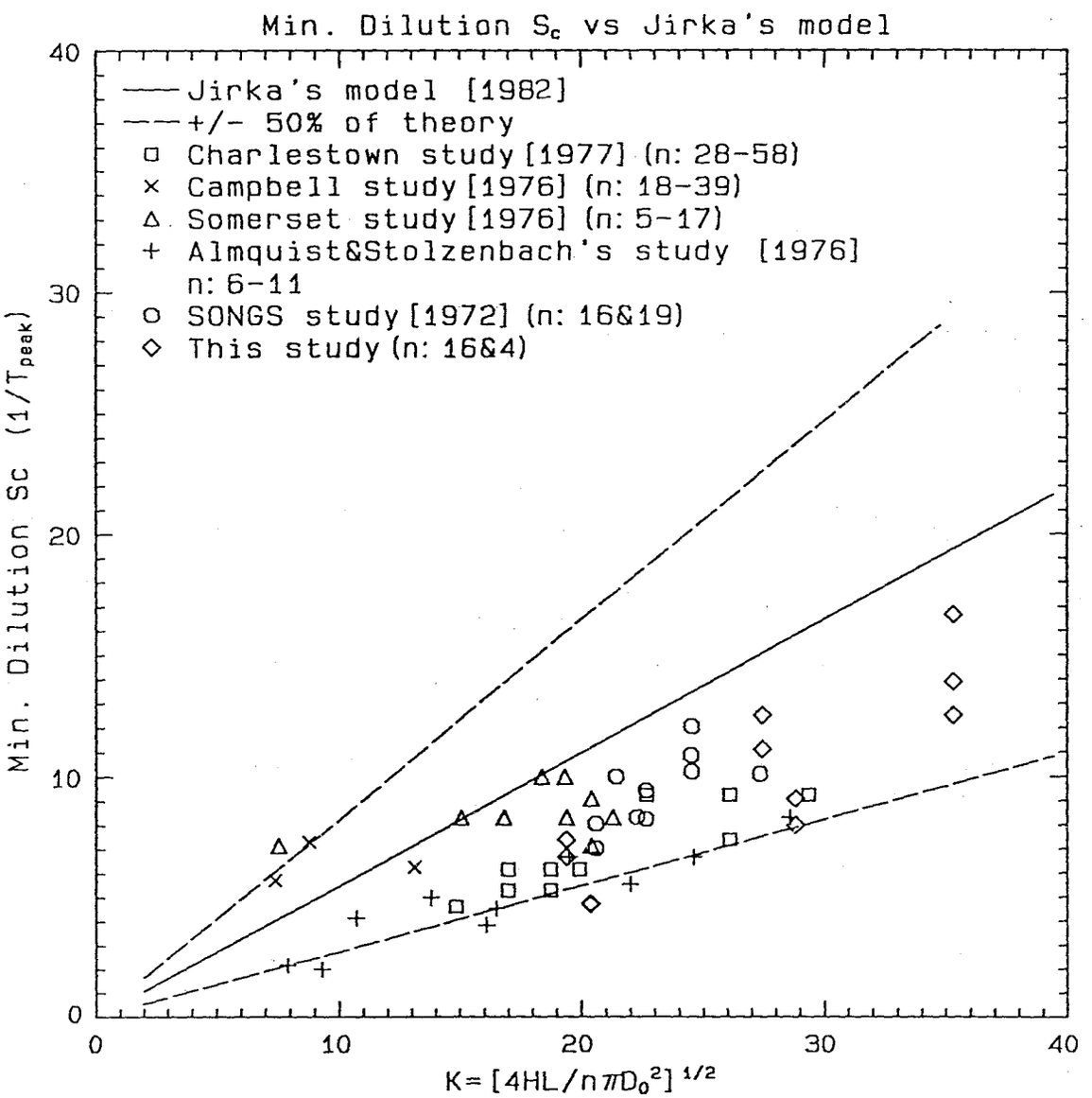

Figure 6.10 Comparison of various laboratory results with the model of Jirka (1982).

(length of the surface buoyant jet zone from the end of the diffuser) is also studied. The definitions of the various relevant results are again illustrated in Figure 5.33.

6.3.1 Normalized Asymptotic Surface Temperature Increase (T_{asym})

When the thermal plume leaves the diffuser region, the $\Delta T_c(x)$ drops rapidly with distance travelled (x) and reaches a plateau value eventually signalling the end of the surface buoyant jet zone. The normalized asymptotic temperature rise T_{asym} (defined as $\Delta T_{asym}/\Delta T_0$) is extracted from the longitudinal temperature profiles measured in the centerline experiments. Figure 6.11 shows the measured T_{asym} versus the source parameter ℓ_Q/H. The asymptotic temperature rise has a similar dependency on ℓ_Q/H as the peak temperature rise; i.e.,

$$T_{asym} = \frac{\Delta T_{asym}}{\Delta T_0} = c_3(\frac{\ell_Q}{H})^{\xi_3} \ . \tag{6.11}$$

Instead of being a constant as ξ_2 is for T_{peak} (Equation (6.3)), both c_3 and ξ_3 are themselves functions of n, resulting in a complex relationship.

The mixing in the intermediate field, and hence T_{asym}, is expected to depend on characteristics such as the dilution, the depth and width of the plume at the end of the diffuser zone, and the lateral and vertical temperature distributions. All of these characteristics are functions of the near-field governing parameter ℓ_Q/H, n and possibly s/H. Since T_{asym} depends on the interplay of the various properties, it changes according to ℓ_Q/H in a complex manner. The best-fit curves for the data can be approximately represented by:

$$100\frac{\Delta T_{asym}}{\Delta T_0} = (160\frac{\ell_Q}{H})^{(n^{1/4})/2} \ , \tag{6.12}$$

for cases with $\sqrt{n}\ell_Q = 0.887$ cm (these include all experiments except those with

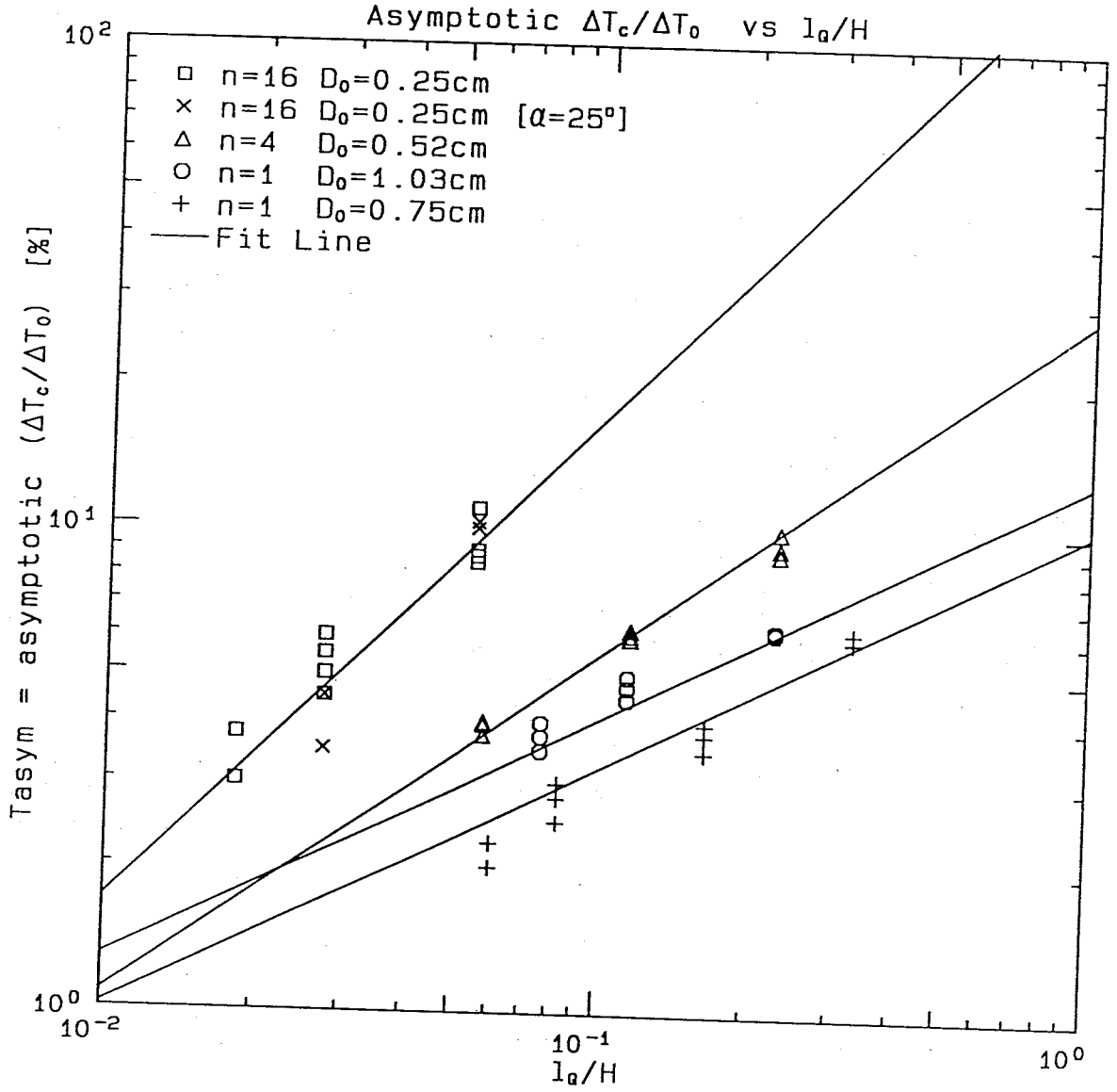

Figure 6.11 T_{asym} $(\Delta T_{asym}/\Delta T_0)$ versus ℓ_Q/H.

$n = 1$ and $D_0 = 0.75$ cm). The function is not universal since the coefficient changes with $\sqrt{n}\ell_Q$, and because it does not include the dependency on s/H (s is fixed at 6 cm for all multiport experiments); a generalized relationship is not yet available.

While the peak temperature rise always decreases with increasing n, ΔT_{asym} does not necessarily behave similarly. For the measured T_{asym} ($\Delta T_{asym}/\Delta T_0$) vs n, Figure 6.12 shows that the performance of the diffuser, in terms of the asymptotic temperature increase, does not improve with increasing n beyond $n = 4$. This leads to the conclusion that the asymptotic dilution achieved in this zone is relatively insensitive to n. However, a complete picture of the mixing process has to include the length of the turbulent mixing zone and the $\Delta T_c/\Delta T_0$ profile with downstream distance (Section 6.3.3 and Section 6.3.4).

6.3.2 Intermediate-field Dilution (S_2)

The intermediate-field dilution S_2 is defined as $(\Delta T_{asym}/\Delta T_{s1})^{-1}$, where ΔT_{s1} is the temperature rise at the end of the diffuser zone. Figure 6.13 shows the experimental values of S_2 vs ℓ_Q/H. Since ℓ_Q is constant for typical experiments, the horizontal axis varies essentially as H^{-1}. The intermediate-field dilution actually increases with decreasing water depth, although not as much in the $n = 16$ cases as for smaller n cases. The intermediate-field dilution has the same form of dependency as T_{asym}:

$$S_2 = c_4(\frac{\ell_Q}{H})^{\xi_4}\ , \tag{6.13}$$

and ξ_4 varies from 3/8 for $n = 1$ to approximately 1/8 for $n = 4$ and to 1/16 for $n = 16$ cases. c_4 is a function of n, also. Therefore, it is conceivable that S_2 depends on T_{s1} ($\Delta T_{s1}/\Delta T_0$), which affects the rate of lateral gravitational spreading. Figure 6.14 shows that this dependency is, in addition, a function of n.

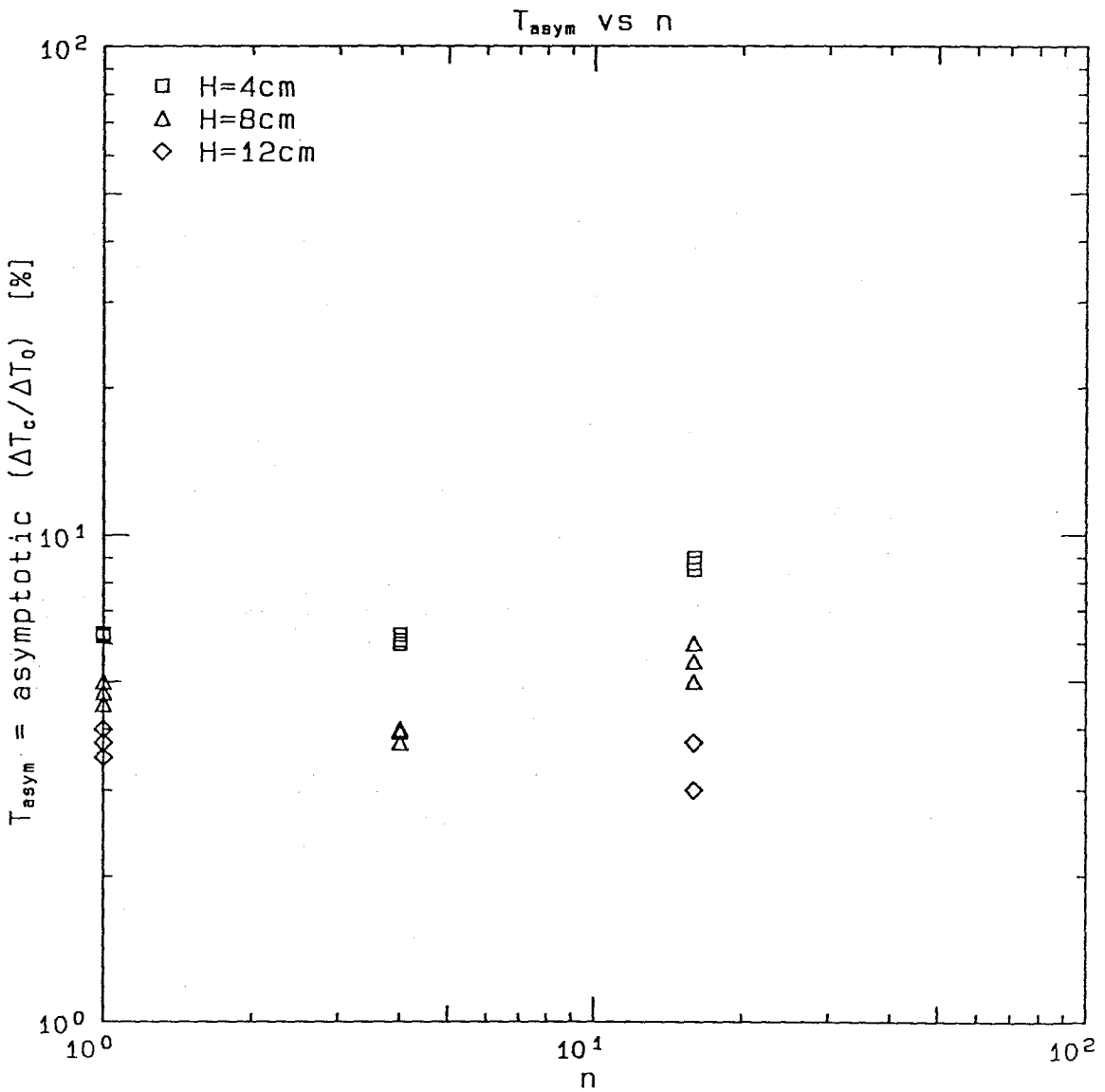

Figure 6.12 T_{asym} $(\Delta T_{asym}/\Delta T_0)$ versus n.

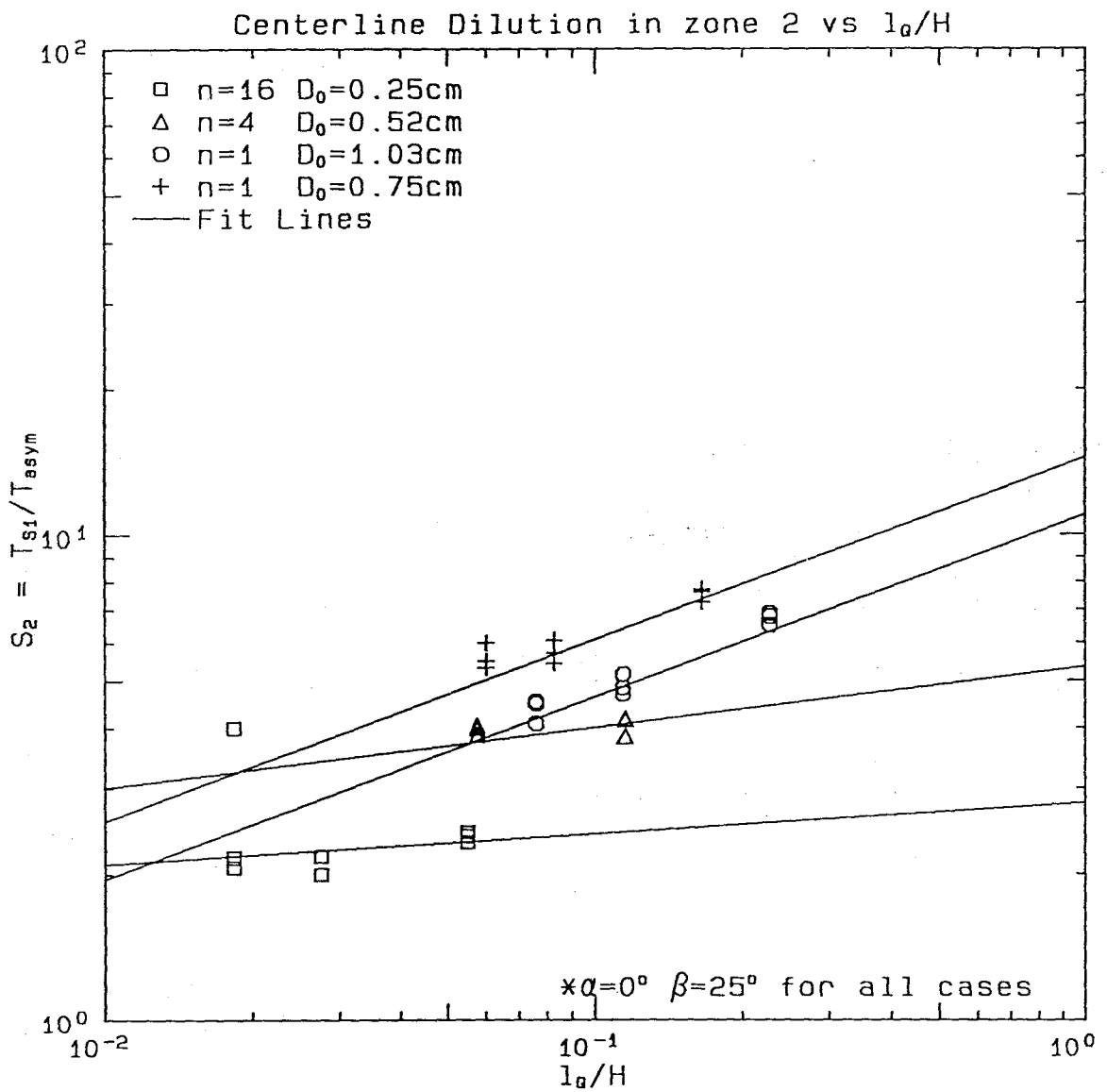

Figure 6.13 Intermediate field dilution S_2 ($\Delta T_{s1}/\Delta T_{asym}$) versus ℓ_Q/H.

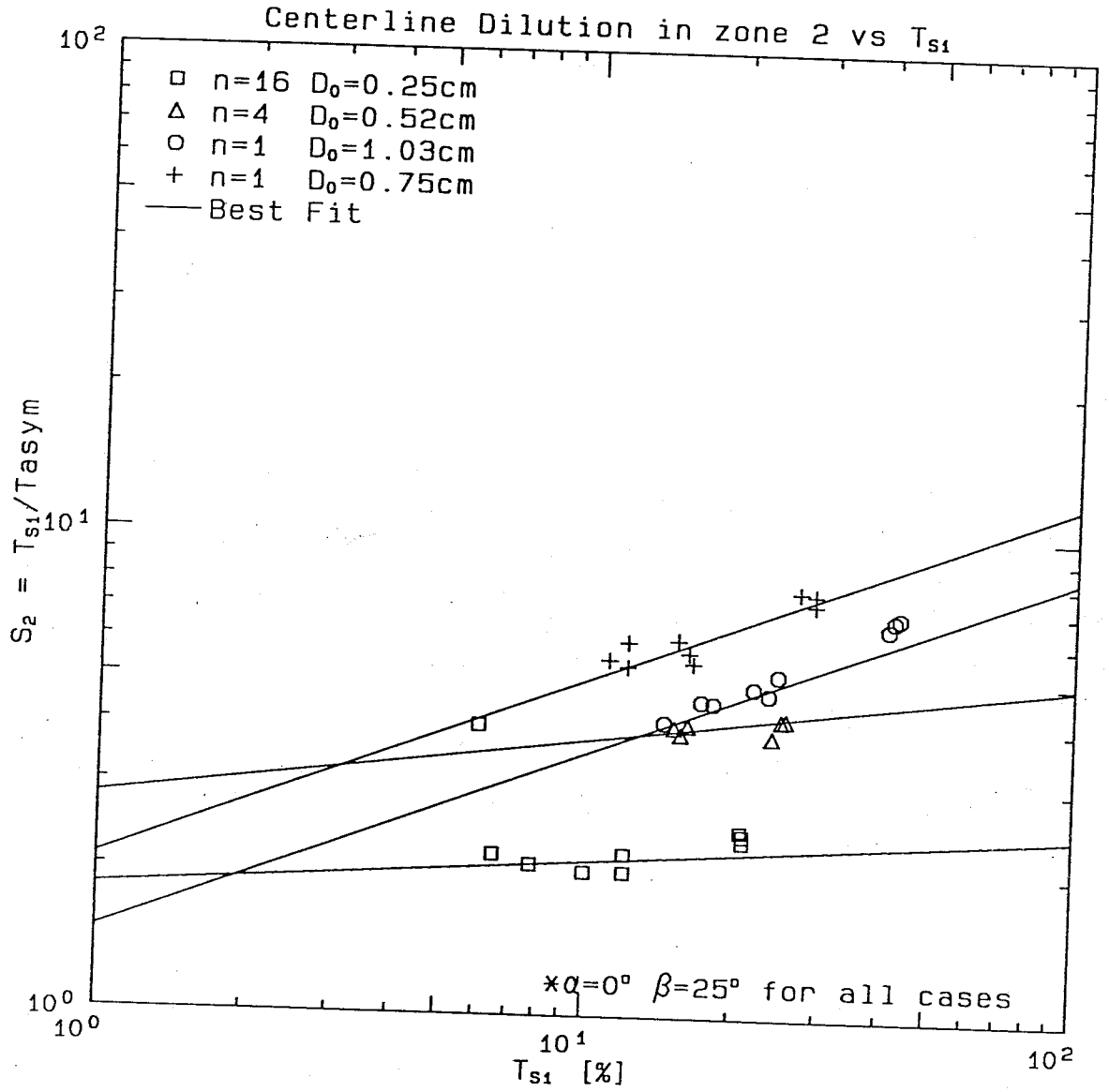

Figure 6.14 Intermediate field dilution S_2 versus T_{s1} $(\Delta T_{s1}/\Delta T_0)$.

6.3.3 Transition Distance (x_t)

The transition distance is measured from the end of the diffuser to a downstream position after which the vertical temperature distribution follows the same profile with the surface values equivalent to T_{asym}. The transition distance should be proportional to ℓ_Q and inversely proportional to H and n, given the same volume flux, momentum flux and buoyancy flux. Figure 6.15 shows the measured values of $x_t/(\sqrt{n}\ell_Q)$ versus ℓ_Q/H. There is a fair amount of scatter in the data; however, the overall dependency is approximately

$$\frac{x_t}{\sqrt{n}\ell_Q} = c_5(\frac{\ell_Q}{H})^{\xi_5} , \tag{6.14}$$

where ξ_5 is in the range of 1/4 to 3/8, while the corresponding range for c_5 is 200 to 270. In the unsteady case for which the thermal plume propagates backward in an arc to the source region, x_t is undefined. Hence, Equation (6.14) is valid only for $\ell_M/H > 1.0$, the criterion for a steady near field.

6.3.4 Temperature Decrease at the Beginning of the Intermediate Field

As the thermal plume leaves the diffuser zone and enters the intermediate field, the temperature excess decreases rapidly initially and eventually reaches an asymptotic value at some farther distance in the longitudinal direction as illustrated in Figure 5.33. The varying rate of temperature decline apparently follows a form of exponential decay with the decay parameter being a function of the discharge and ambient variables. In experiments with a small discharge flow rate and large water depth, such an exponential decay profile may not exist. This is because the radial gravitational spreading mechanism takes over relatively earlier (i.e., closer to the source), and the plume water very likely propagates back to the diffuser zone where it is en-

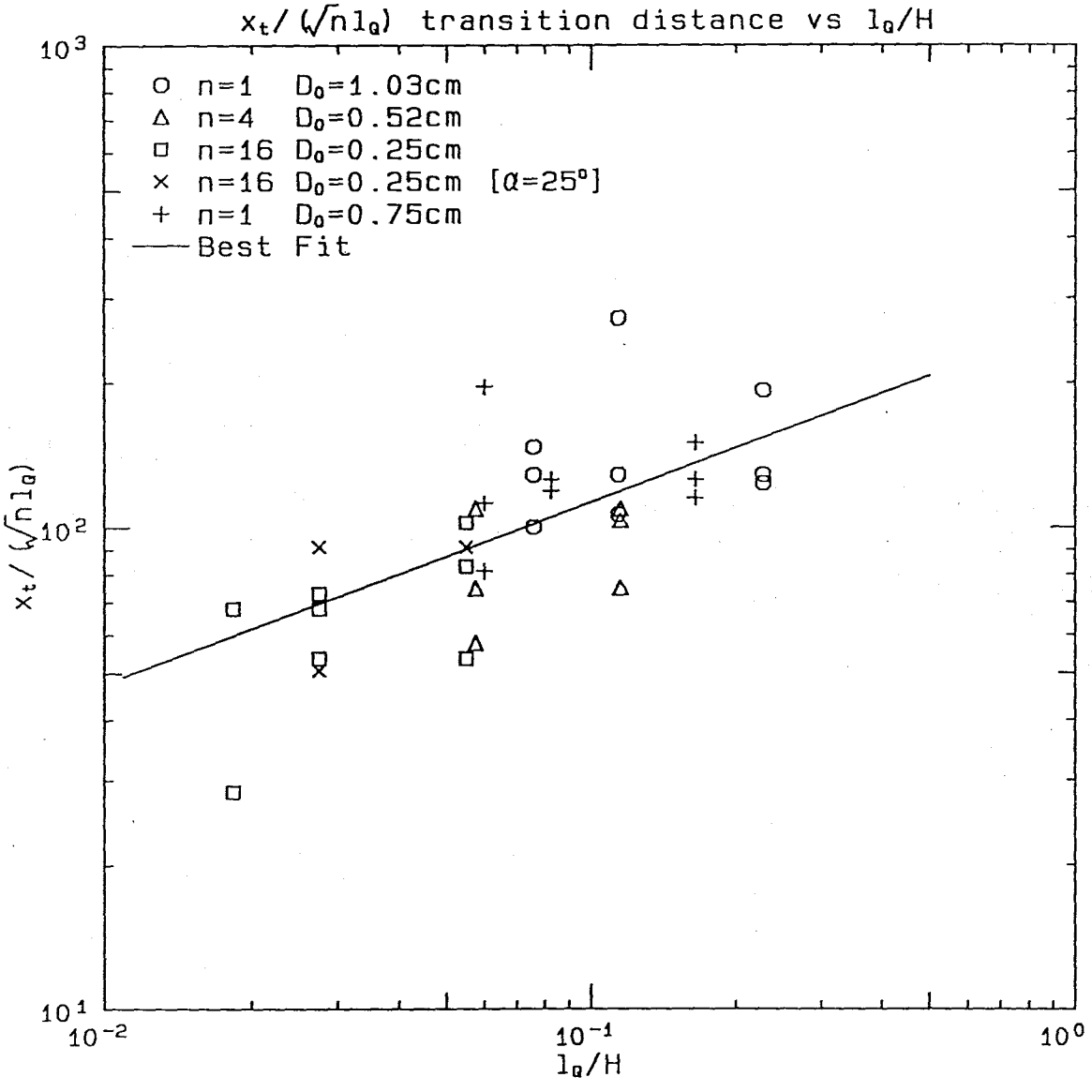

Figure 6.15 Transition distance x_t of the surface-buoyant jet region.

trained back into the plume (re-entrainment and the submerged source condition). This is equivalent to the unsteady near-field condition defined in Section 6.2.4.

In cases where the initial decay profile is defined, the normal temperature excess at a distance x' downstream of the end of the diffuser can be represented by

$$\Delta T(x') = \Delta T_{asym} + (\Delta T_{s1} - \Delta T_{asym})e^{-kx'} , \tag{6.15}$$

where k is the decay constant pertinent to the discharge and ambient characteristics and x' is the downstream distance referenced from the end of the diffuser (i.e., $x' = x - 90$ cm for the16-port diffuser, $x - 18$ cm for the 4-port cases, and is taken as x for the single-port case). The decay constant k can be determined empirically for each measured temperature profile by taking the reciprocal of x'_t ($k = 1/x'_t$) where x'_t is the distance from the end of the diffuser zone to the position where

$$\frac{\Delta T(x') - \Delta T_{asym}}{\Delta T_{s1} - \Delta T_{asym}} = e^{-1} . \tag{6.16}$$

The parameters that are expected to play an important role in the rate of temperature decay are H, ℓ_M and $\sqrt{n}\ell_Q$.

Figure 6.16 is a three-parameter plot of kH, $\sqrt{n}\ell_Q/H$ and $\ell_M/\sqrt{n}\ell_Q$; it shows the dependency of the empirically determined k on the other two parameters. For constant values of $\ell_M/\sqrt{n}\ell_Q$, kH is approximately proportional to $(\sqrt{n}\ell_Q/H)^{-2/3}$ as shown in Figure 6.17. Likewise, for constant values of $\sqrt{n}\ell_Q/H$, Figure 6.18 shows kH to be approximately proportional to $(\ell_M/\sqrt{n}\ell_Q)^{-1/2}$.

An equation for kH can therefore be formed based on approximate fittings to the data:

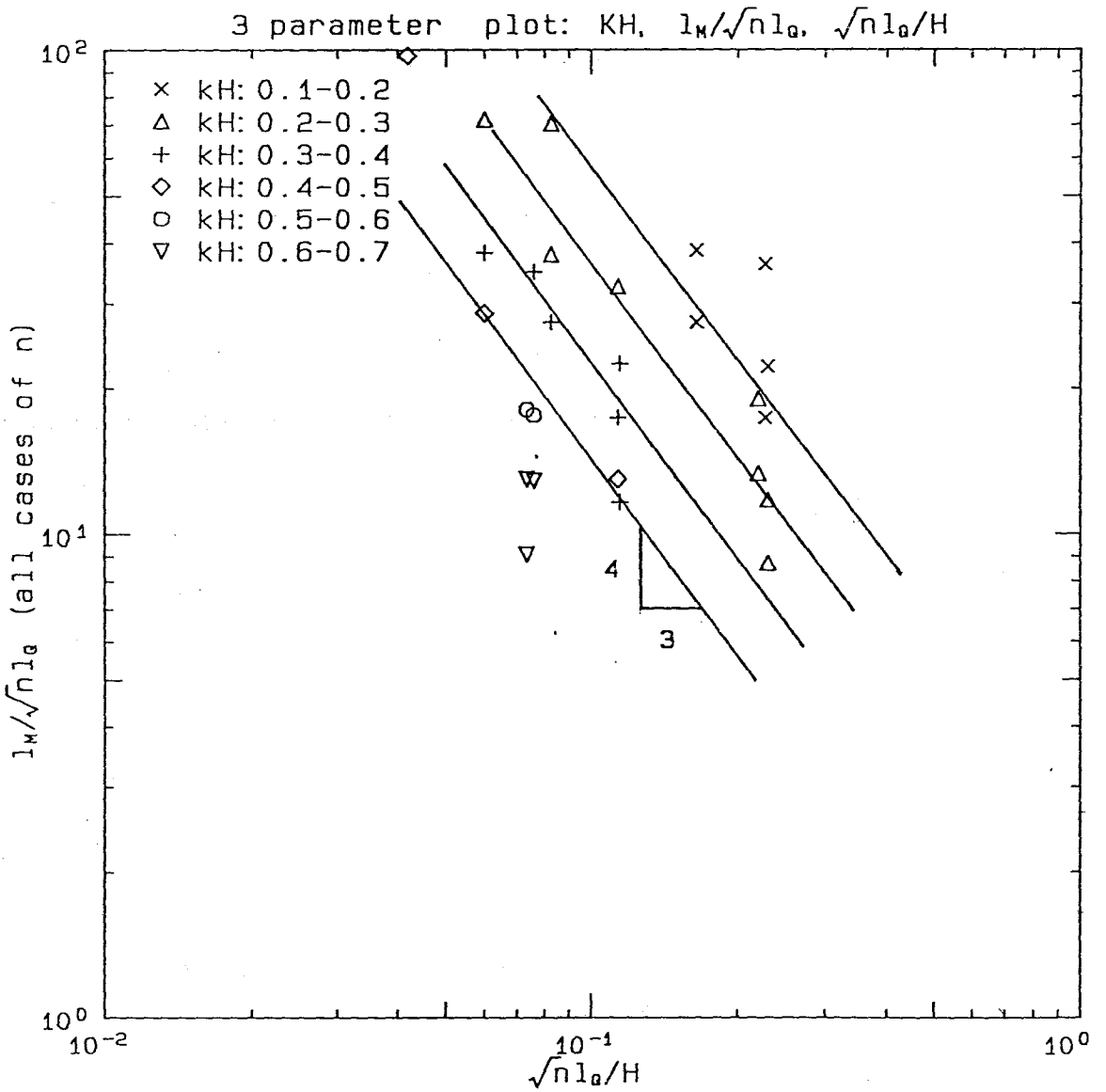

Figure 6.16 Three-parameter plot of the decay constant k, $\sqrt{n}\ell_Q/H$ and $\ell_M/\sqrt{n}\ell_Q$.

$$kH = c_6(\frac{\ell_M}{\sqrt{n}\ell_Q})^{-1/2}(\frac{\sqrt{n}\ell_Q}{H})^{-2/3} . \tag{6.17}$$

Equation (6.17) suggests a length-scale L_s, which equals

$$L_s = H^{1/3}\ell_M^{1/2}(\sqrt{n}\ell_Q)^{1/6} \tag{6.18}$$

for the temperature decay in the intermediate field. A universal profile for the temperature decline can be obtained by scaling the longitudinal distance with L_s, since

$$\frac{\Delta T_c(x') - \Delta T_{asym}}{\Delta T_{s1} - \Delta T_{asym}} = exp(-\xi_7\ x'/\ L_s) . \tag{6.19}$$

Figures 6.19a to 6.19d are measured temperature profiles $T_c(x')$ normalized according to Equation (6.19) for four groups of experiments, namely, $n = 16$, 4, 1 and the special case of $n = 1$ with $D_0 = 0.75$ cm. The longitudinal distance is normalized by L_s. Each set of temperature data has been smoothed, using a filter to remove the minor irregularities in the raw profiles. The irregularities are the result of uncertainties in the experimental and data-reduction procedures; their presence may lead to a spurious conclusion. In all cases, the (smoothed) normalized profiles agree satisfactorily with one another, and the slopes of the approximate fittings for each group of data give:

$\xi_7 = 0.15$ (for $n = 16$ cases)

$\xi_7 = 0.14$ (for $n = 4$ cases)

$\xi_7 = 0.15$ (for $n = 1$, $D_0 = 1.03$ cm cases)

$\xi_7 = 0.15$ (for $n = 1$, $D_0 = 0.75$ cm cases).

The close agreement of the ξ_7's from different data sets validates the length-scale L_s

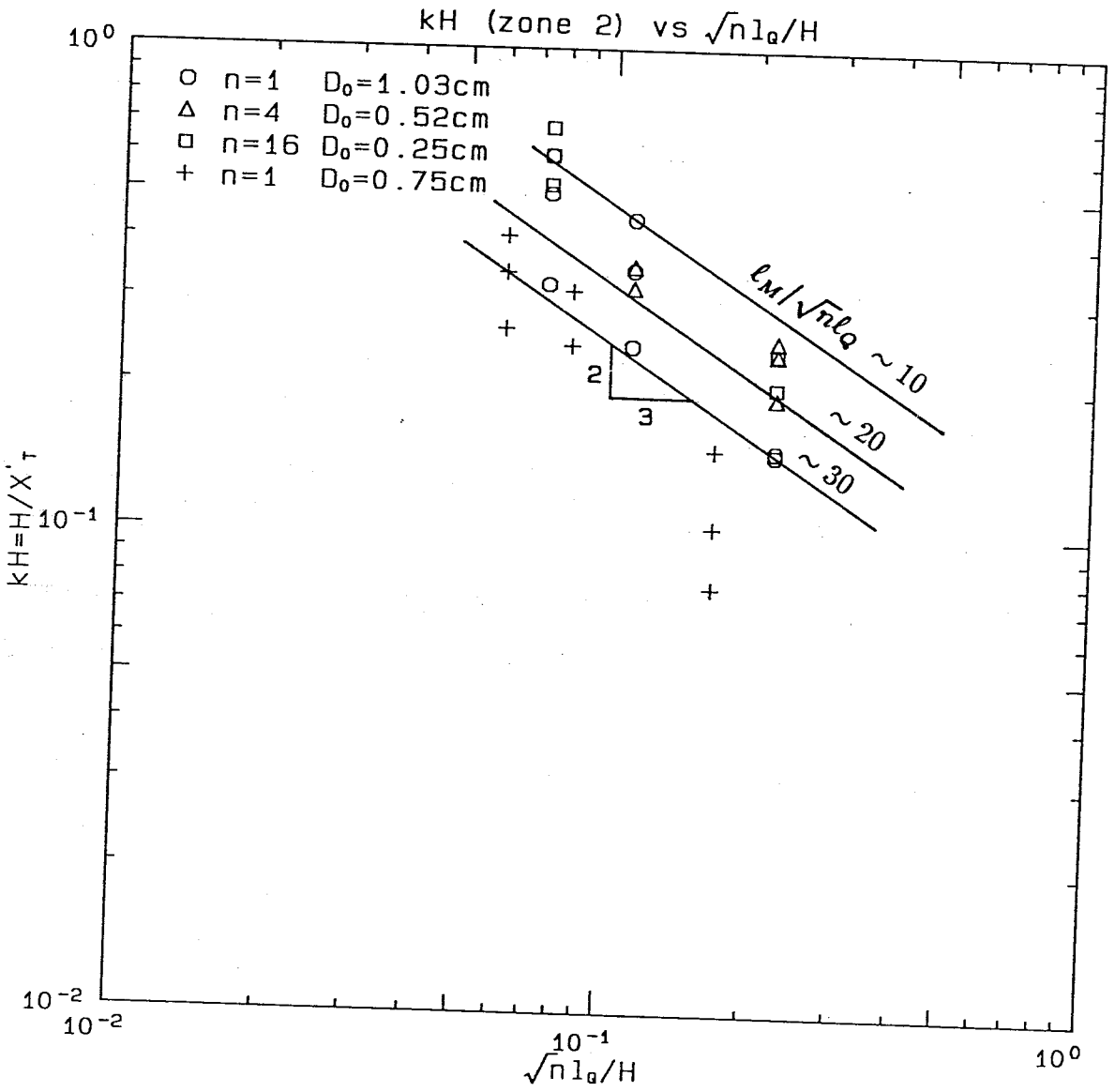

Figure 6.17 Dependence of kH on $\sqrt{n}\ell_Q/H$ for constant values of $\ell_M/\sqrt{n}\ell_Q$.

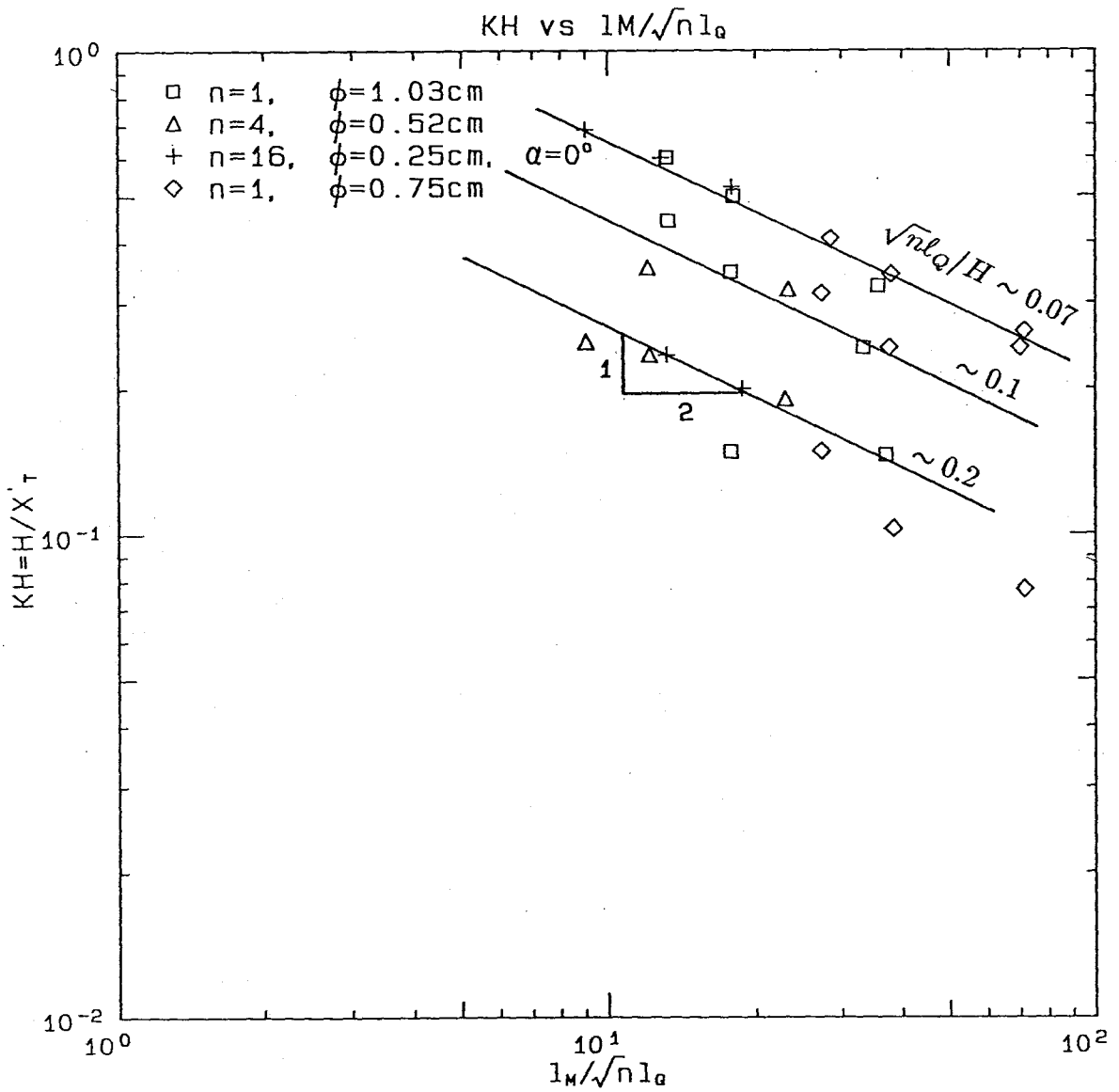

Figure 6.18 Dependence of kH on $\ell_M/\sqrt{n}\ell_Q$ for constant values of $\sqrt{n}\ell_Q/H$.

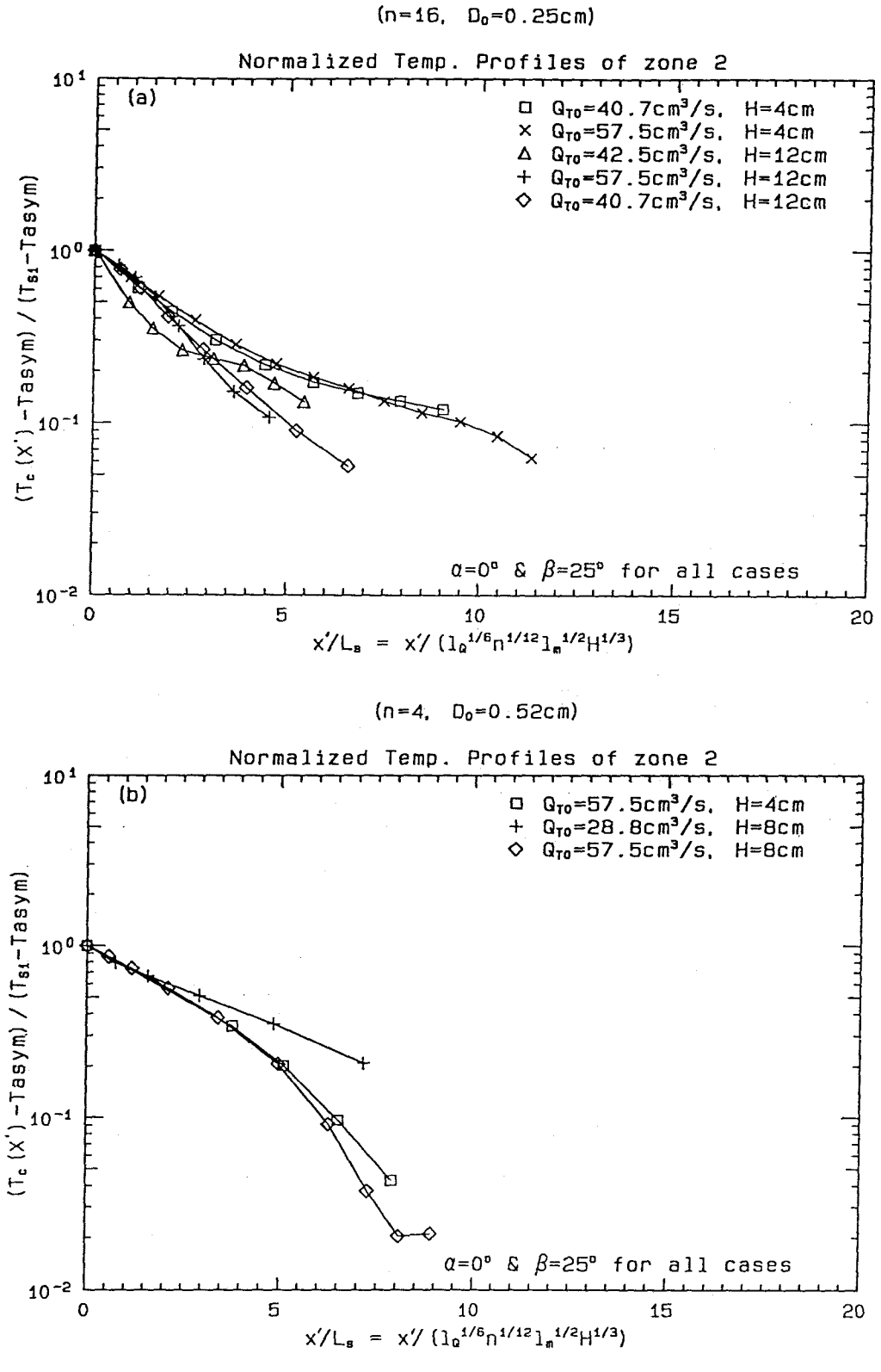

Figure 6.19 Normalized temperature profiles $T_c(x')$. a) $n = 16$; b) $n = 4$.

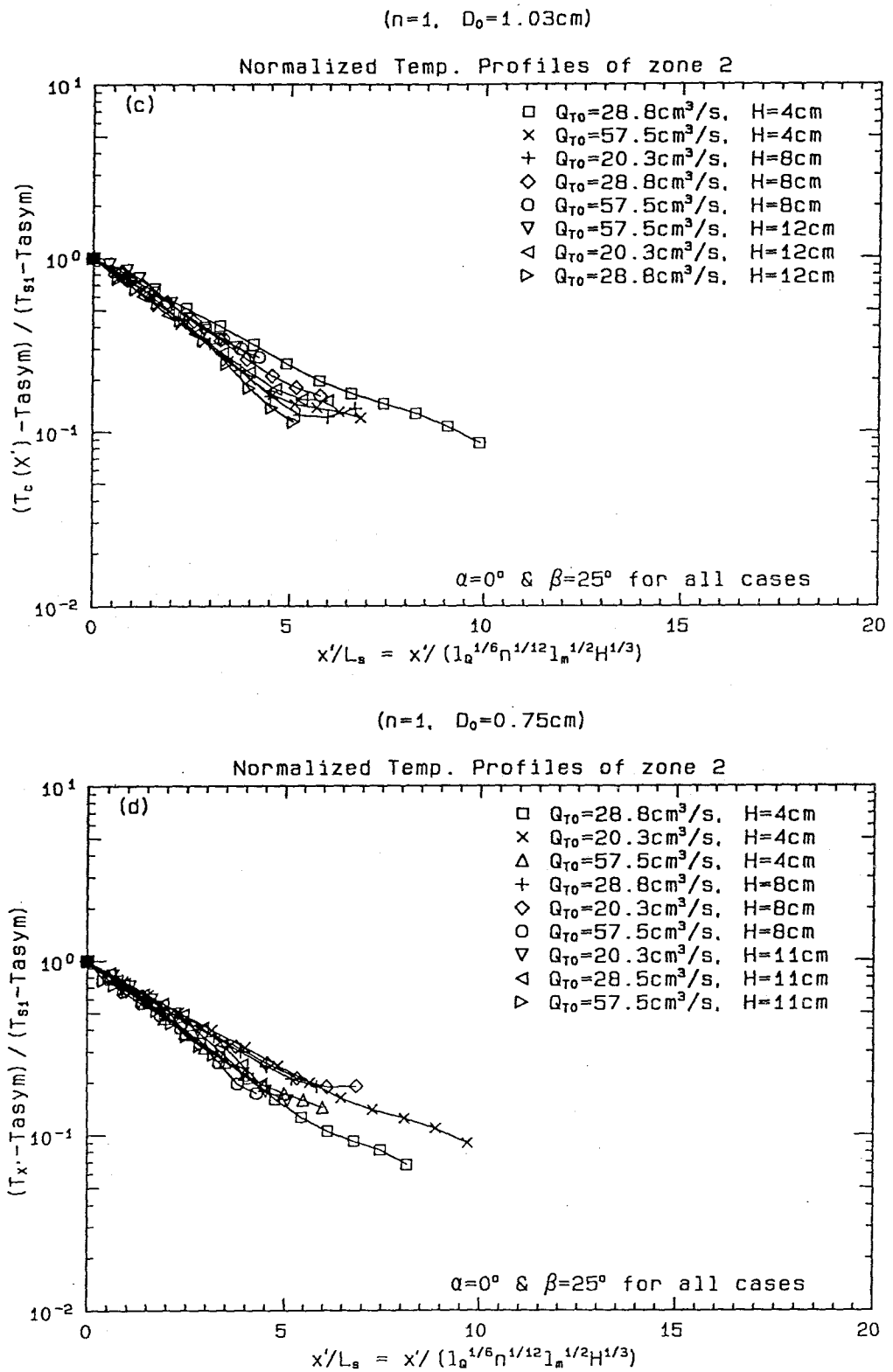

Figure 6.19 Normalized temperature profiles $T_c(x')$. c) $n = 1$ and $D_0 = 1.03$ cm; d) $n = 1$ and $D_0 = 0.75$ cm.

and confirms the hypothesized existence of a universal decay profile of temperature excess at the beginning of the intermediate field. The behavior of the temperature decline (at a rate initially rapid and later steady at a plateau value) is very similiar to that documented for surface thermal buoyant jets (Chu and Jirka, 1986). The length scales used for the surface buoyant jet, however, are very different because of the departure in the flow-field characteristics at the initial section. The surface-buoyant jet case has well-defined source conditions that are also the beginning of the flow field. In a diffuser plume, the start of the intermediate field or the decay section is not the well-defined source conditions, but rather, are the exit conditions of the diffuser zone. The characteristics at the initial section of the intermediate field section are themselves functions of the source parameters and the ambient parameters.

6.4 Distance from End of Diffuser to $\Delta T_c/\Delta T_0 \leq 0.2$ ($x_{0.2}$)

The last key result to be discussed is $x_{0.2}$, which is defined as the longitudinal distance (from the end of the diffuser) within which the temperature increase above ambient value is more than 20%. Figure 6.20 shows the dependency of $x_{0.2}/H$ versus $(n^{1/4}\ell_Q)/H$. A best-fit curve can be represented approximately by

$$\frac{x_{0.2}}{H} = 45\left(\frac{n^{1/4}\ell_Q}{H}\right)^{5/4} . \tag{6.20}$$

In experiments with high near-field dilution, $x_{0.2}$ may not exist (or may turn negative). The experimental data indicate that this zero condition occurs when $(n^{1/4}\ell_Q)/H < 0.1$.

6.5 Comparison with Field Data

A set of prototype data available and appropriate for comparison with the ex-

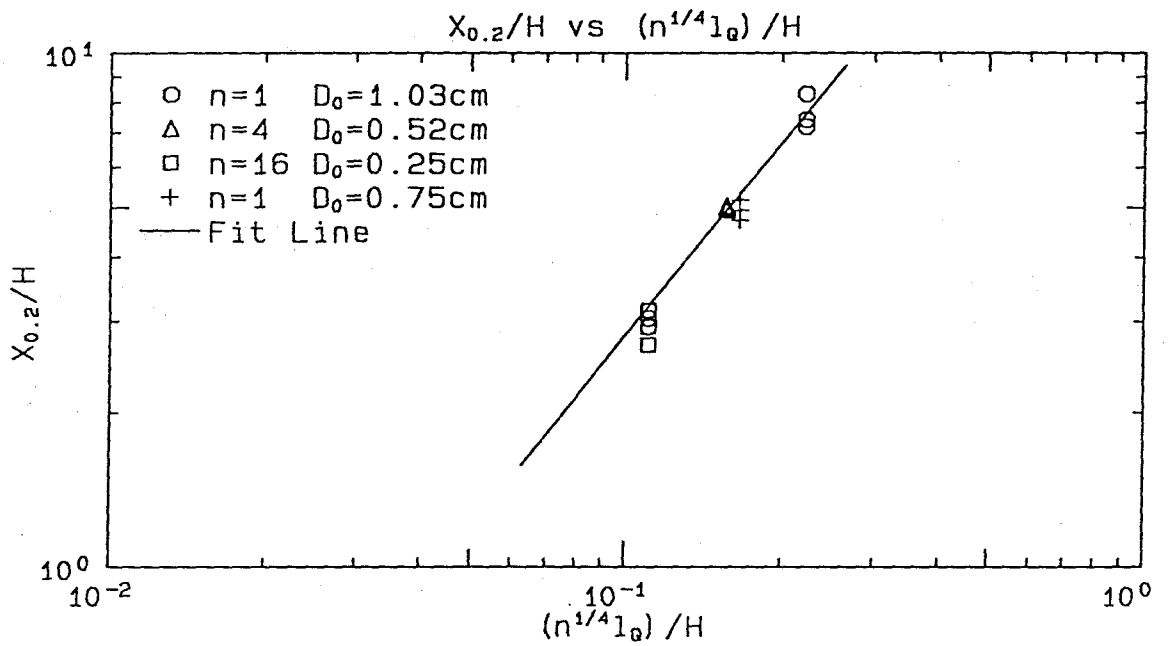

Figure 6.20 $x_{0.2}/H$ versus $(n^{1/4}\ell_Q)/H$.

perimental results and the simple jet hypothesis is the thermistor chain data collected for the thermal plume of SONGS. Two surveys were conducted on August 27, 1985, and August 29, 1985. Figure 6.21 shows the tracklines of the August 29 survey. Each trackline spans approximately 2200 m (7200 ft) across the Unit 2 and Unit 3 diffusers. The vertical coverage of the thermistor chain is about 3 m (10 ft) from the water surface. Continuous current measurements at fixed stations near the diffusers indicated a weak downcoast current of about 5 cm/s (0.1 knot) at the time of the survey. Furthermore, in summer months when the survey has been carried out, there is usually a natural thermal stratification in the water column. The current and the stratification deviate from the idealized conditions of the experiments.

Contour maps of the vertical temperature distribution can be produced from the measurements of each trackline. Figure 6.22 shows the temperature contour map for the trackline marked **E**. Detailed descriptions of the contours are given in the progress report of SONGS (Koh et al., 1973). The prominent feature observed in the vertical contour map is the presence of a cold plume instead of a warm one at the surface. This is due to the ambient stratification. The jet pushes the relatively cold water from the bottom to the top and this could result, depending on the ambient temperature profiles, in a cold surface plume which later sinks away from the diffuser.

The simple jet theory so far has no provision for stratification. However, it is widely accepted that the near field of thermal discharges is dominated by momentum force and that the buoyancy that is due to the temperature difference carried by the plume becomes important only farther downstream in the intermediate field. The relative importance of the momentum force, the buoyancy force and the ambient stratification is discussed in Chapter 3. Using SONGS diffusers and a typical summer ambient-temperature gradient ($\approx 0.5°/\text{m}$) as an example, it is found that ℓ'_M/H and ℓ'_B/H are approximately 0.7 and 0.5, suggesting that stratification ("typical" range)

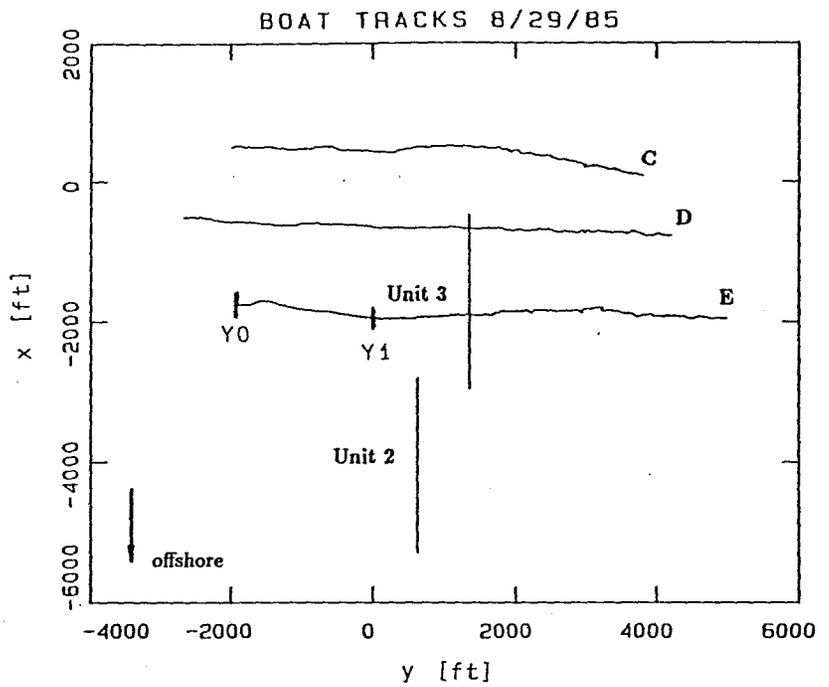

Figure 6.21 Tracklines of the August 29, 1985 thermistor chain data collected for the thermal plume of SONGS.

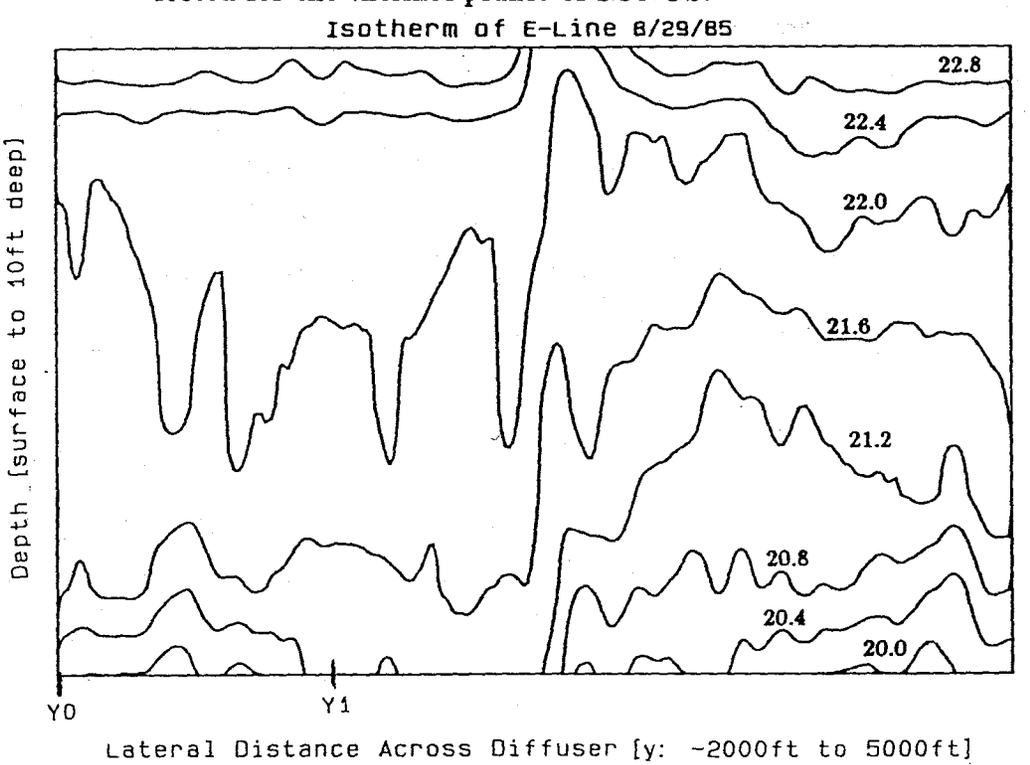

Figure 6.22 Temperature contour map for the trackline marked **E**. Contour values indicated are in [°C]. The vertical domain is from surface to 3 m depth.

may not affect the dynamics of the near-field plume. This hypothesis, if valid (for the prevailing configurations), suggests that the dilution in a weakly stratified receiving water body may be predicted by applying the simple jet theory to discrete layers of the water column.

Accordingly, the modified simple-jet model is used to calculate the surface temperature above the Unit 3 diffuser (trackline **E**, Figure 6.22). Because there was a natural variation of temperature in the lateral directions (Figure 6.21), it was difficult to define an ambient-temperature profile. In view of this, the temperature gradient at two sections, $Y0$ and $Y1$, approximately 1000 m (3310 ft) and 400 m (1307 ft) upcoast of the diffuser were chosen as the ambient profiles (Figure 6.23). The average temperature gradient (from surface to 3 m down the water column) at the two selected sections is approximately 0.7°C/m, which is stronger than the typical values. Although the simple jet model gives predictions of the temperature increase along the jet trajectory, which departs from the vertical depending on the horizontal and vertical jet initial angles, α and β, comparison with the measured temperature (which is in the vertical plane) is possible only at the near-surface level. The surface-temperature increase corresponding to the $Y0$ and $Y1$ ambient profiles can be calculated (based on an initial temperature difference of 11.1°C at the discharge level). The comparison is:

measured surface temperature above Unit 3 = 22.3°C,

prediction based on Y0 ambient profile = 22.2°C,

prediction based on Y1 ambient profile = 22.4°C.

Both predictions agree very well with the field-measured temperature; hence it is reasonable to assume that the stratification does not alter the dilution of the jets, even though the resulting temperature distribution is different. However, the above comparison is only approximate; temperature measurement from only one cross-section

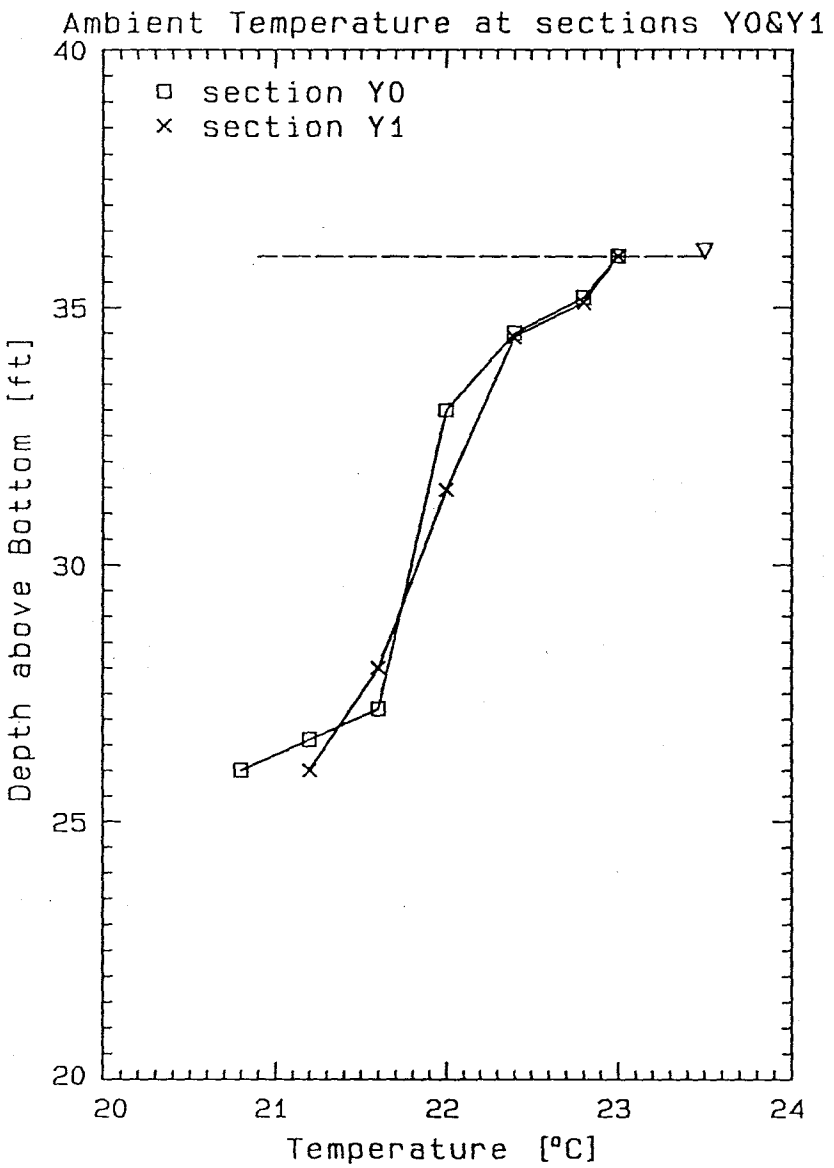

Figure 6.23 Ambient temperature profiles at the two sections, $Y0$ and $Y1$.

is available (i.e., only one centerline surface temperature measurement), and factors such as the the surface layer and the ambient current are not considered. More observations (both laboratory and prototype) with stratified ambient fluids are required before conclusive statements can be made.

6.6 Implication

The relationships for the mean characteristics developed in the previous sections can be used to assist in the hydraulic design of future thermal diffusers. The most important characteristics to be considered during designs of diffusers are the near-field and intermediate-field dilutions. For a proposed power plant with a total volumetric flow rate of Q_{T0}, an initial elevated temperature of ΔT_0, a typical water depth (at the proposed site) of approximately H, and a dilution objective of S, the simple jet model for the near-field dilution, Equation (6.2), can be used to determine the size of the individual jet, D_0, if β is provided. The choice of β depends on two factors. The first is the effective distance of ambient entrainment which is essentially the length of the jet trajectory, D_T, before reaching the water surface. For a straight-line trajectory, $D_T = H/\sin\beta$ and therefore smaller values of β seem more preferable. However, for a smaller angle, the bottom is more susceptible to scouring, which may not be desirable in many sites, especially those with turbidity problems. Values from $10°$ to $20°$ for β, as used in practice, are recommended. When the design size of the jets is chosen (approximately equal to calculated D_0), the number of jets required to discharge Q_{T0} within a normal range of discharge velocity (in the order of 5 m/s or less) can also be found. The actual nozzle diameter must be of the size such that the jet diameter at the vena contracta is D_0.

The modified simple-jet model, Equation (6.4), can be used for a more accurate prediction of the near-field dilution for a diffuser with the selected numbers of

ports, and adjustments of D_0 and n can be made as needed. For minimal jet interactions, the port spacing can be selected according to the $(s/H)_{cr}$, as discussed in Section 3.3.2 (Figure 3.4). Finally, the effect of the horizontal discharge angle from the diffuser axis, α, on the temperature distribution is not included in the empirical relationships. However, experimental observations indicate that α helps to distribute the heat over a wider area and the resulting temperature field (both horizontally and vertically) is more uniform compared to $\alpha = 0°$ discharge. The maximum increase in temperature is therefore less than that of $\alpha = 0°$.

An Illustrative Example

This example is to demonstrate the use of the modified simple jet theory in the preliminary design of a thermal diffuser, given the total discharge flow rate, the typical depth of water at the proposed site and the dilution objective. The discharge and ambient characteristics of SONGS are used for the illustration:

$$Q_{T0} = 52.4\,\mathrm{m}^3/\mathrm{s} \text{ (for each diffuser)};$$

$$\Delta T_0 = 11.1°\mathrm{C};$$

$$H \approx 10\,\mathrm{m}.$$

For a given dilution objective, e.g., 5:1, n can be determined from Equation (6.4):

$$\frac{1}{S} = 4.7(n)^{1/4}\left(\frac{\ell_Q}{H/\sin\beta}\right).$$

Since $\ell_Q = \sqrt{Q_{T0}/(u_0 n)}$ where u_0 is the discharge velocity of the individual jet, Equation (6.4) can be rewritten as:

$$\frac{1}{S} = \frac{4.7}{n^{1/4}(H/\sin\beta)}\sqrt{\frac{Q_{T0}}{u_0}}.$$

Choosing $\beta = 20°$, $\alpha = \pm 25°$ as recommended in the last section (also used in the SONGS diffusers) and $u_0 = 5$ m/s, n is found to be 46 for the required dilution of 5:1. This corresponds to a jet diameter D_0 ($D_0 = \sqrt{\pi/4(Q_{T0}/nu_0)}$) of 0.54 m. The value can be considered only approximate, however, since $n = 46$ is outside the range of experiments. According to Figure 3.5, for $\beta = 20°$, it is suggested that the jet-spacing-to-depth ratio (s/H) be greater than or equal to 2.3 to prevent jet merging. This means that the spacing of the jets s should approximately be 23 m for minimal jet interference. The length of the diffuser (for $n = 46$) is therefore 1035 m.

Comparing these values to the SONGS diffusers for Units 2 and 3, each of which have 63 ports with a jet diameter of 0.52 m and a jet spacing of 12.10 m, the modified simple jet theory estimates that fewer ports (but a similar jet size) are required. The estimated length of the diffuser (1035 m) is longer than that of the prototype (750 m) because a larger spacing was used to prevent jet merging in the above calculation. The predicted values from the modified simple jet theory differ from the hydraulic model study of the SONGS diffusers because the latter has been based on a more conservative dilution objective of 8:1. Further differences include the use of a sloping bottom (which gave an average water depth of 13 m compared to 10 m used in this example) and an unsteady tidal flow in the hydraulic model.

Use of the modified simple jet theory can be beneficial in the preliminary design of a thermal diffuser. However, an analysis of this type is intended only for preliminary screening and is not a substitute for a hydraulic model in the final design process.

7. Conclusions and Recommendations

7.1 Conclusions

Experiments were performed to determine the three-dimensional temperature distribution of the thermal field for submerged staged multiport diffusers in quiescent receiving water bodies. The experiments emphasized homogeneous ambient conditions, although a few exploratory experiments were carried out to investigate the influence of ambient stratification on the plume dynamics. By monitoring the change in behavior of the thermal plume in response to the changes in diffuser configurations, discharge characteristics and ambient conditions, the study aimed at gaining a better understanding of the physics of the thermal plume. However, the extraordinary number of variables involved in diffuser discharge (discussed in Chapter 3) makes a generic study difficult. The variables examined were the number of jets (n), jet diameter (D_0), water depth (H), horizontal angle of jet from the diffuser axis (α) and the total discharge flow rate (Q_{T0}); the port spacing, although important, was not varied in this set of experiments. Also, no experiments were made with an imposed ambient current.

Experimental observations support the hypothesis that the thermal plume can be divided into two regions: a near field (diffuser zone) in the vicinity of the diffuser and

an intermediate field (turbulent mixing zone surrounded by a gravitational spreading zone) downstream of the diffuser. The far field, characterized by passive dispersion, is excluded from the analysis because of the size limitation of the test basin.

The near field is dominated by momentum mixing and interaction of a number of three-dimensional jets. The width of the plume grows more or less linearly with downstream distance. The water column is partially mixed and potentially unstable (in shallow-water conditions) with diluted warm water recirculating to the jet efflux. The entrainment flow is highly three-dimensional. The lateral temperature profiles (across the diffuser) appear to have Gaussian distributions, but are relatively irregular in both the longitudinal and vertical directions, reflecting the influence of the individual jets.

Beyond the diffuser into the intermediate field, a surface buoyant layer usually forms either from deflection of the jets in the diffuser zone, or from stratification of an unstable near field. At the beginning of the intermediate field, turbulent mixing is still the dominant process and the layer behaves like a large surface buoyant jet. This is referred to as the turbulent mixing zone. The temperature profile in the longitudinal direction declines exponentially, and eventually approaches a plateau value at some farther distance where the inertial force diminishes. Since the momentum and heat fluxes are not replenished beyond the diffuser, the buoyancy force becomes progressively more important with downstream distance. The flow field evolves gradually from a turbulent mixing zone with entrainment in both lateral and vertical directions to a gravitational spreading zone where activity is largely limited to the horizontal directions. The plume propagates forward because of the residual momentum from the turbulent mixing zone, and spreads radially because of the density difference between the plume and its immediate surroundings. Thus, this region will extend laterally as well as in the downstream direction with time. Temperature in this zone

is relatively stable and steady, except near the front of the plume, provided heat loss is not significant. In cases of deep receiving water and small discharge momentum, the plume fluid in the gravitational spreading zone may eventually move back to the diffuser zone and result in the unsteadiness in the near-field region.

By coupling the experimental results with dimensional reasoning, the following conclusions can be drawn:

(1) The number of ports, n, and the length scales ℓ_Q ($\propto D_0$) and H are the significant governing parameters of the mean characteristics in both the near and the intermediate fields, providing that there is some buoyancy. The spacing of the jets has not been studied in detail, but it is also expected to be an important control.

(2) Comparison with previous theoretical models of staged diffusers indicates that the assumption of a vertically-mixed near field is not generally justified. Furthermore, the integral technique employed by those models gives only a first-order approximation of the dilution in the near field.

(3) The near-field dilution can be described reasonably well by the simple-jet model adjusted by a factor (function of n), to correct for the contribution from neighboring jets. The dependency of the factor on n has been established (as shown in Section 6.2.2):

$$\frac{1}{S} = \frac{\Delta T_{peak}}{\Delta T_0} = 4.7\left(\frac{n^{1/4}\ell_Q}{H/\sin\beta}\right) \qquad (\text{for } \beta > 10°)\,.$$

Comparisons with previous hydraulic model results show that the modified simple jet theory gives conservative prediction for the near-field dilution. This can be explained by the effect of the jet angle from the diffuser axis, α, which ranges from $\pm 20°$ to $25°$ in the various model

diffusers of the previous hydraulic model studies, but the analysis of the experimental results is based primarily on experiments with $\alpha = 0°$.

(4) The additional dilution in the intermediate field has been found to be relatively insensitive to the number of ports (Section 6.3.1).

(5) Approximate relationships of the other mean characteristics such as the lateral spreading rate of the plume, the characteristic thickness of the surface buoyant layer, the transition distance of the turbulent mixing zone in the intermediate field and asymptotic temperature excess have been established (Chapter 6). These relationships take the general form:

$$\phi_i = c_i(\frac{\sqrt{n}\ell_Q}{H})^{\xi_i} ,$$

where c_i and ξ_i are empirically-determined constants.

(6) The excess temperature profiles at the beginning of the intermediate field decline exponentially. A new length scale L_s has been established as a function of ℓ_M, $\sqrt{n}\ell_Q$ and H by fitting of experimental data:

$$L_s = \ell_M^{1/2}(\sqrt{n}\ell_Q)^{1/6}H^{1/3} .$$

By normalizing the downstream distance with L_s, the centerline temperature excess profiles of the experiments collapse approximately to a common exponential decay profile.

(7) The horizontal orientation of the jets at $\alpha = \pm 25°$ to the axis of the diffuser helps to reduce the near-field jet interference and spreads the plume over a wider area, thereby reducing the maximum temperature increase.

(8) Limited experiments with a stratified ambient (Appendix C) indicate that for weak stratification the near-field behavior is still dominated by the discharge momentum, and the ambient stratification does not significantly modify the dynamics of the plume mixing.

7.2 Recommendations for Future Work

The results regarding the effects of the diffuser length (L), the jet spacing (s), the horizontal as well as the vertical discharge angles (α and β) are not conclusive, and further laboratory investigations on these aspects are recommended. The insensitivity of the diffuser dilution on the number of ports (n) suggests that future model investigations should focus on smaller numbers of jets (i.e., in the range of 5–25), instead of on the large numbers as in some recent outfalls (e.g., $n = 63$ for SONGS).

Velocity measurements will help to resolve some of the uncertainties encountered in the analysis, such as the scaling problem caused by the Reynolds number effect. They will also be useful in determining the reduction in the dilution that is due to recirculation of diluted water to the plume, especially in the near field of a shallow water discharge.

The present analysis of the experimental data focuses on the centerline measurements only. Detailed analysis of the lateral temperature profiles obtained from the scanning experiments is recommended to gain a complete three-dimensional picture on the mixing of thermal plumes.

Collection of prototype data is strongly recommended to provide an adequate data base for model-to-prototype comparisons. The results will be useful in the evaluation of the performance of hydraulic model studies, e.g., the distorted models versus the undistorted models, and the role of Reynolds number in laboratory studies. The possibility of extrapolating the experimental results to a wider range of discharge and

ambient conditions for future design should be examined. Since there is almost always some ambient stratification of various degrees in the field, data from a systematic set of stratified experiments are required for appropriate comparisons.

REFERENCES

Abraham, G. (1965) "Entrainment Principle and its Restrictions to Solve Problems of Jets," *J. Hydraulic Research*, **3**, 1-23.

Abraham, G. (1970) "The Flow of Round Buoyant Jets Issuing Vertically in a Horizontal Direction," *Advan. Water Pollut. Res. Proc., Int. Conf. Water Pollut. Res., 5th Paper*, **III-15**, pp. 7.

Acres American Inc. (1974) "Perry Nuclear Power Plant, Thermal Hydraulic Model Study of Cooling Water Discharge," Buffalo, New York.

Adams, E. E. (1972) "Submerged Multiport Diffusers in Shallow Water with Current," M.S. thesis, R. M. Parsons Laboratory, Massachusetts Institute of Technology, Cambridge, Mass.

Adams, E. E. and Stolzenbach, K. D. (1977) "Comparison of Alternative Diffuser Designs for the Discharge of Heated Water into Shallow Receiving Water," *Proc. Conference on Waste Heat Management and Utilization*, **I**, pp. IIC/171-IIC/189, Miami, Florida.

Albertson, M. L., Dai, Y. B., Jensen, R. A. and Rouse, H. (1950) "Diffusion of Submerged Jets," *Transactions*, ASCE, December, 639-664.

Almquist, C. W. and Stolzenbach, K. D. (1976) "Staged Diffusers in Shallow Water," Report R76-30, R. M. Parsons Laboratory, Massachusetts Institute of Technology, Cambridge, Mass.

Almquist, C. W. and Stolzenbach, K. D. (1980) "Staged Multiport Diffusers," *J. Hydraulics Div.*, ASCE, **106**, HY2, 285-303.

Andreopoulos, J., Praturi, A. and Rodi, W. (1986) "Experiments on Vertical Plane Buoyant Jets in Shallow Water," *J. Fluid Mech.*, **168**, 305-336.

Argue, J. R. and Sayre, W. W. (1973) "The Mixing Characteristics of Submerged Multiple-port Diffusers for Heated Effluents in Open Channel Flow," IIHR Report No. 147, Iowa Institute of Hydraulic Research, University of Iowa, Iowa City, Iowa.

Baddour, R. E. and Chu, V. H. (1978) "Turbulent Gravity-stratified Shear Flows," Fluid Mech. Lab. Tech. Rep. 78-3, Department of Civil Engineering and Applied Mechanics, McGill University.

Brocard, D. N. (1977) "Hydrothermal Studies of Staged Diffuser Discharge in the Coastal Environment–Charlestown Site," Report 136-77/M296EF, September, Alden Research Laboratory, Worcester Polytechnic Institute, Holden, Mass.

Brocard, D. N. (1980) "Discussion on Staged Multiport Diffusers," *J. Hydraulics Div.*, HY10, October, 1723-1725.

Brocard, D. N., Beauchamp, C. H. and Hsu, S. K. (1979) "Analytical Predictions of Staged Diffuser Performance–Palisades Nuclear Generating Station," Report 84-79/M182EF, Alden Research Laboratory, Worcester Polytechnic Institute, Holden, Mass.

Brooks, N. H. (1980) "Synthesis of Stratified Flow Phenomena for Design of Outfalls," *Proceedings, Second International Symposium on Stratified Flows, IAHR*, Trondheim.

Brooks, N. H. and Koh, R. C. Y. (1965) "Discharge of Sewage Effluent from a Line Source into a Stratified Ocean," Intern. Assoc. for Hyd. Res., IXth Congress, Leningrad.

Bühler, J. (1974) "Model Studies of Multiport Outfalls in Unstratified, Stagnant or Flowing Receiving Water," Ph. D. thesis, University of California, Berkeley, Calif.

Cederwall K. (1971) "Buoyant Slot Jets into Stagnant or Flowing Environments," Report KH-R-25, W. M. Keck Laboratory of Hydraulics and Water Resources, California Institute of Technology, Pasadena, Calif.

Cederwall, K. (1970) "Dispersion Phenomena in Coastal Environments," *J. Boston Soc. Civ. Eng.*, January, 34-70.

Chen, J. C. (1980) "Studies on Gravitational Spreading Currents," Report KH-R-40, W. M. Keck Laboratory of Hydraulics and Water Resources, California Institute of Technology, Pasadena, Calif.

Chu, V. H. and Jirka, G. H. (1986) "Surface Buoyant Jets and Plumes," *Encyclopedia of Fluid Mechanics*, Chapter 25, pp. 1053-1083.

Elsayed, E. M. (1981) "Darlington G. S. "A" Thermal-Hydraulic Model Investigation of Submerged Multiport Diffuser for Offshore Discharge of Condenser-cooling Water," Report No. 81499, Flow Systems Laboratory, Ontario Hydro, Toronto, Ontario.

Fan, L. N. (1967) "Turbulent Buoyant Jets into Stratified or Flowing Ambient Fluids," Report KH-R-15, W. M. Keck Laboratory of Hydraulics and Water Resources, California Institute of Technology, Pasadena, Calif.

Fan, L. N. and Brooks, N. H. (1969) "Numerical Solutions of Turbulent Buoyant Jet Problems," Report KH-R-18, W. M. Keck Laboratory of Hydraulics and Water Resources, California Institute of Technology, Pasadena, Calif.

Frankel, R. J. and Cumming, J. D. (1965) "Turbulent Mixing Phenomena of Ocean Outfalls," *J. of Sanitary Engineering Div.*, ASCE, **91**, SA2, 39-59.

Fischer, H. B., List, E. J., Koh, R. C. Y., Imberger, J. and Brooks, N. H. (1979) *Mixing in Inland and Coastal Waters*, Academic Press, New York.

Harleman, D. R. F., Jirka, G. H. and Evans, D. H. (1973) "Experimental Investigation of Submerged Multiport Diffusers for Condenser Water Discharge with Application to the Northport Electric Generating Station," Technical Report 165, R. M. Parsons Laboratory, Massachusetts Institute of Technology, Cambridge, Mass.

Harleman, D. R. F., Jirka, G. H. and Stolzenbach, K. D. (1971) "A Study of Submerged Multiport Diffusers for Condenser Water Discharge with Application to the Shoreham Nuclear Power Station," Technical Report 139, R. M. Parsons Laboratory, Massachusetts Institute of Technology, Cambridge, Mass.

Hart, W. E. (1961) "Jet Discharge into a Fluid with a Density Gradient," *J. Hydraulics Div.*, ASCE, **87**, HY6, 171-200.

Hirst, E. A. (1971) "Analysis of Round, Turbulent, Buoyant Jets Discharged to Flowing Stratified Ambients," Oak Ridge National Laboratory, Report No. ORNL-4685, Oak Ridge, Tenn.

Hoult, D. P. and Weil, J. C. (1972) "Turbulent Plume in a Laminar Cross Flow," *Atmos. Environ.*, **6**, 513-531.

Iamandi, C. and Rouse, H. (1969) "Jet-Induced Circulation and Diffusion," *J. Hydraulics Div.*, ASCE, **95**, HY2, 589-601.

Imberger, J. (1983) "Tidal Jet Frontogenesis," *Mechanical Engineering Transactions Inst. Eng. Aust.*, **8**, 171-180.

Jain, S. C., Sayre, W. W., Akyeampong, Y. A., McDougall, D. and Kennedy, J. F. (1971) "Model Studies and Design of Thermal Outfall Structures Quad-Cities Nuclear Plant," Technical Report 135, Iowa Institute of Hydraulic Research, University of Iowa, Iowa City, Iowa.

Jirka, G. H. (1979) "Discussion on Line Plume and Ocean Outfall Dispersion," *J. Hydraulics Div.*, ASCE, **105**, HY12, 1573-1575.

Jirka, G. H. (1982) "Multiport Diffusers for Heat Disposal: A Summary," *J. Hydraulics Div.*, ASCE, **108**, HY12, 1425-1468.

Jirka, G. H. and Harleman, D. R. R. (1979) "Stability and Mixing of a Vertical Plane Buoyant Jet in Combined Depth," *J. Fluid Mech.*, **94**, 275-304.

Jirka, G. H. and Harleman, D. R. F. (1973) "The Mechanics of Submerged Multiport Diffusers for Buoyant Discharges in Shallow Water," Report R73-22, R. M. Parsons Laboratory, Massachusetts Institute of Technology, Cambridge, Mass.

Kannberg, L. D. (1976) "An Experimental and Analytical Investigation of Deep Submerged Multiple Buoyant Jets," Ph. D. thesis, Oregon State University, Corvallis, Oregon.

Kannberg, L. D. and Davis, L. R. (1977) "An Analysis of Deep Submerged Multiple-Port Buoyant Discharges," *J. Heat Transfer*, **99**, 648-654.

Kirby, J. T. and Brocard, D. N. (1979) "Hydrothermal Model Studies of a Diffuser Discharge in a Coastal Environment for the Jamesport Nuclear Power Station," Report 127-79/M71BF, Alden Research Laboratories, Worcester Polytechnic Institute, Holden, Mass.

Koh, R. C. Y. (1976) "Buoyancy-driven Gravitational Spreading," *Proc. Int. Conf. Coastal Eng. 15th*, **4**, pp. 2956-2975, Honolulu, Hawaii.

Koh, R. C. Y. (1983) "Wastewater Field Thickness and Initial Dilution," *J. Hydraulic Engineering*, **109**, 1232-1240.

Koh, R. C. Y. and Brooks, N. H. (1975) "Fluid Mechanics of Waste-Water Disposal in the Ocean," *Ann. Rev. of Fluid Mechanics*, **7**, 187-211.

Koh, R. C. Y., Brooks, N. H., Wolanski, E. J. and List. E. J. (1973) "Basin Model Studies of Diffusers, Hydraulic Investigations of Thermal Outfalls for the San Onofre Nuclear Power Plant, Progress Report No. 4," Tech. Memo No. 73-5, W. M. Keck Laboratory of Hydraulics and Water Resources, California Institute of Technology, Pasadena, Calif.

Koh, R. C. Y., Brooks, N. H., List, E. J. and Wolanski, E. J. (1974) "Hydraulic Modeling of Thermal Outfall Diffusers for the San Onofre Nuclear Power Plant," Report KH-R-30, W. M. Keck Laboratory of Hydraulics and Water Resources, California Institute of Technology, Pasadena, Calif.

Koh, R. C. and Fan, L. N. (1970) "Mathematical Models for the Prediction of Temperature Distributions Resulting from the Discharge of Heated Water into Large Bodies of Water," Report 16130, Tetra Tech, Pasadena, Calif.

Lantz, C. H. and Lisauskas, R. A. (1972) "Zion Discharge Model Study–Zion Station, Commonwealth Edison Company of Illinois," Alden Research Laboratory, Worcester Polytechnic Institute, Holden, Mass.

Lee, J. H. W. (1980) "Near Field Mixing of Staged Diffuser," *J. Hydraulics Div.*, ASCE, **106**, HY8, 1309-1325.

Lee, J. H. W., Jirka, G. H. and Harleman, D. R. F. (1977) "Modeling of Unidirectional Diffusers in Shallow Water," Report 228, R. M. Parsons Laboratory, Massachusetts Institute of Technology, Cambridge, Mass.

Lee, J. H. W., Jirka, G. H. and Harleman, D. R. F. (1979) "Heat Recirculation Induced by Thermal Diffusers," *J. Hydraulics Div.*, ASCE, **105**, HY10, 1219-1231.

Lee, J. H. and Jirka, G. H. (1979) "Multiport Diffuser as Line Source of Momentum in Shallow Water," *Water Resources Research*, **16**, 695-708.

Lee, S. L. and Emmons, H. W. (1951) "A Study of Natural Convection above a Line Fire," *J. Fluid Mechanics*, **11**, 353-368.

Liseth, P. (1970) "Mixing of Merging Buoyant Jets from a Manifold in Stagnant Receiving Water of Uniform Density," Report HEL 23-1, Hydraulic Engineering Laboratory, University of California, Berkeley, Calif.

List, E. J. (1982) "Turbulent Jets and Plumes," *Ann. Rev. Fluid Mech.*, **14**, 189-212.

List, E. J. and Imberger, J. (1973) "Turbulent Entrainment in Buoyant Jets and Plumes," *J. Hydraulics Div.*, ASCE, **99**, HY9, 1461-1474.

Liu, S. L. (1976) "Mixing of Submerged Two-dimensional Buoyant Jets in Uniform Bodies of Water in the Absence and Presence of Wind Action," Hydraulic Engineering Laboratory, Technical Report HEL 23-5, University of California, Berkeley.

Mih, W. C. and Hoopes, J. A. (1972) "Mean and Turbulent Velocities for Plane Jet," *J. Hydraulics Div.*, ASCE, **98**, HY7, 1275-1294.

Morton, B., Taylor, G. I. and Turner, J. S. (1956) "Turbulent Gravitational Convection from Maintained and Instantaneous Sources," *Proc. R. Soc. London Ser. A*, **234**, 1-23.

Murota, A. and Muraoka, K. (1967) "Turbulent Diffusion of a Vertically Upward Jet," *Proc. 12th Cong. IAHR*, **4**, pp. 60-70, Colorado.

Ng, K. Y. and Koh, R. C. Y. (1986) "Behavior of the SONGS Thermal Plume, a Progress Report," *San Onofre Report on 1985 Data*, Report 86-RD-26, Chapter 3, Southern California Edison Company.

Paddock, R. A. and Ditmars, J. D. (1978) "An Assessment of the Once-Through Cooling Alternative for Central Stream-Electric Generating Stations," Report ANL/WR-78-5, Argonne National Laboratory, Argonne, Illinois.

Papanicolaou P. N. (1984) "Mass and Momentum Transport in a Turbulent Buoyant Vertical Axisymmetric Jet," Ph. D. thesis, W. M. Keck Laboratory of Hydraulics and Water Resources, California Institute of Technology, Pasadena, Calif.

Priestley, C. H. B. and Ball, F. K. (1955) "Continuous Convection from an Isolated Source of Heat," *Quart. J. Roy. Met. Soc.*, **81**, 144-157.

Prych, E. A. (1972) "A Warm Water Effluent Analyzed as a Buoyant Surface Jet, Notiser och Preliminara Rapporter Series Hydrologi," Nr 21, Sverires Meteorologiska och Hydrologiska Institut.

Rawn, A. M. and Palmer, H. K., (1929) "Pre-Determining the Extent of a Sewage Field in Sea Water," *Proceedings*, ASCE, **55**, 1167-1191.

Ricou, F. P. and Spalding, D. B. (1961) "Measurements of Entrainment by Axisymmetrical Turbulent Jets," *J. Fluid Mechanics*, **11**, 21-32.

Roberge, J. C. (1976) "Optimization of an Offshore Momentum Diffuser in Shallow Water–A Hydrothermal Model Study for the J. H. Campbell Electric Generating Station," Report 104-76/M182BF, Sept., Alden Research Laboratories, Worcester Polytechnic Institute, Holden, Mass.

Roberts P. J. W. and Toms, G. (1987) "Inclined Dense Jets in Flowing Current," *J. Hydraulic Engineering*, **113**, 323-341.

Roberts, P. J. W. (1977) "Dispersion of Buoyant Waste Water Discharged from Outfall Diffusers of Finite Length," Report KH-R-35, W. M. Keck Laboratory of Hydraulics and Water Resources, California Institute of Technology, Pasadena, Calif.

Roberts, P. J. W. (1979) "Line Plume and Ocean Outfall Dispersion," *J. Hydraulics Div.*, ASCE, **105**, HY4, 313-331.

Roberts, P. J. W. and Matthews, P. R. (1987) "Behavior of Low Buoyancy Jets in a Linearly Stratified Fluid," *J. Hydraulic Research*, **25**, 503-519.

Rouse, H., Yih, C. S. and Humphreys, H. W. (1952) "Gravitational Convection from a Boundary Source," *Tellus*, **4**, 201-210.

Schatzman, M. (1978) "The Integral Equations for Round Buoyant Jets in Stratified Flows," *J. Applied Mathametics & Physics (ZAMP)*, **29**, 608-620.

Schatzman, M. (1979) "An Integral Model of Plume Rise," *Atmos. Environ.*, **13**, 721-731.

Simpson, J. E. (1982) "Gravity Currents in the Laboratory, Atmosphere and Ocean," *Ann. Rev. Fluid Mechanics*, **14**, 213-234.

State Water Resources Control Board (1975) "Water Quality Control Plan for Control of Temperature in the Coastal and Interstate Waters and Enclosed Bays and Estuaries of California," State of California—the Resources Agency, Sacramento, Calif.

Stolzenbach K. D. and Harleman, D. R. F. (1971) "An Analytical and Experimental Investigation of Surface Discharges of Heated Water," Report 135, R. M. Parsons Laboratory, Massachusetts Institute of Technology, Cambridge, Mass.

Stolzenbach, K. D., Almquist, C. W., Adams, E. E. and Freudberg, S. A. (1976) "Analytical and Experimental Studies of Discharge Designs for the Cayuga Station at the Somerset Alternative Site," Report R76-21, R. M. Parsons Laboratory, Massachusetts Institute of Technology, Cambridge, Mass.

Wiuff, R. (1978) "Experiments on Surface Buoyant Jet," *J. Hydraulics Div.*, ASCE, **104**, HY5, 667-679.

Wolanski, E. J. and Koh, R. C. Y. (1973) "Preliminary Report on Secondary Circulation in Surface Buoyant Jets," Tech. Memo. 73-10, December, W. M. Keck Laboratory of Hydraulics and Water Resources, California Institute of Technology, Pasadena, Calif.

Wong, D. R. and Wright, S. J. (1988) "Submerged Turbulent Jets in Stagnant Linearly Stratified Fluids," *J. Hydraulic Research*, **26**, 199-223.

Wright, S. J. (1977a) "Effects of Ambient Crossflows and Density Stratification on the Characteristic Behavior of Round Turbulent Buoyant Jets," Report KH-R-36, May, W. M. Keck Laboratory of Hydraulics and Water Resources, California Institute of Technology, Pasadena, Calif.

Wright, S. J. (1977b) "Mean Behavior of Buoyant Jets," *J. Hydraulics Div.*, ASCE, **103**, HY5, 499-513.

Wright, S. J. and Wallace, R. B. (1979) "Two-dimensional Buoyant Jets in a Stratified Fluid," *J. Hydraulics Division*, ASCE, **105**, HY11, 1393-1406.

APPENDIX A. Sample Data Acquisition Program

This appendix contains a sample computer program which was used to collect the experimental data as previously described in Section 4.2.4. The software was used with an IBM PC which had a 512K random access memory and was equipped with an analog and digital input/output board to convert the voltage signals into digital data. The program, written in Turbo Basic language (Borland), issues a software trigger to initiate the conversion and collection procedures at the start of each experiment. The program also signals the end of the data acquisition and stores the digital data in files for future retrieval and analysis.

```
''''''''''''''''''''''''''''''''''''''''''''''''''''''''''''''''''''''''''''''''
'                                                                               '
'            Sample Program for Data Acquisition and Control                    '
'                                                                               '
''''''''''''''''''''''''''''''''''''''''''''''''''''''''''''''''''''''''''''''''

'Program : modify5.bas (updated modify4.bas)
Dim gcr%(8,20),adr%(8,20)
cls
print " *** Data Acquisition with position tracking ***"
print "     Channel10 (lateral) and Channel12 (longitudinal) "
Line Input "Experiment  : "; Title$
Input "Starting Probe  : "; PStart%
Input "Ending Probe :"; PMany%
input "Number of thermistors in each probe to monitor :";Tmany%
Input "gain desired (1,2,4,8) :";gain%
Input "Output Data Filenames (1&2)  :"; Fileout1$, Fileout2$
Input "Time of Experiment (Minute)  :"; Durmin
Badr=&H218                              'ADCSR-control/status
Badr1=Badr+1                            'ADGCR-gain/channel
Badr2=Badr+2                            'ADDAT-low byte
Badr3=Badr+3                            'ADDAT-high byte
Badr6=Badr+6                            'Digital input/output port (0/1)
Badr7=Badr+7                            'TMRCTR-timer/counte
Open Fileout1$ for output as 1
open fileout2$ for output as 2
Print #1, "Experiment  : "; Title$
Print #1, "Date  : "; Date$
Print #1, "Starting Probe  : ";PStart%
Print #1, "Ending Probe : "; PMany%
Print #1, "Number of Thermistors in each probe to monitor :";Tmany%
print #1, "Gain Selected  :"; Gain%
print #1, "Output filenames  :";Fileout1$;Fileout2$
Dursec=durmin*60
Durno%=Int(Dursec/(pmany%*tmany%/114))      'approx 114s/s
print "No of cycle : ";durno%
print #1, "No of Cycle : ";durno%
durnoa%=int(durno%/2)
durnob%=durno%-durnoa%
if gain%=0 then gainratio%=0
if gain%=2 then gainratio%=64
if gain%=4 then gainratio%=128
if gain%=8 then gainratio%=192
for P%=pstart% to pmany%
ch%=p%-1
if p% >= 5 then ch%=p%
gcr%(p%,1)=ch%+gainratio%
adr%(p%,1)=ch%*4
if P% >= 5 then adr%(p%,1)=(ch%-5)*4
for T%=2 to Tmany%
gcr%(p%,t%)=gcr%(p%,t%-1)
adr%(p%,t%)=adr%(p%,t%-1)+1
if adr%(p%,t%)<= 15 goto 3
adr%(p%,t%)=adr%(p%,t%)-16
gcr%(p%,t%)=gcr%(p%,1)+1
```

```
3    next T%
     next p%
     St1gcr%=11+gainratio%                'channel 11 devoted to ST1
     Out Badr,&H0                         'Board initialisation
     For I%=0 to 100
     Next I%
     LowByte=Inp(Badr2)
     HighByte=Inp(Badr3)
     Csr=&H10
     Out Badr, Csr
     Out Badr6, 0
     Print "Strike any key to initiate conversion !!!"
10   Dump$=Inkey$ :
     if Dump$="" then goto 10
     print "Time Started  :";Time$
     Print #1, "Time Started  :"; Time$
     For k%=1 to Durnoa%
     Out Badr1, 74                        'gcr=10+64, channel 10 and gain 2
     call takedata (1,Badr, Badr2, Badr3)
     out badr1,76                         'gcr=12+64, channel 12 and gain 2
     call takedata (1,badr,badr2,badr3)
     out Badr1, st1gcr%
     call takedata (1,badr,badr2,badr3)
     print #1,
     For t%=1 to tmany%
     for p%=pstart% to Pmany%
     out Badr6,adr%(p%,T%)
     Out Badr1,gcr%(p%,t%)
     call takedata (1,Badr, Badr2, Badr3)
     Next p% :print #1,
     Next t%
     Next K%
     For k%=1 to Durnob%
     Out Badr1, 74                        'gcr=10+64, channel 10 and gain 2
     call takedata (2,Badr, Badr2, Badr3)
     Out Badr1, 76                        'gcr=12+64, cahnnel 12 and gain 2
     call takedata (2,badr,badr2,badr3)
     out badr1,st1gcr%
     call takedata (2,badr,badr2,badr3)
     print #2,
     For t%=1 to tmany%
     for P%=pstart% to pmany%
     out Badr6,adr%(p%,T%)
     Out Badr1,gcr%(p%,t%)
     call takedata (2,Badr, Badr2, Badr3)
     Next p% :print #2,
     Next t%
     Next K%
40   Print #2,
     print "Time Finished : ";Time$
     Print #2, "Time Finished  :" ;Time$
     goto 50
     ADError:
     Print "A/D Error !!!"
     Print "Reduce Base Frequency"
     Stop
50   Close #1  :close #2
     sub takedata (io%,Badr, badr2, badr3)
20   Csr=Inp(Badr)
     Mask=&HC0
```

```
    A=Csr and Mask
    If (A=&HC0) or (A=&H40) Then goto ADError
    If A=&H80 Then 30
    goto 20
30  LowByte=Inp(Badr2)
    HighByte=Inp(Badr3)
    total=highByte*256+lowbyte
    print #io%, using "####"; total;
    end sub
    End
```

APPENDIX B. Sample Calibration Curves

Sample calibration curves for the thermistors and potentiometers are presented in this appendix. The calibration procedures have been described previously in Section 4.5 and are only summarized here.

The thermistors were calibrated individually by immersing the thermistor probes into a water bath of known temperature for a period of time (1 to 2 minutes) until stable readings were obtained. This procedure was then repeated for the range of experimental temperatures expected. Second-order regression analysis of the calibration data yielded zero-, first-, and second-order constants of the regression equation:

$$T(^{\circ}C) = a_0 + a_1 D + a_2 D^2 \,,$$

where D is the averaged digital reading over the time period with relatively stable signals. Since the characteristics of thermistors varied from one another, a separate calibration curve was required for each one. Figure B.1a is the calibration curve for the thermistor which was located inside the diffuser (in order to monitor the discharge temperature), while Figure B.1b is the curve for the bottom thermistor of the first probe. Correlation coefficients (R^2 values) were better than 0.998.

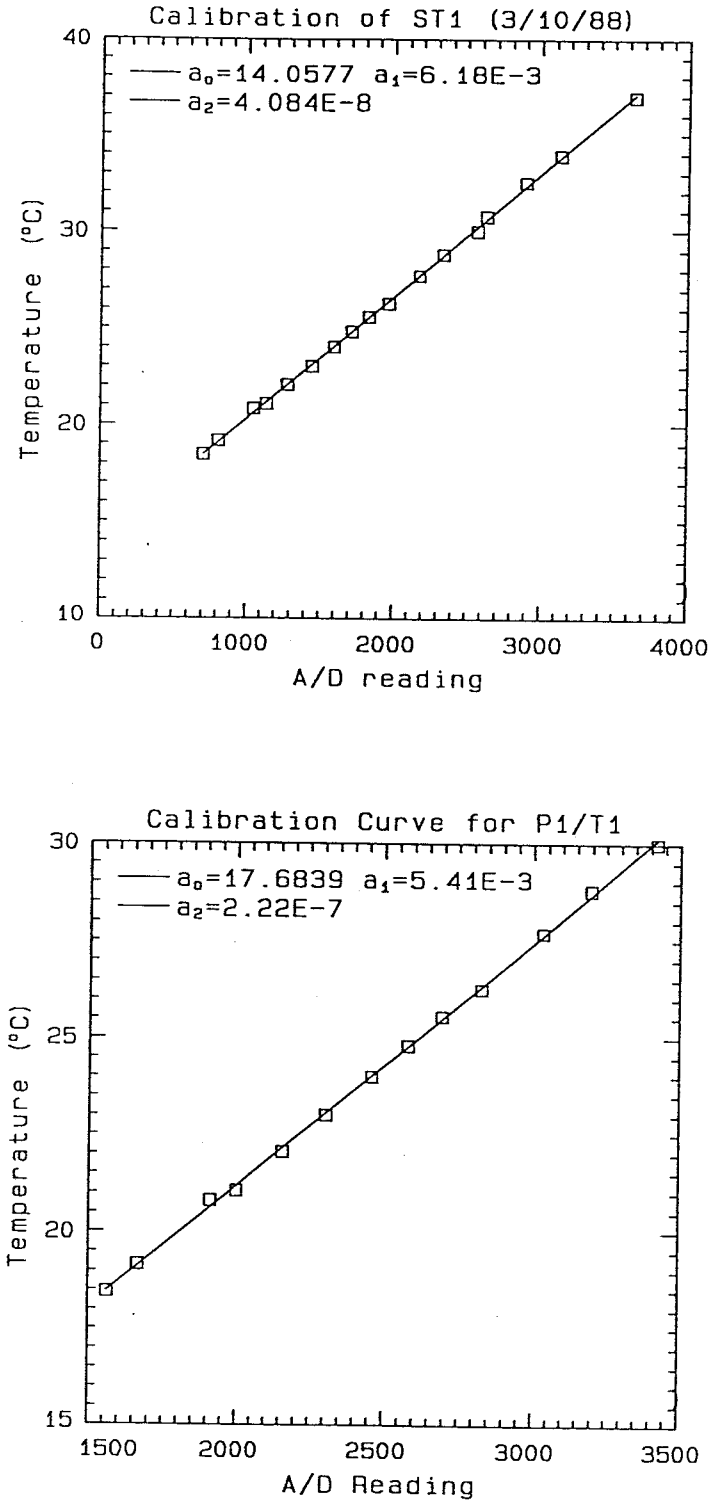

Figure B.1 Sample calibration curves for two thermistors. Second-order regression coefficients are denoted for each. a) ST1—thermistor located inside diffuser to monitor discharge temperature; b) P1/T1—bottom thermistor located on the first probe.

The calibration for the potentiometers was done similarly for relative lateral and horizontal positions. A first-order regression equation was found to be sufficient:

$$Y(m) = a_0 + a_1 D \, .$$

Figure B.2 is the calibration curve for the potentiometer located on the carriage. Again, correlation coefficients were better than 0.998.

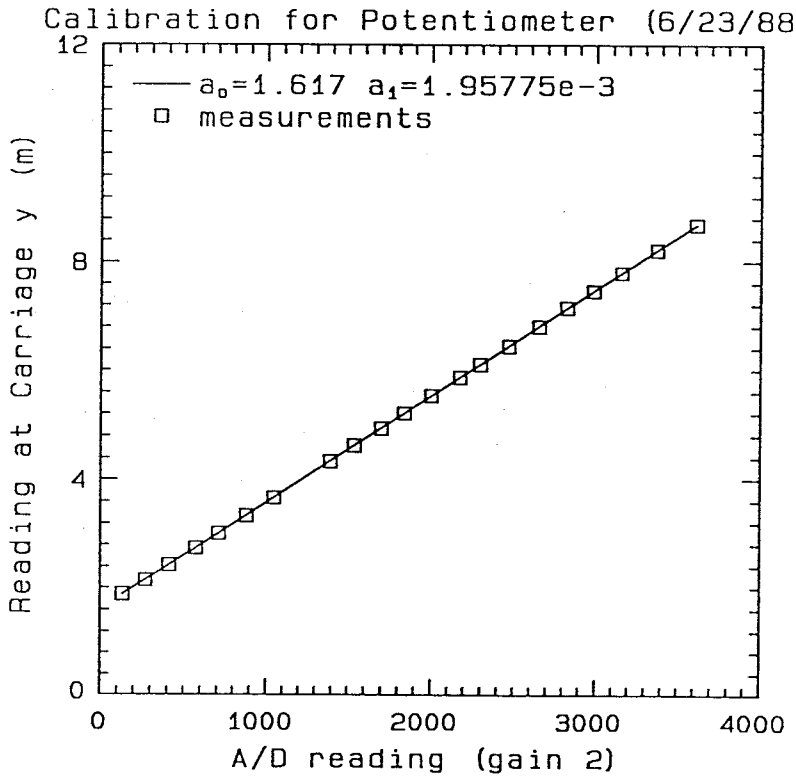

Figure B.2 Sample calibration curve for the potentiometer which located the position of the carriage. First-order regression coefficients are denoted.

APPENDIX C. Experimental Results–Stratified Ambient

C.1 Motivation

A few experiments have been performed where the receiving water in the basin is thermally stratified rather than homogeneous as for the previously described experiments. The water columns of inland and coastal waters are often thermally stratified in the summer, with higher temperature near the surface. For example, in the vicinity of the SONGS outfalls, the average temperature gradient between surface and bottom temperatures can be as high as 0.5°C/m from May to September. With the presence of such stratification, field monitoring of the discharges frequently results in surface plume manifestations cooler than the surroundings. Since a truly uniform ambient condition rarely exists in the field as in the main set of experiments, it has been decided to conduct a few exploratory experiments to study the effect of stratification on the dynamics of mixing in thermal discharges. However, the purpose is not to model a particular observed field temperature profile, which is a more difficult procedure than time permitted.

C.2 Experimental Preliminaries

Except for the preparation of a thermally stratified ambient, the experimental

procedures were similar to the experiments with uniform ambient conditions. The reference for the longitudinal distance ($x = 0$), and the measurement positions of the thermistor probes were also the same as in the uniform experiments (Chapter 5). Ambient currents were not examined. A stratified ambient was created by preparing two layers of water of different temperatures. The bottom layer was made colder than the equilibrium temperature by mixing water at room temperature with ice. The required amount of ice depended on the desired temperature difference between the two layers, the thickness of each layer and other factors such as the rate of heat gains and losses. When the ice melted and the water in the basin was uniformly mixed, water of normal temperature was added slowly at the surface to minimize mixing with the colder bottom water. This was done in the laboratory with the use of floating wooden boards about 1.0 m by 1.0 m in size. Water was introduced at a controlled rate to the center of the boards and allowed to flow from the edges to the top of the cold layer, thus reducing the entrance velocity. Assuming little mixing was induced during the process, a nearly two-layered thermal structure should theoretically be formed. The basin was then allowed to sit undisturbed for approximately three to five hours and during this period, heat exchange with the environment as well as thermal diffusion would occur, modifying the temperature gradient. The nearly two-layered profile would gradually evolve over time to form a smooth and continuous profile. The dynamic situation required that the ambient temperature distribution in the basin be monitored at frequent intervals to determine if the stratification pattern was suitable for the designated experiment.

Three different stratified basin experiments were made, but the desired stratification of 1.0°C/cm was not achieved. With a 200:1 scaling in the vertical direction and a g'_r (g'_p/g'_m ratio) of 0.75, this corresponds to 0.38°C/m in the prototype, a reasonable simulation of the field conditions. The first stratification pattern was prepared using approximately 800 lb of crushed ice mixed with water initially at 18.6°C. The

total depth of water after the ice melted was 11.0 cm (2.0 cm above the discharge level because of the presence of the false bottom shown in Figure 4.2) and the temperature of the mixture when uniformly mixed was calculated to be 14.5°C, allowing 10% for heat gain. A surface layer of 2.0 cm at 18.2°C was added as described. The idea was to construct an ambient with 2.0 cm of warmer water on the surface (about 18.6°C) and 2.0 cm of colder water (about 13.5°C) below forming a stratified water column of 4.0 cm above the discharge level.

In the experiment, the initial two-layered structure was not observed due to practical problems such as insufficient mixing within the 11.0 cm cold bottom layer before addition of the surface layer, heat gains from the walls and floor of the basin and heat loss from the surface during the settling period. Furthermore, the evolution of the temperature profiles with time shown in Figure C.1 suggests that the introduction of the surface layer generated significant mixing throughout the entire water column, thus weakening the stratification. Experiments 9307cl and 9307scan were performed at the end of the five-hour settling period and the final ambient profiles had only about 0.7°C temperature difference over the 4.0 cm water depth (0.07°C/m in the prototype). Thus, the water column could be considered only weakly stratified, much less than most field situations.

A second attempt was conducted to create a more significant stratification. The amount of ice used was increased to 2200 lb and the bottom layer was also raised to 12.0 cm, thus leaving 1.0 cm for the top layer. The resulting temperature pattern had a slightly stronger stratification of 1.4°C from the surface to the jet level (corresponding to 0.13°C/m in the prototype). Experiments 9312cl and 9312scan were carried out under this ambient condition, and $5\frac{1}{2}$ hours later when the residual current in the basin was negligible, another experiment (9312cl2) was performed. The ambient by then had developed into a much weaker stratification as in experiment 9307cl.

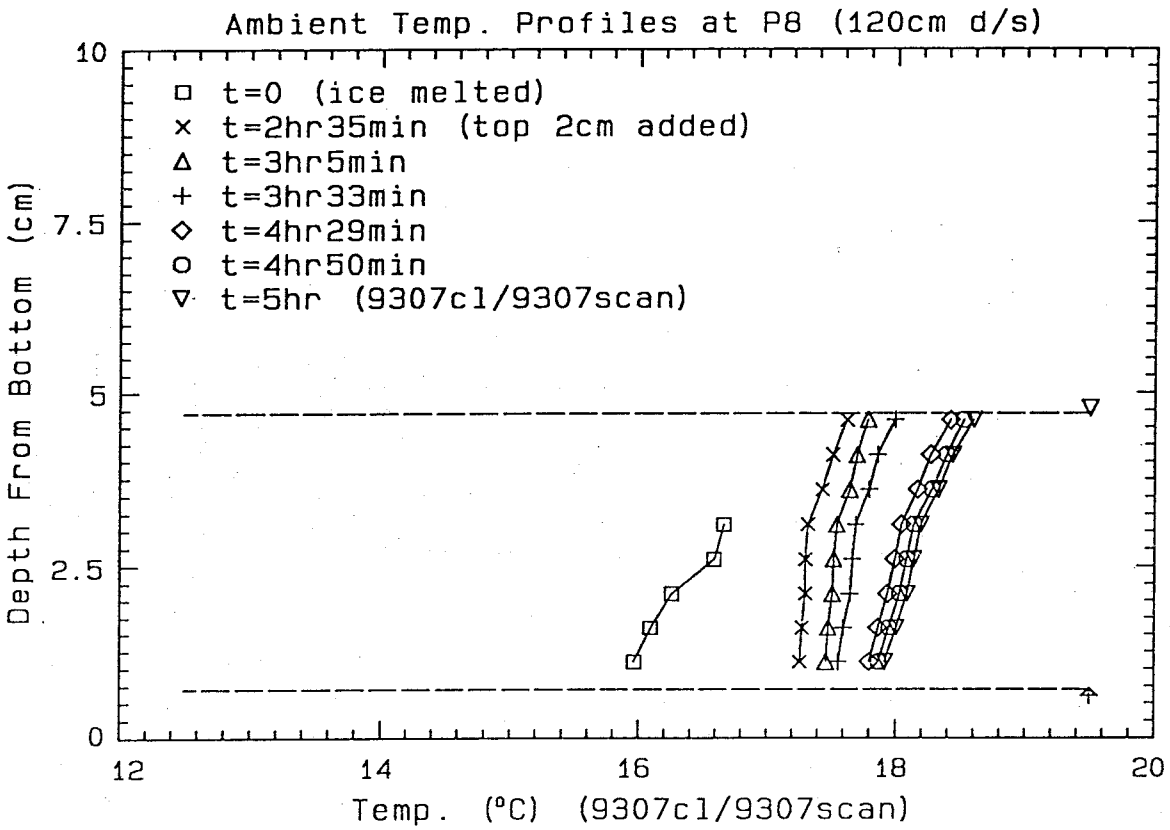

Figure C.1 Variations of the ambient temperature at $x = 120.0$ cm with time (first stratification process).

Figure C.2 is the variation of the ambient temperature distribution with time in this operation and similar behavior as before was observed. It is therefore concluded that the method employed in creating the ambient stratification needs to be improved. It is likely that the desired 1.0°C/cm (0.38°C/m prototype) temperature gradient can not be achieved in practice with such a shallow water depth over a large basin area using the procedures employed.

Future attempts would be more successful using water at room temperature in the lower layer, overlain with a layer of hot water heated well above the target; the water would then gradually cool and mix down to the thermocline. When the target surface temperature was reached, the experiment would begin.

C.3 Normalization of Measured Temperature Values

Before discussing the observations of the stratified ambient experiments, it is important to note that the normalized excess temperatures were obtained by subtracting the ambient temperature (which varied with depth) from the induced temperature field, and then normalizing with the temperature excess of the effluent over the ambient temperature at the discharge level, i.e.,

$$\frac{\Delta T}{\Delta T_{0b}} = \frac{T(z) - T_a(z)}{T_0 - T_a(0)} .$$

This is straightforward for the uniform case since the ambient temperature was the same everywhere, but for stratified experiments, there are two possible sources of confusion: (a) the profile of $\Delta T/\Delta T_{0b}$ depicts the temperature relative to the ambient stratification, and can be negative (the shape of the profile is <u>not</u> like that of the temperature itself); and (b) the temperature excess of the effluent over that of the ambient could be specified at other levels giving different results. For example,

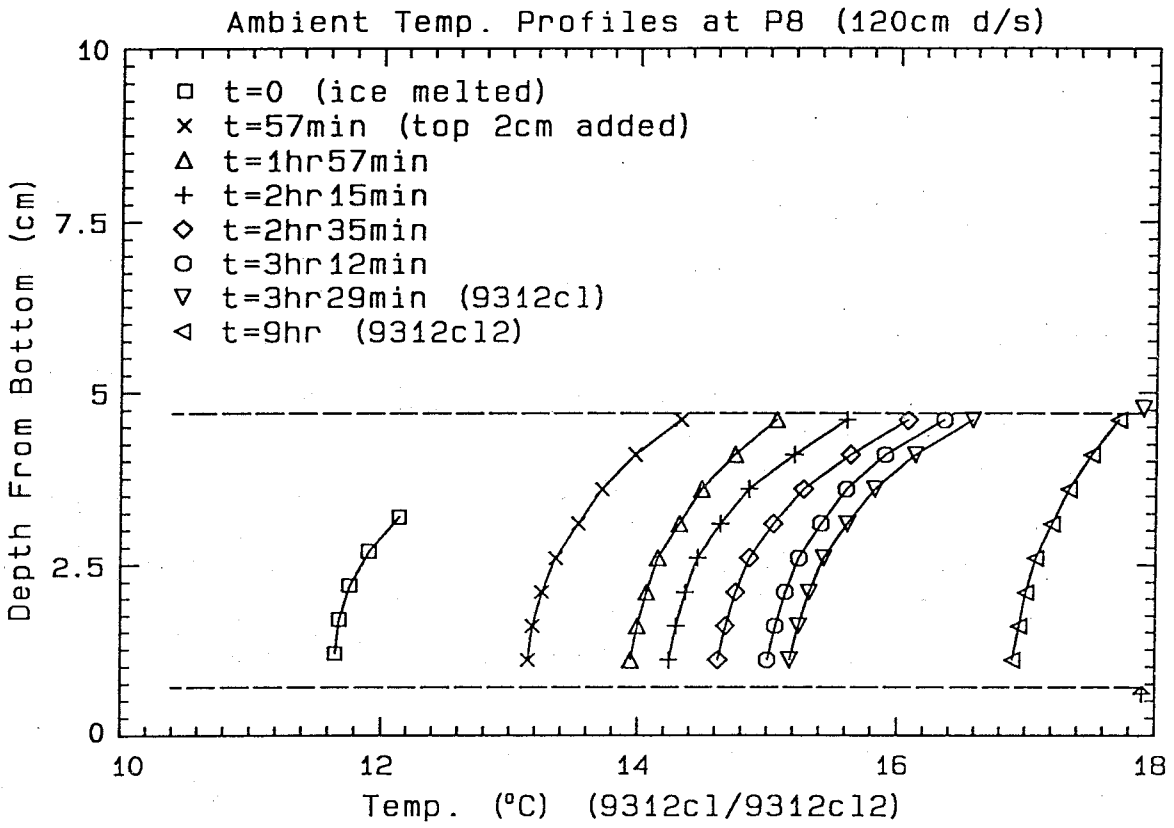

Figure C.2 Variations of the ambient temperature at $x = 120.0\,\text{cm}$ along the diffuser axis with time (second stratification process).

if the measurements were normalized with respect to the ambient temperature at the surface, the resulting normalized profiles would be larger than the present values because the ambient was warmer at the surface, giving a smaller denominator in the equation above. The reason for presenting the results this way is that regulations on thermal waste in coastal oceans usually refer to the temperature excess as the temperature above the ambient value at the same level.

C.4 Results from Stratified Experiments

Three centerline experiments (9307cl, 9312cl, 9312cl2) and two scanning experiments (9307scan, 9312scan) experiments were conducted under two ambient stratification conditions—weak (0.18 – 0.21 °C/cm) and small (0.35 °C/cm). Experiments 9307cl/9307scan and 9312cl/9312scan were based on the same diffuser configuration with 16 ports of 0.25 cm jet diameter, aligned in the offshore or downstream direction, and a discharge flow rate of 28.8 cm^3/s. With the same configuration as the others, experiment 9312cl2 was tested with a flow rate of 57.5 cm^3/s. The water depth used in all the experiments was 4.0 cm. The experimental conditions and the relevant parameters of each test are listed in Table C.1.

(i) The ambient temperature field

The initial temperature distributions in the basin are presented in Figure C.3 to Figure C.5 for experiments 9307cl/9307scan, 9312cl/9312scan and 9312cl2, respectively. With the exception of the 9307cl/9307scan profiles, the ambient of the experiments indicates the existence of lateral temperature gradients in addition to the vertical stratifications. The horizontal variations in temperature range from 0.25 °C to 0.4 °C and may have been caused by incomplete mixing in the bottom layer before introducing the surface layer.

Table C.1 Summary of the experiments with stratified ambient.

Parameter	9307cl/9307scan	9312cl/9312scan	9312cl2
n	16	16	16
D_0	0.25 cm	0.25 cm	0.25 cm
s	6.0 cm	6.0 cm	6.0 cm
α	0°	0°	0°
β	25°	25°	25°
H	4.0 cm	4.0 cm	4.0 cm
$\Delta T_a/\Delta H$	0.18°C/cm	0.35°C/cm	0.21°C/cm
Q_{T0}	28.8 cm^3/s	28.8 cm^3/s	57.5 cm^3/s
$\Delta T_0(z=0)$	15.3°C	19.6°C	19.8°C
Fr_0	37	33	64
$M_{i0}(M_{T0})$	65.8(1053) cm^4/s^2	65.8(1053) cm^4/s^2	263(4205) cm^4/s^2
$B_{i0}(B_{T0})$	7.0(112) cm^4/s^3	8.7(139) cm^4/s^3	18.9(303) cm^4/s^3
ℓ_M	8.72 cm	7.85 cm	15.0 cm
ℓ_Q	0.22 cm	0.22 cm	0.22 cm
ℓ_M/H	2.17	1.96	3.70
ℓ_Q/H	0.058	0.058	0.058
Re_0	1260	1260	2530
$-(g/dz)(d\rho_a/\rho_0)$	2.3x10^{-2} s^{-2}	5.0x10^{-2} s^{-2}	3.4x10^{-2} s^{-2}
$(\Delta\rho/\rho)_0$	4.0x10^{-3}	5.0x10^{-3}	5.4x10^{-3}

(ii) The induced temperature field

The resulting temperature distributions are presented with comparisons to their counterparts in uniform ambient conditions. Figures C.6a to C.6c are the normalized longitudinal temperature distributions of the experiment 9307cl, the weakly stratified case with a thermal gradient of 0.7°C over the 4.0 cm water depth. Throughout the entire region of measurements, which starts from the beginning of the diffuser to approximately 7.5 times the diffuser length, the surface profile indicates a lower $\Delta T/\Delta T_{ob}$, by an average of 2.0%, compared to the uniform ambient results. Going down the water column, the difference decreases until z/H=0.56 where the profiles (at $x/L \leq 2$) essentially coincide. Below this level, the 9307cl profiles increase continuously with depth compared to the uniform profiles, and the difference is as large as 4% near the bottom.

A very similar phenomenon is observed in the 9312cl experiment (Figures C.7a to C.7c) but with a larger difference, from 3.0% to 6.0%, in response to the more stratified ambient (1.4°C/4 cm). The increase in the difference, however, should not be interpreted as the physical realization of the difference in temperature, as discussed in Section C.3. It is, in fact, a result of the normalization scheme (Section C.3), since $T_a(H)$ is higher in the case of a stronger stratification, and therefore, $T(H) - T_a(H)$ is smaller compared to the weaker stratified case and the uniform case. The discrepancy between the normalized profiles in Figures C.7 diminishes at approximately z/H=0.56. Comparison of the $\Delta T/\Delta T_{ob}$ profiles of the third experiment (9312cl2) and the uniform case in Figures C.8a to C.8c reveals an average difference of 3.5% over the entire measurement region despite a weaker initial stratification of 0.9°C/4.0 cm.

Examples of the normalized temperature excess in the vertical direction at various downstream positions (x/L) are shown in Figures C.9a to C.9d for 9307cl and 9312cl, together with the results of the uniform ambient experiment 0816cl. The profiles in the diffuser zone (Figures C.9a and C.9b) have similar geometry over the full depth, but the magnitudes decrease with an increasing degree of stratification.

Beyond the diffuser region, the stratified experiments have similar $\Delta T/\Delta T_{ob}$ distributions with the 9312cl profiles constantly staying lower than the 9307cl profiles. Near the surface, the $\Delta T/\Delta T_{ob}$ varies with the strength of the ambient stratification as previously discussed. The profiles of the uniform case, however, have steeper gradients (because of the normalization method) and therefore become smaller in magnitude than the 9307cl and 9312cl experiments shortly down the water column. The normalized profiles, again, should not be taken as that of the resulting temperature (which may be very different in shape).

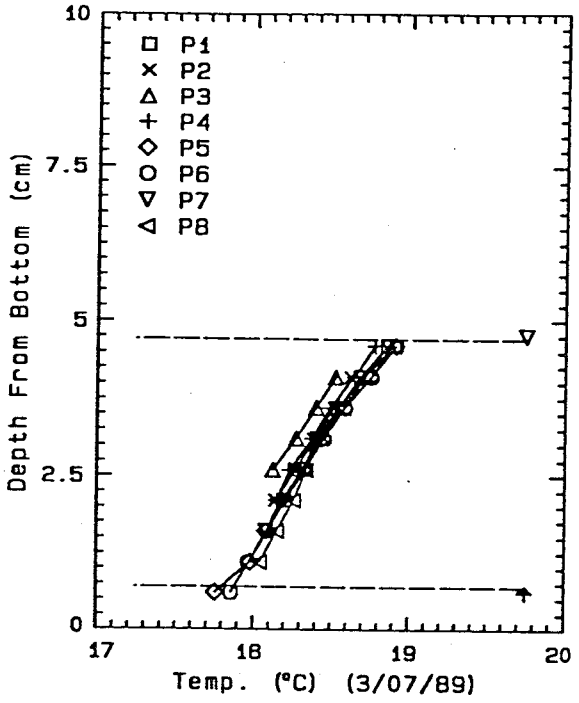

Figure C.3 Ambient temperature distribution of experiment 9307cl. P1–P8 (at 30.5 cm spacing; P1 at $x = -1.9$ cm) are the positions of the thermistor probes.

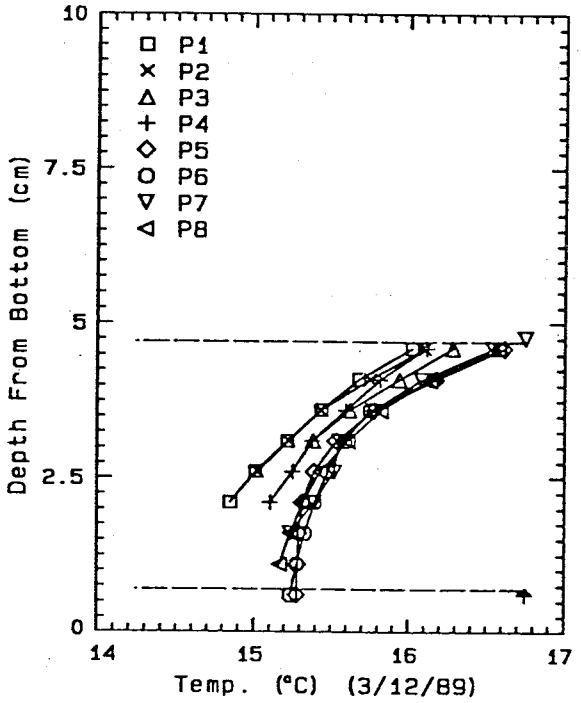

Figure C.4 Ambient temperature distribution of experiment 9312cl. P1–P8 (at 30.5 cm spacing; P1 at $x = -1.9$ cm) are the positions of the thermistor probes.

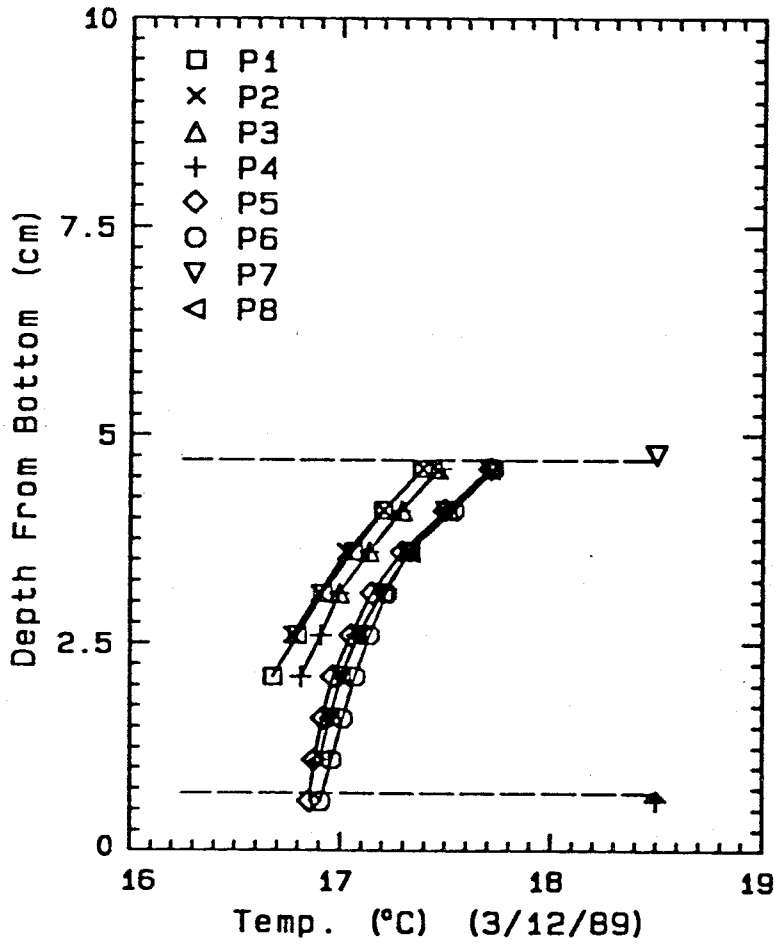

Figure C.5 Ambient temperature distribution of experiment 9312cl2. P1–P8 (at 30.5 cm spacing; P1 at $x = -1.9$ cm) are the positions of the thermistor probes.

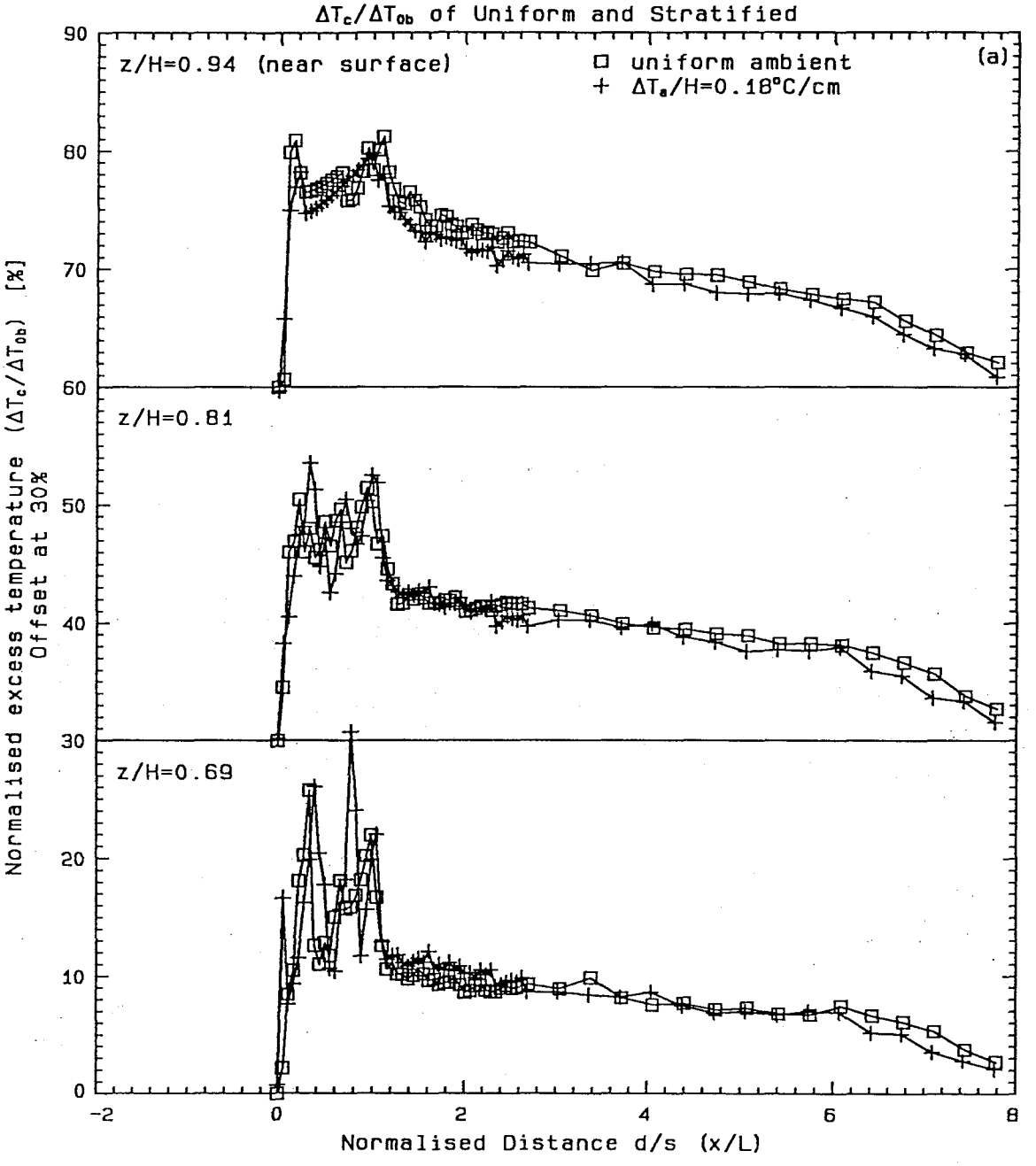

Figure C.6a Comparison of normalized temperature excess along diffuser axis at near-surface levels for experiment 9307cl and the uniform experiment 0816cl.

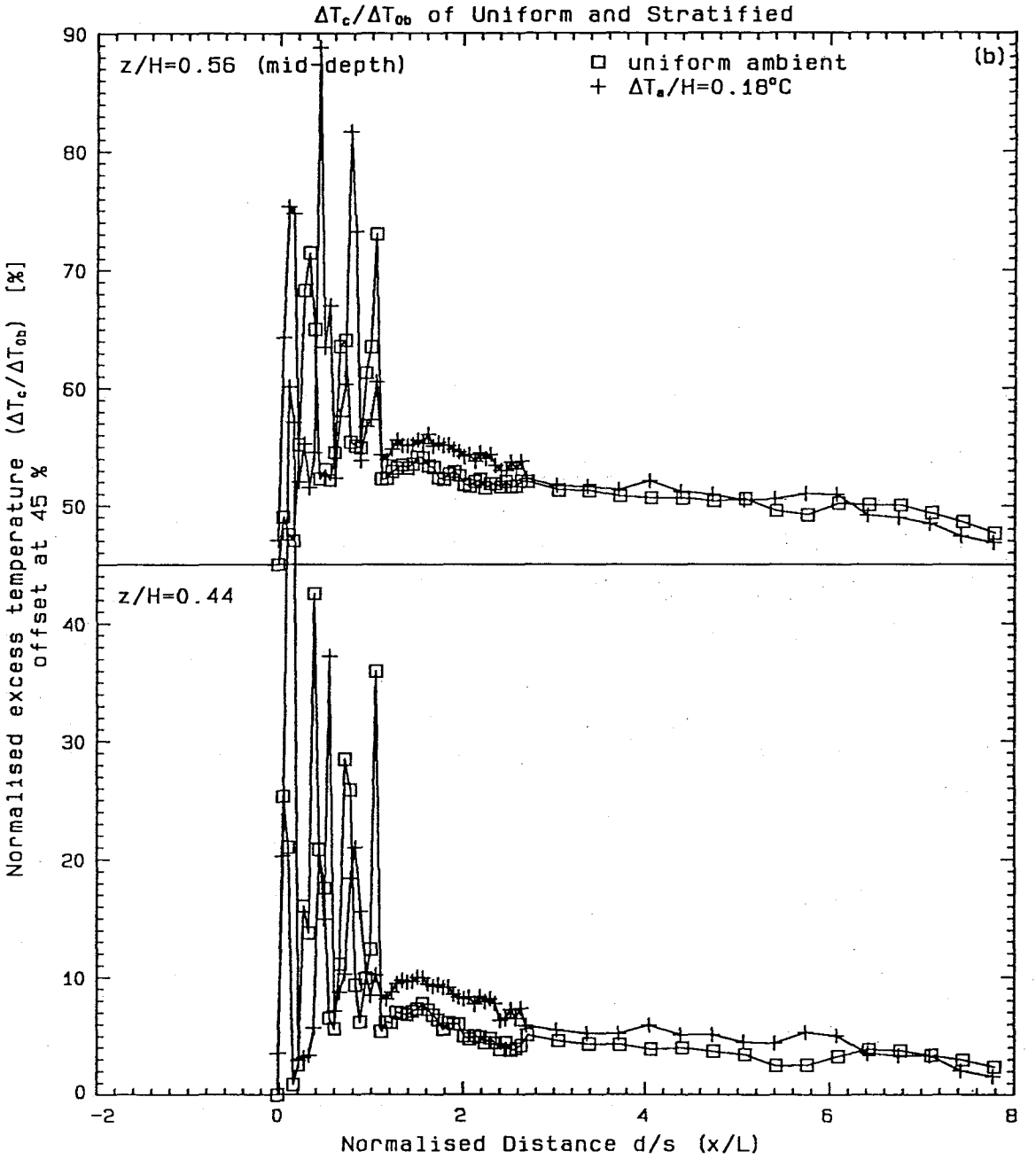

Figure C.6b Comparison of normalized temperature excess along diffuser axis at midlevels for experiment 9307cl and the uniform experiment 0816cl.

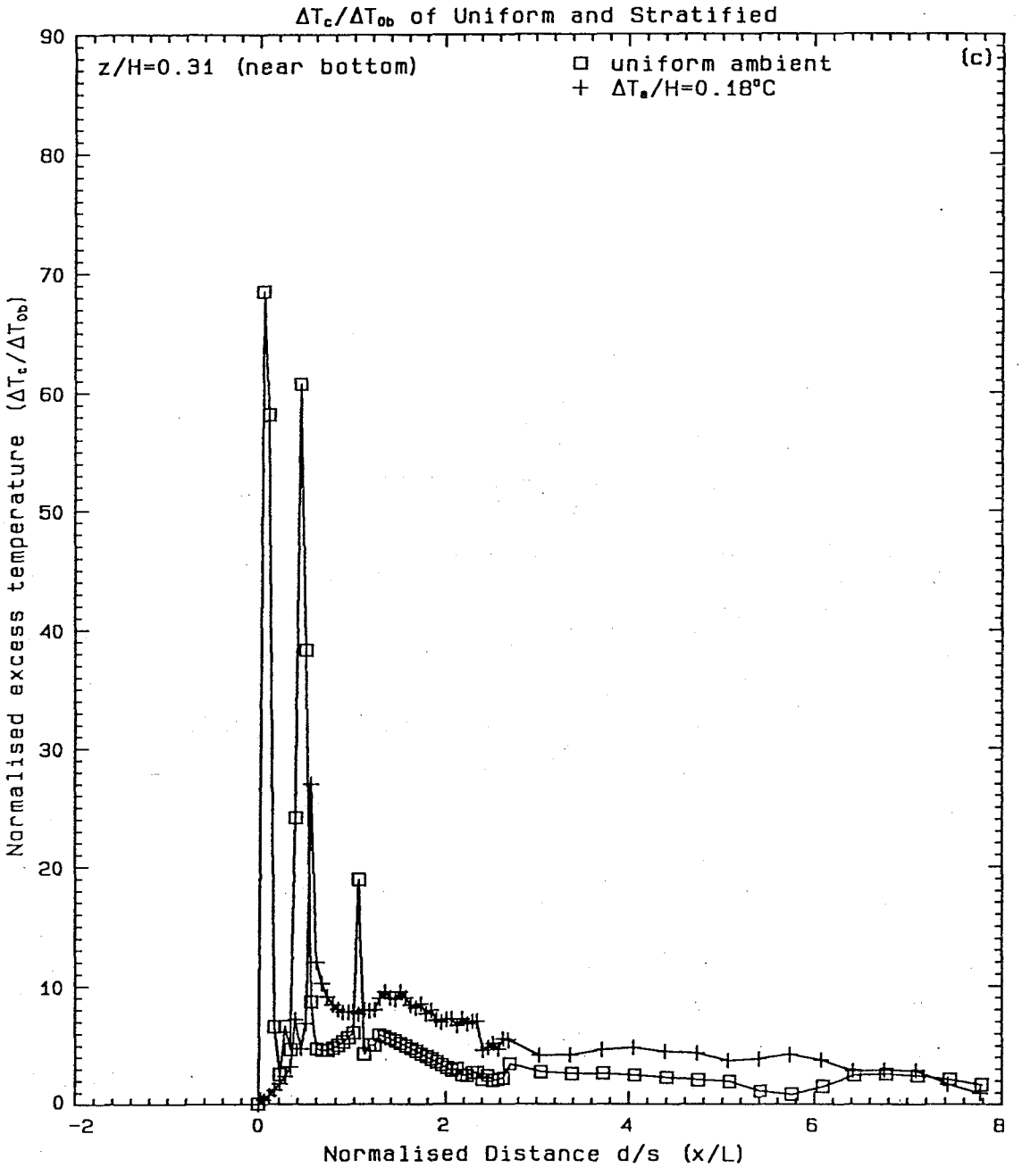

Figure C.6c Comparison of normalized temperature excess along diffuser axis at bottom level for experiment 9307cl and the uniform experiment 0816cl.

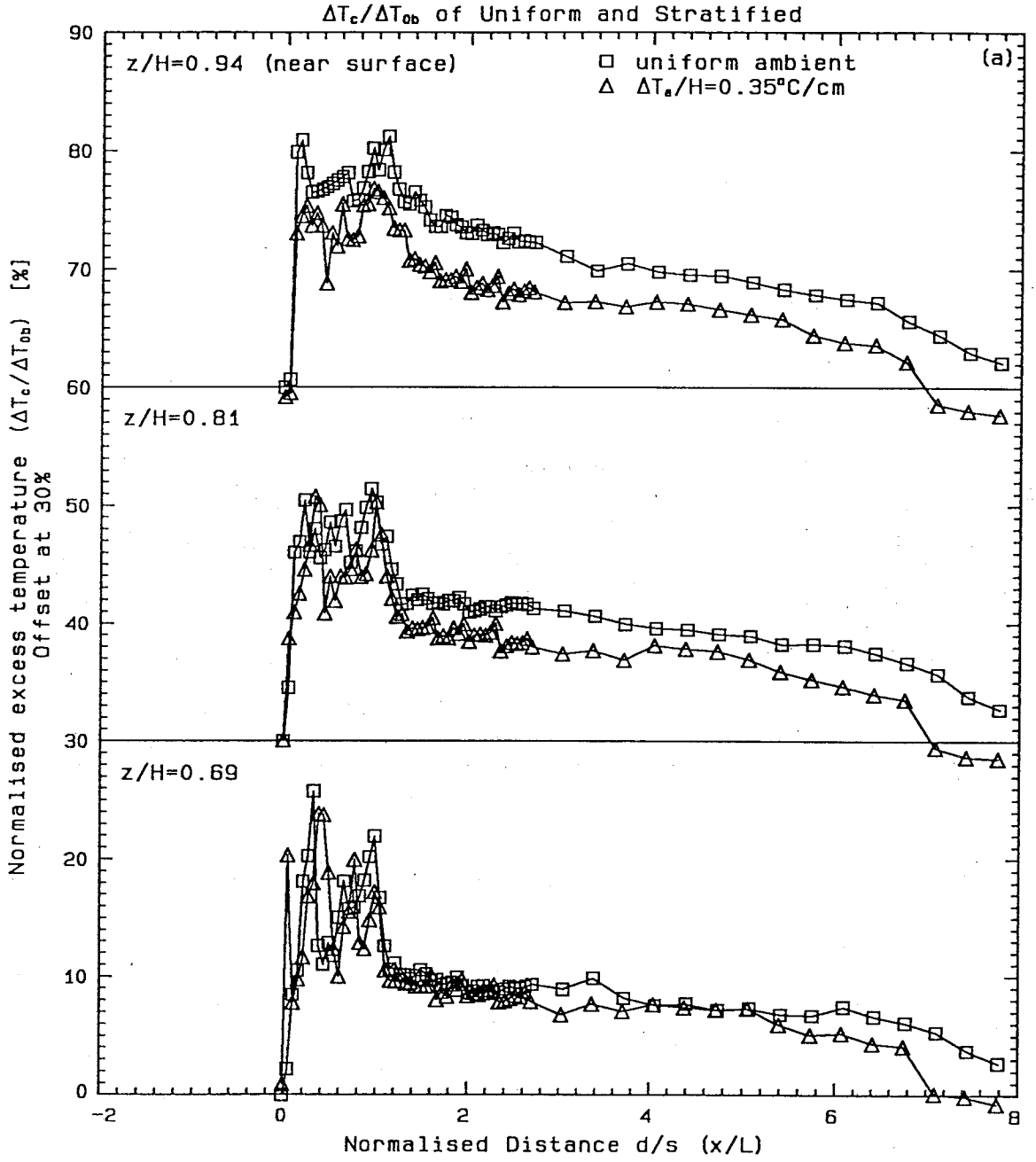

Figure C.7a Comparison of normalized temperature excess along diffuser axis at near-surface levels for experiment 9312cl and the uniform experiment 0816cl.

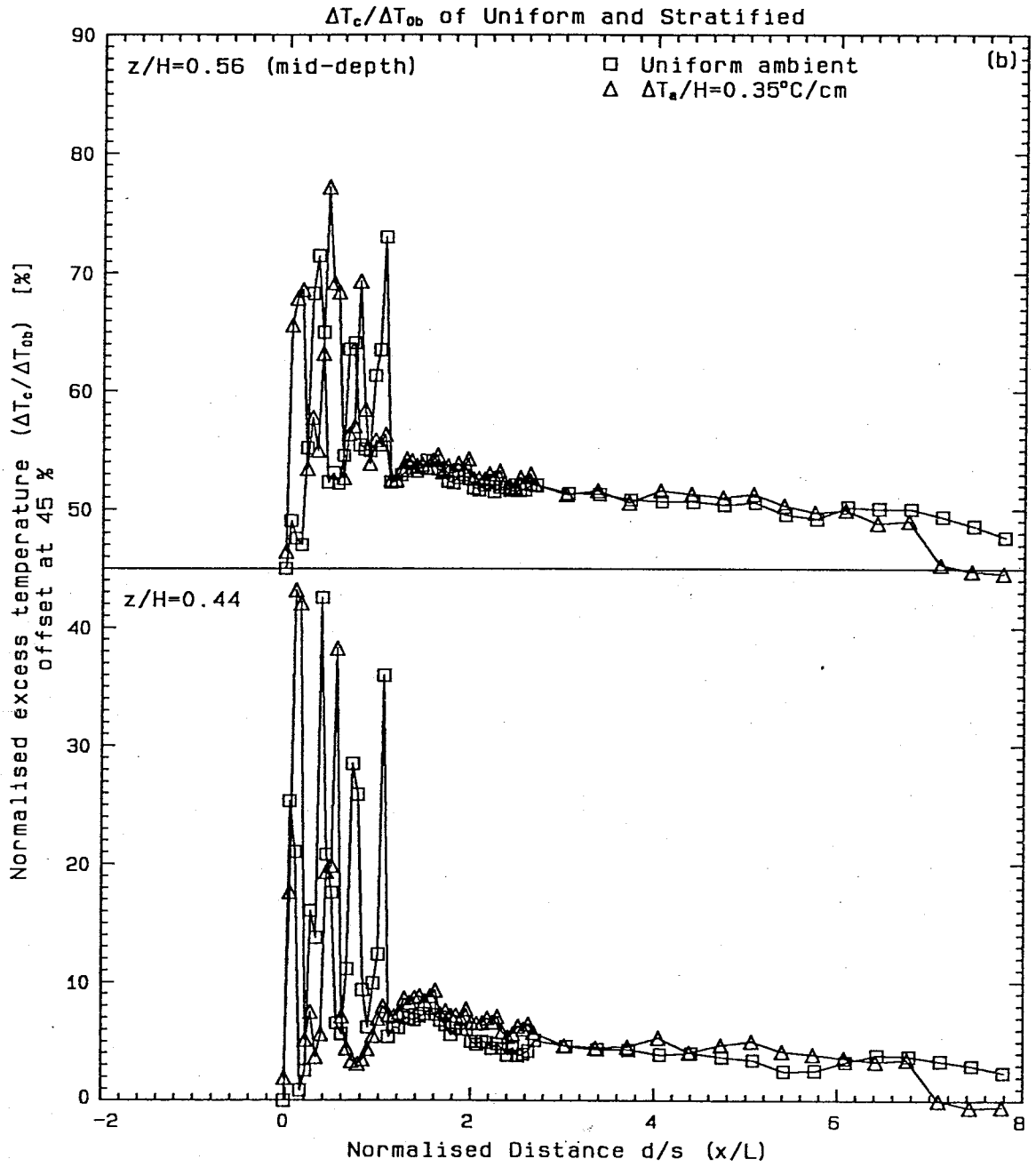

Figure C.7b Comparison of normalized temperature excess along diffuser axis at midlevels for experiment 9312cl and the uniform experiment 0816cl.

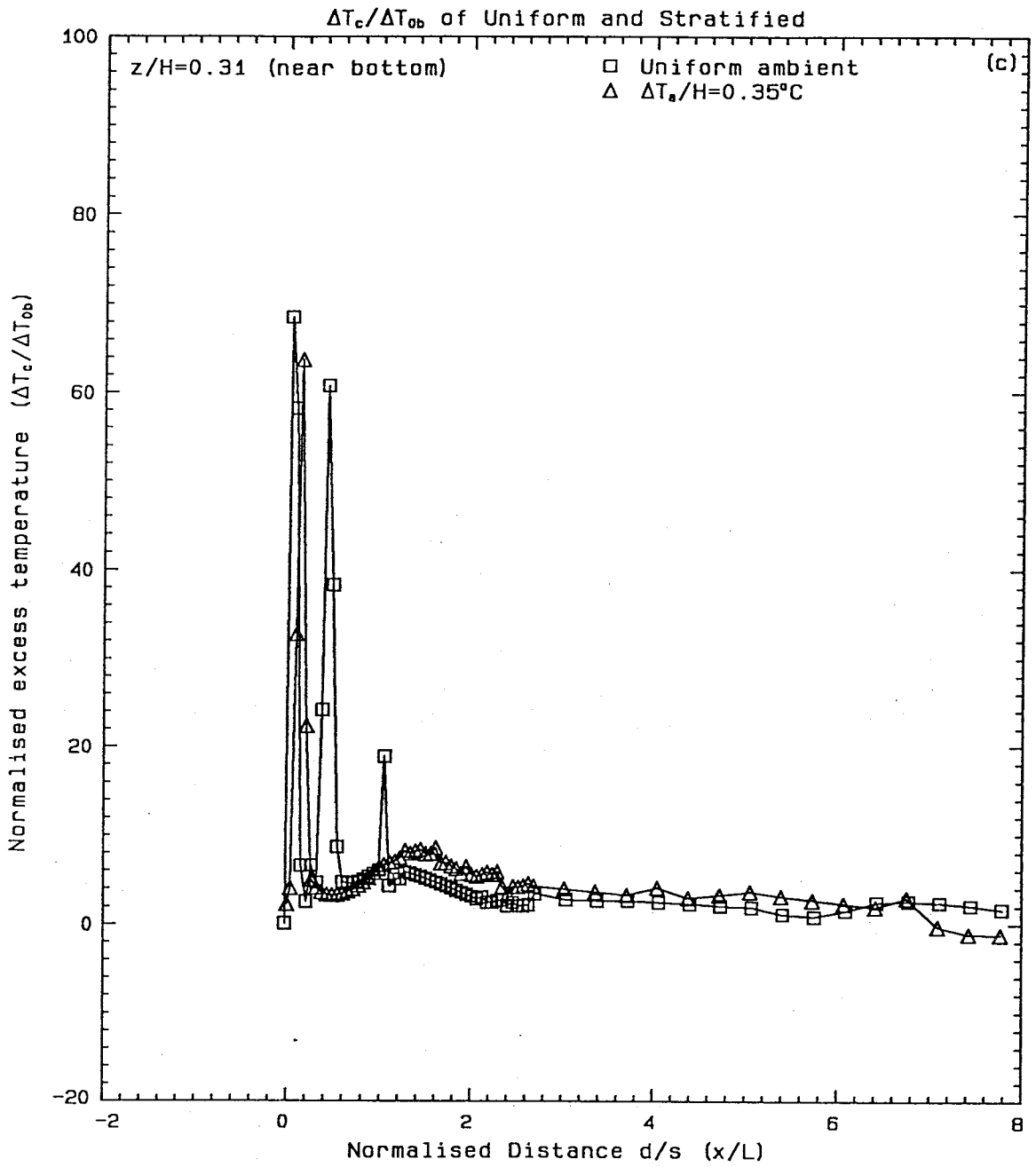

Figure C.7c Comparison of normalized temperature excess along diffuser axis at bottom level for experiment 9312cl and the uniform experiment 0816cl.

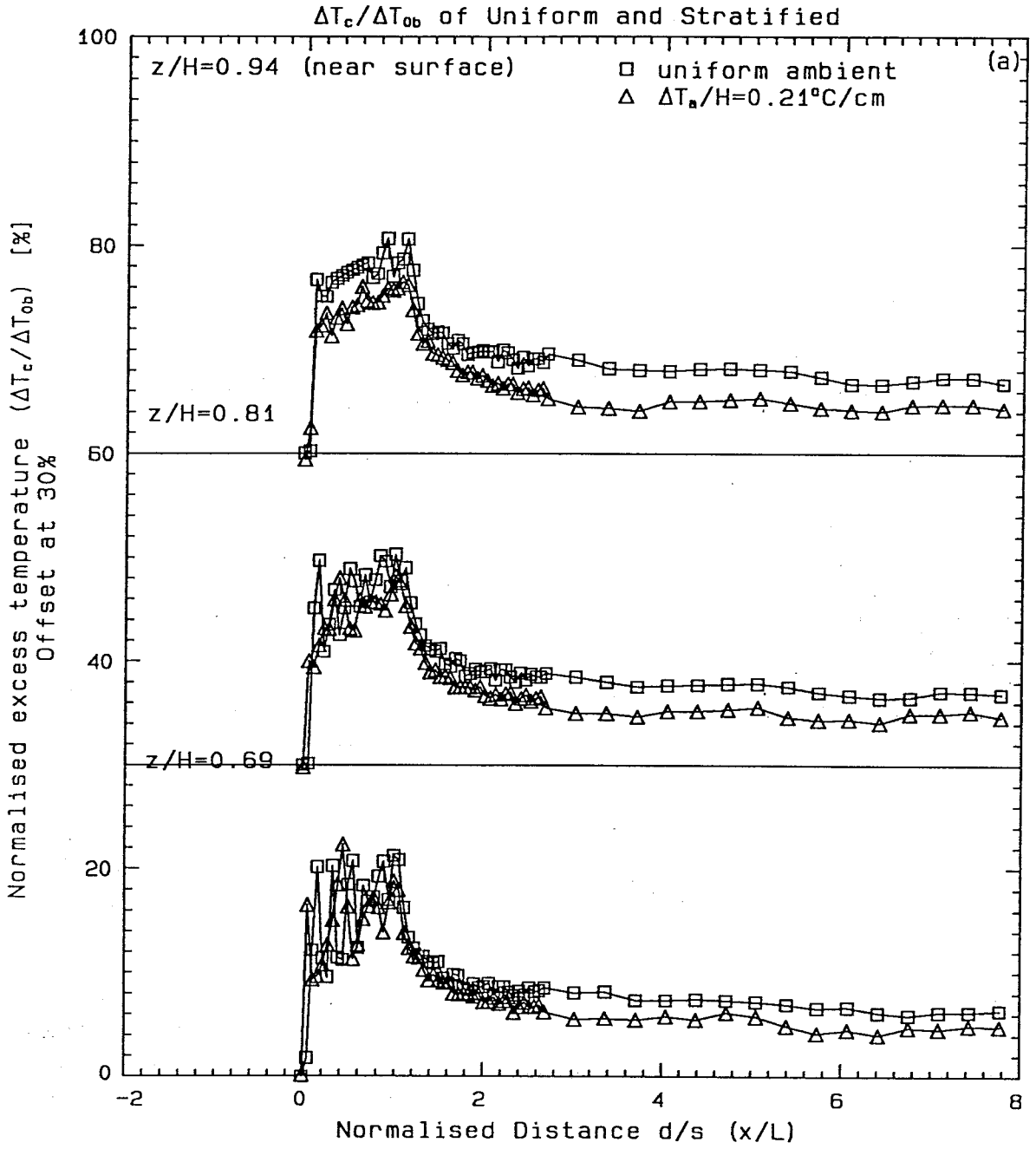

Figure C.8a Comparison of normalized temperature excess along diffuser axis at near-surface levels for experiment 9312cl2 and the uniform experiment 0816cl.

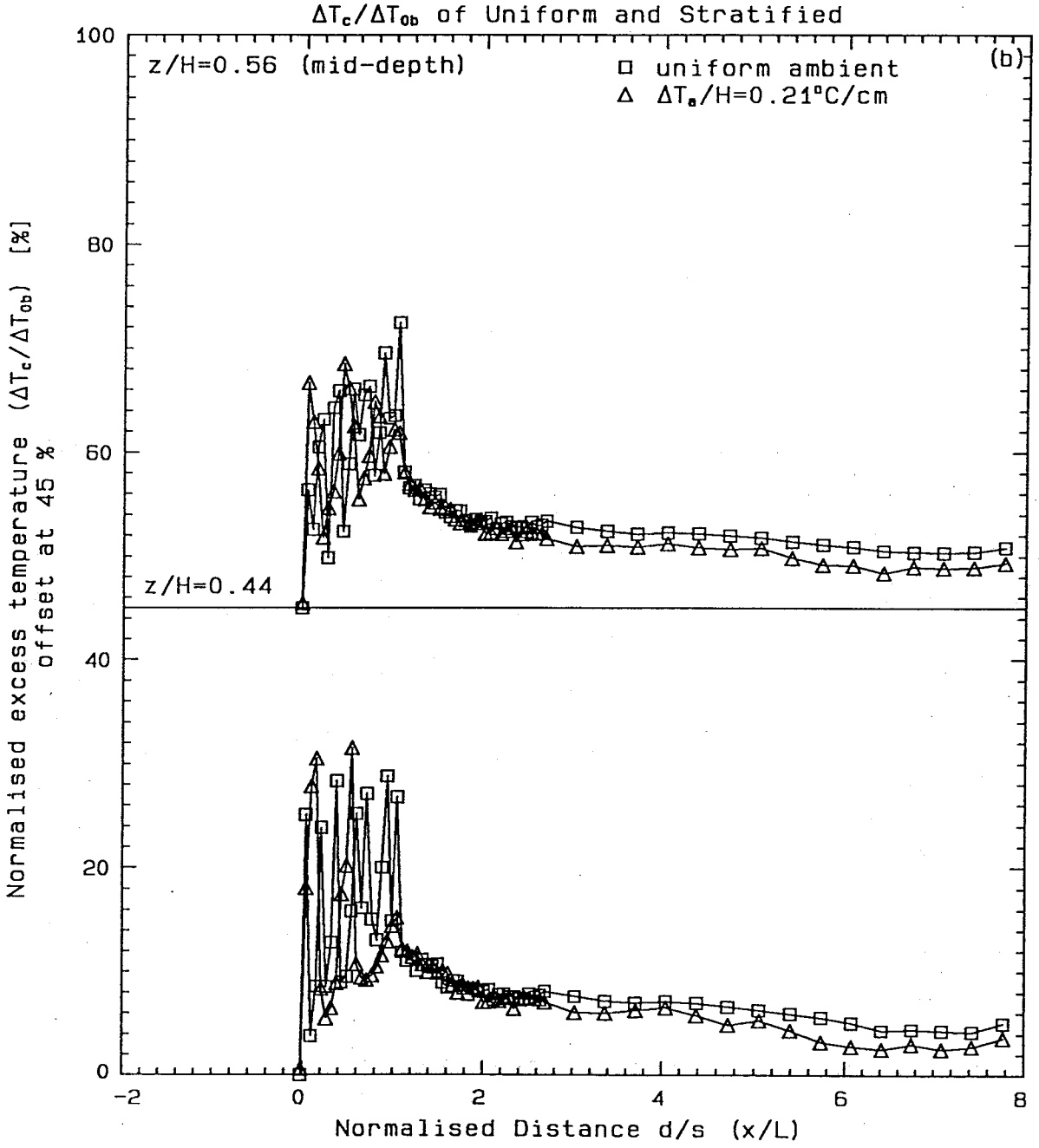

Figure C.8b Comparison of normalized temperature excess along diffuser axis at midlevels for experiment 9312cl2 and the uniform experiment 0816cl.

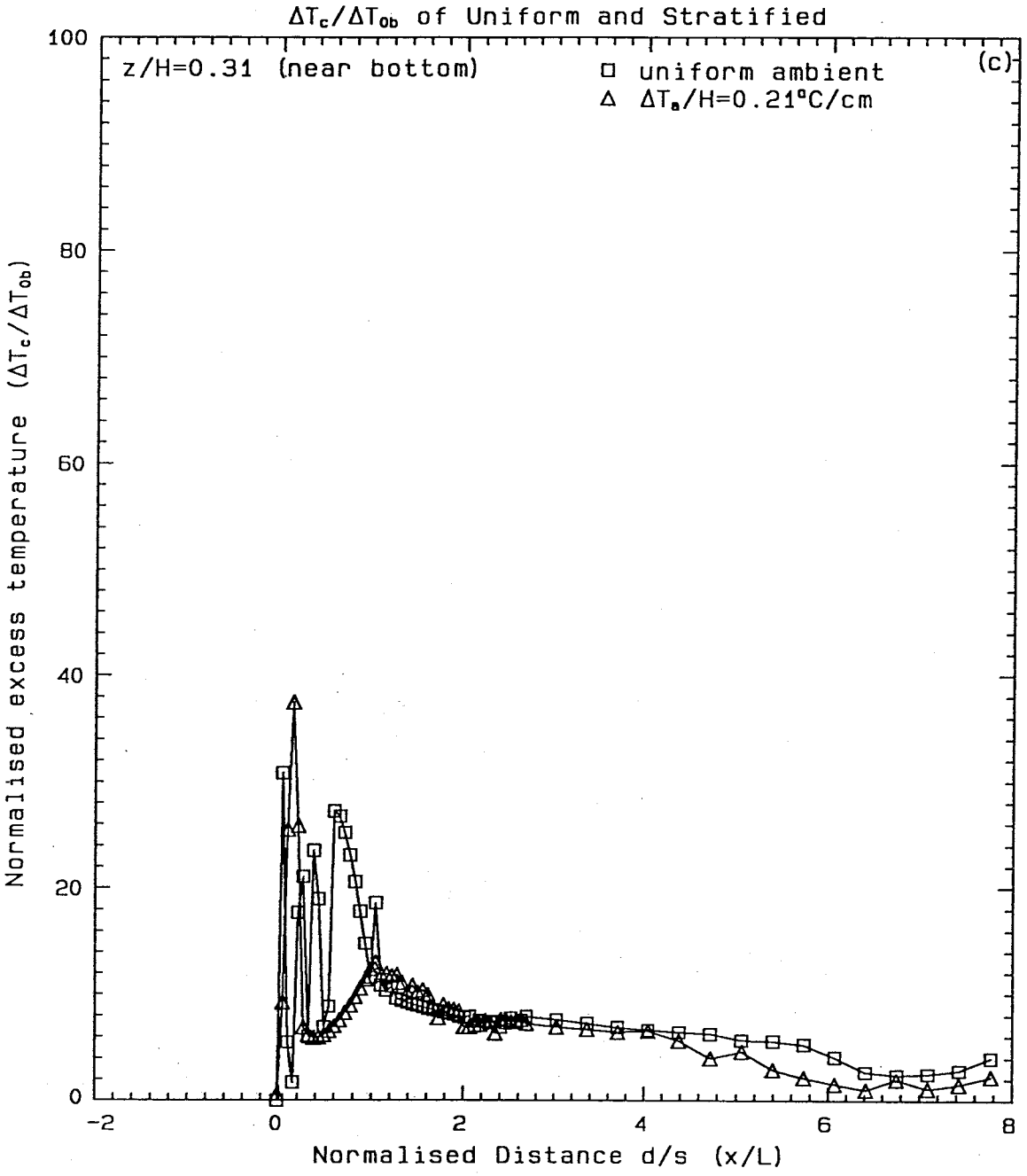

Figure C.8c Comparison of normalized temperature excess along diffuser axis at bottom level for experiment 9312cl2 and the uniform experiment 0816cl.

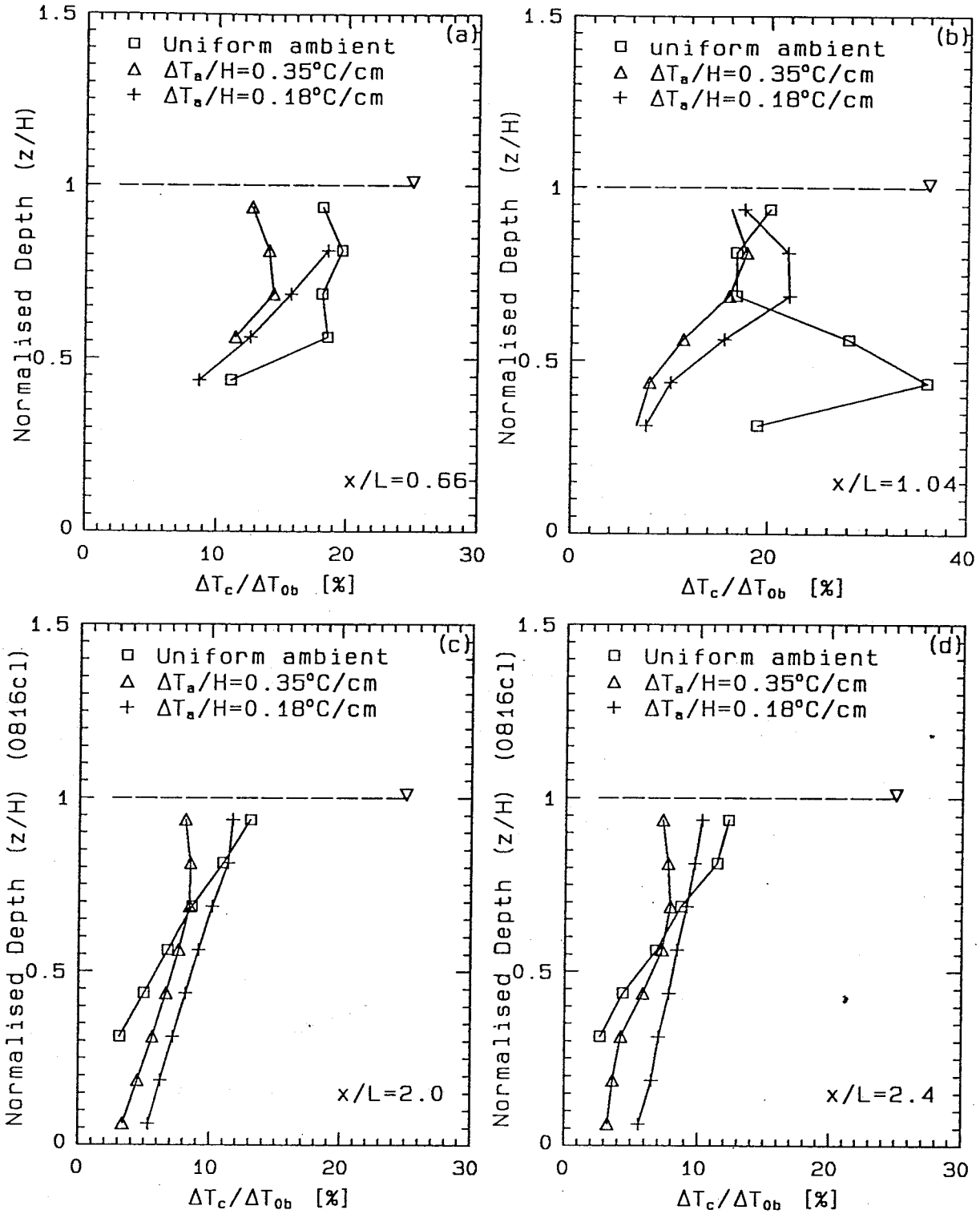

Figure C.9 Vertical profiles of $\Delta T/\Delta T_{ob}$ along diffuser axis for experiments 9307cl, 9312cl and the uniform experiment 0816cl. a)$x/L = 0.66$; b)$x/L = 1.04$; c)$x/L = 2.00$; d)$x/L = 2.40$.

(iii) Interpretations

The similarities in the normalized temperature excess profiles between the stratified and uniform ambient experiments suggest that weak stratifications do not significantly alter the dynamics of the diffuser mixing. This is a reasonable assumption in the near field where momentum is the dominant factor. Figure C.10 is the hypothetical vertical profiles of the peak normalized temperature excess $(T(z) - T_a(z))/(T_0 - T_a(0))$ of a three-dimensional pure jet (assuming a Gaussian distribution in the lateral direction and no dynamic effect of stratification) under the four different ambient conditions in the aforementioned experiments. All four curves agree closely with each other in the lower levels ($z/H \leq 0.4$) and depart gradually towards the surface as in the normalized longitudinal profiles discussed above, i.e., the stronger the ambient stratification, the lower will be the temperature excess. However, the hypothetical $\Delta T/\Delta T_{ob}$ at the surface is smaller than the peak values obtained from the experiments. An explanation for this discrepancy is the existence of a surface-blocking layer as the individual jets reach the surface and are deflected. Some researchers (Fischer et al., 1979) believe that the dilution process ceases at the bottom of the blocking layer. Koh (1983) calculated the thickness of the layer for a pure plume in a uniform ambient and a stratified ambient to be approximately 30% and 40% to 45%, respectively, of the depth of the receiving water. Figure C.11 which contains the hypothetical $(T(z) - T_a(H))/(T_0 - T_a(0))$ profiles is produced. By matching the surface $\Delta T/\Delta T_{ob}$ from the experiments with the respective curves, it is possible to find the hypothetical level at which dilution ceased and therefore a characteristic thickness of the blocking layer. Table C.2 gives the hypothetical thickness of the blocking layer found by this method for the different experiments. Based on the above argument, a cold surface plume as in Figure C.12 (hypothetical stratification of 1.0 °C/cm) could have resulted in strongly stratified water bodies such as those encountered in the field.

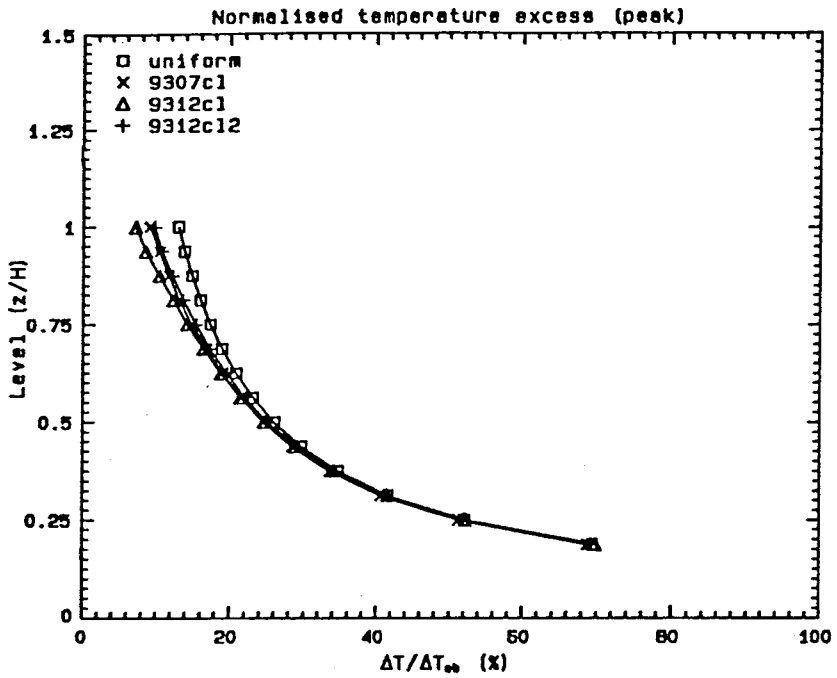

Figure C.10 Calculated $\Delta T/\Delta T_{ob}$ profiles of a three-dimensional jet in various stratified ambient conditions, based on mixing due to momentum only and neglecting jet interference.

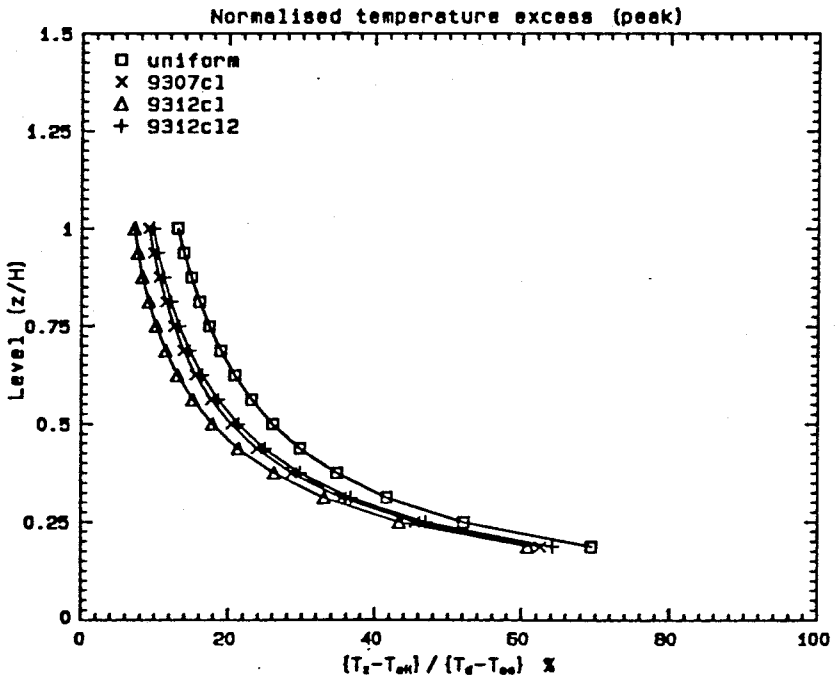

Figure C.11 Calculated $(T(z)-T_a(H))/\Delta T_{ob}$ profiles of a three-dimensional jet in various stratified ambient conditions, based on mixing due to momentum only and neglecting jet interference.

Table C.2 Calculated thickness of the blocking layer under various ambient stratification conditions, based on three-dimensional jet mixing due to momentum only and neglecting jet interference.

Experiment	0816cl	9307cl	9312cl	0628cl2	9312cl2
ΔT_a/H	uniform	0.18°C/cm	0.35°C/cm	uniform	0.21°C/cm
thickness/H	0.40	0.49	0.47	0.38	0.38

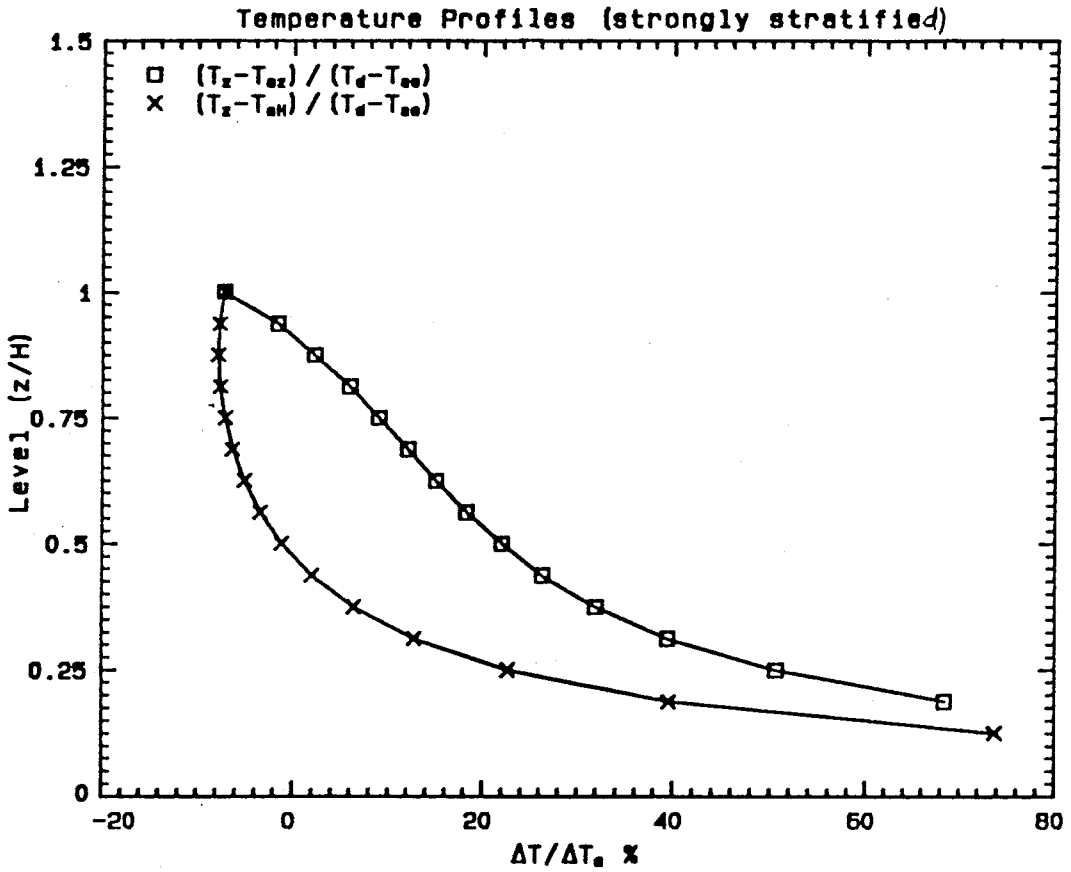

Figure C.12 Calculated $\Delta T/\Delta T_{ob}$ profiles of a three-dimensional jet in a strongly stratified ambient (1.0°C/cm), based on mixing due to momentum only and neglecting jet interference.

APPENDIX D. Parameters and Key Results

This appendix contains the list of parameters and key results of all the experiments performed as described in Section 5.5. The definitions for all the variables are found in the List of Symbols and in Section 5.5. The length L is taken as the diffuser length for the 16-port experiments (90.0 cm = 15 spacings) and for the 4-port experiments (18.0 cm = 3 spacings). For single jet experiments the length L was arbitrarily taken as 90.0 cm for data presentation and normalization. For data indicated in units $[L]$ or $[L^2]$, these values of L were used for normalization.

Table D1a List of parameters and key results of centerline experiments

Experiment:	0816cl	0627cl	0628cl	0628cl2	0714cl	0714cl2	0715cl
n	16	16	16	16	16	16	16
D_0 [cm]	.25	.25	.25	.25	.25	.25	.25
α [°]	0.	0.	0.	0.	0.	0.	0.
H [cm]	4.0	4.0	4.0	4.0	8.0	8.0	8.0
ΔT_0 [°C]	16.0	15.6	14.9	13.7	13.6	16.4	17.0
g_0' [cm/s^2]	4.49	4.35	4.25	3.74	3.77	4.67	4.78
Q_{T0} [cm^3/s]	28.8	40.7	57.5	20.3	28.8	40.7	57.5
M_{T0} [cm^4/s^2]	1052.5	2109.1	4204.8	524.7	1052.5	2109.1	4204.8
B_{T0} [cm^4/s^3]	129.3	176.8	244.1	76.1	108.6	189.8	273.8
ℓ_M [cm]	8.13	11.70	16.70	6.28	8.86	11.30	15.80
ℓ_Q [cm]	.22	.22	.22	.22	.22	.22	.22
Fr$_0$	35.	50.	71.	27.	38.	48.	67.
Re$_0$	1260.	1790.	2530.	890.	1260.	1790.	2530.
T_{peak} [%]	21.2	21.0	21.0	41.0	11.0	12.5	12.5
$T_{L/2}$ [%]	15.0	11.8	11.5	20.5	8.0	9.5	9.5
T_L [%]	13.5	10.5	10.0	17.5	6.0	8.0	6.5
T_{2L} [%]	11.0	9.8	8.5	13.3	5.0	7.0	6.3
T_{4L} [%]	9.0	8.8	8.5	*	*	6.0	5.5
T_{4H} [%]	18.0	16.0	15.5	22.0	8.0	10.5	10.3
T_{8H} [%]	15.8	12.3	11.8	21.3	7.0	9.0	7.0
T_{16H} [%]	14.0	11.0	10.0	19.0	5.0	7.3	6.3
T_{32H} [%]	13.0	10.0	9.0	16.0	5.0	6.5	6.0
T_{64H} [%]	10.3	9.8	8.5	11.0	*	6.0	5.5
T_{128H} [%]	*	8.8	8.5	*	*	*	*
$x_{0.1}$ [L]	2.33	2.22	1.00	2.98	.00	.41	.46
$x_{0.2}$ [L]	.12	.13	.14	.56	.00	.00	.00
T_{S1} [%]	21.0	21.0	20.8	23.5	10.0	12.0	12.0
T_{b_1} [%]	4.3	8.0	11.0	.5	.0	2.0	4.5
h_1 [cm]	1.3	1.2	1.3	.5	2.0	2.2	2.3
x_t [L]	1.01	.82	.53	*	.67	.53	.72
T_{asym} [%]	13.0	9.8	10.0	*	4.0	8.0	6.3
T_{b_2} [%]	3.0	5.8	7.8	*	.0	.0	3.0
h_2 [cm]	1.4	1.6	1.0	*	2.2	3.0	2.5

Table D1b List of parameters and key results of scanning experiments

Experiment:	1122scan	no data	1122scn2	no data	1123scan	no data	1123scn2
n	16		16		16		16
D_0 [cm]	.25		.25		.25		.25
α [°]	0.		0.		0.		0.
H [cm]	4.0		4.0		8.0		8.0
ΔT_0 [°C]	16.6		18.5		15.7		18.5
g_0' [cm/s^2]	4.70		5.43		4.48		5.43
Q_{T0} [cm^3/s]	28.8		57.5		28.8		57.5
M_{T0} [cm^4/s^2]	1052.5		4204.8		1052.5		4204.8
B_{T0} [cm^4/s^3]	135.4		312.0		129.0		312.0
ℓ_M [cm]	7.94		14.80		8.13		14.80
ℓ_Q [cm]	.22		.22		.22		.22
Fr$_0$	34.		63.		35.		63.
Re$_0$	1260.		2530.		1260.		2530.
b_1 [L]	.26		.21		2.32		.43
b_2 [L]	.60		1.00		2.70		1.30
$A_{0.1}$ [L^2]	1.40		.70		.14		.00
$A_{0.2}$ [L^2]	.04		.00		.00		.00
ϵ	.52		.35		.72		*
V_t [cm/s]	.48		.63		.23		*

† – no steady-state * – data not recorded/not applicable

Table D2a List of parameters and key results of centerline experiments

Experiment:	0811cl	0818cl	0818cl2	0819cl	0819cl2	0823cl	0823cl2
n	16	16	16	16	16	16	16
D_o [cm]	.25	.25	.25	.25	.25	.25	.25
α [°]	0.	0.	0.	0.	0.	0.	0.
H [cm]	8.0	2.0	2.0	2.0	2.0	12.0	12.0
ΔT_o [°C]	12.9	15.0	15.4	16.2	18.4	15.9	16.3
g_o' [cm/s^2]	3.14	4.18	4.33	4.59	5.41	4.65	4.72
Q_{To} [cm^3/s]	20.3	28.8	20.3	40.7	57.5	28.8	57.5
M_{To} [cm^4/s^2]	524.7	1052.5	524.7	2109.1	4204.8	1052.5	4204.8
B_{To} [cm^4/s^3]	63.8	120.4	88.0	186.4	310.6	133.9	271.0
ℓ_M [cm]	6.85	8.42	5.84	11.40	14.80	7.98	15.90
ℓ_Q [cm]	.22	.22	.22	.22	.22	.22	.22
Fr_o	29.	35.	25.	48.	63.	34.	67.
Re_o	890.	1260.	890.	1790.	2530.	1260.	2530.
T_{peak} [%]	19.5	45.0	54.0	38.5	37.0	6.0	8.0
$T_{L/2}$ [%]	10.0	22.0	27.0	21.5	17.0	3.5	6.5
T_L [%]	8.5	21.0	22.0	20.0	15.0	3.0	5.0
T_{2L} [%]	7.0	19.0	18.0	17.5	14.0	3.0	4.5
T_{4L} [%]	4.5	14.0	9.0	15.0	12.0	3.0	3.8
T_{4H} [%]	11.0	34.0	48.0	32.5	31.0	3.5	6.0
T_{8H} [%]	9.0	19.5	42.0	28.0	26.0	3.0	4.8
T_{16H} [%]	7.8	22.0	28.0	25.0	20.0	3.0	4.0
T_{32H} [%]	6.0	21.0	24.8	21.5	16.3	3.0	3.8
T_{64H} [%]	4.5	19.0	19.5	18.0	14.5	*	*
T_{128H} [%]	*	16.0	13.5	16.0	12.3	*	*
$x_{0.1}$ [L]	.50	5.33	3.90	6.40	5.70	.00	.00
$x_{0.2}$ [L]	.00	2.00	1.33	1.00	.39	.00	.00
T_{S1} [%]	11.5	45.0	54.0	38.5	37.0	6.0	7.8
T_{b_1} [%]	.0	18.0	13.0	22.0	16.3	.0	2.0
h_1 [cm]	1.7	.9	.6	1.0	1.1	3.1	3.3
x_f [L]	.33	*	*	*	.86	.28	.67
T_{asym} [%]	5.0	*	*	*	14.0	2.5	5.0
T_{b_2} [%]	.0	*	*	*	12.0	.0	.0
h_2 [cm]	2.5	*	*	*	1.6	3.7	6.7

Table D2b List of parameters and key results of scanning experiments

Experiment:	no data	no data	no data	no data	no data	no data	no data
n							
D_o [cm]							
α [°]							
H [cm]							
ΔT_o [°C]							
g_o' [cm/s^2]							
Q_{To} [cm^3/s]							
M_{To} [cm^4/s^2]							
B_{To} [cm^4/s^3]							
ℓ_M [cm]							
ℓ_Q [cm]							
Fr_o							
Re_o							
b_1 [L]							
b_2 [L]							
$A_{0.1}$ [L^2]							
$A_{0.2}$ [L^2]							
ϵ							
V_f [cm/s]							

† – no steady-state * – data not recorded/not applicable

Table D3a List of parameters and key results of centerline experiments

Experiment:	0824cl	0824cl2	0827cl	0828cl	0829cl	0829cl2	0830cl
n	16	16	16	16	16	16	16
D_o [cm]	.25	.25	.25	.25	.25	.25	.25
α [°]	0.	0.	25.	25.	25.	25.	25.
H [cm]	12.0	12.0	4.0	4.0	8.0	8.0	2.0
ΔT_o [°C]	16.3	15.6	15.1	15.7	14.1	16.3	15.5
g_o' [cm/s^2]	4.61	4.40	4.27	4.45	3.96	4.67	4.33
Q_{To} [cm^3/s]	40.7	20.3	28.8	57.5	28.8	57.5	28.8
M_{To} [cm^4/s^2]	2109.1	524.7	1052.5	4204.8	1052.5	4204.8	1052.5
B_{To} [cm^4/s^3]	187.5	89.4	123.0	255.3	114.1	268.1	124.8
ℓ_M [cm]	11.40	5.80	8.30	16.30	8.65	16.00	8.27
ℓ_Q [cm]	.22	.22	.22	.22	.22	.22	.22
Fr_o	48.	25.	35.	69.	37.	68.	35.
Re_o	1790.	890.	1260.	2530.	1260.	2530.	1260.
T_{peak} [%]	7.2	7.0	15.0	13.5	8.0	9.0	20.0
$T_{L/2}$ [%]	4.8	4.0	14.5	12.5	7.5	8.5	17.0
T_L [%]	4.3	3.5	13.0	11.5	7.0	7.0	16.0
T_{2L} [%]	3.8	3.0	11.0	10.8	5.8	6.7	14.8
T_{4L} [%]	3.0	3.0	10.0	10.4	3.5	5.7	12.0
T_{4H} [%]	4.8	4.0	14.8	13.5	7.6	8.5	19.0
T_{8H} [%]	4.5	3.0	13.5	13.0	7.3	7.6	19.0
T_{16H} [%]	4.0	3.0	13.3	12.0	6.0	6.6	17.5
T_{32H} [%]	3.0	*	12.0	11.0	4.0	6.0	16.8
T_{64H} [%]	*	*	10.0	10.8	*	4.5	16.0
T_{128H} [%]	*	*	*	10.3	*	*	13.8
$x_{0.1}$ [L]	.00	.00	2.89	4.56	.00	.00	4.56
$x_{0.2}$ [L]	.00	.00	.00	.00	.00	.00	.00
T_{S1} [%]	6.5	4.0	14.0	13.5	8.0	9.0	20.0
T_{b_1} [%]	.0	.0	6.5	11.0	.0	5.0	13.8
h_1 [cm]	2.8	3.3	2.1	1.6	3.7	4.1	1.4
x_f [L]	.28	.22	.90	.90	.50	.90	†
T_{asym} [%]	5.0	4.0	12.0	12.0	7.0	7.0	†
T_{b_2} [%]	.0	.0	3.0	9.0	.0	2.5	†
h_2 [cm]	4.3	3.2	2.0	1.1	3.0	4.1	†

Table D3b List of parameters and key results of scanning experiments

Experiment:	no data	no data	0828scan	0829scan	0830scan	0830scn2	0830scn3
n			16	16	16	16	16
D_o [cm]			.25	.25	.25	.25	.25
α [°]			25.	25.	25.	25.	25.
H [cm]			4.0	4.0	8.0	8.0	2.0
ΔT_o [°C]			16.1	16.9	15.8	17.5	16.1
g_o' [cm/s^2]			4.55	4.62	4.48	5.04	4.35
Q_{To} [cm^3/s]			28.8	57.5	28.8	57.5	28.8
M_{To} [cm^4/s^2]			1052.5	4204.8	1052.5	4204.8	1052.5
B_{To} [cm^4/s^3]			131.0	265.4	129.0	289.5	125.3
ℓ_M [cm]			8.07	16.00	8.13	15.30	8.25
ℓ_Q [cm]			.22	.22	.22	.22	.22
Fr_o			34.	68.	35.	65.	35.
Re_o			1260.	2530.	1260.	2530.	1260.
b_1 [L]			1.11	.60	1.44	.72	.75
b_2 [L]			1.20	1.45	2.00	1.40	†
$A_{0.1}$ [L^2]			†	1.24	.00	.00	5.72
$A_{0.2}$ [L^2]			.00	.00	.00	.00	.20
ϵ			1.08	.88	†	*	*
V_f [cm/s]			†	.76	.30	*	*

† – no steady-state * – data not recorded/not applicable

Table D4a List of parameters and key results of centerline experiments

Experiment:	0830cl2	0909cl	0909cl2	0910cl	0912cl	0913cl	0913cl2
n	16	1	1	1	1	1	1
D_0 [cm]	.25	.75	.75	.75	.75	.75	.75
α [°]	25.	0.	0.	0.	0.	0.	0.
H [cm]	2.0	4.0	4.0	4.0	8.0	8.0	8.0
ΔT_0 [°C]	17.6	15.6	14.4	17.6	15.9	15.2	17.9
g_0' [cm/s^2]	5.09	4.34	4.28	4.98	4.52	4.27	5.22
Q_{T0} [cm^3/s]	57.5	28.8	20.3	57.5	28.8	20.3	57.5
M_{T0} [cm^4/s^2]	4204.8	1871.0	932.8	7486.5	1871.0	932.8	7486.5
B_{T0} [cm^4/s^3]	292.6	124.8	86.9	286.6	129.9	86.7	300.2
ℓ_M [cm]	15.30	25.50	18.10	47.50	25.00	18.10	46.50
ℓ_Q [cm]	.22	.66	.66	.66	.66	.66	.66
Fr_0	65.	36.	26.	67.	35.	26.	66.
Re_0	2530.	6740.	4760.	9990.	6740.	4760.	9990.
T_{peak} [%]	18.0	29.0	29.0	27.0	16.3	16.0	15.2
$T_{L/2}$ [%]	15.0	10.0	10.8	11.0	9.0	8.5	9.0
T_L [%]	13.0	6.5	7.3	6.5	5.0	5.5	4.5
T_{2L} [%]	11.5	5.3	6.0	5.0	4.0	4.0	3.0
T_{4L} [%]	11.5	4.2	4.5	4.3	3.3	3.0	2.5
T_{4H} [%]	17.5	24.8	24.5	23.8	11.5	9.0	9.3
T_{8H} [%]	17.0	13.0	14.5	14.3	6.5	6.5	5.8
T_{16H} [%]	15.3	8.0	9.0	8.5	4.5	4.8	4.0
T_{32H} [%]	14.0	6.0	6.3	6.0	3.5	4.1	3.0
T_{64H} [%]	13.0	5.0	5.8	4.5	3.0	2.8	2.5
T_{128H} [%]	11.0	3.8	4.0	3.5	*	*	*
$x_{0.1}$ [L]	5.90	.43	.58	.56	.44	.36	.33
$x_{0.2}$ [L]	.00	.21	.22	.23	.00	.00	.00
T_{S1} [%]	*	29.0	29.0	27.0	16.3	16.0	15.2
T_{h_1} [%]	*	.0	.0	1.0	.0	.0	.0
h_1 [cm]	*	2.1	2.0	2.2	3.0	2.7	3.4
x_f [L]	*	.85	.93	1.11	.93	.93	.88
T_{asym} [%]	*	6.0	6.5	5.3	5.3	5.3	4.3
T_{h_2} [%]	*	4.0	4.0	4.0	2.0	1.0	4.0
h_2 [cm]	*	1.5	1.6	3.2	3.2	4.2	8.0

Table D4b List of parameters and key results of scanning experiments

Experiment:	0831scan	0911scn2	0911scan	0912scan	0914scan	0913scan	no data
n	16	1	1	1	1	1	
D_0 [cm]	.25	.75	.75	.75	.75	.75	
α [°]	25.	0.	0.	0.	0.	0.	
H [cm]	2.0	4.0	4.0	4.0	8.0	8.0	
ΔT_0 [°C]	17.4	15.7	14.3	17.8	16.0	15.6	
g_0' [cm/s^2]	5.00	4.41	3.91	5.16	4.51	4.38	
Q_{T0} [cm^3/s]	57.5	28.8	20.3	57.5	28.8	20.3	
M_{T0} [cm^4/s^2]	4204.8	1871.0	932.8	7486.5	1871.0	932.8	
B_{T0} [cm^4/s^3]	287.6	126.7	79.3	296.8	129.8	88.8	
ℓ_M [cm]	15.40	25.30	18.90	46.70	25.00	17.90	
ℓ_Q [cm]	.22	.66	.66	.66	.66	.66	
Fr_0	65.	36.	27.	66.	35.	25.	
Re_0	2530.	6740.	4750.	9990.	6740.	4750.	
b_1 [L]	.91	.04	.03	.03	*	*	
b_2 [L]	*	.43	.52	.50	.92	.88	
$A_{0.1}$ [L^2]	5.70	.05	.04	.04	.04	.04	
$A_{0.2}$ [L^2]	.06	.00	.00	.00	.00	.00	
ϵ	.37	.67	.63	.61	.78	.81	
V_f [cm/s]	.70	.68	†	1.50	.34	.25	

† – no steady-state * – data not recorded/not applicable

Table D5a List of parameters and key results of centerline experiments

Experiment:	0914cl	0915cl	0915cl2	0916cl	0916cl2	0917cl	0917cl2
n	1	1	1	1	1	1	1
D_0 [cm]	.75	.75	.75	.75	.75	.75	.52
α [°]	0.	0.	0.	0.	0.	0.	0.
H [cm]	2.0	2.0	2.0	11.0	11.0	11.0	11.0
ΔT_0 [°C]	14.2	15.8	16.6	13.8	15.4	17.2	15.5
g_0' [cm/s^2]	3.90	4.48	4.70	3.97	4.45	5.02	4.45
Q_{T0} [cm^3/s]	20.3	28.8	57.5	20.3	28.8	57.5	5.4
M_{T0} [cm^4/s^2]	932.8	1871.0	7486.5	932.8	1871.0	7486.5	138.2
B_{T0} [cm^4/s^3]	79.0	128.8	270.3	80.5	127.9	288.7	24.1
ℓ_M [cm]	19.00	25.10	49.00	18.90	25.20	47.40	8.21
ℓ_Q [cm]	.66	.66	.66	.66	.66	.66	.46
Fr_0	27.	36.	69.	27.	36.	67.	17.
Re_0	4760.	6740.	9990.	4760.	6740.	9990.	1830.
T_{peak} [%]	47.0	47.0	38.0	12.5	12.0	11.0	14.0
$T_{L/2}$ [%]	12.5	11.5	13.0	7.8	8.0	8.0	6.5
T_L [%]	9.2	8.3	8.5	4.0	4.0	4.0	5.5
T_{2L} [%]	8.0	6.3	7.0	3.5	3.0	2.5	3.0
T_{4L} [%]	6.0	6.3	6.0	2.0	2.5	2.0	*
T_{4H} [%]	33.0	34.5	38.0	7.8	8.0	8.0	6.5
T_{8H} [%]	22.5	22.5	27.0	4.0	4.0	4.0	5.5
T_{16H} [%]	14.0	14.0	15.5	3.5	3.0	2.5	3.0
T_{32H} [%]	9.0	8.5	8.3	2.0	2.3	2.0	*
T_{64H} [%]	8.5	8.2	8.0	*	*	*	*
T_{128H} [%]	8.0	6.3	6.0	*	*	*	*
$x_{0.1}$ [L]	.67	.64	.66	.31	.32	.33	.28
$x_{0.2}$ [L]	.14	.20	.22	.00	.00	.00	.00
T_{S1} [%]	47.0	47.0	38.0	12.0	12.0	11.0	14.0
T_{b1} [%]	3.0	3.8	4.0	.0	.0	.0	.0
h_1 [cm]	1.4	1.3	1.3	3.3	4.2	4.6	2.0
x_f [L]	.88	.88	2.70	.60	.83	1.45	†
T_{asym} [%]	8.0	7.5	7.0	5.0	5.0	3.0	†
T_{b2} [%]	6.5	7.0	7.0	.0	1.0	2.0	†
h_2 [cm]	2.0	2.0	2.0	3.7	4.0	11.0	*

Table D5b List of parameters and key results of scanning experiments

Experiment:	0915scan	0915scn2	0915scn3	no data	no data	no data	no data
n	1	1	1				
D_0 [cm]	.75	.75	.75				
α [°]	0.	0.	0.				
H [cm]	2.0	2.0	2.0				
ΔT_0 [°C]	14.4	15.7	16.8				
g_0' [cm/s^2]	4.00	4.45	4.83				
Q_{T0} [cm^3/s]	20.3	28.8	57.5				
M_{T0} [cm^4/s^2]	932.8	1871.0	7486.5				
B_{T0} [cm^4/s^3]	81.1	128.1	278.0				
ℓ_M [cm]	18.70	25.10	48.30				
ℓ_Q [cm]	.66	.66	.66				
Fr_0	27.	36.	68.				
Re_0	4750.	6740.	9990.				
b_1 [L]	.07	.06	.06				
b_2 [L]	.42	.48	2.14				
$A_{0.1}$ [L^2]	.08	.07	.06				
$A_{0.2}$ [L^2]	.01	.01	.01				
ϵ	.51	.50	.50				
V_f [cm/s]	.42	.85	2.15				

† – no steady-state * – data not recorded/not applicable

Table D6a List of parameters and key results of centerline experiments

Experiment:	0917cl3	0918cl	0919cl	0920cl	0920cl2	0922cl	0922cl2
n	1	1	4	4	4	4	4
D_0 [cm]	.52	.52	.52	.52	.52	.52	.52
α [°]	0.	0.	0.	0.	0.	0.	0.
H [cm]	11.0	11.0	2.0	2.0	2.0	4.0	4.0
ΔT_0 [°C]	14.7	15.0	13.6	15.4	17.7	14.5	15.7
g_0' [cm/s^2]	4.10	4.23	3.77	4.45	5.28	4.10	4.50
Q_{T0} [cm^3/s]	20.3	28.8	20.3	28.8	57.5	20.3	28.8
M_{T0} [cm^4/s^2]	1940.4	3892.1	485.6	973.4	3892.1	485.6	973.4
B_{T0} [cm^4/s^3]	83.2	121.5	76.7	128.0	303.7	83.4	129.5
ℓ_M [cm]	32.00	44.70	8.35	10.90	20.00	8.02	10.80
ℓ_Q [cm]	.46	.46	.46	.46	.46	.46	.46
Fr_0	66.	91.	17.	22.	41.	16.	22.
Re_0	6870.	9720.	1720.	2430.	4860.	1720.	2430.
T_{peak} [%]	11.0	11.0	39.0	38.5	39.0	24.5	25.0
$T_{L/2}$ [%]	6.5	7.0	28.0	30.0	28.0	24.0	24.0
T_L [%]	3.0	3.5	19.5	19.5	18.5	20.3	20.0
T_{2L} [%]	2.5	2.0	16.0	15.0	14.0	12.5	11.5
T_{4L} [%]	2.0	2.0	13.0	12.5	12.5	11.5	9.5
T_{4H} [%]	6.5	7.0	29.0	30.5	28.8	21.5	20.8
T_{8H} [%]	3.0	3.5	20.0	20.0	20.0	15.3	14.0
T_{16H} [%]	2.5	2.0	16.5	15.0	13.8	11.0	9.0
T_{32H} [%]	2.0	2.0	13.0	13.0	11.2	10.5	9.0
T_{64H} [%]	*	*	12.8	12.0	10.5	8.0	6.8
T_{128H} [%]	*	*	9.3	10.0	9.0	6.3	6.0
$x_{0.1}$ [L]	.31	.33	16.10	24.20	12.80	2.89	2.31
$x_{0.2}$ [L]	.00	.00	.97	1.10	.83	1.10	1.11
T_{S1} [%]	11.0	11.0	39.0	38.5	39.0	24.0	25.0
T_{b1} [%]	.0	.0	15.0	15.0	13.5	6.5	6.3
h_1 [cm]	3.1	3.6	.9	.9	.9	1.7	1.6
x_f [L]	.83	.88	6.39	4.12	4.12	5.10	5.39
T_{asym} [%]	5.3	4.0	14.3	11.8	10.5	10.8	8.5
T_{b2} [%]	.0	1.0	8.0	10.0	10.0	2.0	5.0
h_2 [cm]	4.7	5.7	1.5	2.0	2.0	1.6	1.9

Table D6b List of parameters and key results of scanning experiments

Experiment:	no data	no data	0921scan	0921scn2	0921scn3	0922scan	0922scn2
n			4	4	4	4	4
D_0 [cm]			.52	.52	.52	.52	.52
α [°]			0.	0.	0.	0.	0.
H [cm]			2.0	2.0	2.0	4.0	4.0
ΔT_0 [°C]			14.1	16.2	17.5	14.8	15.4
g_0' [cm/s^2]			3.95	4.68	5.11	4.14	4.33
Q_{T0} [cm^3/s]			20.3	28.8	57.5	20.3	28.8
M_{T0} [cm^4/s^2]			485.6	973.4	3892.1	485.6	973.4
B_{T0} [cm^4/s^3]			80.3	134.5	294.0	84.0	124.5
ℓ_M [cm]			8.16	10.60	20.30	8.00	11.00
ℓ_Q [cm]			.46	.46	.46	.46	.46
Fr_0			17.	22.	42.	16.	23.
Re_0			1720.	2430.	4860.	1720.	2430.
b_1 [L]			†	†	†	†	†
b_2 [L]			4.45	3.00	2.23	5.20	4.50
$A_{0.1}$ [L^2]			64.80	25.70	20.40	8.00	3.30
$A_{0.2}$ [L^2]			1.38	.38	.38	.32	.32
ϵ			.42	.42	.46	.65	.56
V_f [cm/s]			.35	.75	1.70	.31	.65

† – no steady-state * – data not recorded/not applicable

Table D7a List of parameters and key results of centerline experiments

Experiment:	0922cl3	0924cl	0924cl2	0925cl	1101cl	1102cl	1102cl2
n	4	4	4	4	1	1	1
D_o [cm]	.52	.52	.52	.52	1.03	1.03	1.03
α [°]	0.	0.	0.	0.	0.	0.	0.
H [cm]	4.0	8.0	8.0	8.0	4.0	4.0	4.0
ΔT_o [°C]	17.4	14.0	16.0	16.9	15.2	14.2	14.4
g'_o [cm/s^2]	5.09	3.93	4.61	4.92	4.35	4.00	4.02
Q_{To} [cm^3/s]	57.5	20.3	28.8	57.5	28.8	20.3	57.5
M_{To} [cm^4/s^2]	3892.1	485.6	973.4	3892.1	992.0	494.6	3968.0
B_{To} [cm^4/s^3]	292.5	79.9	132.6	283.2	125.2	81.2	231.2
ℓ_M [cm]	20.40	8.20	10.70	20.70	15.80	11.60	32.90
ℓ_Q [cm]	.46	.46	.46	.46	.91	.91	.91
Fr_o	42.	17.	22.	42.	16.	12.	34.
Re_o	4860.	1720.	2430.	4860.	4910.	3470.	9810.
T_{peak} [%]	26.5	15.0	15.5	16.0	42.0	41.0	43.0
$T_{L/2}$ [%]	24.0	15.0	15.5	16.0	14.0	15.5	14.0
T_L [%]	20.0	13.8	15.0	15.8	9.8	12.0	11.0
T_{2L} [%]	11.0	10.5	10.5	10.0	8.0	9.5	8.0
T_{4L} [%]	9.0	9.0	7.5	5.5	6.2	6.5	7.0
T_{4H} [%]	21.3	11.0	11.0	11.0	29.5	29.0	31.0
T_{8H} [%]	14.0	9.0	8.0	6.5	19.3	19.0	19.8
T_{16H} [%]	9.0	7.0	7.0	5.0	12.0	13.0	12.5
T_{32H} [%]	8.3	4.0	4.5	4.0	8.0	10.5	9.0
T_{64H} [%]	6.8	3.8	4.0	4.0	7.8	8.5	8.0
T_{128H} [%]	6.1	*	*	*	6.2	6.3	6.3
$x_{0.1}$ [L]	2.32	2.33	2.21	2.22	.89	1.44	1.33
$x_{0.2}$ [L]	1.12	.00	.00	.00	.32	.33	.37
T_{S1} [%]	25.5	15.0	15.5	16.0	42.0	41.0	43.0
T_{b1} [%]	6.8	.0	.0	.0	1.0	.0	1.5
h_1 [cm]	1.7	2.3	2.6	3.0	2.2	2.0	2.3
x_t [L]	3.70	5.40	2.85	3.69	1.90	1.22	1.27
T_{asym} [%]	8.0	6.8	6.5	5.5	8.0	9.0	8.0
T_{b2} [%]	7.0	.0	.0	4.0	2.0	1.0	6.0
h_2 [cm]	4.0	3.1	3.7	4.9	3.1	2.3	4.0

Table D7b List of parameters and key results of scanning experiments

Experiment:	0923scan	0925scan	0925scn2	0926scan	1103scn2	1103scan	1104scan
n	4	4	4	4	1	1	1
D_o [cm]	.52	.52	.52	.52	1.03	1.03	1.03
α [°]	0.	0.	0.	0.	0.	0.	0.
H [cm]	4.0	8.0	8.0	8.0	4.0	4.0	4.0
ΔT_o [°C]	17.2	14.5	16.1	15.9	15.1	13.0	16.9
g'_o [cm/s^2]	5.00	4.04	4.58	4.52	4.26	3.57	4.93
Q_{To} [cm^3/s]	57.5	20.3	28.8	57.5	28.8	20.3	57.5
M_{To} [cm^4/s^2]	3892.1	485.6	973.4	3892.1	992.0	494.6	3968.0
B_{To} [cm^4/s^3]	287.5	82.1	131.7	260.0	122.5	72.5	283.5
ℓ_M [cm]	20.50	8.08	10.70	21.60	16.00	12.30	29.70
ℓ_Q [cm]	.46	.46	.46	.46	.91	.91	.91
Fr_o	42.	17.	22.	44.	17.	13.	31.
Re_o	4860.	1720.	2430.	4860.	4910.	3470.	9810.
b_1 [L]	†	†	†	†	.09	.05	.02
b_2 [L]	3.06	10.90	5.00	2.80	1.10	.56	.70
$A_{0.1}$ [L^2]	1.46	4.30	2.40	2.10	.23	.78	.05
$A_{0.2}$ [L^2]	.52	.00	.00	.00	.01	.01	.00
ϵ	.52	†	.78	.67	.62	.60	.54
V_t [cm/s]	1.65	.20	.34	.60	.42	.30	1.20

† – no steady-state * – data not recorded/not applicable

Table D8a List of parameters and key results of centerline experiments

Experiment:	1107cl	1107cl2	1108cl	1110cl	1111cl	1111cl2
n	1	1	1	1	1	1
D_0 [cm]	1.03	1.03	1.03	1.03	1.03	1.03
α [°]	0.	0.	0.	0.	0.	0.
H [cm]	8.0	8.0	8.0	12.0	12.0	12.0
ΔT_0 [°C]	13.9	15.3	17.0	15.2	14.2	15.1
g_0' [cm/s^2]	3.90	4.35	4.96	4.33	4.00	4.27
Q_{T0} [cm^3/s]	20.3	28.8	57.5	57.5	20.3	28.8
M_{T0} [cm^4/s^2]	494.6	992.0	3968.0	3968.0	494.6	992.0
B_{T0} [cm^4/s^3]	78.7	125.1	285.2	249.0	81.0	122.8
ℓ_M [cm]	11.80	15.80	29.60	31.70	11.70	16.00
ℓ_Q [cm]	.91	.91	.91	.91	.91	.91
Fr_0	12.	16.	31.	33.	12.	17.
Re_0	3470.	4910.	9810.	9810.	3470.	4910.
T_{peak} [%]	24.5	23.5	21.8	14.3	18.0	17.0
$T_{L/2}$ [%]	12.0	12.3	14.0	13.5	10.0	11.8
T_L [%]	10.0	9.0	8.0	6.5	7.0	6.5
T_{2L} [%]	8.0	7.0	5.5	4.0	6.0	5.5
T_{4L} [%]	4.8	5.3	4.5	3.5	4.0	3.8
T_{4H} [%]	15.5	14.8	16.5	11.5	8.0	10.0
T_{8H} [%]	13.0	10.0	10.5	6.0	7.0	6.3
T_{16H} [%]	9.5	8.0	7.3	4.0	6.0	5.5
T_{32H} [%]	6.0	6.5	4.8	3.5	4.0	3.8
T_{64H} [%]	4.8	5.0	4.5	*	*	*
T_{128H} [%]	*	*	*	*	*	*
$x_{0.1}$ [L]	1.11	.89	.72	.67	.44	.56
$x_{0.2}$ [L]	.28	.27	.26	.00	.00	.00
T_{S1} [%]	24.5	23.5	21.8	14.3	18.0	17.0
T_{h_1} [%]	.0	.0	.0	.0	.0	.0
h_1 [cm]	2.6	3.3	3.6	4.8	4.0	3.9
x_t [L]	1.05	2.69	1.27	1.27	.99	1.45
T_{asym} [%]	8.5	6.0	6.0	5.0	6.0	6.0
T_{h_2} [%]	.0	.0	3.5	1.8	.0	.0
h_2 [cm]	2.5	2.1	3.7	6.2	2.3	2.7

Table D8b List of parameters and key results of scanning experiments

Experiment:	1109scan	1109scn2	1110scan	1113scan	1112scan	1112scn2
n	1	1	1	1	1	1
D_0 [cm]	1.03	1.03	1.03	1.03	1.03	1.03
α [°]	0.	0.	0.	0.	0.	0.
H [cm]	8.0	8.0	8.0	12.0	12.0	12.0
ΔT_0 [°C]	14.4	16.1	18.1	16.2	13.1	15.1
g_0' [cm/s^2]	4.00	4.55	5.32	4.66	3.57	4.22
Q_{T0} [cm^3/s]	20.3	28.8	57.5	57.5	20.3	28.8
M_{T0} [cm^4/s^2]	494.6	992.0	3968.0	3968.0	494.6	992.0
B_{T0} [cm^4/s^3]	81.2	130.9	305.9	267.9	72.5	121.4
ℓ_M [cm]	11.60	15.50	28.60	30.50	12.30	16.00
ℓ_Q [cm]	.91	.91	.91	.91	.91	.91
Fr_0	12.	16.	30.	32.	13.	17.
Re_0	3470.	4910.	9810.	9810.	3470.	4910.
b_1 [L]	†	†	†	†	†	†
b_2 [L]	†	2.00	.72	1.35	2.08	2.67
$A_{0.1}$ [L^2]	†	.20	.14	.10	.08	.06
$A_{0.2}$ [L^2]	†	.00	.00	.00	.00	.00
ϵ	.70	.75	.67	*	.83	.82
V_t [cm/s]	.30	.45	.68	*	.36	.43

† – no steady-state * – data not recorded/not applicable